(72)

Surface Water–Groundwater Interaction: The Spatial Organization of Hydrologic Processes Over Complex Terrain

by

Karen Plaut Berger

B.S., Stanford University (1994)
M.S., University of California, Berkeley (1995)

Submitted to the Department of Civil and Environmental Engineering
in partial fulfillment of the requirements for the degree of

Doctor of Philosophy
in Hydrology

at the

MASSACHUSETTS INSTITUTE OF TECHNOLOGY

June 2000

Author .....
Department of Civil and Environmental Engineering
June 2000

Certified by .....
Dara Entekhabi
Professor, Civil and Environmental Engineering
Thesis Supervisor

Accepted by .....
Daniele Veneziano
Chairman, Department Committee on Graduate Students

Surface Water–Groundwater Interaction: The Spatial Organization of Hydrologic Processes Over Complex Terrain

by

Karen Plaut Berger

Submitted to the Department of Civil and Environmental Engineering
on June 2000, in partial fulfillment of the
requirements for the degree of
Doctor of Philosophy
in Hydrology

Abstract

This research is motivated by two questions: (1) what is the spatial organization of hydrologic response resulting from the two-way coupling of the surface water and groundwater systems? (2) how much should new research and operational hydrologic models incorporate spatially distributed variables?

Distributed hydrologic processes are modeled using GSEM, a coupled groundwater–surface water equilibrium model. Long-term integrations of a mixed numerical-analytical treatment of two-way coupled groundwater flow and unsaturated soil moisture dynamics are performed. GSEM calculates equilibrium evaporation, runoff, recharge, and depth to saturation at each active cell in a two-dimensional horizontal grid. The model is applied to ten study basins from diverse climates and landscapes. Surface features are captured by digital topography at a grid resolution of 30 m. Mean annual climate characteristics are derived from monthly Poisson storm parameters and pan evaporation records. Daily precipitation and streamflow are assembled for use in flood-frequency analysis where available.

Patterns of subbasin variability exist in the spatial distribution of water table depth (Z_w). The water table is shallow in the riparian zone and deep near ridges. Formation of an intermediate midline zone depends on climate, soil transmissivity, and slope. Hillslope shape further influences Z_w across the midline region. The spatial patterns persist even under additional sources of variability, including vegetation and heterogenous soil depth and texture. The exact relationship of Z_w and fluxes to topographic indices differs between basins. Dominant modes of interbasin variability are characterized using principal component analysis. Four components, representing lateral moisture transport efficiency, basin climatic wetness, midline extent, and relief, together explain 80 percent of the variance in the original data. Stepwise regression reveals that basin climatic wetness and infiltration capacity best predict the runoff ratio.

The dynamic runoff response of catchments is investigated by assuming equilibrium hydrology is the most likely pre-storm condition. A probability distribution of runoff, applicable to both lumped and distributed soil moisture, is derived. Observed time series of precipitation and streamflow are divided into discrete events and aggregated into an exceedence probability distribution. The variable-moisture derived distribution agrees well with the observed distribution.

Thesis Supervisor: Dara Entekhabi
Title: Professor, Civil and Environmental Engineering

Acknowledgments

So many people to acknowledge, so little space. I am grateful for the continued guidance and support of my advisor, Dara Entekhabi, who had enough trust to let me finish this thesis from the other side of the country. The other members of my committee, Guido Salvucci, Kelin Whipple, and Rafael Bras, provided valuable input and suggestions. John Galantowicz, Rene Kim, and Chris Forest generously offered incalculable help in those early days on the steep learning curves of new computer languages. My colleagues in the Parsons Lab made it a wonderful place to work, providing friendship, academic advice and support, coffee breaks, and greatly easing the numerous little challenges of working remotely. And a further thanks to the people who aren't in Cambridge: to my father, for his encouragement at all things mathematical or scientific from an early age; and to my sister, for her unconditional love and our mutual support along the winding path to a doctorate. To the memory of my mother, whose words of pride still echo in my head; and to the memory of Laurie Kinsey, who passed away with just one chapter left to write and a world of opportunities at her doorstep. Last and most importantly, to my husband and best friend, Andrew, who was with me every step of the way, who was my patient teacher of subjects ranging from LaTeX to ultimate, and who in the process learned more about hydrology than he ever expected, my deepest love and gratitude.

Contents

List of Figures

List of Tables

Chapter 1

Introduction

1.1 Motivation

Topography and lithology combine with climate to influence local hydrologic conditions. The influence is felt on both short and long time scales. Within individual storms, runoff-generating saturated areas expand and contract in topography-based near-channel zones. On longer time scales, physical factors govern the distribution of net recharge and discharge zones with effects on the type of plant species, soil chemistry, and the occurrence of surface water bodies. The interaction of the surface and subsurface hydrologic systems plays a key role in determining the spatial variability of soil moisture and related fluxes.

This research is targeted at better understanding long-term surface water–groundwater interaction and the effects of catchment characteristics on this interaction. The two-way coupling of surface water and groundwater processes is best exemplified by the soil moisture content at the ground surface. Soil moisture can result from either surface or subsurface processes. Surface processes that affect soil moisture distribution are principally related to the local difference between infiltration and evaporation. Saturated subsurface flow redistributes moisture laterally; this brings moisture to the upper soil layers when the water table approaches the ground surface. The amount of moisture at the soil surface both governs and is governed by the magnitude and direction of these surface and subsurface fluxes.

Catchment characteristics influence how a basin responds hydrologically to a given set of forcing conditions. Surface topography drives the lateral redistribution of subsurface moisture through gravity-driven saturated flow. A steep landscape will tend to have high lateral transport and horizontal heterogeneity associated with the surface topography. The presence of convergent and divergent regions further affects soil moisture levels beyond what would be predicted by the downhill slope and thus directly impact local hydrology. Soil properties also affect the rate of water movement within the soil: vertical conductivity is a limiting factor for infiltration and recharge; horizontal conductivity governs lateral moisture movement; and porosity and pore-size distributions govern the amount of capillary rise above the saturated layer. The nature of the interaction between climate, physiography, and hydrology and its effect on spatial variability in soil moisture and runoff have been the focus of much field and modeling research.

1.2 Organization

This thesis addresses several questions:

- Does a physically-based model identify a quantifiable spatial organization in hydrologic fluxes?
- What combination of physical and climatic features influences interbasin variability in hydrologic response?
- What is the role of distributed information in estimating runoff response?

The thesis uses GSEM (Groundwater–Surface water Equilibrium Model), a distributed, physically based model with coupled surface water–groundwater interaction, to generate the equilibrium hydrology in a number of basins. GSEM is an extention of a groundwater–surface water equilibrium model that was developed for a two-dimensional cross-section of a simple hillslope (Salvucci 1994; Salvucci and Entekhabi 1995) and has been expanded for application to natural topography (Ateljevich 1995; Levine and Salvucci 1999). Chapter 2 describes the model assumptions and flux equations. Fluxes are integrated over a stochastic distribution of wet and dry periods to generate the long-term average values. The equilibrium conditions are used as the basis for all subsequent analysis.

The model is implemented over ten basins located in a range of climates and landscapes. Chapter 3 summarizes the physical, lithologic, and climatic characteristics of the selected basins. It includes the location and properties of field observations used in model assessment and runoff-response analysis.

Chapter 4 presents the spatial structure of the water table position and hydrologic fluxes within each basin. We investigate the spatial organization of hydrology within each basin and the extent of and reasons for the formation of the midline zone. In Chapter 5, we relax the initial assumptions of bare-soil and uniform soil properties. This allows examination of the sensitivity of the equilibrium hydrology to perturbations in the basins' physical characteristics.

The equilibrium hydrology is combined with geomorphologic and climatic features in an investigation of the principal modes of variability between basins in Chapter 6. We use principal component analysis to identify combinations of parameters that vary in unison and explain a significant amount of the aggregated variance of the original dataset. Stepwise regression allows identification of variable combinations which are highly correlated to hydrologic fluxes.

Chapter 7 derives runoff frequency distributions based on the assumption that the equilibrium distribution of soil moisture is the most likely condition prior to any storm. The response curves are compared against observed data for two of the basins to verify model performance and to identify the value of distributed hydrologic information in flood forecasting models.

1.3 Summary

It has long been known that most watersheds contain hydrologically distinct regions (*e.g.*, Penman 1951; Toth 1962; Dunne and Black 1970a). The distinctions may occur over short temporal scales (such as the expansion of runoff-contributing areas during a storm) or over long temporal scales (such as the presence of persistent net recharge and discharge

zones). This thesis seeks to combine characterization of long-term subbasin and interbasin variability to advance our understanding of the interaction between geomorphology and hydrology and its implications for basin-aggregated runoff response.

Chapter 2

Groundwater–Surface water Equilibrium Model (GSEM)

Precipitation occurring on the land surface may be partitioned into evaporation, runoff, recharge to the groundwater zone, and changes in the soil moisture storage. The relative magnitudes of these fluxes are important for many human activities, including agriculture, flood control, water supply, and hydropower generation. Hydrologists have sought for decades to model the surface water balance to better understand and predict the components of the hydrologic cycle. Models are characterized by how the individual processes and their interdependencies are represented. Many different approaches exist. The method and assumptions employed in a model depend, among other things, on the model purpose (*e.g.*, for real-time flood mitigation, incorporation into a general circulation model, or irrigation planning), the quantity and resolution of input data, and efficiency requirements (*e.g.*, whether the model must be run in real time or on a limited budget). Below we describe several different types of water balance models which have been used to characterize the partitioning of hydrologic fluxes in a watershed. The structure of the model used in this study is described in the context of this project's goals and available data.

2.1 Background

Field studies investigating relationships between spatially variable hydrology and physical features have identified consistent patterns in diverse landscapes. Toth (1966) studied a prairie in Canada and found evidence of persistent recharge and discharge zones, as identified by long-term indicators of water availability such as vegetation and chemical concentrations in the soil. Direct measurements of soil moisture have revealed that saturation tends to occur in valley bottoms, swales, and other concave areas (*e.g.*, Dunne and Black 1970a, 1970b; Anderson and Burt 1978). This has led to efforts to quantify the relationship between soil moisture and position on a hillslope or in a basin. Carson and Kirkby (1972) introduced the contributing area per unit contour length, a, as an indicator of the amount of moisture that will have aggregated from upslope areas and influence the soil moisture at a point. The influence of local relief was incorporated with the division of contributing area by the ground surface slope. This gave rise to a class of quasi-distributed models which use a topographic index to predict hydrology (*e.g.*, Kirkby 1975, 1978; Beven and Kirkby 1979; O'Loughlin 1981, 1986).

At the same time as quasi-distributed models were being developed and refined, hydrol-

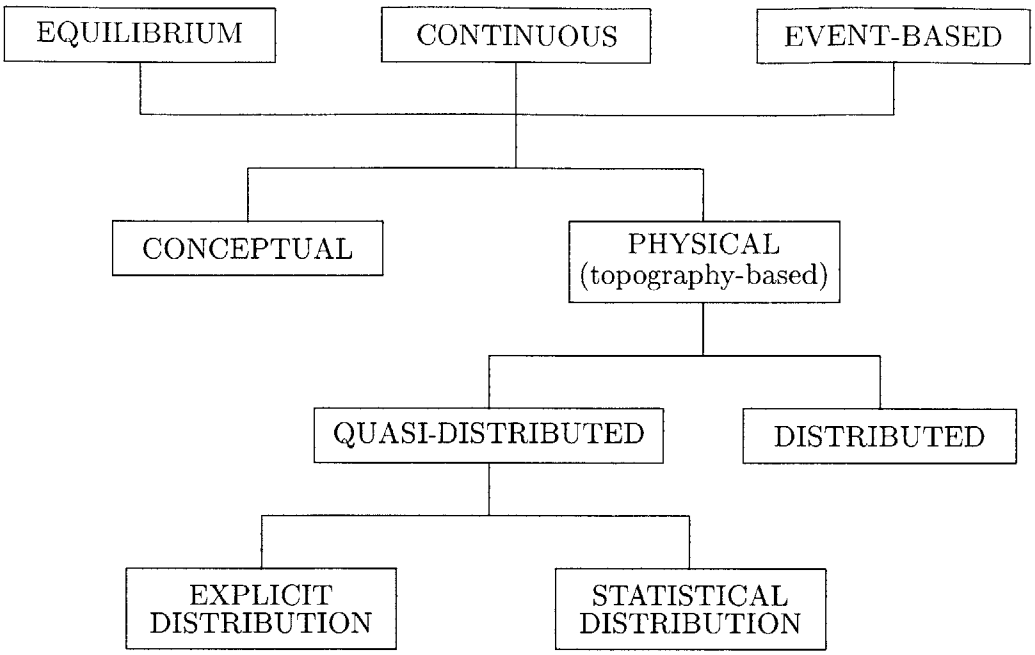

Figure 2-1: Schematic of different watershed model types.

ogists have been working on watershed models that aggregate from the underlying physical processes to the desired spatial scale. Initial watershed models were lumped, *i.e.*, heterogeneity is incorporated implicitly through the calibration of basin-scale parameters (*e.g.*, Burnash *et al.* 1973). With increases in computing power, the ability to model distributed processes has grown. Distributed models often use detailed formulations to describe the small-scale hydrologic fluxes, and numerical methods to solve for the hydrology in a three-dimensional system (*e.g.*, Abbot *et al.* 1986; Julien and Saghafian 1991; Garrote and Bras 1995).

2.2 Types of watershed models

A wide variety of models has been developed for the characterization and prediction of watershed hydrology. Differences in the goals of the model developers (*i.e.*, interest in flood prediction versus characterization of the entire hydrologic cycle) have led to significant differences between the models. Singh (1995) characterizes watershed models according to process description, scale (both spatial and temporal), and technique. These are not the only bases for classification; other differentiating criteria could include land use (*e.g.*, forested, rangeland, or urban) and model use (*e.g.*, planning, forecasting, or management). We combine some of the relevant information from the three classification systems described by Singh (1995) into a single schematic, shown in Figure 2-1. Our outline is designed to illustrate the differences between some of the main models used by hydrologists. Below we discuss the distinctions between the categories and cite examples of the different model types.

Equilibrium models concern themselves with long-term mean water balance characteristics as an indicator of how the equilibrium climate influences land surface hydrologic

processes. An early climatonomy model was introduced by Lettau (1969); climatonomy is defined as "a study of man's physical environment that is significantly more numerically and theoretically oriented than conventional climatology" (Lettau 1969, p. 691). The model predicts mean monthly hydrology—evapotranspiration, runoff, soil moisture, and change in storage—based on forcing by insolation and precipitation and a response governed by the "evaporivity" of the environment and a parameterized delay in evaporation and runoff. Lettau and Baradas (1973) modified the climatonomic model to incorporate the effect of soil moisture on model parameters, including albedo, evaporivity, and residence time. One sample application of the model is an examination of the relative role of rainfall and insolation on long-term features of the water balance, in a study of the persistence of drought in the West Africa Sahel (Nicholson and Lare 1990).

The Lettau climatonomy approach uses a simple model to examine equilibrium conditions with a few forcing and response parameters. A more detailed model of the physical processes governing the long-term average water balance was introduced by Eagleson (1978a). The model rests on the assumption that an equilibrium soil moisture, determined from the long-term balance of soil moisture inputs and outputs, adequately represents the conditions prior to all storms and interstorms (Salvucci and Entekhabi 1994b). The mean water balance is based on a linear average of forcing or response characteristics; the equilibrium hydrology is determined from a stochastic storm distribution applied to the equilibrium moisture state. Eagleson derived the long-term average water balance for a single vertical soil column (Eagleson 1978b, c, d, e, f g). Milly and Eagleson (1987) assembled a set of independent one-dimensional soil columns with distributed soil characteristics to examine the effects of physical spatial variability on the water balance. Salvucci and Entekhabi (1995) coupled the Eagleson equilibrium model for unsaturated zone fluxes to Darcy flow in the saturated zone to assess hydrologic conditions on a simple hillslope. The long-term water balance generated by the equilibrium model provides both information on sources of uncertainty in the water balance and a mechanism for examining long-term effects of changes to climate and landscape characteristics influencing the hydrologic cycle.

Event-based models are designed to investigate the response of a basin to a single event. Basins are modeled as the aggregate response of homogeneous sub-units. Units may be distinguished by lithology, land cover or use, elevation, or any other defining physical characteristic. Historic precipitation and streamflow records are used to calibrate the model parameters. While these models may do well in predicting the hydrologic response to individual events that fall within the range of the historic record, they often fail to capture longer-term effects such as slow-response groundwater or climatic variability.

Continuous models calculate a time series of hydrologic conditions based on a time series of forcing conditions (*i.e.*, rainfall, temperature, hours of sunlight). Unlike event-based models, continuous schemes are able to incorporate the effects from prior conditions on the response to storms. Soil moisture levels, for example, are kept track of over interstorm periods, providing information on low-frequency effects in the calculation of streamflow for any individual storm.

Conceptual models can be defined as models that "represent physical process dynamics using analytically tractable solutions to governing equations" (Troch

1993). These models are generally used for forecasting of flood volumes and levels; this information is valuable for engineering hydrology concerns such as reservoir management and damage mitigation. The Sacramento Model, for example, is the scheme used for catchment modeling in the operational National Weather Service River Forecasting System (Burnash *et al.* 1973). HSPF is a related model designed to integrate water quality processes into hydrologic modeling (Johanson *et al.* 1980). The models may be run either as continuous or event-based, depending on the desired output.

Because conceptual models are designed for operational purposes, they tend to minimize data and computational requirements. Both input and output are spatially lumped. A basin is separated into several hydrologic components, such as saturated and unsaturated stores, deep groundwater, and surface storage. Similarly to event-based models, calibration is based on historic records; general equations are solved by regression with time series of precipitation and streamflow. Although the identification of hydrologic components is based on the physical dynamics of the system, the parameters in conceptual models are often unrelated to a specific physical process or suite of processes. Consequently, it may be difficult to use conceptual models to assess the sensitivity of the hydrologic system to altered conditions such as climatic change or urbanization.

Quasi-distributed models are designed to incorporate the spatial variability of hydrologic processes without the intensive data and computational requirements of a fully distributed model. This compromise is achieved by using principles of hydrologic similarity between different locations in a basin. The distribution of similar subunits of a basin may be characterized either explicitly or statistically, as discussed below.

- **Explicit distribution:** Models which calculate a physically-based index to identify hydrologic similarity are considered to have an explicit distribution. The most widely used quasi-distributed model is TOPMODEL (Beven and Kirkby 1979), in which gridded digital elevation data are used to calculate a topographic index; the index can then be utilized to predict saturated areas, runoff, and evaporation. O'Loughlin (O'Loughlin 1981, 1986) developed TAPES–C, a related topography-based model in which a basin is subdivided into hydrologically similar hillslope strips. An alternative basis for identifying hydrologic similarity is land cover; this technique was incorporated into the SLURP model (Kite 1978).

  One concern with models based on topographic indices is that they may fail to incorporate temporal variability; TOPMODEL and TAPES–C both assume a series of steady-state solutions. Ladson (1990) found that weekly measurements of soil water showed a seasonal pattern. Several models have been developed to account for the lack of steady-state behavior in observed soil moisture in some locations. Barling *et al.* (1994) introduced a "quasi-dynamic" wetness index. Grayson *et al.* (1997) proposed a dual–index model that has a criterion for the transition between wet and dry conditions. Based on field data, they found support for two preferred states of soil moisture: a wet state, during which lateral flow (nonlocal control) drives the hydrology; and a dry state, during which the dominant fluxes are vertical, representing control by local conditions.

The quasi-distributed TOPMODEL framework for lateral moisture redistribution was coupled to more detailed physical representation of soil-atmosphere interactions by Famiglietti and Wood (1994a). They introduced the TOPMODEL based Land surface–Atmosphere Transfer Scheme (TOPLATS), a continuous model which uses the TOPMODEL index for representing topographic effects on the distribution of soil moisture, and a soil-vegetation-atmosphere transfer scheme (SVAT) for representing vertical water and energy fluxes. The model has closely matched evaporation and runoff measurements from a field project in the Kings Creek catchment in Kansas (Famiglietti and Wood 1994b; Peters-Lidard *et al.* 1997).

- **Statistical distribution:** The Variable Infiltration Capacity (VIC) model proposed by Wood *et al.* (1992) uses a statistical distribution for storage capacity. Instead of generating a distribution from physical characteristics, the statistical distribution has a single parameter which can be determined from calibration with historical records. The model was designed to allow for heterogeneous conditions within a grid square in a general circulation model without requiring extensive physical information. Sivapalan *et al.* (1997) used a similar approach in developing a variable bucket capacity model (VBC) based on a statistical distribution of the TOPMODEL topographic index. The topography-based distribution of soil moisture storage used in the VBC model was originally implemented in a gamma distribution for dimensionless flood frequency by Sivapalan *et al.* (1987).

Quasi-distributed models incorporate computationally-efficient ways of representing spatial heterogeneity in input and output. However, the explicitly-distributed models have several limitations that can potentially compromise their accuracy, including the following: (1) they require assumptions about the physical characteristics and processes defining hydrologic similarity; (2) the spatial sphere of influence on a single location is limited by the extent of the topographic index; and (3) sensitivity of the index to grid resolution and orientation may influence the model prediction. The limitations of statistically-distributed models stem from the use of a single statistical distribution to represent the storage capacity in different landscapes and the sensitivity of the model to the calibrated parameters.

Distributed models contain relatively detailed representations of the physical processes occurring in a watershed, resolved in both time and space. In order to capture the multiple processes, they are generally numerical models. For example, the European SHE model (Abbot *et al.* 1986) is a finite difference model; IHDM, the Institute of Hydrology distributed model (Calver and Wood 1995), is a finite element model; and THALES (Grayson *et al.* 1995) can be either a finite difference or finite element model along one-dimensional stream tubes. In the United States, the distributed runoff model is CASC2D (Julie and Saghafian 1991; Ogden 1997) is used by both Army Corps of Engineers and Department of Defense hydrologists. CASC2D has numerous built-in options for the representation of different physical processes, from interception, infiltration, and moisture routing to erosion and sediment transport. Garrote and Bras (1995) developed a distributed rainfall-runoff model for real-time forecasting in medium- to large-scale watersheds. Their model incorporates heterogeneous rainfall and uses an

elevation grid to characterize topographic influences on soil moisture and and runoff.

One benefit of distributed models is that they do not require a long time series for calibration. This makes them easy to test under different scenarios for the effects of physical or climatic changes in part or all of the basin. Additionally, fully distributed models do not depend on assumptions about hydrologic similarity, steady-state, or the distance at which the influence of physical characteristics becomes negligible. However, disadvantages of distributed models include the need for numerous input parameters, intensive computational requirements, and the questionable accuracy of process descriptions at the model scale.

2.3 Model description

We use a distributed equilibrium model which couples the processes in the saturated and unsaturated zones. The computational demand is reduced by using a numerical-analytic model instead of a fully numerical model (unsaturated fluxes are solved analytically). The approach is designed to optimize the physical realism of the model with minimal data requirements while providing distributed output that can be used in an examination of the quality and influence of spatially organized hydrologic processes. This section describes the rationale for the particular model attributes, the model assumptions, the main equations for unsaturated and saturated fluxes, and the iteration procedure used to generate the equilibrium hydrology.

2.3.1 Motivation

GSEM is a distributed, terrain-based, equilibrium model that allows the investigation of the influence of complex topography on the spatial distribution of hydrology. Our motivation for selecting the specific branches of the tree in Figure 2-1 in deciding to use a model of this class is the following:

Equilibrium: GSEM characterizes the long-term water balance using an equilibrium framework based on Eagleson's statistical dynamic formulation. The dynamic equilibrium is maintained through the water table–dependent recharge flux which either drains to or discharges from the saturated zone. The surface-atmosphere fluxes are balanced through the assumption of long-term stationarity of the mean moisture state. The equilibrium model is selected because it provides a climatic-scale overview of the water balance. Analysis of individual events or shorter time scale hydrology would limit our ability to consider the longer-term influence that groundwater has on rapid-response components of the hydrologic cycle such as runoff.

Physical: One of the main goals of this work is to identify the signature of surface topography in the distribution of water table depth and surface fluxes. It is therefore crucial that we use a topography-based, physical model to incorporate landscape characteristics. Furthermore, the hydrologic fluxes are based on soil hydraulic characterization such that there are no tunable parameters in the model.

Distributed: There are several models in widespread use which take a semi-distributed approach to physical watershed modeling. Our goal is to obtain distributed information about the hydrologic characteristics of a basin without making assumptions

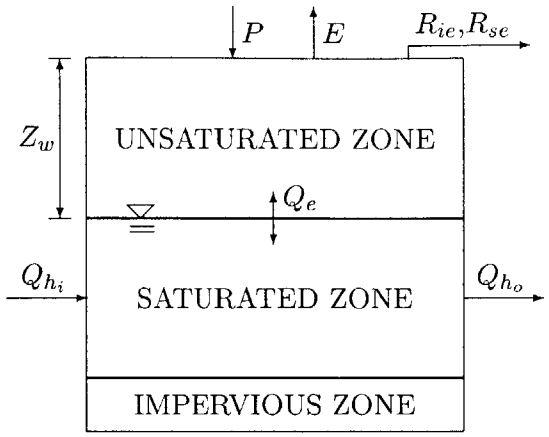

Figure 2-2: Schematic of coupling between saturated and unsaturated zones. Z_w is water table depth; P is precipitation; E is evaporation; R_{ie} is infiltration-excess runoff; R_{se} is saturation-excess runoff; Q_e is net recharge; and Q_{h_i} and Q_{h_o} are lateral influx and outflux between a pixel and its neighbors.

about the similarity of the response at different locations. This allows investigation of whether a fully distributed simulation supports the similarity relationships used in other models.

Beyond the framework outlined in Figure 2-1 is the interaction between surface water and groundwater processes. A fourth defining characteristic motivating the GSEM structure is the coupling of the unsaturated and saturated zones as illustrated in Figure 2-2. Although surface water and groundwater vary over different frequencies in time and space, groundwater anchors the soil moisture profile in the overlying unsaturated zone. Knowledge of the soil moisture profile is often the key parameter to accurate characterization of surface fluxes. In a continuous model, both recharge to the saturated zone and the influence of the water table on surface fluxes simultaneously influence hydrology. The interdependence of surface and subsurface processes are represented through the coupling of the two zones. In the next section, we present a description of GSEM, including the main process and parameter assumptions, derivation of the main flux equations, and the technique for applying the model to generate the equilibrium hydrology of a watershed.

2.3.2 GSEM assumptions

GSEM is based on the soil water dynamics model developed by Eagleson (1978a, b, c, d, e, f, g) and modified by Salvucci (1994) for a finite water table. Key assumptions about hydrologic processes include the following:

- Atmospheric forcing is represented by a Poisson series of rectangular pulses of precipitation with duration t_r and constant intensity i_r. Both duration and intensity are exponentially distributed, with inverse mean values δ and α, respectively. The

time between storms, t_b, is also exponentially distributed. During interstorm periods, evaporation is limited by the potential evaporation rate e_p.

- The Time Compression Approximation (TCA) is used to collapse a statistical sequence of flux and concentration boundary conditions to one solution (Salvucci and Entekhabi 1994b). Flux boundary conditions exist when the soil is climate controlled, *i.e.*, the soil can either infiltrate water at the rate of precipitation during storms or evaporate water at the atmospherically-demanded rate during interstorms. Concentration boundary conditions exist when the rate of infiltration or evaporation is limited by the soil rather than the atmospheric forcing; for example, a dry soil that cannot supply moisture at the potential evaporation rate will have a concentration boundary condition. The concept was extended to include transpiration following the Richard-Cowan framework by Levine and Salvucci (1999b). Given the probability distributions of storm and interstorm characteristics, the TCA integrates over the ensemble of possible storm intensities and durations to determine the long-term annual equilibrium value of each hydrologic flux. The equilibrium result is more realistic than that calculated from annual mean precipitation and evaporation depths because it incorporates the cycling of storm and interstorm events with the switching between soil- and climate-controlled boundary conditions.

- The time-averaged soil moisture profile that transmits the long-term mean recharge is used as the antecedent near-surface moisture profile before each storm and interstorm event (Salvucci and Entekhabi 1994b). This steady moisture profile is equal to the temporal mean moisture profile in linear soils and an adequate approximation of the mean in nonlinear soils (Salvucci and Entekhabi 1994a).

- Flow in the unsaturated zone is treated as a one-dimensional (vertical) process through a homogeneous soil. Both field observations and modeling studies (*e.g.*, Freeze 1972; Pan *et al.* 1997; Kim *et al.* 1997) have found that lateral unsaturated flow is insignificant relative to saturated flow. Freeze (1972) concluded that subsurface flow is only significant on convex hillslopes with high soil conductivities and deeply incised channels. Kim *et al.* (1997) found lateral unsaturated flow to be on average two orders of magnitude less than saturated flow. Several modeling studies linking the unsaturated and saturated zones have similarly assumed one-dimensional recharge (*e.g.*, Orlandini *et al.* 1996; Beverly *et al.* 1999; Sophocleous *et al.* 1999).

- Re-infiltration of runoff is negligible; precipitation is the only above-ground moisture source. This assumption is reasonable in an environment where runoff generation is dominated by saturation-excess rather than infiltration-excess, since saturation generally begins at the bottom of slopes and moves uphill in the absence of lithologic irregularities.

In addition to the above assumptions about hydrologic processes, we make several assumptions about model climate forcing and physiographic parameters. In any physical model, it is almost always possible to add finer resolution data. However, such improved resolution of input data comes at a price. Finer-scale models take more time and more powerful computers to run. High-resolution data are often unavailable or expensive to obtain for all of the relevant parameters. Simplifying assumptions are made so that the model has reasonable input and run-time requirements while maintaining physical realism. The assumptions

allow us to focus on some key climatic and physiographic processes and their partial roles in determining hydrologic response. These include the following:

- We neglect seasonality, using instead the Poisson parameters that give precipitation and evaporation depths equal to the mean annual values. Admittedly, most environments outside the tropics have a seasonal cycle in precipitation, temperature, and solar radiation (the latter two influence the potential evaporation rate). In this analysis, we look at annual values instead of seasonal for two reasons:

  1. When comparing the behavior in different basins, it is more straightforward to consider just one temporal state than a range of states in each environment.
  2. The expected value of soil moisture is assumed to represent the most likely antecedent soil moisture distribution in a given climate at any time throughout the year. If we used a seasonal cycle, generation of the flood-frequency curves would require additional information about the time of year during which large or small storms occur.

- The ground surface is assumed to be unvegetated. This assumption does not imply that vegetation is unimportant in the surface water balance in natural environments; in contrast, it can have significant effects on the distribution of evaporation and other fluxes. We calculate evaporation from bare soil to reduce the number of necessary modeling assumptions that arise when incorporating vegetation in a hydrologic model. As a recognition of the potential impact of plant cover, we perform a sensitivity study to investigate how vegetation may alter the results of the bare-soil model.

- We assume that the soil texture is spatially homogeneous in the lateral and vertical directions. Soil type varies stochastically on small spatial scales—hydraulic conductivity has been observed to follow a log-normal distribution in many geologic formations (Domenico and Schwartz 1990). Additionally, large-scale variation in soil type may arise from the presence of multiple lithologic units within a single watershed. Despite the known occurrence of stochastic and formational soil heterogeneity, we consider homogeneous soil texture to reduce the sources of variability to topographic effects. A sensitivity study examines the effect of different soil texture on the basin-scale hydrology.

- Soil depth is treated as uniform throughout each basin. In a sensitivity study, the implications of this assumption are investigated by introducing heterogeneous soil depth based on a model of landscape and soil mantle evolution and examining the impact on equilibrium hydrologic characteristics.

The results of the sensitivity studies are presented in Chapter 5.

2.3.3 Flux equations

Precipitation input at the ground surface may be partitioned into either evaporation, runoff, recharge, or a change in storage, as expressed in the surface water balance:

$$P = E + R + Q_e + \Delta S \tag{2.1}$$

where P is precipitation, E is evaporation, R is runoff, Q_e is recharge to the saturated zone, and ΔS is the change in soil moisture storage. At equilibrium, ΔS goes to zero

and the precipitation is partitioned between the first three terms only. Runoff may occur as either infiltration-excess or saturation-excess, depending on the local soil moisture and precipitation intensity.

The following paragraphs describe the relationships for unsaturated zone fluxes used in GSEM. For a full derivation of fluxes for an infinite water table, see Eagleson (1978a-g); modifications for a shallow water table are given in detail in Salvucci (1994). Supplementary equations are provided here in Appendix B.

Infiltration-excess runoff

Infiltration-excess runoff occurs when precipitation intensity exceeds the capacity of the soil to transport water vertically downward. Infiltration may be either soil- or climate-controlled. If soil-controlled, the infiltration rate is limited by the soil's infiltration capacity f_i^*. If soil hydraulics are not limiting, the infiltration flux is limited by the intensity of incident precipitation. The equilibrium infiltration is determined by integrating over the range of storm intensities and durations,

$$I = m_v \int_0^\infty \int_0^\infty \left(\min\left[f_i^*(t), i\right] dt\right) f_{t_r}(t) f_{i_r}(i) dt di \tag{2.2}$$

where $f_{i_r}(i)$ and $f_{t_r}(t)$ are the probability distributions of storm intensity and duration, respectively. Eagleson (1978e) uses the Philip solution (1957) to characterize infiltration, which gives the following expression for soil infiltration capacity:

$$f_i^* = \frac{1}{2} S_i t^{-\frac{1}{2}} + A_o \tag{2.3}$$

where S_i is the sorptivity and A_o predominantly represents gravitational effects. The two terms depend on soil characteristics and soil moisture, as explained in Appendix B. For a soil unbounded by a finite water table depth, mean annual infiltration-excess runoff is determined by integrating Equation 2.2 and subtracting from the total precipitation P, to give:

$$R_{ie}^{Eag} = P \left\{ \exp\left(-\alpha A_o - \mu\right) \cdot \Gamma\left(1 + \frac{1}{2}\mu\right) \cdot \left(\frac{1}{2}\mu\right)^{-\frac{1}{2}\mu} \right\} \tag{2.4}$$

with

$$\mu = \left[\alpha^2 \delta S_i^2\right]^{1/3} \tag{2.5}$$

The variable P is mean annual precipitation, α and δ are the inverse mean storm intensity and duration, respectively, $\Gamma(\cdot)$ is the Gamma function, and S_i and A_o are the sorptivity and gravity terms from the Philips infiltration formulation.

Salvucci (1994) modified this expression in two ways. First, sorptivity is changed to account for diffusivity in the tension saturated zone of the soil column (from the surface down to a depth equal to the bubbling pressure head); see Appendix B for details. Second, the presence of a bounding water table introduces column saturation as a factor in the equation. When the unsaturated zone has a finite depth, there exists an upper limit of infiltration, represented by the time to saturation t_s. Integration of infiltration using an upper bound on the time variable equal to t_s gives the following expression for infiltration-excess runoff for a finite-depth water table:

$$R_{ie} = R_{ie}^{Eag} \cdot \left(1 - e^{-\delta t_s}\left(1 + \delta t_s\right)\right) \tag{2.6}$$

where the time to saturation is calculated as

$$t_s = \begin{cases} \left(\sqrt{\frac{S_i^2}{4A_o^2} + \frac{\forall_e}{A_o}} - \frac{S_i}{2A_o}\right)^2 & A_o > 0 \\ \left(\frac{\forall_e}{S_i}\right)^2 & A_o = 0 \end{cases} \tag{2.7}$$

in which $\forall_e$ is the depth of available storage in the unsaturated zone.

Saturation-excess runoff

Saturation can result from either local infiltration, which causes a saturated wetting front to form at the surface and move downward through the column, or the lateral redistribution of groundwater. We assume here that the latter process is insignificant over the time scale of individual storms; it is accounted for by the saturated component of the model. Saturation-excess runoff due to wetting from above can be calculated by integrating over all possible storm intensities and durations, given the time to soil column saturation t_s, using the following equation:

$$R_{se} = \int_0^\infty \alpha e^{-\alpha i} \int_{t_s}^\infty i(t - t_s)\delta e^{-\delta t} dt di \tag{2.8}$$

In the calculation of infiltration-excess runoff, the approximation of time to saturation assumed that the pattern of infiltration prior to saturation was soil-controlled. Storms large enough to cause soil saturation tend to have large total storm depths; in this case, climate control is more significant than soil control. The climate-based time to saturation is the time needed for the precipitation intensity to fill the antecedent moisture deficit in the soil, or $t_s = \forall_e / i_r$, where $\forall_e$ is the depth of available moisture storage in the unsaturated zone. Using this approximation for the time to saturation gives the solution for mean annual runoff:

$$R_{se} = 2m_v \forall_e \mathrm{K}_2\left[2\sqrt{\alpha\delta\forall_e}\right] \tag{2.9}$$

where m_v is the mean number of storms per year and $\mathrm{K}_2[\cdot]$ is the modified Bessel function of the second order.

Bare-soil evaporation

When the soil is not covered by vegetation, evaporation is limited either by the ability of the soil to transport water upward to the ground surface or by the capacity of the atmosphere to evaporate available moisture. The average flux is therefore determined by integration of the smaller of potential evaporation (atmospheric control) and exfiltration capacity (soil control) over all possible interstorm durations:

$$E_{bs} = m_v \int_0^\infty \left[\int_0^t \min\left(f_e^*, e_p\right) dt\right] f_{t_b}(t) dt \tag{2.10}$$

where $f_{t_b}(t)$ is the probability distribution of time between storms and f_e^* is the exfiltration capacity. The exfiltration capacity for an unvegetated soil is defined by Eagleson (1978c)

as

$$f_e^* = \frac{1}{2} S_e t^{-\frac{1}{2}} - \frac{1}{2} K_{s_*} + w \tag{2.11}$$

where S_e is the soil- and moisture-dependent exfiltration desorptivity, K_{s_*} is the unsaturated hydraulic conductivity at soil saturation, and w is the maximum capillary rise. The solution of the integral results in Eagleson's expression (1978d) for mean annual evaporation:

$$E_{bs} = \bar{e_p} \left[1 - \left(1 + \sqrt{2} E e^{-E} + \sqrt{2E} \right) \right] \cdot \left(\Gamma \left[\frac{3}{2} \right] - \gamma \left[\frac{3}{2}, E \right] \right) \tag{2.12}$$

where $\bar{e_p}$ is the mean annual potential evaporation rate and $\gamma(\cdot, \cdot)$ is the incomplete gamma function. The quantity E is the evaporation effectiveness, which considers the interstorm climate and desorptivity characteristics of the soil:

$$E = \eta S_e^2 / (2 \bar{e_p}^2) \tag{2.13}$$

where η is the inverse mean interstorm duration, S_e is the exfiltration desorptivity, and $\bar{e_p}$ is the mean potential evaporation rate.

Salvucci and Entekhabi (1994a) make one important modification to Eagleson's evaporation scheme. Eagleson (1978c) assumed that the unsaturated hydraulic conductivity at soil saturation is much smaller than the soil desorptivity term in the exfiltration capacity (Equation 2.11). Salvucci and Entekhabi retain the K_{s_*} term; it appears in the modified dimensionless parameter Λ. The resulting modified equation for mean annual bare-soil evaporation is:

$$\begin{aligned} E_{bs} \;=\; & \frac{\bar{e_p} m_v}{\eta} \left\{ 1 - \left(1 + \sqrt{2\Lambda E} + (2\Omega)^{-\frac{1}{2}} \right) e^{-\Lambda E} + \right. \\ & \left. \left((2\Omega)^{-\frac{1}{2}} + \sqrt{2\Omega E} \right) e^{-\Omega E} + \sqrt{2E} \cdot \left(\gamma \left[\frac{3}{2}, \Omega E \right] - \gamma \left[\frac{3}{2}, \Lambda E \right] \right) \right\} \end{aligned} \tag{2.14}$$

where Λ and Ω are dimensionless parameter groups defined in Appendix B.

Transpiration by vegetation

The presence of vegetation affects the rate of moisture flux from the surface because roots provide access to deep regions of the soil profile that are moister than the near-surface soil. Bare-soil evaporation is limited by the available moisture at the surface; deeply penetrating roots may tap water far beneath the surface, resulting in higher flux rates. The vertical distance of root penetration is represented by the rooting depth Z_r.

The effect of vegetation on evaporation depends on the local moisture state, as illustrated in Figure 2-3. If the water table is at or very near the surface, the evaporative flux is limited by its atmospheric potential rather than by soil moisture; vegetation will not influence the flux rate. If the water table is located such that there is a moisture deficit at the surface, but the roots extend into the saturated zone, the vegetation increases the evaporation flux from a soil-limited rate to the atmospheric potential rate. When the water table lies below the rooting depth, evaporation occurs at the moisture-limited rate corresponding to the soil moisture at the deepest level of the root system. This flux rate is higher than the bare-soil rate, which is a function of the soil moisture at the ground surface.

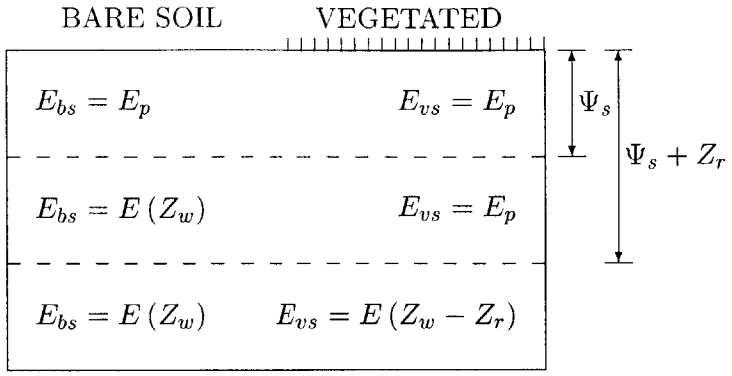

Figure 2-3: Conceptual illustration of the dependence of evaporation rate on position of the water table relative to Ψ_s and Z_r. Note that the mathematical expression for the delineation of the three zones differs slightly from the conceptual identification illustrated in this figure, since the mathematical expression uses capillary rise instead of water table depth as the dependent variable.

An alternative mathematical representation of the different vertical zones influencing evaporation is done using the maximum capillary rise, w. This variable represents the maximum height to which water can move upward due to capillary pressure in the soil matrix; in this case, it signifies the potential moisture influx from the saturated zone available to meet external moisture demands from the unsaturated zone such as percolation and atmospheric evaporative demand. Capillary rise depends on the depth of the water table; for Brooks-Corey soils, the expression is:

$$w = \frac{K_s}{(Z_w/\Psi_s)^{mc} - 1} \tag{2.15}$$

where K_s is the saturated hydraulic conductivity, Ψ_s is the bubbling head, m is the pore size distribution index, and c is the pore disconnected index. The evaporation rate depends on the value of w relative to the atmospheric evaporative demand e_p and the gravitational percolation associated with the surface soil moisture $\frac{1}{2}K_s s_*^c$. When the capillary rise is greater than the sum of moisture removal due to percolation and atmospheric demand, evaporation is able to occur at the potential rate. In other words, the capillary tension in the soil provides a vertical influx of moisture to the surface that exceeds the outflux of moisture to percolation and evaporation, keeping the soil fully saturated. This corresponds to the upper layer of the soil, where both bare-soil and vegetated-soil experience potential evaporation. In the lowest zone, where the capillary rise is less than percolation, the pressure-induced moisture influx is not even enough to meet the percolation flux. In this region, the formula is the same as that in Equation 2.14 except for a modified definition of the dimensionless parameter Λ. Combining the three zones gives the following equation for evaporation from a vegetated surface (Levine and Salvucci 1999):

$$E_{vs} = \begin{cases} \frac{e_p m_v}{\eta} & w > \frac{1}{2} K_s s_*^c + e_p \\ \frac{e_p m_v}{\eta} \left\{ 1 - \left(1 + \sqrt{2\Lambda} E + \frac{K_s s_*^c}{2 e_p} - \frac{w}{e_p} \right) e^{-\Lambda E} + \right. & \frac{1}{2} K_s s_*^c < w < \frac{1}{2} K_s s_*^c + e_p \\ \left. \sqrt{2E} \cdot \left(\Gamma \left[\frac{3}{2} \right] - \gamma \left[\frac{3}{2}, \Lambda E \right] \right) \right\} & \\ \frac{e_p m_v}{\eta} \left\{ 1 - \left(1 + \sqrt{2\Lambda} E + (2\Omega)^{-\frac{1}{2}} \right) e^{-\Lambda E} + \right. & \\ \left((2\Omega)^{-\frac{1}{2}} + \sqrt{2\Omega} E \right) e^{-\Omega E} + & w < \frac{1}{2} K_s s_*^c \\ \left. \sqrt{2E} \cdot \left(\gamma \left[\frac{3}{2}, \Omega E \right] - \gamma \left[\frac{3}{2}, \Lambda E \right] \right) \right\} & \end{cases} \tag{2.16}$$

The modified parameter groups Λ and Ω are defined in Appendix B.

Recharge

Recharge, the flux between the unsaturated and saturated zones, is the residual of a mass balance for the unsaturated zone, as illustrated in Figure 2-4 and expressed by the equation

$$Q_e = P - (E + R_{ie} + R_{se}) \tag{2.17}$$

Recharge may be either positive or negative, depending on whether the net flux is to or from the saturated zone. Recharge is generally positive when the water table is deep because there is little evaporation or runoff from dry soil. In the limit, as evaporation tends to zero and no runoff occurs, $Q_e \to P$. In wet or saturated soils, in contrast, evaporation is climate-limited and therefore occurs at the potential rate. High evaporation rates can rarely be supported by infiltration without supplementary moisture from the underlying saturated zone. Neglecting runoff, the net flux may be simplified as $Q_e \to -E_p$.

Saturated flow

The equation for flow in the saturated zone is

$$\frac{\partial}{\partial x} \left(K_x \frac{\partial h}{\partial x} \right) + \frac{\partial}{\partial y} \left(K_y \frac{\partial h}{\partial y} \right) + \frac{\partial}{\partial z} \left(K_z \frac{\partial h}{\partial z} \right) = S_y \frac{\partial h}{\partial t} \tag{2.18}$$

where K_i is the hydraulic conductivity in the i direction and h is the hydraulic head. S_y is the specific yield of the soil, defined as the "volume of water extracted from the groundwater per unit area when the water table is lowered a unit distance" (Hillel 1998, p. 481). When conductivity is isotropic ($K_x = K_y = K_z = K_s$), the equation simplifies to

$$K_s \left[\frac{\partial^2 h}{\partial x^2} + \frac{\partial^2 h}{\partial y^2} + \frac{\partial^2 h}{\partial z^2} \right] = S_y \frac{\partial h}{\partial t} \tag{2.19}$$

The steady-state water table position is constant in time. Under these conditions, the specific yield term equals zero, and Equation 2.19 becomes the Laplace equation:

$$\nabla^2 h = 0 \tag{2.20}$$

The saturated zone is modeled using a three-dimensional finite difference formulation.

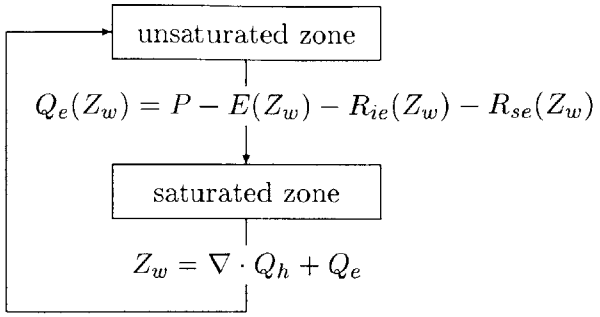

Figure 2-4: Technical schematic of GSEM iteration procedure. Q_e is recharge, P is precipitation, E is evaporation, R_{ie} is infiltration-excess runoff, R_{se} is saturation-excess runoff, Z_w is water table depth, and Q_h is horizontal saturated flux.

2.3.4 Model application

The equilibrium water table state is estimated through a transient simulation of GSEM, as illustrated in Figure 2-2. The coupling of the unsaturated and saturated zones through the recharge and water table depth is illustrated in Figure 2-4. The saturated zone is modeled using MODFLOW, a finite difference flux model developed by the U.S. Geological Survey (McDonald and Harbaugh 1988). The coupling of the Eagleson-Salvucci unsaturated fluxes to the groundwater model was originally carried out by Ateljevich (1995). The effective recharge calculated from the unsaturated zone analysis is input into MODFLOW in place of the recharge and evaporation subroutines. The distribution of water table depths calculated by the groundwater model is returned to the unsaturated zone code for calculation of a new recharge rate. This procedure is iterated until a stable solution is reached, beginning from a water table that is parallel to the ground surface. The simulation is considered to have reached equilibrium when at least 95 percent of the active pixels vary less than one centimeter between subsequent time steps (*i.e.*, the right hand side of Equation 2.19 is negligible). When the water table is calculated to lie above the ground surface, the excess moisture is "drained" off and the water table is set at the ground surface. In the opposite extreme, when the depth to saturation exceeds the depth of the soil column, the water table is set at the soil-bedrock interface and all incident precipitation is routed downhill.

2.4 Summary

We have described here GSEM, a coupled surface water–groundwater model which integrates over storm and interstorm periods to characterize the equilibrium hydrology in a catchment. The model is distributed in space, combining an analytical solution of unsaturated zone fluxes with a numerical model of saturated flow. GSEM provides equilibrium values for evaporation, saturation-excess runoff, infiltration-excess runoff, recharge, and depth to saturation at each active cell in a two-dimensional grid. This fully distributed dataset enables us to characterize the spatial patterns in hydrologic response at the resolution of the input data. In the next chapter, we describe characteristics of the basins selected for use in this study.

Chapter 3

Data selection

In the previous chapter, we presented GSEM, the model which is used to convert easily measurable physical characteristics into equilibrium hydrology. Ten basins from diverse climates and landscapes are selected for hydrologic comparison using GSEM. In this chapter we present the datasets used to characterize the study basins and related records. The relevant physical, climatic, and lithologic features of the basins are described. Surface features are captured by digital topography at a gridded resolution of 30 m. Mean annual climate characteristics are derived from monthly Poisson storm parameters and pan evaporation records. Information on soil type is obtained from the STATSGO database; spatially uniform values for soil depth and hydraulic properties are adopted according to the Brooks-Corey model. The combination of soil and climatic influences are represented through a single set of curves for each basin showing the dependence of the equilibrium hydrologic fluxes on water table location. Additional observed datasets of annual runoff and precipitation are used to compare modeled and observed basin-average runoff ratios. Time series of daily precipitation and streamflow are assembled for analysis of the response of basins to individual events at two of the ten locations.

3.1 Basin selection and characteristics

We select ten basins from across the continental United States for use in this study. The locations of the basins are shown in Figure 3-1; coordinates and information on basin size are summarized in Table 3.1. The basins' topographic features are characterized by 30 m resolution digital elevation models (DEMs). We select basins with a contributing area between 10 and 500 km^2. The minimum basin size is selected to ensure the presence of diverse physical features contributing to the complexity of the terrain. Convergent and divergent areas, for example, have been observed to have distinct hydrologic responses; the juxtaposition of multiple topographic features in a natural landscape may influence the spatial nature of hydrologic response in a way that would be missed in analysis of hillslopes or very small subcatchments. Larger basins are not considered to avoid the need for a detailed channel routing algorithm.

A map of the climatic wetness for the continental United States is provided in Figure 3-2 for reference. The climatic wetness is defined as the mean annual precipitation divided by potential evaporation. Long-term average gridded precipitation is available from the Oregon Climate Service's PRISM dataset (Daly *et al.* 1994). Potential evaporation is calculated from monthly temperature values using the Thornthwaite technique (Bras 1990), which

Basin	Latitude [deg:min N]	Longitude [deg:min W]	Area [km^2]	S_{50} [%]	ΔH [m]
Bear	37:38	120:08	10.6	34	956
Big Creek	47:30	116:15	147	43	1104
Brushy	34:24	87:23	322	11	165
Midland	38:37	77:45	32.6	4	78
Moshannon	41:00	48:30	325	13	383
Ogden	39:08	96:45	11.7	8	99
Sacramento	38:38	121:30	19.4	1	29
Schoharie	42:15	74:15	113	18	760
Tombstone	31:45	110:08	12.9	11	227
Yreka	41:45	122:45	32.8	32	811

Table 3.1: Physical characteristics of study basins. S_{50} is the median of the steepest slope at each pixel; ΔH is the difference in elevation between the highest and lowest points in the basin.

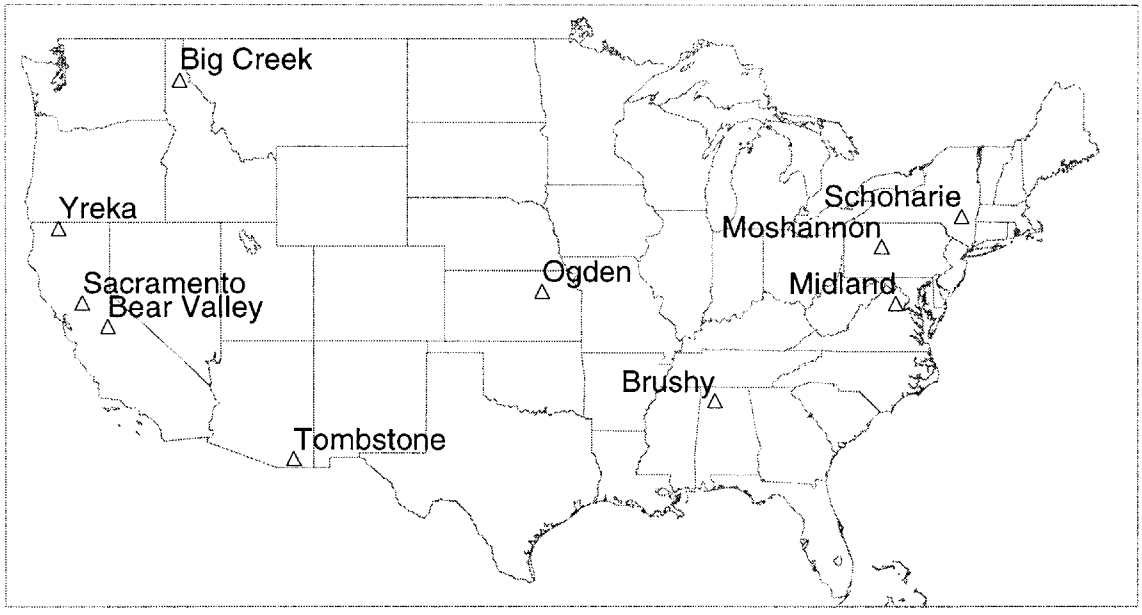

Figure 3-1: Study basin locations.

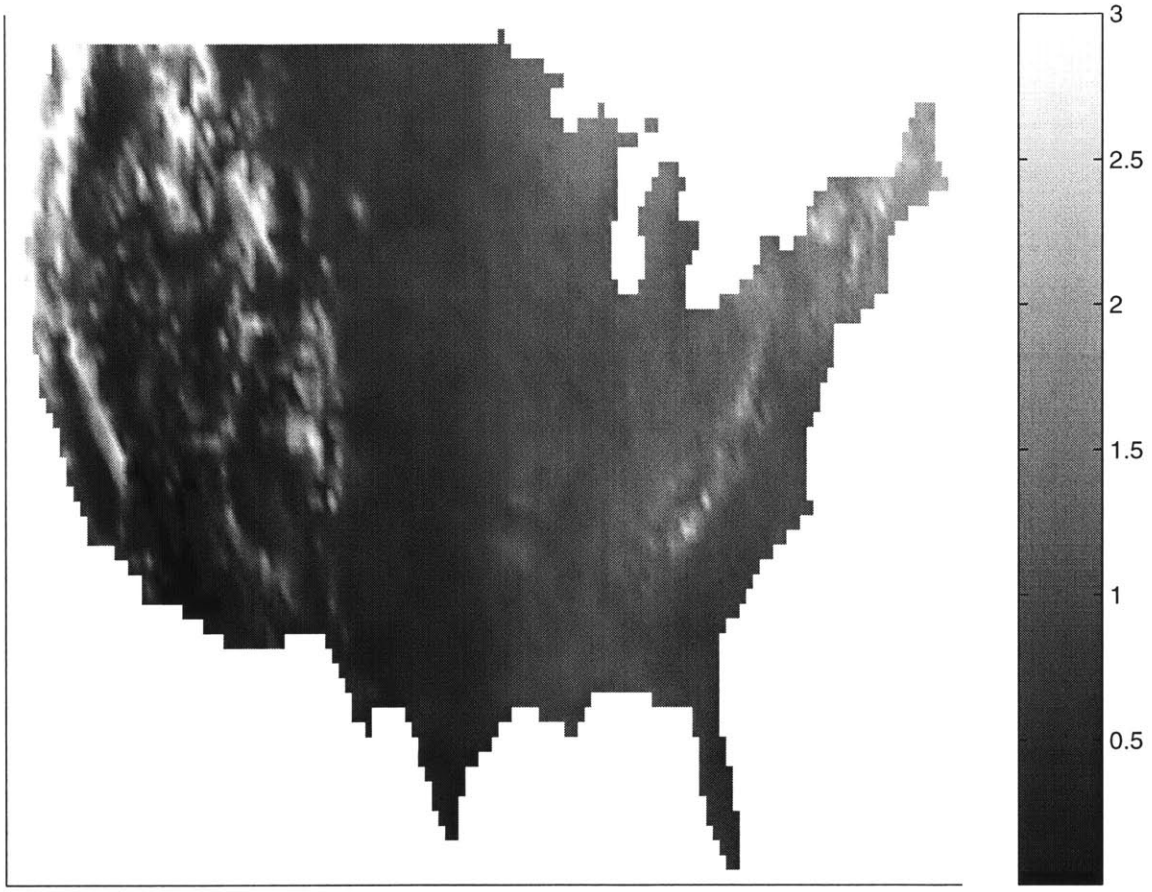

Figure 3-2: Map of climatic wetness for the continental United States. Wetness is defined as the ratio of mean annual precipitation to potential evaporation.

Basin	Total number of pixels	% of pixels adjusted	Mean adjustment [m]	Percent adjusted pixels with given fill depth 1–5 [m]	6–10 [m]	11–20 [m]	20+ [m]	Max fill [m]
Bear	11784	0	–	–	–	–	–	–
Midland	36246	10.2	2.0	98	2	0	0	9
Ogden	13019	4.7	2.2	94	6	0	0	10
Sacramento	21598	5.0	7.4	68	23	2	7	33
Tombstone	14298	2.5	1.7	99	1	0	0	6
Yreka	36451	0.2	2.6	86	14	0	0	8

Table 3.2: Statistics of adjustments made in filling pits in DEMs.

states that

$$E_p = 1.62b\left(\frac{10T}{I}\right)^a \tag{3.1}$$

where b is a sunshine index, which is a function of geometry (latitude); T is temperature in degrees Celsius;, I is a function of the monthly temperature,

$$I = \sum_{i=1}^{12}\left(\frac{T_i}{5}\right)^{1.51} \tag{3.2}$$

and a is a function of the temperature index I,

$$a = (67.5 \times 10^{-8})I^3 - (7.71 \times 10^{-6})I^2 + 0.0179I + 0.492 \tag{3.3}$$

Monthly temperature values are also obtained from the PRISM dataset. The monthly sunshine index is approximated as each month's average for the latitude range of the continental United States (30 - 45°), from Bras (1990). Notable features of the contour map are high wetness indices in the Pacific Northwest and along the Rocky, Sierra Nevada and Appalachian mountain ranges. The lowest values are found in the southwestern United States. The white pixels represent those areas with P/E_p greater than or equal to 3; the range was cut off at this level to highlight the variability across the United States.

3.1.1 Topographic characteristics

Digital elevation models often contain pits, where a single pixel is lower elevation than any of its neighbors. On horizontal scales of 10 m or more, pits occur rarely in natural topography; in DEMs they are generally due to data errors or sampling effects (Tarboton *et al.* 1991). Table 3.2 summarizes the adjustments made to the raw DEMs to fill any topographic pits. The adjustments are made using an automated routine developed by Tarboton *et al.* (1989). For most of the basins, the number and magnitude of the adjustments are small. Figures 3-3 through 3-7 contains maps of where pits were filled and by how much.

Maps of the surface topography of the basins are presented in Figures 3-11 through 3-20 at the end of this chapter. The basins differ not only in total or average relief, but also in the distribution of relief within the basin. Schoharie Creek, for example, consists of two sections, one of which contains much greater relief than the other. Sacramento, located

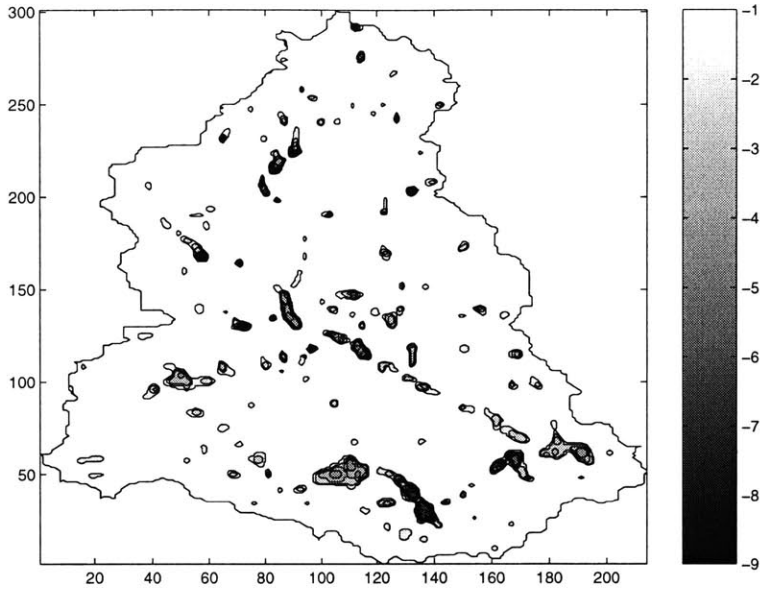

Figure 3-3: Map of filled pits, Midland, VA.

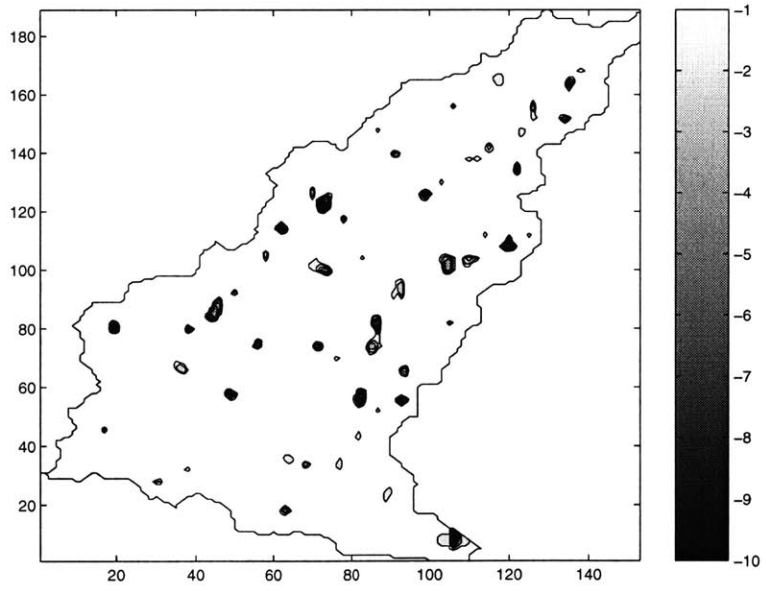

Figure 3-4: Map of filled pits, Ogden, KS.

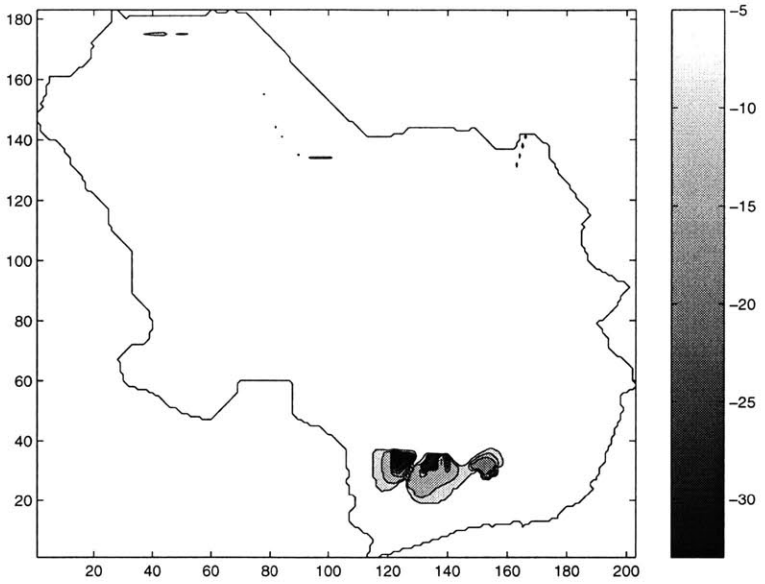

Figure 3-5: Map of filled pits, Sacramento, CA.

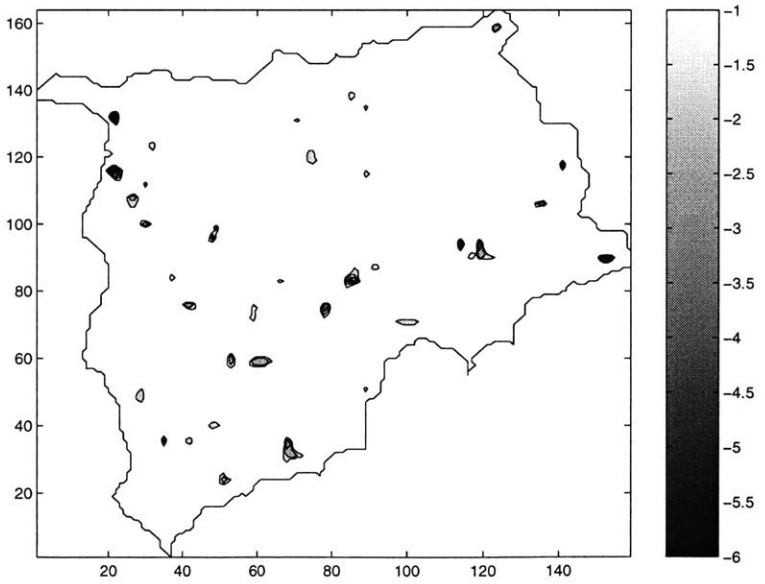

Figure 3-6: Map of filled pits, Tombstone, AZ.

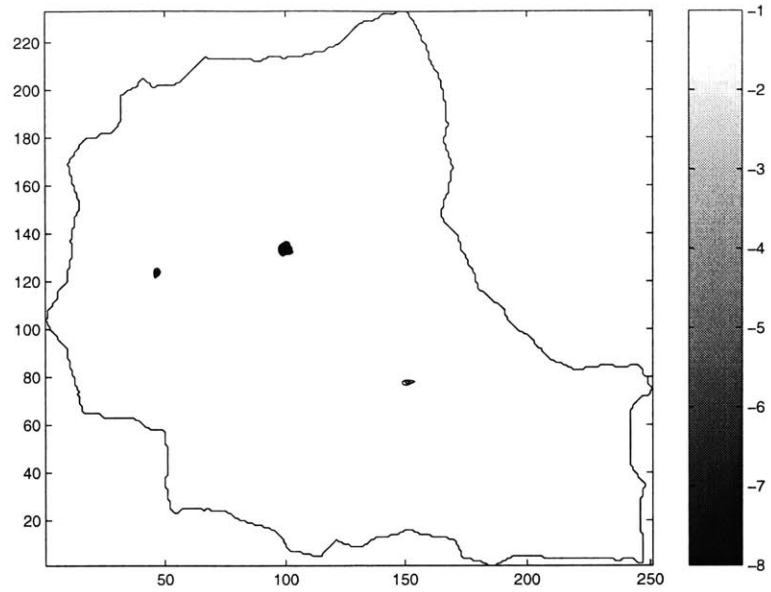

Figure 3-7: Map of filled pits, Yreka, CA.

within California's Central Valley, has very few visible features; the relatively coarse vertical resolution of the DEM results in the loss of most topographic variation in a basin this flat.

Within the constraints of DEM availability, we select basins to optimize diversity of climate, landscape, and soil characteristics. An underlying goal of this research is to investigate how different combinations of climate, landscape, and soil are related to the equilibrium hydrologic response of a basin. It is therefore desirable to ensure that the study basins contain different combinations of features, *e.g.*, that not all dry basins have similar terrain and lithology.

3.1.2 Climate characteristics

Monthly pan evaporation rates were assembled for the United States by Farnworth and Thompson (1982). The relationship between measured pan evaporation and atmospheric potential evaporation is defined as

$$E_p = \alpha E_{pan} \tag{3.4}$$

where α is assumed to be 0.7 (Linsley *et al.* 1992).

We obtain the Poisson parameters characterizing the stochastic nature of rainfall from Hawk and Eagleson (1992), who calculated monthly Poisson parameters from hourly National Climate Data Center precipitation records. Since we are interested in annual equilibrium, we calculate the annual average storm intensity and duration as the mean of the monthly values. An independent average of all four storm parameters would not necessarily maintain the observed annual precipitation and evaporation depths. The annual rainfall intensity and duration are calculated as the simple average of the twelve monthly values. The equations for the total flux depths are then used to calculate the effective mean values of interstorm duration $\bar{t_b}$ and potential evaporation rate $\bar{e_p}$. By definition, the total precipitation and evaporation depths of a Poisson process are given by the following equations:

Basin	P [m/y]	E_p [m/y]	P/E_p [–]	i_r [mm/d]	t_r [d]	t_b [d]	e_p [mm/d]
Bear	0.8	0.7	1.2	17	0.60	4.0	2.1
Big Creek	0.4	1.3	0.3	13	0.55	4.9	3.9
Brushy	1.4	1.3	1.1	50	0.24	3.0	3.9
Midland	1.1	1.1	1.0	41	0.24	3.0	3.3
Moshannon	1.1	0.6	1.8	35	0.23	2.5	1.9
Ogden	0.5	1.4	0.4	33	0.28	5.7	3.9
Sacramento	0.4	1.9	0.2	20	0.75	12.1	5.4
Schoharie	1.0	0.7	1.4	30	0.25	2.4	2.2
Tombstone	0.4	2.0	0.2	25	0.49	11.6	5.6
Yreka	0.5	0.8	0.6	14	0.85	8.5	2.4

Table 3.3: Climate characteristics of study basins. P is mean annual precipitation; E_p is mean annual evaporation; i_r is mean storm intensity; t_r is mean storm duration; t_b is mean time between storms, and e_p is mean potential evaporation.

$$P = \frac{i_r t_r}{t_r + t_b} \tag{3.5}$$

$$E_p = \frac{e_p t_b}{t_r + t_b} \tag{3.6}$$

Using the mean values of storm intensity and duration, Equation 3.5 can be rewritten to give the mean time between storms:

$$\bar{t_b} = \frac{\bar{i_r}\bar{t_r}}{P} - \bar{t_r} \tag{3.7}$$

The mean evaporation rate during interstorm periods is calculated using the annual potential evaporation depth adjusted from Farnworth and Thompson (1982),

$$\bar{e_p} = \frac{E_p(\bar{t_r} + \bar{t_b})}{\bar{t_b}} \tag{3.8}$$

This provides us with the annual average values of the four storm parameters—storm intensity, storm duration, interstorm duration, and potential evaporation—that correspond to the observed total precipitation and evaporation depths. The values for each of the basins are provided in Table 3.3. In all subsequent discussion, references to the climate characteristics assume the annual mean value.

The coordinates of the precipitation and evaporation measurements for each basin are summarized in Appendix C. Climatic records are selected from the nearest available site to each watershed. Where there was no precipitation record close to the basin, storm parameters are read from contour maps generated by Hawk and Eagleson (1992); this is the case in Bear Valley, Moshannon, Sacramento, Schoharie, and Yreka basins.

Basin	Ash	Loam-skeletal	Coarse loam	Loam	Fine loam	Fine silt	Fine	Clay
Bear	-	-	-	0.87	0.13	-	-	-
Big Creek	0.51	0.49	-	-	-	-	-	-
Brushy	-	-	-	0.33	0.17	-	-	0.50
Midland	-	0.02	-	-	0.85	0.10	0.03	-
Moshannon	-	0.03	-	-	0.79	0.03	-	0.15
Ogden	-	-	-	0.02	-	0.24	0.72	0.02
Sacramento	-	-	0.01	-	0.11	-	0.88	-
Schoharie	-	-	0.88	0.12	-	-	-	-
Tombstone	-	0.60	0.25	0.14	-	-	-	-
Yreka	-	0.85	-	-	0.14	-	0.01	-

Table 3.4: Fractional distribution of soil classes within each basin, from STATSGO database.

Basin	K_s [m/d]	Ψ_s [m]	n_e	m
Bear	1.5	0.36	0.31	2.1
Big Creek	2.9	0.25	0.25	3.3
Brushy	0.56	0.65	0.39	1.1
Midland	0.28	0.47	0.35	1.2
Moshannon	0.24	0.54	0.37	1.0
Ogden	0.14	0.72	0.41	0.75
Sacramento	0.14	0.72	0.41	0.74
Schoharie	2.8	0.26	0.26	3.2
Tombstone	2.0	0.32	0.29	2.6
Yreka	1.5	0.36	0.31	2.1

Table 3.5: Soil characteristics of study basins. K_s is saturated hydraulic conductivity; Ψ_s is Brooks-Corey bubbling head; n_e is effective porosity; and m is the Brooks-Corey pore size distribution index.

Basin	Z^* [m]
Bear	0.6
Big Creek	0.5
Brushy	1.5
Midline	1.1
Moshannon	0.7
Ogden	3.0
Sacramento	3.1
Schoharie	0.4
Tombstone	0.7
Yreka	0.8

Table 3.6: Depth in the soil column at which the flux between the unsaturated and saturated zones is zero.

3.1.3 Soil characteristics

Information on soil texture is obtained from STATSGO, the State Soil Geographic database (National Soil Survey Center 1992). The STATSGO database often contains multiple lithologic units within the bounds of a single watershed. The combinations of soil types found in each basin are presented in Table 3.4. We assume a single soil type across each basin to minimize the sources of subbasin variability. The representative soil type is identified as the average of up to three soil classifications with the largest areal coverage. Once the soil type is identified (*i.e.*, sandy-loam, fine-sand, etc.), we assign the Brooks-Corey soil hydraulics parameters according to the categories in Bras (1990); these values are provided in Table 3.5. We similarly assume a constant soil depth throughout the basin. The implications of these two assumptions (uniform soil texture and depth) are examined further in the sensitivity studies presented in Chapter 5.

3.1.4 Characteristic equilibrium fluxes

For a given soil and climate, the equilibrium fluxes depend on a single free variable: water table depth, Z_w. Every value of Z_w has an associated flux. The calculation of the depth-dependent fluxes can be done off-line from the model using the analytical equations for the unsaturated zone fluxes. Each combination of soil and climate results in its own distinct set of profiles. The profiles of the dimensionless fluxes for each basin are presented in Figure 3-8. The fluxes are normalized by precipitation to highlight the distribution of the incident precipitation to the different surface fluxes. Information about the climate and soil characteristics of the different basins is reflected in the variability of the equilibrium fluxes with depth and the associated Z^*, the depth at which the recharge flux is zero.

The values and shape of the flux curves depend on the joint influences of climate and soil. We focus initially on evaporation. For near-surface water tables, where evaporation is climate-controlled rather than soil-controlled, the normalized flux is equal to the inverse of the climatic wetness index P/E_p. As the water table depens, the behavior of the evaporation curve depends on the soil texture. In coarse-soiled environments, E/P tends to zero for deep Z_w. In finer soils, even large values of Z_w maintain a significant allocation of incident precipitation to evaporation. Finer soils are able to sustain a high rate of evaporation at deeper water table levels because fine soil can sustain more capillary pressure. The high

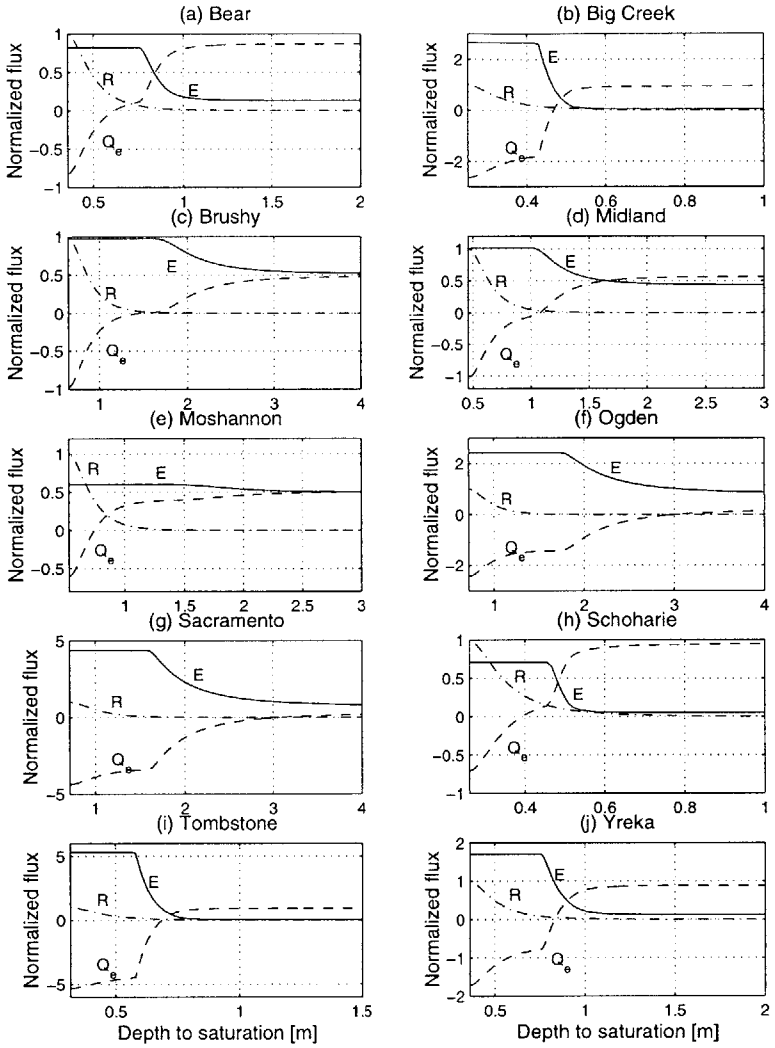

Figure 3-8: Equilibrium hydrologic fluxes, normalized by mean annual precipitation, as a function of water table depth. Solid line is evaporation; dashed line is recharge; dash-dot line is saturation-excess runoff. Infiltration-excess runoff is negligible for all depths. Recharge is positive downward.

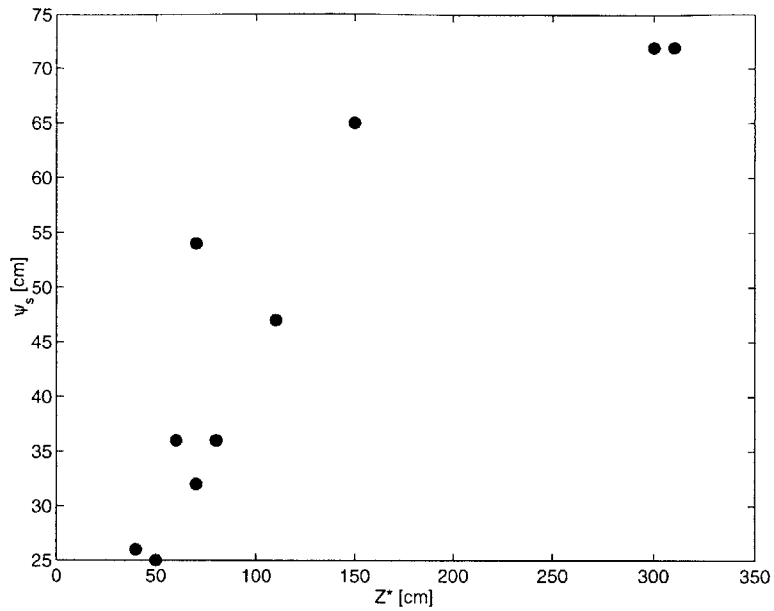

Figure 3-9: Relationship between zero-recharge depth and Ψ_s, for all basins.

capillary tension can also be seen in the large range of water table depths over which recharge is negative (upward) in fine-grained basins. Coarser soils are more likely to have gravity-dominated drainage, resulting in their rapid decline in evaporation with water table depth. This can be seen through a comparison of the zero-recharge depth Z^* and the Brooks-Corey bubbling head Ψ_s. The comparison is shown in Figure 3-9. The magnitude of Z^* represents the rapidity of the decline in evaporation and increase in recharge with deepening of the water table. The value of Ψ_s is inversely related to the coarseness of the soil. Figure 3-9 shows that the rate of change in flux values is positively related to the coarseness of the soil.

As seen in Figure 3-8, Z_w is the independent variable upon which evaporation, runoff, and recharge are based. In any basin, the local water table depth determines the corresponding flux values. This enables us to use Z_w as a proxy for any of the three fluxes (evaporation, runoff, and recharge) in studies of the spatial distribution of hydrologic processes.

3.2 Selection of long-term streamflow and precipitation data

In addition to identifying the climate and soil characteristics of the study basins, we require precipitation and streamflow records for comparison with the model output. Long-term average gridded precipitation is available from the Oregon Climate Service's PRISM dataset (Daly *et al.* 1994). Daily time series of rainfall are compiled by the National Climate Data Center (NCDC 1997). Daily streamflow is available from the U.S. Geological Survey (USGS) on-line surface water data (1999). A subset of the USGS stations have been screened for quality and duration of the record; these are provided in the Hydro-Climatic Data Network (HCDN) by Slack *et al.* (1992, 1993). Data for the Tombstone basin are obtained from Agricultural Research Service (ARS) measurements of both runoff and precipitation at the experimental watershed at Walnut Gulch, AZ (1999).

Basin	Station number	Latitude [deg:min N]	Longitude [deg:min W]	Datum [m]	Area [km^2]	Dates of record
Bear	11321500	38:13	120:58	N.A.	13.5	1932–1934
Big Creek	12414350	47:18	116:07	N.A.	100	1980–1981
Brushy	03586500	34:40	87:19	164	430	1948–1997
Midland	01655500	38:44	77:47	128	31.9	1950–1987
Moshannon	01542000	40:51	78:16	441	178	1940–1993
Ogden	06879650	39:06	96:36	334	10.6	1979–1998
Sacramento	11447030	38:36	121:24	N.A.	13.0	1972–1975
Schoharie	01365000	41:52	74:29	266	90.1	1938–1980
Yreka	11512000	41:59	122:22	720	37.8	1933–1959

Table 3.7: Location and characteristics of USGS streamflow observations.

The precipitation and streamflow data are used for two purposes: (1) to compare long-term, basin-averaged runoff ratios, and (2) to characterize the runoff response of model and observations. The duration of the observed record is of critical importance for the latter investigation given the low probability of an extreme event occurring at any time in the record. Below we describe the procedure for data selection from the rainfall and streamflow datasets.

Several issues must be considered in selecting specific records from the datasets, including gage location, elevation, drainage area, and series length. The availability of high-quality streamflow sites is more limited than the number of precipitation gages. Many U.S. streams and rivers have been subject to hydraulic controls that affect the measured streamflow regime. Controls may include flow diversion or augmentation, regulation of streamflow by a containment structure, base flow reduction from high ground-water pumping, and explicit channel modification (Slack and Landwehr 1992). Exclusion of impaired basin conditions reduces the number of possible streamflow records.

We begin by selecting a stream gage that is relatively near and drains an area similar in size to the model basin to which it will be compared. The gage locations and characteristics are given in Table 3.7. Only two of the ten study basins had a high-quality streamflow record in close proximity to the basin with at least ten years of observations, the limit set for the flood-frequency analysis. The extended, high-quality streamflow dataset largely contains basins of two extremes with respect to drainage area: small, headwater catchments that have not experienced anthropogenic hydraulic controls; and large, expansive basins over which the hydraulic controls have had a uniform impact on hydrology over the period of record.

Once a streamflow site is selected, precipitation values are obtained from the PRISM Climate Mapping Program. PRISM (Parameter-elevation Regressions on Independent Slopes Model) uses point data and digital elevation maps to create gridded estimates of monthly and annual precipitation. The model is designed to accomodate complex climatic behavior such as orographic forcing of precipitation and coastal effects (Daly *et al.* 1994; Daly *et al.* 1997). The grid resolution is 0.04 degrees.

Basin	model P [m]	model R_T [m]	model R/P [–]	obs. P [m]	obs. R_T [m]	obs. R/P [–]
Bear	0.81	0.18	*0.21*	0.50	0.04	*0.08*
Big Creek	0.48	0.34	*0.72*	1.11	1.02	*0.92*
Brushy	1.35	0.15	*0.11*	1.43	0.56	*0.39*
Midland	1.10	0.08	*0.07*	1.04	0.36	*0.35*
Moshannon	1.06	0.39	*0.36*	0.97	0.56	*0.61*
Ogden	0.56	0.00	*0.00*	0.85	0.06	*0.07*
Sacramento	0.42	0.00	*0.00*	0.48	0.26	*0.54*
Schoharie	1.03	0.56	*0.53*	1.22	0.89	*0.73*
Tombstone	0.37	0.05	*0.14*	0.33	0.00	*0.01*
Yreka	0.47	0.13	*0.26*	0.51	0.94	*1.80*

Table 3.8: Model and observed precipitation and total streamflow values, for all basins.

Basin	model P [m]	model R [m]	model R/P [–]	obs. P [m]	obs. R [m]	obs. R/P [–]
Bear	0.81	0.13	*0.17*	0.50	0.03	*0.07*
Big Creek	0.48	0.01	*0.03*	1.11	0.27	*0.25*
Brushy	1.35	0.15	*0.11*	1.43	0.33	*0.23*
Midland	1.10	0.08	*0.07*	1.04	0.15	*0.14*
Moshannon	1.06	0.38	*0.34*	0.97	0.13	*0.14*
Ogden	0.56	0.00	*0.00*	0.85	0.00	*0.00*
Sacramento	0.42	0.00	*0.00*	0.48	0.23	*0.47*
Schoharie	1.03	0.23	*0.22*	1.22	0.26	*0.21*
Tombstone	0.37	0.04	*0.13*	0.33	0.00	*0.01*
Yreka	0.47	0.06	*0.14*	0.51	0.05	*0.09*

Table 3.9: Model and observed precipitation and storm runoff (base flow removed), for all basins.

3.3 Comparison of equilibrium runoff ratios

The runoff ratio (runoff per unit area divided by precipitation) indicates the fraction of precipitation which is routed into channels as either surface or subsurface runoff. A rough comparison of modeled and observed runoff is performed using annual average observed values from the USGS and PRISM datasets and the modeled equilibrium fluxes. Tables 3.8 and 3.9 summarize the modeled and observed runoff and precipitation depths and resulting runoff ratios. Table 3.8 presents values for total streamflow (R_T); the runoff values in Table 3.9 have had base flow removed.[1]

Figure 3-10 provides a visual comparison of the ten runoff ratios based on total and storm (base flow–subtracted) runoff. Given that the model is uncalibrated, the results are in reasonable agreement with the observed total streamflow. The most extreme outlier in the total streamflow case is Yreka; it has an observed R/P ratio of 1.8. The discrepancy could be caused by human alterations to the environment, the resolution of the precipitation

[1] A description of the base flow separation technique is presented in Appendix E. The smoothed-minima approach is the technique used in this analysis.

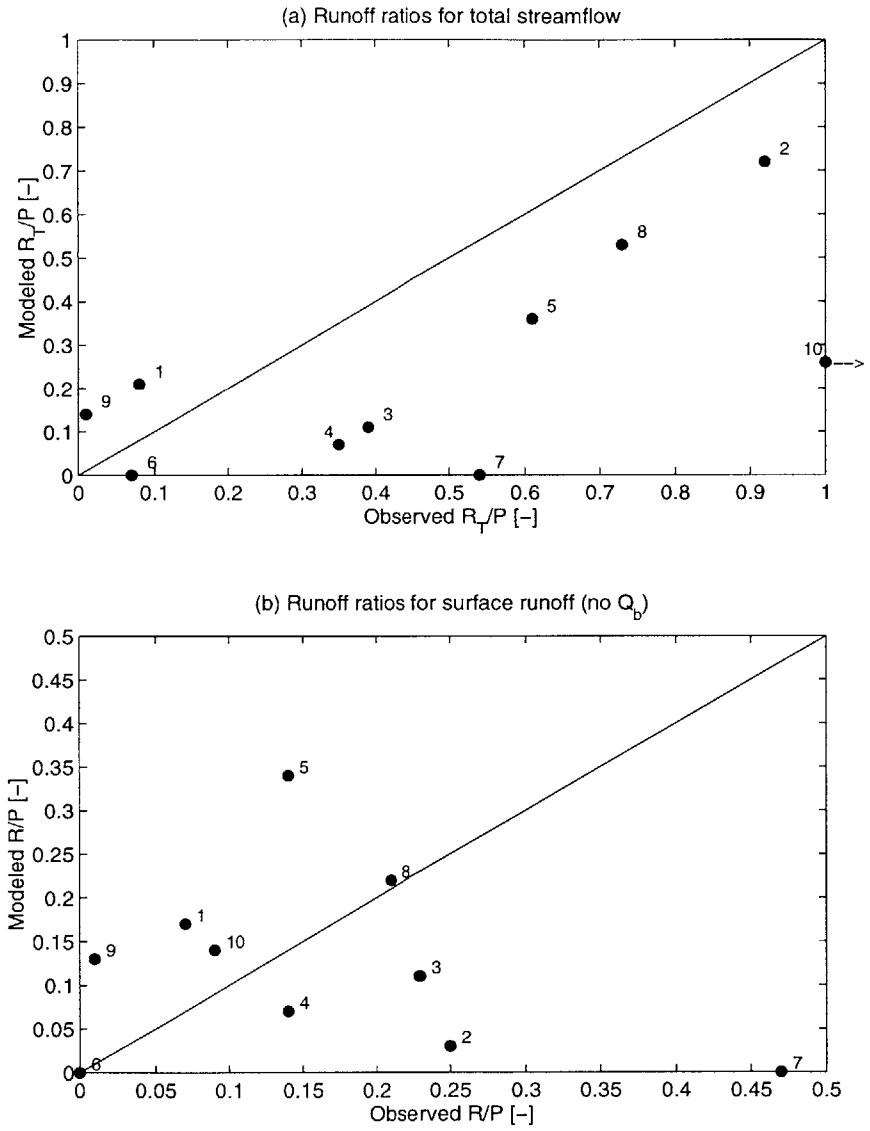

Figure 3-10: Comparison of modeled and observed runoff ratios for (a) total streamflow and (b) surface runoff only (base flow removed). The line represents a 1:1 fit for reference. Numbered circles represent (1) Bear, (2) Big Creek, (3) Brushy, (4) Midland, (5) Moshannon, (6) Ogden, (7) Sacramento, (8) Schoharie, (9) Tombstone, and (10) Yreka.

data, or the limited availability of rainfall and streamflow measurements in close proximity. The hydrology of California has been modified by both imports and exports between basins. Imports of water into the Yreka basin could explain how runoff exceeds precipitation. Alternatively, the the steep local terrain could result in highly variable rainfall that is not adequately modeled in the PRISM data. Although the PRISM precipitation values have been adjusted for topographic effects, the use of a single average value over the basin may nonetheless fail to represent the actual incident rainfall. Furthermore, because the rainfall varies over small spatial scales, a slight discrepancy between the location of the basin and the rain gage could result in significant differences in local precipitation. Similar problems may also explain the discrepancy in the modeled and observed values of the Sacramento basin. Of the remaining eight basins, each exhibits a deviation on the scale of 20 percent or less.

When base flow is removed from the streamflow depths, as shown in subplot (b), Yreka moves to fairly close agreement between model and observations. With very little estimated base flow, Sacramento is the largest outlier. The remaining basins are almost evenly split between those in which observed R/P exceeds modeled and vice versa. On average, the base flow removed from the observed time series is larger than the base flow estimated by the model.

Below we summarize numerous possible explanations for the discrepancies between observed and modeled runoff ratios, both with and without base flow. They include the following:

- The area drained by the USGS gages does not always perfectly overlap the contributing area of the GSEM basin. The latitude and longitude of the DEM and USGS streamflow gages are provided in Tables 3.1 and 3.7, respectively. A slight difference in the horizontal location of a measurement could affect either or both of the climate and physiography.

- The USGS contributing area differs from the GSEM contributing area by up to 45 percent. The difference is due to the limited number of high-quality USGS gages. In most environments, runoff does not scale linearly with contributing area (*e.g.*, Moore and Morgan 1969). The basin area reveals itself in the comparison of runoff ratios after base flow has been removed. Excluding the three driest basins, the four large basins—Big Creek, Brushy, Moshannon, and Schoharie—are clearly separated from the three smaller basins—Bear, Midland, and Yreka—by the magnitude of their runoff ratios.

- As previously discussed, observed runoff comes from spatially heterogeneous precipitation. This has two implications. First, runoff is normalized by a single value of precipitation; even if that value has been adjusted for topographic effects, it may not fully reflect actual incident rainfall within the particular basin. Second, the model assumes uniform precipitation; this causes a different prediction of runoff than if it was forced with spatially variable rainfall.

- Precipitation and evaporation vary seasonally. The annual runoff will be very different if the same annual rainfall falls almost entirely in a short time period (which is happening in some of the observed basins) or spread out over the entire year (which is what is implicitly assumed by the use of average annual climate parameters in the model).

- Some of the incident precipitation may occur as snow. Accumulation of snowpack and rapid snowmelt affect the distribution of precipitation into evaporation, runoff, and infiltration. The USGS records do not distinguish precipitation occurring as snow.
- Human interventions in the hydrologic cycle (*e.g.*, dams, water imports or exports from/to other watersheds, irrigation, and consumptive use) influence the amount of water both entering the basin as "precipitation" and exiting the basin as "runoff." Aqueduct imports, for example, increase the moisture available for runoff above the incident precipitation. The gages provided by the USGS are not screened for anthropogenic influences.[2]
- The model assumes uniform soil texture and depth. Any difference in the actual physical characteristics of the observed basin could affect the modeled runoff.

Discrepancies between the modeled and observed runoff ratios are to be expected given the lack of model of calibration and the use of a catchment-averaged, annual variable. The brief explanations provided here include some of the assumptions which may enhance the discrepancy and highlight the difficulty in adapting field measurements for use in hydrologic models.

3.4 Selection of time series for flood-frequency analysis

The flood-frequency investigation requires a time series of precipitation rather than long-term monthly or annual averages. We therefore use precipitation values from the NCDC dataset rather than PRISM. The selection of precipitation records is limited by the imposed requirement of at least ten years of measurements. Many of the rain gages have significant periods of missing data or were taken out of service after a few years of operation. It is imperative that the time series be long enough that some infrequent events are included since basin response to extreme events is an area of significant hydrologic interest. We select rain gages that fall within the same hydrologic unit as the stream gage, as specified by the USGS hydrologic unit code. While this means that the stream and rain gages are in the same general location, it does not ensure that the rain gage is physically located within the gaged drainage area. However, precipitation in these moist, relatively mild-sloped basins is not dominated by orographic forcing. We therefore assume that rain gages located within the larger hydrologic unit provide an adequate representation of incident precipitation in the subbasin of interest.

Table 3.10 summarizes the temporal characteristics of the two rain gage and stream gage sites selected for the flood-frequency analysis. We separate out summer storms (May through October, inclusive) to avoid contamination from snowmelt in the streamflow record.

3.5 Summary

We have selected ten study basins from diverse climates and landscapes. Surface features are captured by digital topography at a grid resolution of 30 m. Mean annual climate characteristics are derived from monthly Poisson storm parameters and pan evaporation records.

[2]The HCDN (Slack *et al.* 1992, 1993) dataset screens out basins with significant artificial influences on the hydrologic record. However, this dataset contains no basins that match all of the modeled basins in both size and location.

Variable	Brushy Creek	Schoharie Creek
Joint years	7/48–7/77	1/49–12/72
of record		1/75–9/80
Number of years	29	36.4
Number of storms	1686	1426
Summer storms	664	547

Table 3.10: Basin characteristics of observed streamflow and precipitation time series.

Information on soil type is obtained from the STATSGO database; spatially uniform values for soil depth and hydraulic properties are adopted according to the Brooks-Corey model. Mean annual precipitation and runoff values are used to compare the agreement between modeled and observed R/P values, both with and without base flow. Additional time series of daily precipitation and streamflow are assembled for comparison of the probability-based runoff response. Two of the ten basins have data which are of sufficient quality and duration for use in flood-frequency analysis. In the next chapter, we investigate the relationships between topography and the spatial organization of hydrologic response within each basin.

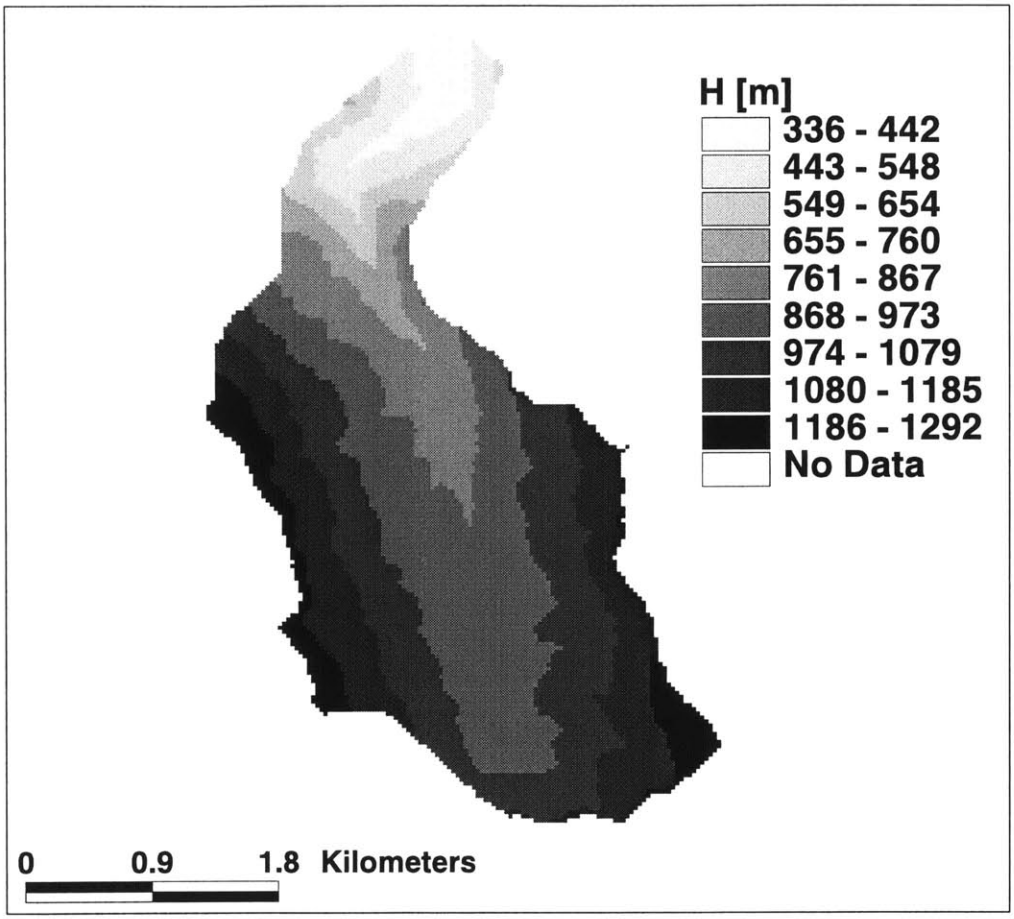

Figure 3-11: Surface elevation from 30-m DEM, Bear Valley, CA.

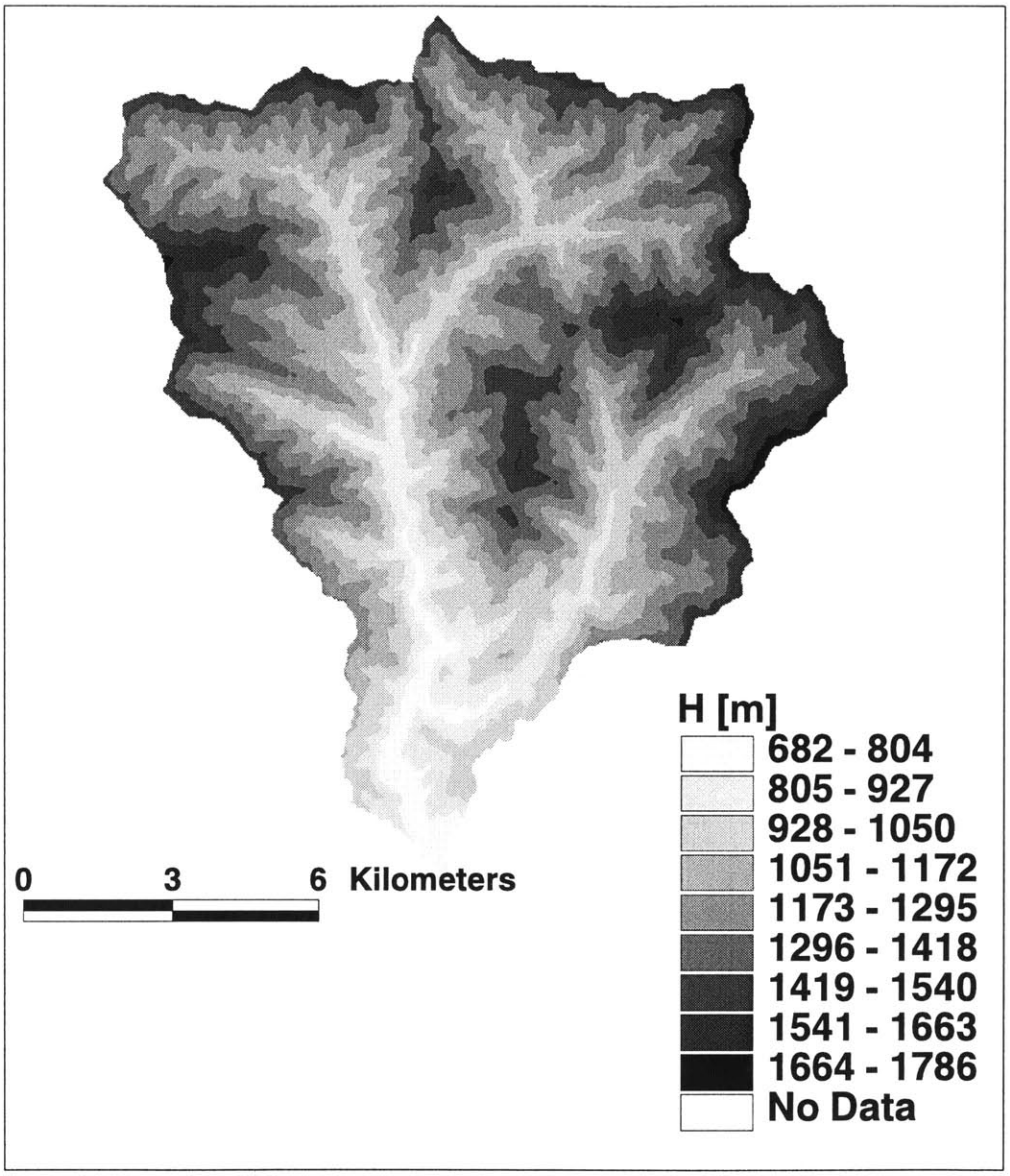

Figure 3-12: Surface elevation from 30-m DEM, Big Creek, ID.

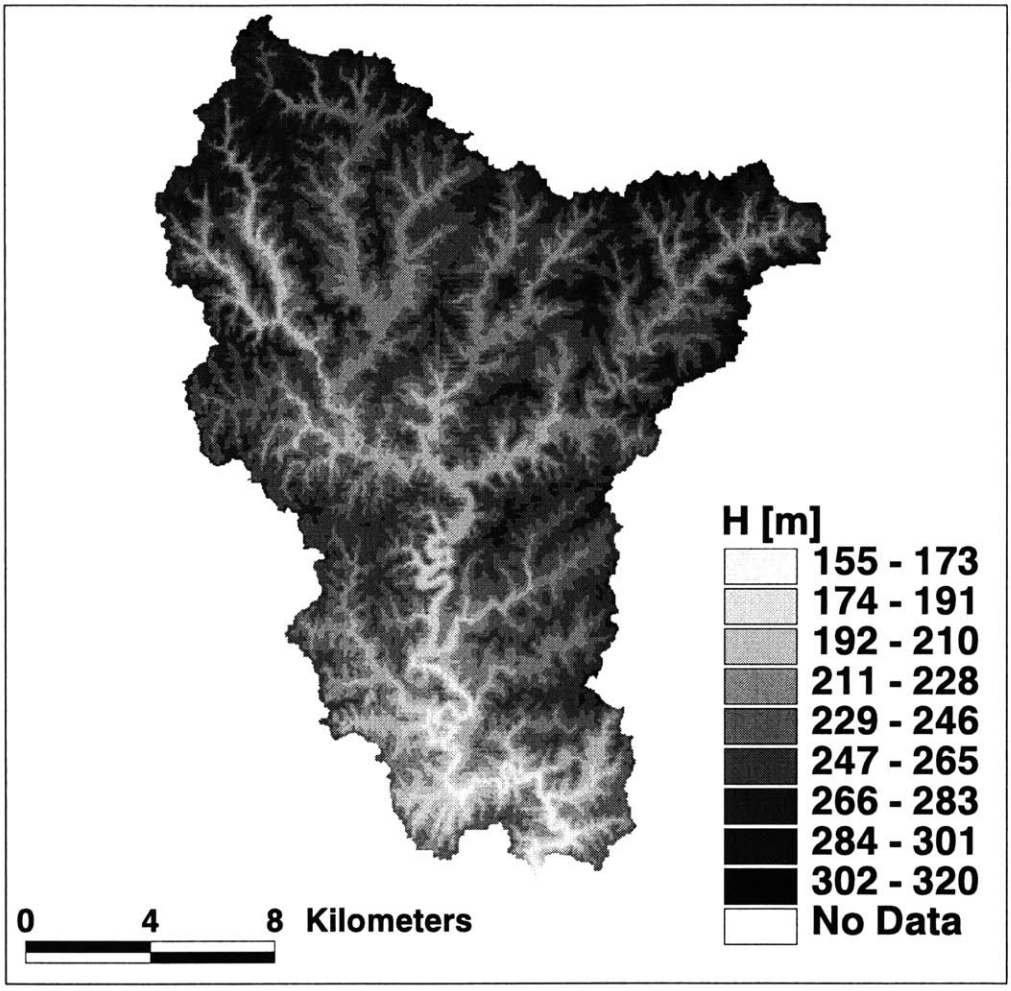

Figure 3-13: Surface elevation from 30-m DEM, Brushy Creek, AL.

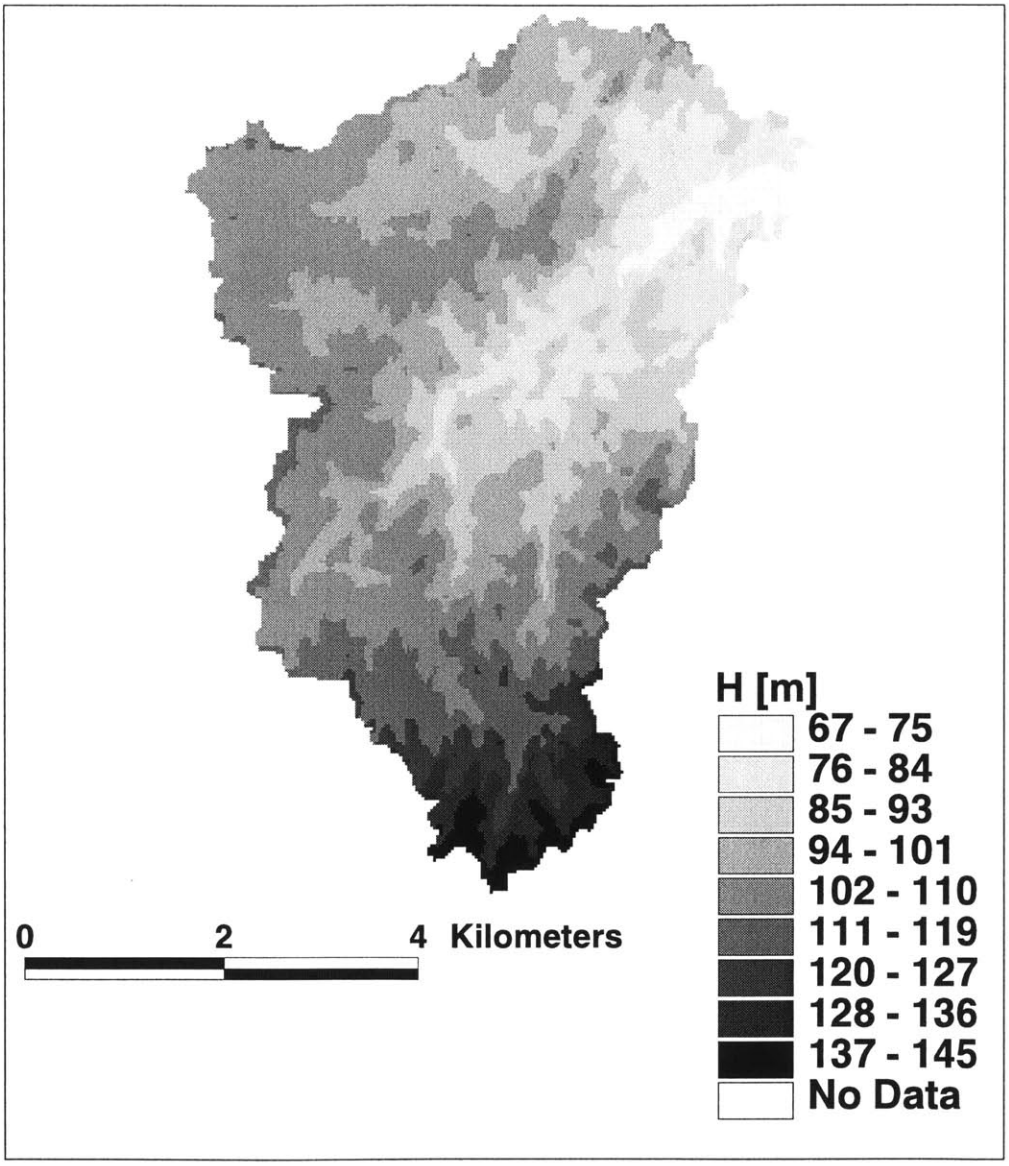

Figure 3-14: Surface elevation from 30-m DEM, Midland, VA.

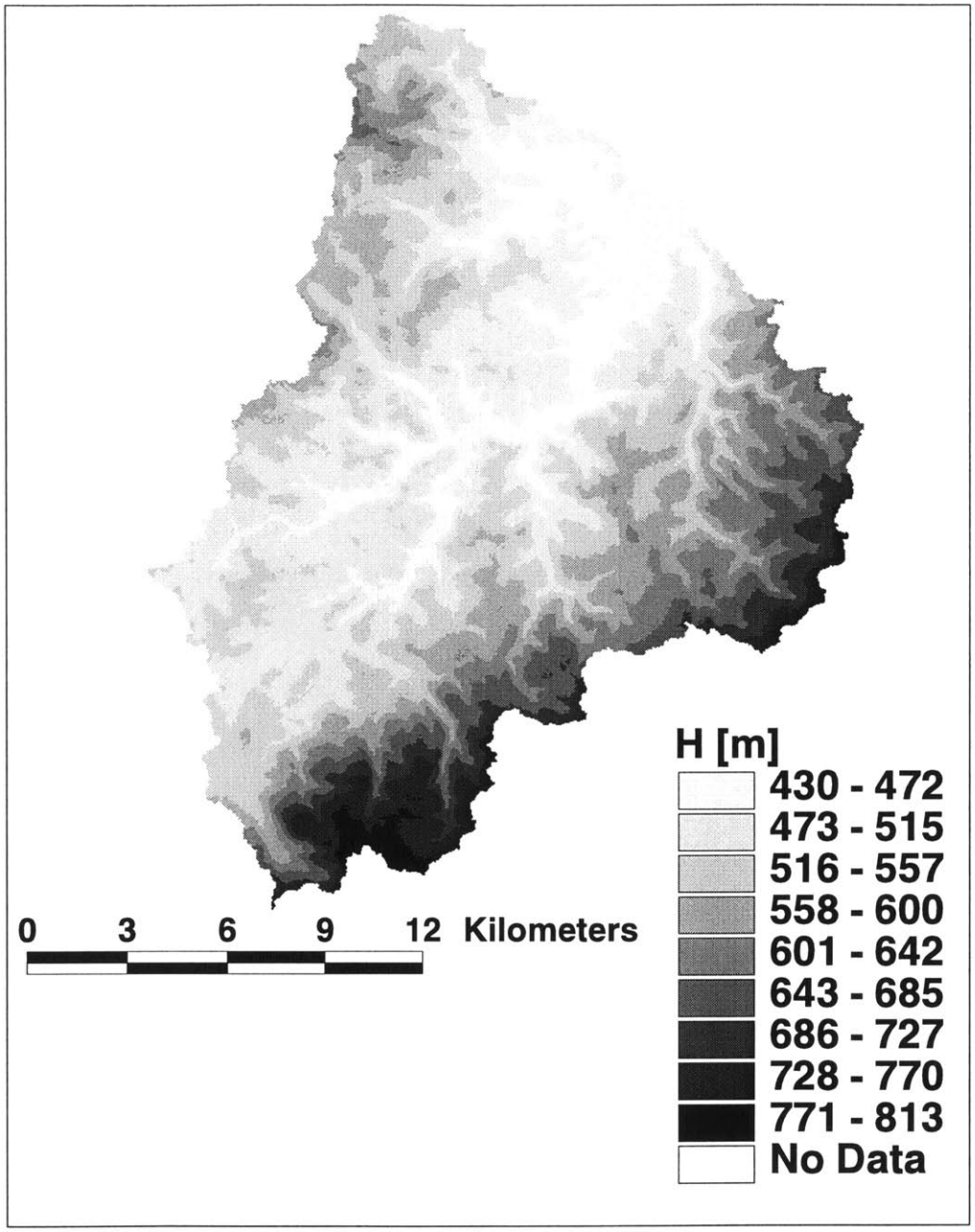

Figure 3-15: Surface elevation from 30-m DEM, Moshannon, PA.

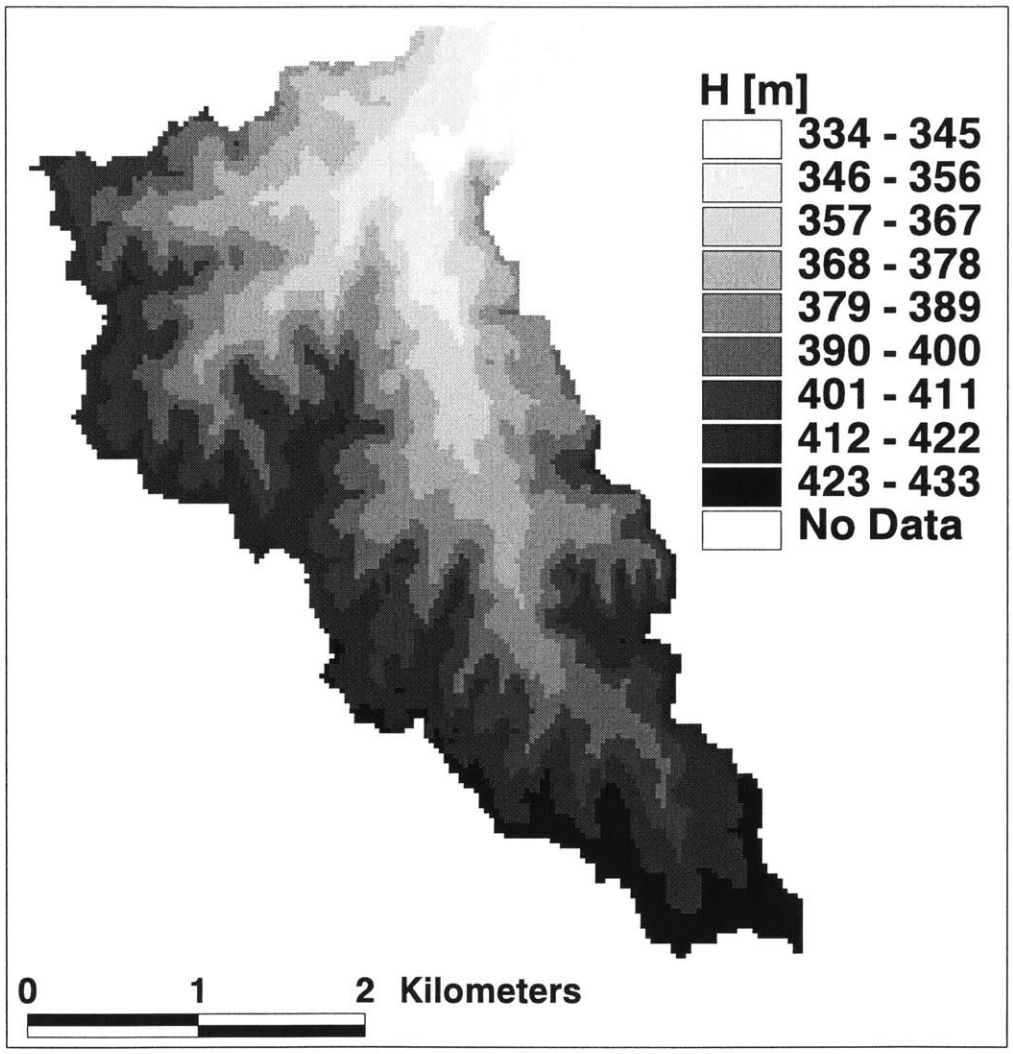

Figure 3-16: Surface elevation from 30-m DEM, Ogden, KS.

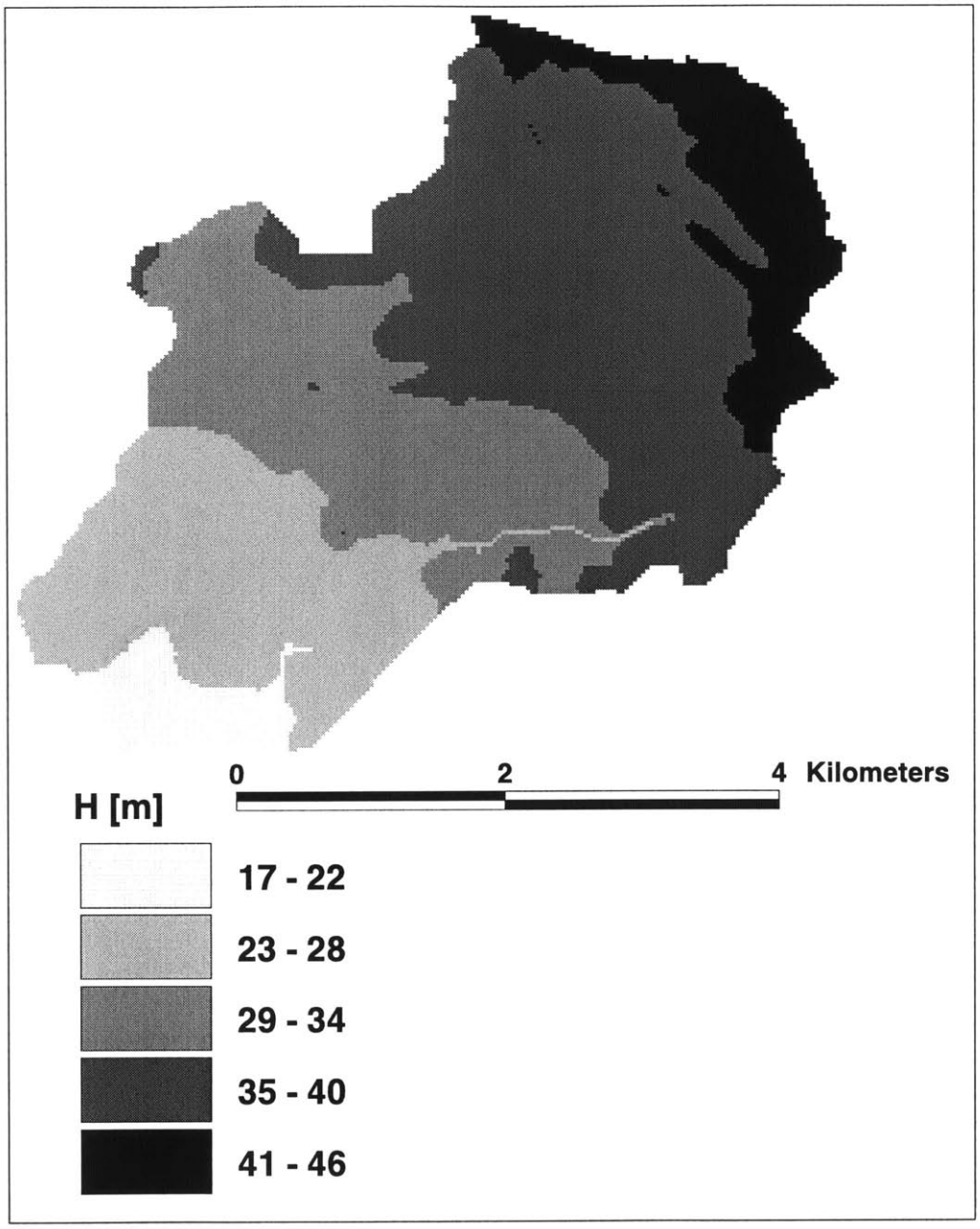

Figure 3-17: Surface elevation from 30-m DEM, Sacramento, CA.

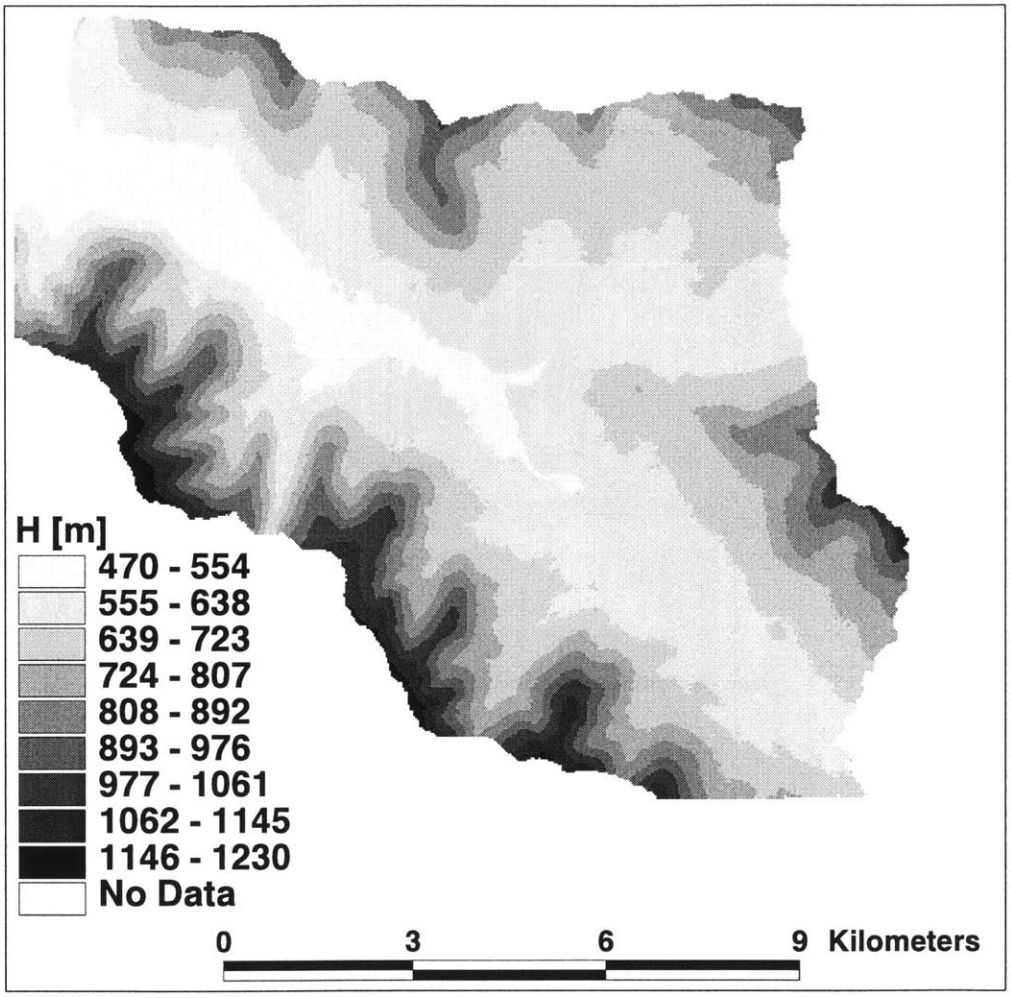

Figure 3-18: Surface elevation from 30-m DEM, Schoharie, NY.

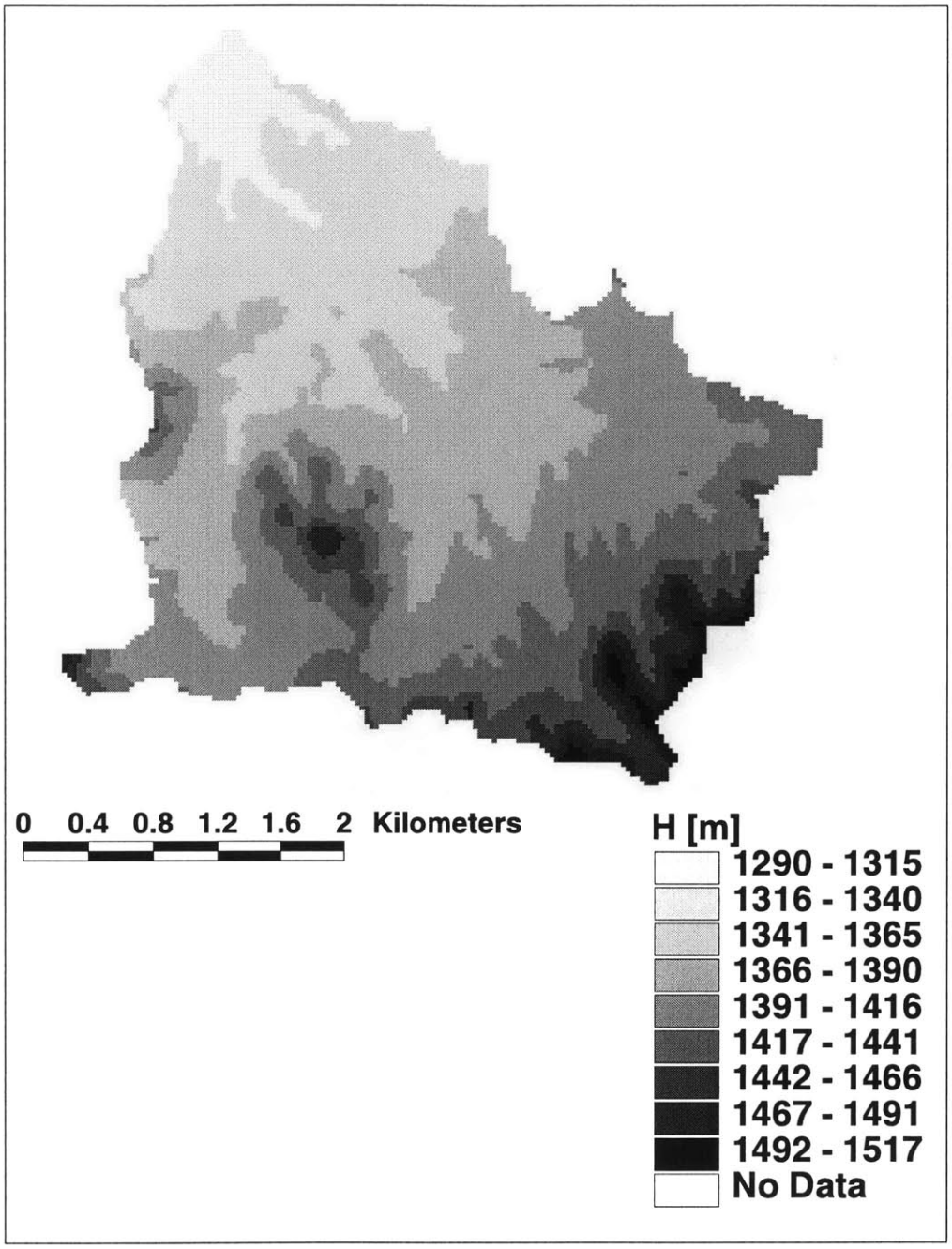

Figure 3-19: Surface elevation from 30-m DEM, Tombstone, AZ.

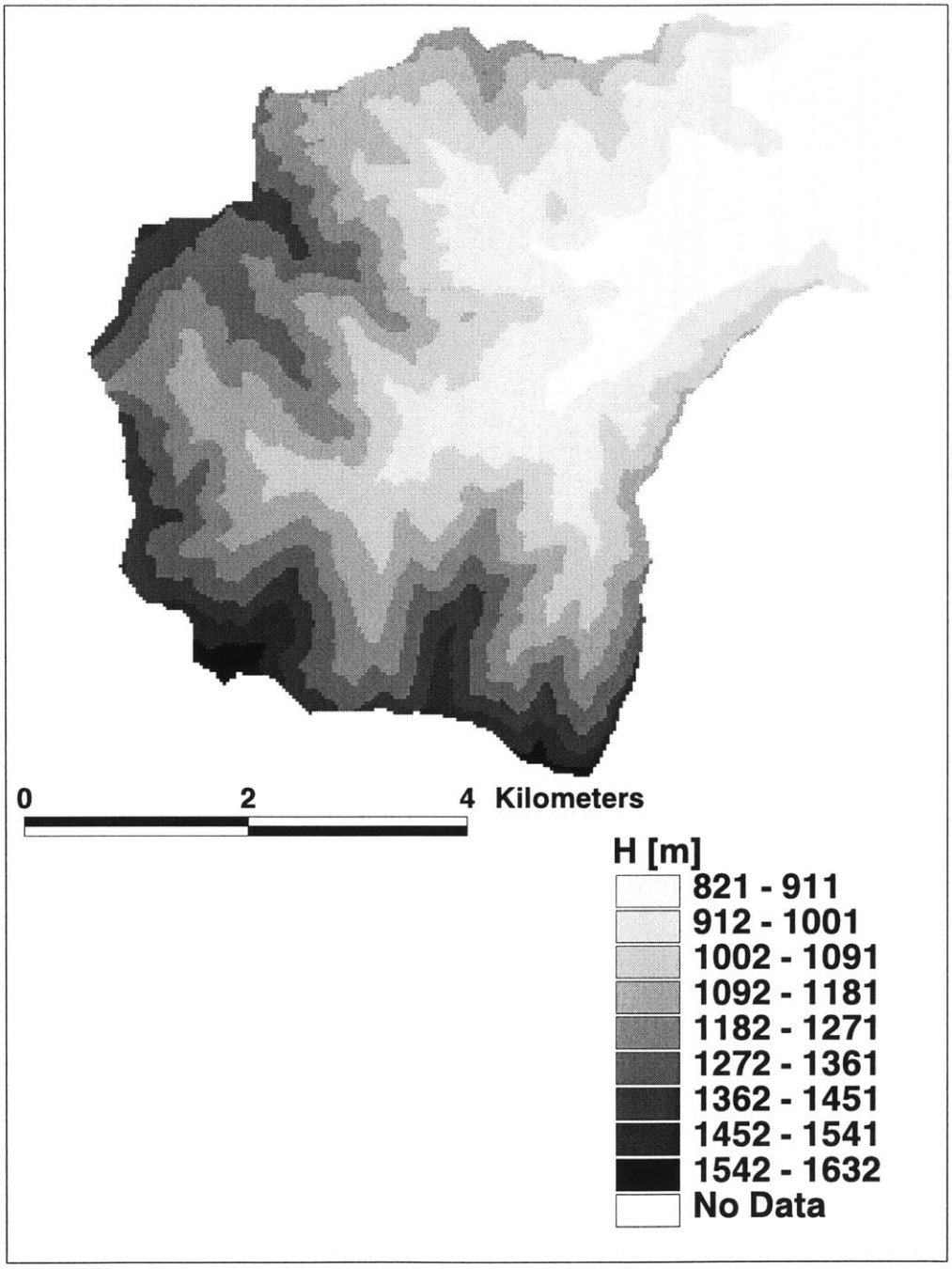

Figure 3-20: Surface elevation from 30-m DEM, Yreka, CA.

Chapter 4

Spatial variability at the subbasin scale

In the previous chapters, we presented the model and data which are used to generate hydrologic characteristics in ten study basins. The goal of this chapter is to identify the existence of spatial patterns in the modeled equilibrium hydrologic response that may be related to location and topographic factors within each basin. There are several possible approaches to scaling between well-understood point processes and large-scale measurements. Processes may be assumed to be either (1) constant in space, (2) varying randomly in space, or (3) varying according to a deterministic pattern. In this chapter, we look first at the organization of modeled equilibrium hydrology within each basin, relating key hydrologic variables to location within the watershed and local hillslope shape. A consistent qualitative pattern is observed in all basins with differentiation between the downslope riparian zone, the upslope zone, and the intermediate midline zone. The formation of the intermediate zone in which the water table runs approximately parallel to the ground surface is investigated; comparison of how the midline extent differs between basins reveals the midline's dual dependence on the dynamics of the saturated and unsaturated zones.

4.1 Introduction

The ability to characterize and quantify the spatial organization of hydrology is important for a number of reasons. The distribution of water table depths is important for identifying runoff-generating areas within a basin for storms of different magnitudes. The range over which the water table and surface fluxes vary could have implications for the magnitude of the distributed signal in basin response. Characterization of a reliable relationship between topography and soil moisture would allow for the scaling up or down of hydrologic variables (*e.g.*, a remotely sensed basin-average soil moisture content could be disaggregated to a smaller spatial scale given the relevant topographic features). From an applied standpoint, ecologists or agriculturalists may need information on soil moisture patterns because plants often depend on a certain water supply to survive and prosper.

It is expected that the model will qualitatively conform to the intuitive understanding of relatively dry upslope areas and wet downslope areas with an intermediate transitional zone. This spatial pattern is caused by the lateral transport of moisture by gravity-driven saturated flow. The saturated flow translates moisture from high-elevation recharge zones downslope to convergent or low-elevation areas where the water is discharged to the sur-

face. The discharge zone includes the permanently-saturated areas and near-saturated areas that contribute surface runoff during storms. The differentiation into upslope and downslope regions, in addition to being intuitively expected from gravity-driven processes, has been modeled by an equilibrium model on a planar hillslope (Salvucci 1994; Salvucci and Entekhabi 1995). This investigation extends that work by considering the quantitative distribution of hydrologic regimes in complex topography, with juxtaposition of convex and concave hillslopes, incised channels, and variable-length hillslopes.

4.2 Relevant literature

Most efforts to characterize spatial variability and topographic influences in hydrologic response focus on soil moisture (with particular emphasis on saturated regions) and runoff generation. Field studies can be broadly subdivided into two categories: (1) qualitative descriptions, which relate hydrologic variables to observed landforms and/or soil properties; and (2) quantitative analyses, which use physiographic indices to describe spatially variable hydrology.

4.2.1 Qualitative descriptions of spatial variability

An early study of the interaction between topography and hydrology was undertaken by Hewlett and Hibbert (1963). They constructed a steep, soil-filled trough to investigate the transient response of the slope to artificial precipitation. In non-evaporative conditions, they found that the entire unsaturated column contributed to outflow. While this study marked one of the first experimental investigations of hydrology on a sloped surface, it was limited in application by the straightness and steepness of the slope and the artificial conditions (*i.e.*, impermeable bedrock and no evaporation). Aided by subsequent advances in measurement techniques and automated data recorders, numerous studies have since investigated the effect of topography on soil moisture and runoff generation in real catchments under natural forcing conditions.

Betson (1964) observed that storm runoff occurred only over a fraction of a basin's area. This was one of the first identifications of the role of partial contributing areas in runoff generation. Betson theorized that storm response models tend to underpredict extreme events because they do not account for the variability in runoff-generating areas within a basin. Dunne and Black (1970a,1970b) expanded the theory of partial runoff-generating areas and the dependence of contributing areas on physiography. In a field study of three differently-shaped, adjacent hillslopes in the Sleepers River watershed in Vermont, Dunne and Black identified a connection between topography and the likelihood of saturation. Saturation is most likely to occur in valley bottoms and convergent swales; during the wet season, the saturated zones extend upward, generally following convergent areas of the landscape (Dunne *et al.* 1975). Numerous studies have found similar support for saturation or near-surface water table levels in convergent regions (*e.g.*, Anderson and Burt 1978; Moore *et al.* 1988; Woods and Rowe 1996).

Other studies have looked at the relationship between soil moisture and elevation. Li *et al.* (1995) indirectly examined soil moisture patterns in their study of the topographic zonation of infiltration. From measurements in a hilly loess region, the authors observed that the steady infiltration rate decreased with distance downslope; this could be related to systematic variation in soil moisture. Crave and Gascuel-Odoux (1997) observed that surface soil moisture was correlated with the elevation difference to the basin outlet in a

small catchment in France. They distinguished a lower elevation region, where moisture is highly variable, and an upper region, where soil moisture is nearly constant over time. However, findings of a significant relationship between elevation and soil moisture have been limited to small catchments with simple topographic features. It is expected that the observed influence of slope curvature on hydrology will be of greater importance in complex landscapes.

Recently, researchers have begun trying to separate the influences of topography and other physical characteristics, such as soil texture. Western *et al.* (1998a) sought to identify the relative influence of soil texture and topography on soil moisture in a small catchment in New Zealand. They found that in the wet winter, the moist or saturated areas are connected in ways that are related to the topography; in the dry summer, the spatial pattern is random, likely influenced by small-scale variability in the soil texture. Gallart *et al.* (1997) identified a similar pattern in the mountains of Catalonia. Only in the winter was the spatial pattern of soil moisture determined by topographically-driven subsurface flow. Yeakley *et al.* (1998) observed the opposite effect along a hillslope transect in a humid watershed. In wetter periods, the soil storage characteristics were more important for the soil moisture profile, while topographic effects dominated in drier periods. More work is needed to identify the source of the divergent results found in these studies.

4.2.2 Quantitative descriptions of spatial variability

The repeated observation of spatial patterns in hydrology supports the potential for quantitative measures that relate topography and/or location to soil moisture or the likelihood of saturation and runoff generation. Such indices can be useful in extrapolating point measurements to areal coverage and in developing relatively efficient, quasi-distributed models. Kirkby and Chorley (1967) proposed a relationship between hillslope drainage and several physical features, including local contour curvature, gradient, soil thickness, and proximity to stream channels. The relationship was quantified by Carson and Kirkby (1972) with the introduction of the parameter a, the area drained per unit contour length. This single variable captures both the contour curvature and the proximity to streams; as an index of the lateral concentration of subsurface flow, it helps determine the pattern of soil moisture.

Subsequent studies identifying the presence of saturated soils in hollows not necessarily near riparian zones led to the recognition that relief often combines with location to influence soil moisture patterns. The continuity equation for subsurface flow was combined with the Darcy equation for gradient-driven flow to give a joint index for soil moisture, a/S, where a is the contributing area per unit contour length and S is the slope of the ground surface. The index contains information both on the concentration of moisture from upslope areas (through a, a proxy for proximity to the channel and degree of curvature-induced convergence of flow) and on the flux rate through the soil (moisture will accumulate in low-gradient regions where the slope causes deceleration of the downslope moisture flux). Combined area-slope indices have been used as the basis for numerous modeling efforts, including Kirkby (1975, 1978), TOPMODEL (Beven and Kirkby 1979), and O'Loughlin (1981, 1986).

The correlation between a or a/S and observed soil moisture has been examined in numerous watersheds. Burt and Butcher (1985) compared soil moisture with an a/S term and an index of plan convexity. They found that the correlation between the a/S index and depth to saturation was stronger than with the plan convexity index but was not particularly significant, especially in drier conditions. Nyberg (1996) compared soil water

content with several physical descriptors. Soil moisture was about as well correlated with contributing area as with a/S; he concluded that contributing area plays a more signficant role in moisture determination than surface slope. However, a linear correlation between a/S and soil depth could imply that part of the pattern in soil moisture is due to the thickness of the soil layer rather than the surface topography.

Certain limitations exist in the use of a/S indices as a direct indicator of hydrology. The presence of small-scale heterogeneities or piping within the soil matrix can lead to moisture patterns that are not explained by any form of an a/S index (Jones 1986). There may also be a disconnect between the surface landscape, which is the common source of topographic information in index-based models, and the underlying bedrock topography. Shallow bedrock could produce saturation in areas other than low-lying or convergent regions. Freer *et al.* (1997) investigated the relative role of bedrock topography in two small catchments. They found that in some environments bedrock topography plays a significant role in determining local hydrological gradients; this could influence flow pathways and the accuracy of surface-based topographic indices in predicting soil moisture patterns. Here we will show that the contributing area is a necessary but not sufficient predictor of hydrologic response based on location. It will be shown that local topographic features have a large influence on local soil moisture and hydrologic response and that GSEM captures those effects.

4.3 Results

The results presented here correspond to the equilibrium water table and hydrologic fluxes generated by the coupled model described in Chapter 2. We look first at the distribution of water table depth in the study basins. Maps of water table depth illustrate the spatial connectivity of the water table position throughout each basin. The mean and range value of water table depth is compared against location in the basin (represented by a) and position along a hillslope (parameterized as the distance from the closest drain normalized by the hillslope length) to identify how much of the spatial variability is explained by position. We then consider hillslope shape to examine whether curvature can explain variability not explained by the positional index. Finally, we investigate whether the midline region, which was found to occupy a dominant fraction of a planar hillslope in work by Salvucci and Entekhabi (1995), is similarly present in the complex terrain of natural catchments, and whether it is correlated with any identifiable physical characteristics.

4.3.1 Spatial organization of equilibrium hydrology

Connectivity of water table position

Figures 4-1 to 4-10 present maps of the equilibrium water table depth calculated by the model in each of the study basins. The maps are smoothed by averaging over a moving subgrid of five by five pixels. This is done to minimize the noise caused by the discrepancy between the vertical resolution of the DEMs and the modeled water table elevation. The horizontal scale in Figures 4-1 to 4-10 varies so that basins of different sizes can be mapped in the available space. Appendix D contains maps of 2.25 km^2 square subsections of each basin to illustrate features on the same scale.

The maps of water table depth highlight a connected pattern in the equilibrium hydrologic state of the basins. The position of the water table reveals a fairly well-defined,

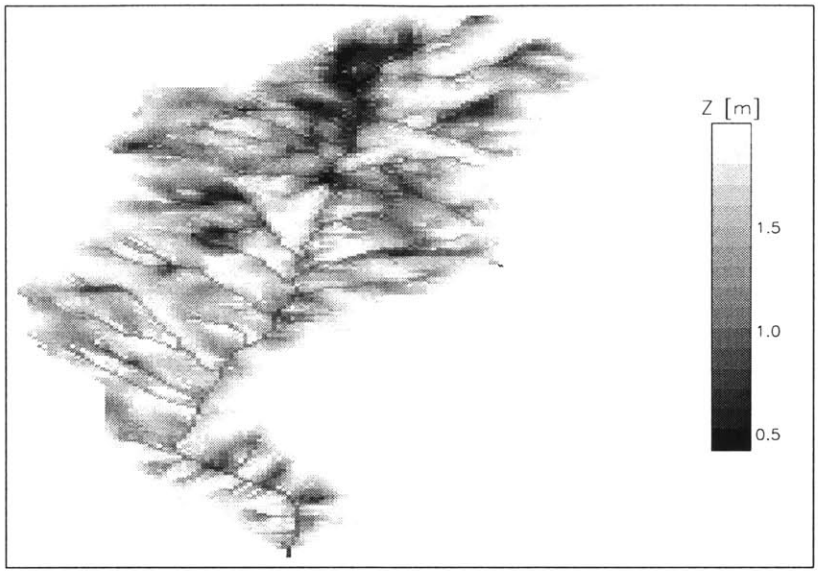

Figure 4-1: Spatial distribution of depth to saturation, Bear Valley, CA. See Figure 3-11 for horizontal scale.

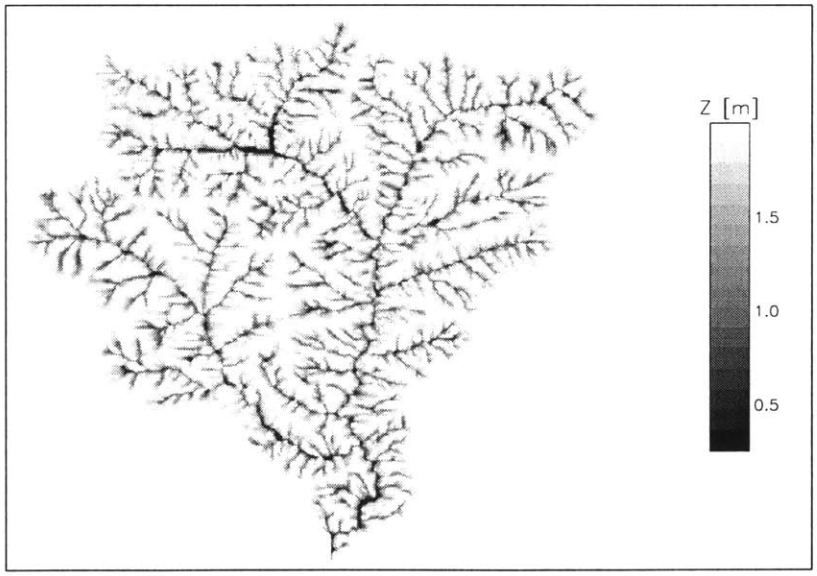

Figure 4-2: Spatial distribution of depth to saturation, Big Creek, ID. See Figure 3-12 for horizontal scale.

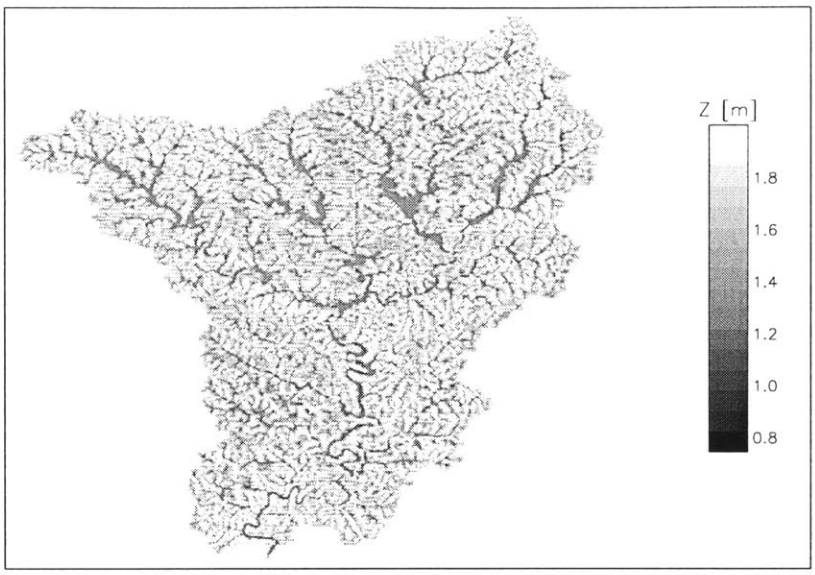

Figure 4-3: Spatial distribution of depth to saturation, Brushy Creek, AL. See Figure 3-13 for horizontal scale.

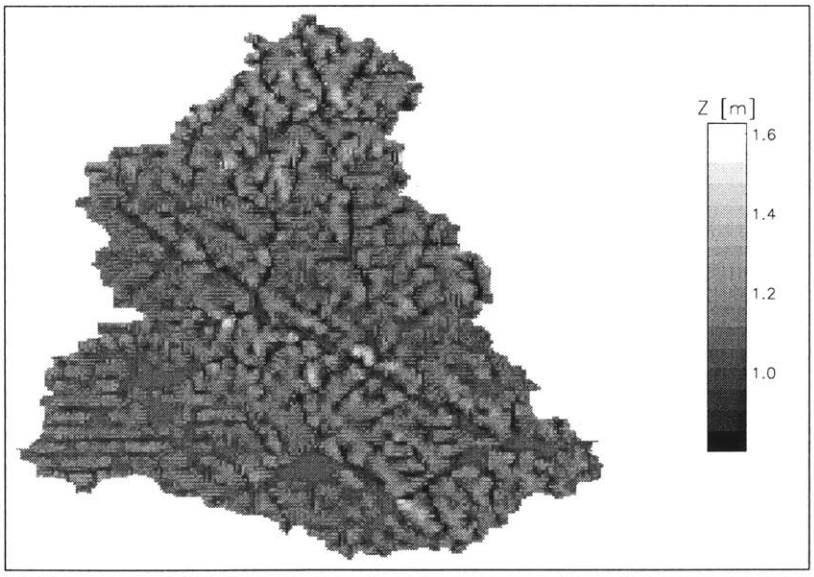

Figure 4-4: Spatial distribution of depth to saturation, Midland, VA. See Figure 3-14 for horizontal scale.

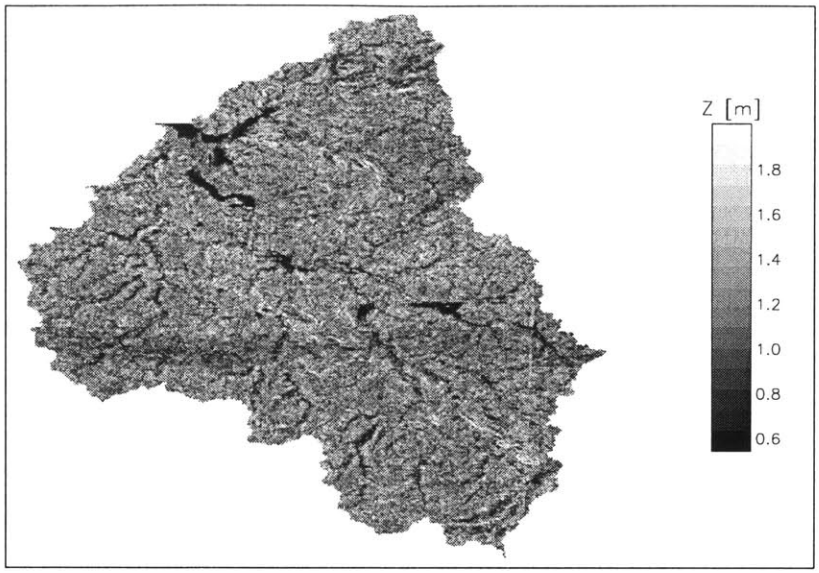

Figure 4-5: Spatial distribution of depth to saturation, Moshannon, PA. See Figure 3-15 for horizontal scale.

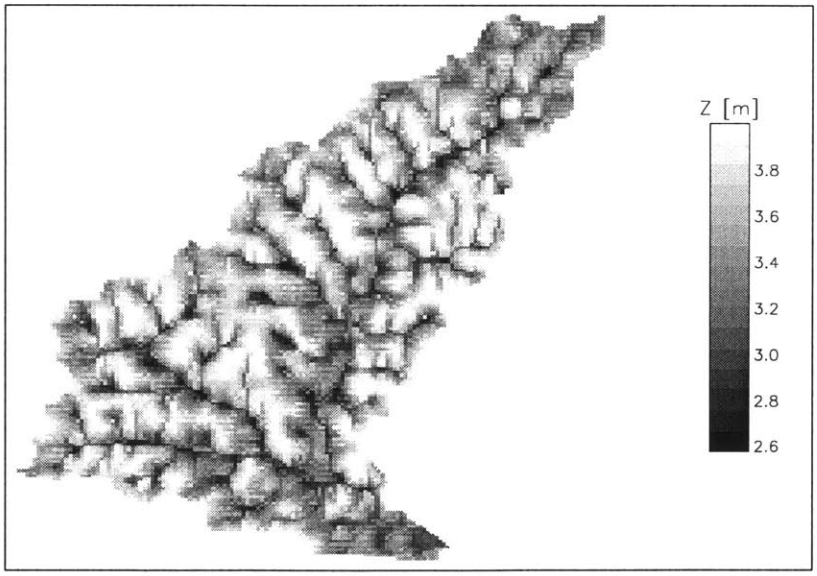

Figure 4-6: Spatial distribution of depth to saturation, Ogden, KS. See Figure 3-16 for horizontal scale.

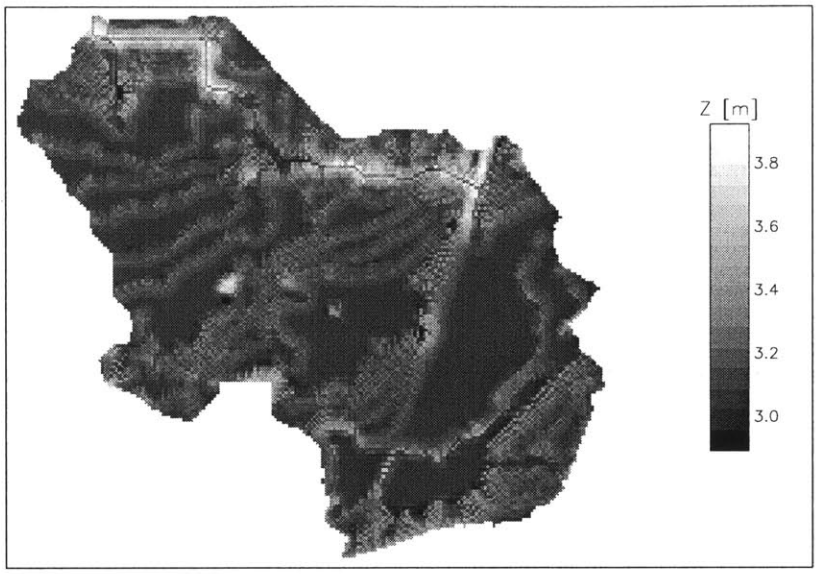

Figure 4-7: Spatial distribution of depth to saturation, Sacramento, CA. See Figure 3-17 for horizontal scale.

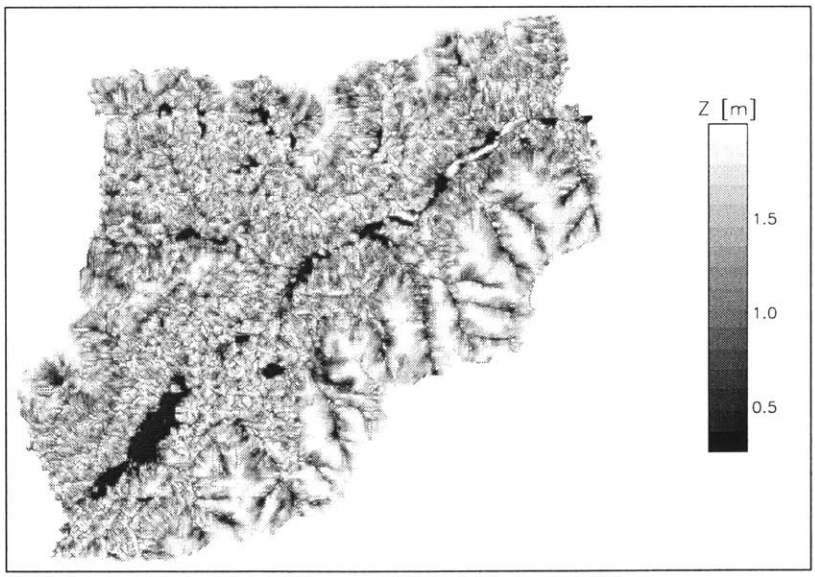

Figure 4-8: Spatial distribution of depth to saturation, Schoharie, NY. See Figure 3-18 for horizontal scale.

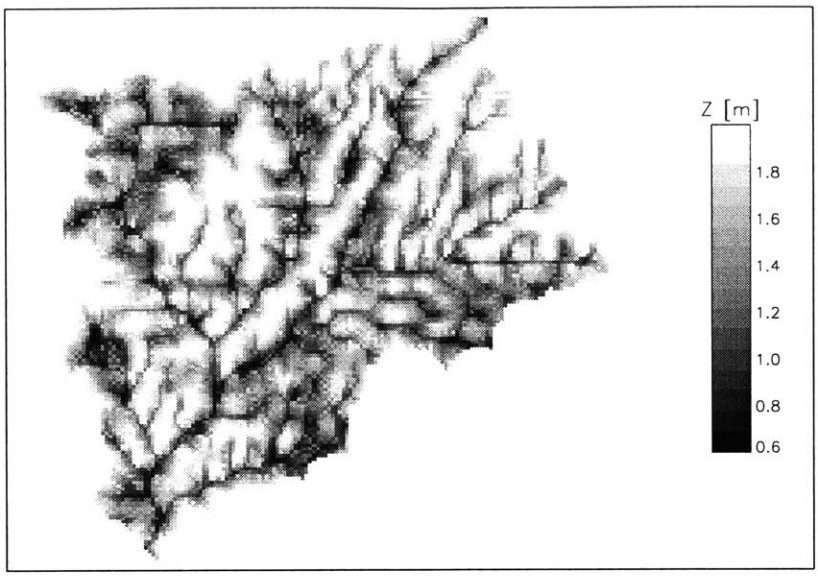

Figure 4-9: Spatial distribution of depth to saturation, Tombstone, AZ. See Figure 3-19 for horizontal scale.

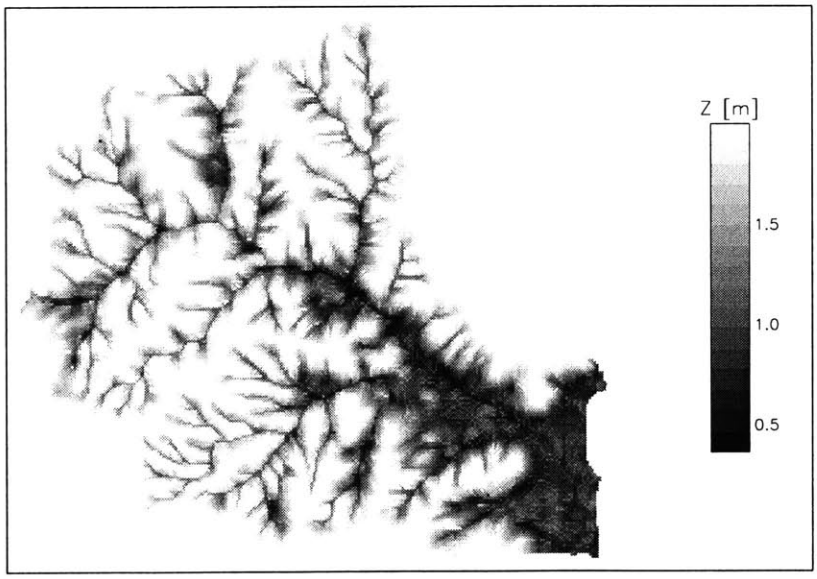

Figure 4-10: Spatial distribution of depth to saturation, Yreka, CA. See Figure 3-20 for horizontal scale.

continuous network in several of the basins. A comparison of the network of saturated or near-saturated cells with surface elevation (provided previously in Figures 3-11 to 3-20) reveals that the moisture state is related to the topography. In Big Creek, for example, the riparian zone, where the water table is at or near the ground surface, is clearly differentiated from the relatively dry hillslopes. The riparian zone occurs in the valley bottoms; this is the area that contributes runoff to the stream channels. Saturation expands and contracts within this portion of the basin, depending on the moisture supply. Efforts to predict the rapid runoff response from saturated contributing areas should focus on characterization of the soil moisture levels in the riparian zone. Hillslopes, in contrast, are characterized by deep water tables. Gravity-driven flow is responsible for the transport of water away from ridges and hilltops to the low-elevation and convergent regions of the landscape.

Not all of the basins present a well-defined riparian network with differentiation between channel and hillslope areas. The likely reason for a weak or absent network is the vertical resolution of the digital topography. Sacramento, for example, displays an unusual distribution of water table position. The water table is very deep, ranging from three to four meters below the surface; nowhere does the model predict saturation. This is probably because the climate is very dry (the ratio of annual precipitation to potential evaporation is 0.22). However, this alone should not necessarily result in a poorly-defined spatial structure of hydrology. What is more significant is the extremely low relief; the median surface slope is just one percent. The plot of water table depth strongly resembles a contour map, with decreasing elevation from the southeast to the northwest. The areas of homogeneous depth represent the extensive area where the terrain is flat. Only when the surface elevation drops a meter is there a change in water table depth; these locations are seen as the curving grey lines. The channel, which is located near the northern border of the basin, is distinctly defined along its jagged course. A DEM with a finer vertical resolution would likely smooth out the abrupt drops in the surface topography and lead to a more continuous, gradual variation in depth to saturation.

In the Brushy and Midland basins, some of the channel network structure is visible; however, parts of the two basins have a striped pattern in water table depth that is not physically realistic. The occurrence of alternating rows with shallow and deep water tables is likely also due to the vertical resolution of the DEM. On slopes where the elevation difference between pixels is less than one meter, the rounding of elevation to one-meter intervals results in a jagged surface topography. The model smooths out the water table elevation. The juxtaposition of a smooth water table beneath a stepped ground surface leads to this spurious striped pattern of water table depth. The phenomenon does not appear in the steeper basins because the relief between pixels exceeds the one-meter vertical resolution on many of the slopes. The moving average performed on the original data before plotting reduced, but could not fully remove, the stair-stepping effect seen in the Brushy and Midland basins.

When looking at the spatial structure of the equilibrium water table, it is also important to consider any possible impacts of the horizontal resolution of the DEMs. Each cell in the elevation grid is a 30-m by 30-m square. Most channels, even at their flooded levels, are significantly narrower than 30 m. The moisture values produced by the model are averaged across each grid cell; therefore, a pixel might contain a permanently saturated channel while having an average equilibrium water table that lies deep below the surface. If more detailed information on the specific location of permanent or intermittent channels within pixels were desired, the resolution of the topographic data would have to be increased. However, for looking at large-scale organization of hydrologic conditions across medium-sized basins, the

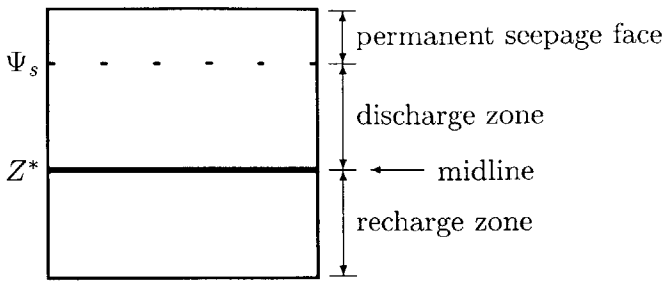

Figure 4-11: Schematic illustrating dependence of net recharge on water table depth.

30-m resolution topography effectively differentiates between riparian and hillslope zones.

Relationship to topographic indices

One method of quantifying the connectivity seen in the maps of water table depth is to look at the relationship between hydrology and positional indices. There are several ways of quantifying location. The contributing area (A) measures the amount of flow accumulation upstream of the pixel of interest. The area per unit contour length (a) was introduced by Carson and Kirkby (1972) as a modified location index combining a limited measure of contour curvature with upstream area. For two pixels with the same upslope area A, a pixel on a divergent slope will have a smaller a than a pixel on a convergent slope to which several upslope pixels drain. A further modification of the contributing area concept was introduced by dividing the area per unit contour length by local surface slope, giving the parameter a/S. The inclusion of slope contains information on the rate of gravity-induced moisture flux in addition to position within a basin. The area-slope index and related metrics have been used in numerous modeling and field studies as a predictor of soil moisture or water table position.

In this section, we examine whether the basins display a consistent relationship between water table depth and location of the pixel in the basin and along a hillslope. We use a, contributing area per unit contour length, as the measure of pixel location relative to the outlet. The analysis presented here uses a rather than a/S because it is designed as an index of location rather than a tool for hydrologic prediction. In all subsequent discussion, references to contributing area refer to contributing area per unit contour length; the abbreviated term is used for convenience. An alternative locator index is to consider the location of a pixel along a single hillslope. We develop a metric for the position of a pixel along a flow path between the ridge and the closest drain. The fractional distance is defined as the distance from the drain, normalized by the total hillslope length from drain to ridge. The flow path is determined by the direction of steepest descent between pixels. The water table depth is compared against the hillslope position to investigate whether the relationship is more clearly defined than between water table position and location relative to the basin outlet.

The position of the water table is important for the surface water balance and interaction with the saturated zone, as shown in Figure 4-11. When the water table is shallower than Ψ_s, the maximum capillary rise supported by the soil matrix, the soil column is effectively saturated. This represents the portions of the basin in which a permanent seepage face

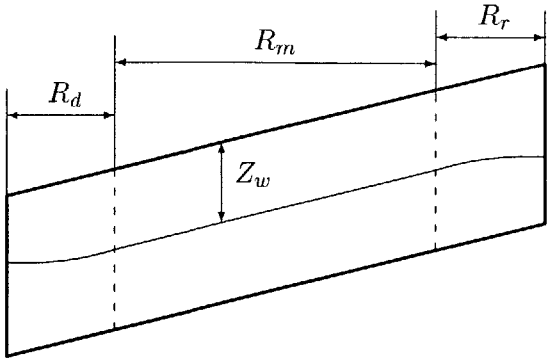

Figure 4-12: Cartoon of equilibrium water table profile on a planar hillslope, from Salvucci (1994). Vertical scale is exaggerated for illustration. Hillslope is divided into recharge region R_r, midline region R_m, and discharge region R_d.

is found. Areas where the water table lies below Ψ_s but above the zero-recharge depth Z^* experience net discharge from the groundwater to the unsaturated zone. These cells are most likely to saturate during storms, representing the part of the riparian zone that generates overland flow during wet periods. When the water table lies below Z^*, the net vertical flux is downward; the saturated zone is recharged by moisture percolating through the overlying unsaturated zone. Areas where the water table is located at Z^* represent the midline region of the hillslope, as described by Salvucci (1994). The midline region is significant because it is the depth at which there is no net flux between the saturated and unsaturated zones. When the water table is in the midline position, the hydraulic gradient is parallel to the ground surface. The physical reasons for the development of the midline zone and its occurrence within the basins will be discussed in greater detail in Section 4.3.3 below.

We begin with a comparison of water table depth versus contributing area. It has been shown in previous field and modeling studies that the water table tends to be shallower in and near the riparian zone where the contributing area is relatively large (see Section 4.2). Looking at the hydrology across values of contributing area is a way of providing a "hillslope view," aggregating across multiple hillslopes in a single basin. Figure 4-12 illustrates the conceptual behavior of water table depth along a planar hillslope as found by Salvucci (1994). From this schematic, we expect that the water table depth will exceed Z^* in the upslope recharge zone, be approximately equal to Z^* in the midline zone, and be less than Z^* in the discharge zone.

The mean difference shown in Figure 4-13 is calculated as the average value of $(Z_w - Z^*)$ for all pixels within a given range of contributing area. The dependent parameter, contributing area, is one way to approximate the location on a hillslope, with increasing values away from the ridge. In complex terrain, however, hillslopes are of different lengths and occur in different locations relative to the basin outlet. In aggregating all pixels with similar contributing area, pixels which are at different locations along a hillslope are lumped together. Although sorting by contributing area reduces the clear signal of the hillslope position-dependence of the water table depth, it provides an efficient way of looking at some positional relationship in the hydrology of an entire basin.

In all of the basins, the difference has a high positive value for low contributing areas,

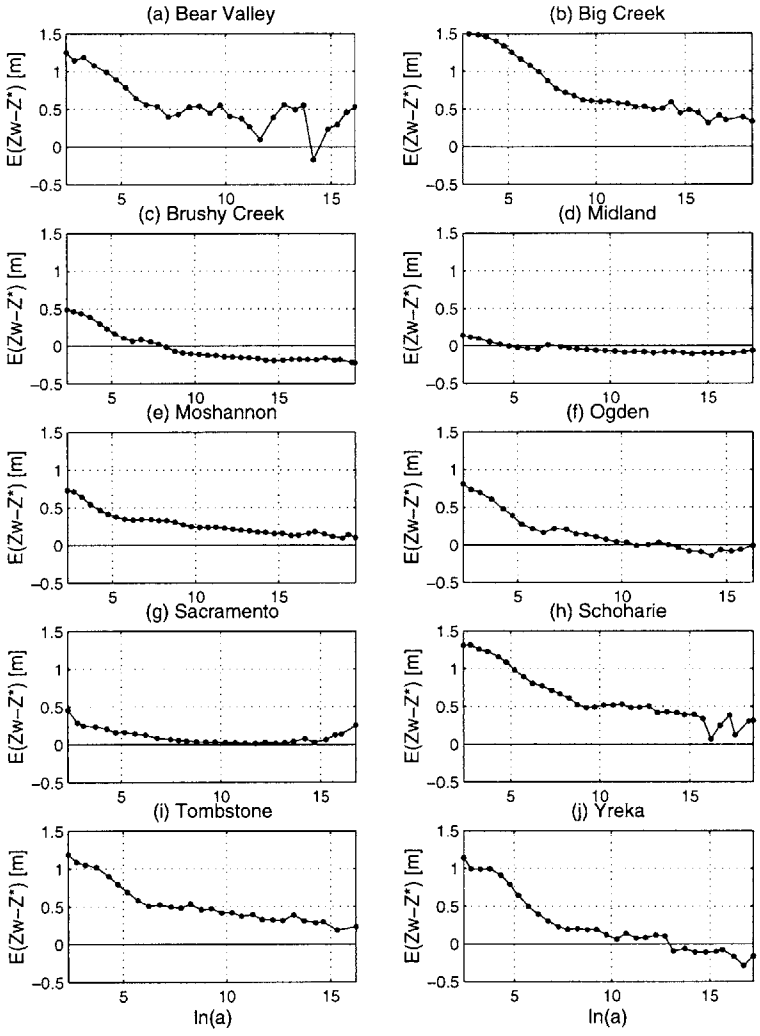

Figure 4-13: Mean difference between Z_w and Z^* as a function of contributing area per unit contour length, for all basins. Positive numbers indicate the water table is deeper than Z^*. Negative numbers correspond to a water table shallower than Z^*.

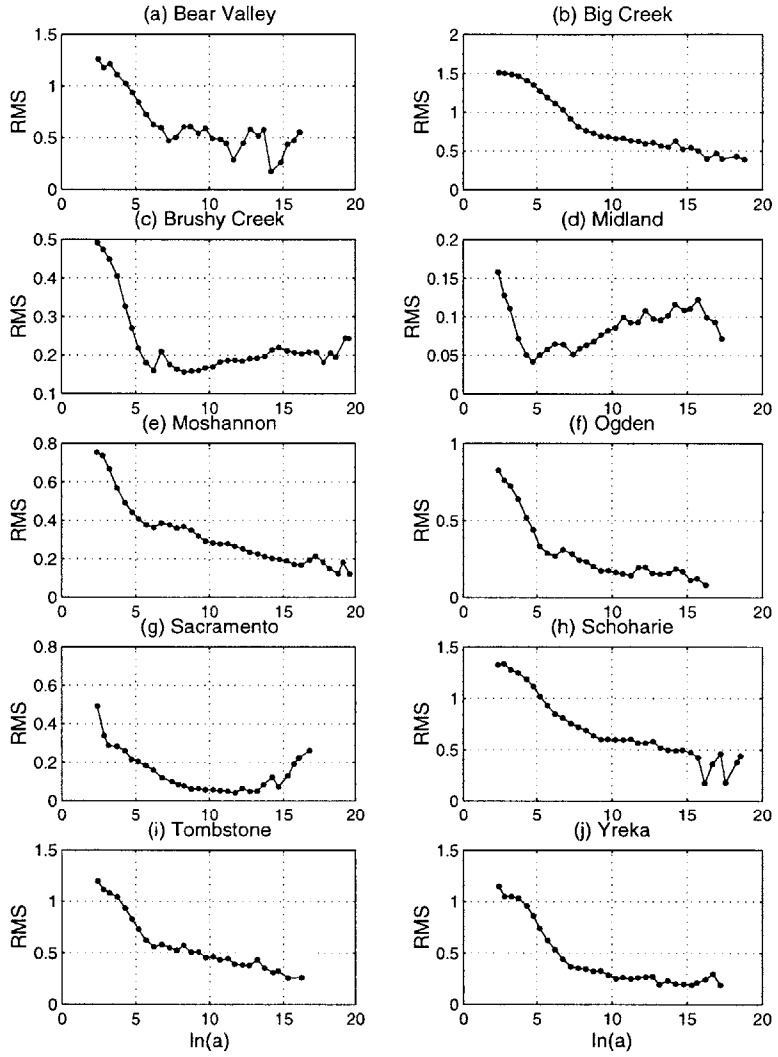

Figure 4-14: Root mean square (RMS) between Z_w and Z^* as a function of contributing area, for all basins.

i.e., the modeled water table is deeper than the zero-recharge depth and the net recharge flux is positive downwards. The water table is deep in upslope areas because of the negligible amount of lateral influx from upslope areas. We expect the difference to decrease approximately monotonically with increasing contributing area, passing zero in the midline region and becoming negative in the discharge zone. Brushy and Yreka conform to this expected behavior. Big Creek, Brushy, Moshannon, Schoharie and Tombstone all decrease monotonically, but the mean difference remains positive across the entire range. This result does not indicate that there are no discharge areas in these basins; rather, the calculation of the mean difference over many pixels hides the negative difference at some locations. Midland, Ogden, and Sacramento each experience increases in the mean difference at the largest contributing areas. The lack of clear differentiation may be because these basins have the lowest relief among the study sites (median surface slope is 4, 8, and 1 percent, respectively). The differentiation in soil moisture between upslope and downslope areas is diminished when the surface slope is mild. Bear Valley exhibits the noisiest behavior over a range of large contributing areas. The basin has high relief (S_{50}= 0.34) across a relatively small area; the noise may arise from the small number of pixels averaged for large contributing areas.

A related variable which also provides information on water table position is the root mean square (RMS) of $Z_w - Z^*$, calculated as

$$RMS = \sqrt{\frac{\sum (Z_w - Z^*)^2}{n}} \tag{4.1}$$

where n is the total number of pixels. Whereas the difference indicated the mean value of water table depth relative to Z^*, the RMS provides the mean distance between Z^* and Z_w, independent of direction. Furthermore, it quantitatively indicates the variability in water table depth with respect to Z^* at each level of contributing area. The general pattern of RMS as a function of contributing area is similar to that of the mean difference; seven of the ten basins decrease monotonically. The failure of this analysis to clearly identify a midline region with a negligible RMS is probably due to the use of contributing area as the dependent variable across hillslopes of different lengths in different locations within the basin. Three of the seven basins, however, exhibit the expected behavior of a minimum RMS at intermediate values of a. Brushy, Midland, and Sacramento each undergo a transition from a negative to a positive slope in the central part of the basin. There are two possible explanations for the behavior to occur in these basins and not in the others: (1) contributing area may be a better approximation of hillslope location, or (2) the presence of large flat areas with a well-defined midline and similar values of a results in a strong signal of midline in the RMS calculation. These three basins have among the three highest percentages of rectilinear slopes (16, 34, and 74 percent, respectively). This indicates that the second factor may influence the RMS results shown in Figure 4-14. In the other basins, the complexity of the landscape limits the ability of a single value at any contributing area to capture the full range of location-dependent hydrologic behavior.

Figure 4-13 showed the expected monotonic decrease in water table depth with increasing contributing area in most of the study basins. However, the failure of the mean difference to achieve negative values in some of the basins—even though it is known that significant areas of discharge exist—indicates that looking at contributing area per unit contour length to characterize location as a predictor of hydrologic response does not fully capture the pattern of water table depths across the basin. We therefore look next at the spread of

water table depths around the mean value. Figure 4-15 contains plots of water table depth as a function of contributing area per unit contour length (a). Depths are averaged within constant-width bins; the vertical lines represent one standard deviation around the mean value within each bin.

Steep basins tend to have great variability in water table elevation, both in the range of mean values and in the deviation at each location. In contrast, a basin with few significant topographic features has a relatively homogeneous response; a perfectly flat basin responds hydrologically like a uniform bucket. Big Creek and Yreka, the two steepest basins, both have great variation in mean water table depth. Sacramento and Midland, with median slopes of one and four percent, respectively, exhibit a relatively homogeneous hydrologic response. When the hydrologic response is so poorly differentiated throughout the basin, it is difficult to characterize the role of spatial position on hydrologic response. The flat basins essentially behave like buckets with some noise, where the noise is likely due to the coarse vertical resolution of the surface elevation data.

Quasi-distributed models that use positional indices to characterize water table position, such as TOPMODEL, generally assume a linear relationship between the index and water table depth. The plots of mean water table depth presented here reveal a positive, linear slope over a small range of intermediate locations. However, most of the basins have a limited extent of dry cells and a fairly extensive range in which the slope flattens out as the water table approaches the surface. The discharging zone and saturated areas found in downslope areas with high values of a pose potential conflicts with the assumptions of index-based models.

Figure 4-16 presents the water table depth as a function of position along a hillslope. The values are normalized by the total hillslope length, enabling the aggregation of slopes of different lengths into a single plot. There are several striking differences between the results shown in Figure 4-16 and Figure 4-15, comparing water table depth to hillslope and basin position, respectively. First, the hillslope position is a poorer index of water table position as judged by the larger standard deviation for all basins across the entire dynamic range. Second, the clear delineation between dry upslope pixels and saturated near-channel pixels seen in many of the basins when sorting by contributing area is not seen when sorting by hillslope position. Rather, most of the basins show a gradual deepening of the water table with distance from the drain. The calculation of distance from drain excludes saturated pixels in the plots of Figure 4-16. This does not, however, fully explain the absence of desaturated cells and the mild slope in the subplots of Figure 4-15. Although the position on a hillslope is a good predictor of local water table depth along a single hillslope, aggregating across hillslopes reduces the quality of the relationship. Location relative to the basin outlet, as quantified by the contributing area per unit contour length, provides a cleaner relationship between pixel location and local hydrology.

Equilibrium surface fluxes

The distributions of runoff and evaporation are of concern for streamflow control and crop management. We look now at the distribution of the fluxes as a function of a and the degree of correlation between the equilibrium water table depth and surface fluxes. Figures 4-17 through 4-26 plot water table depth and surface fluxes as a function of the contributing area per unit contour length. As in Figure 4-15, each circle represents the mean value over a range of contributing areas and the vertical lines are plus/minus one standard deviation. Figure 3-8, shown previously, illustrated the nonlinear relationship between water table

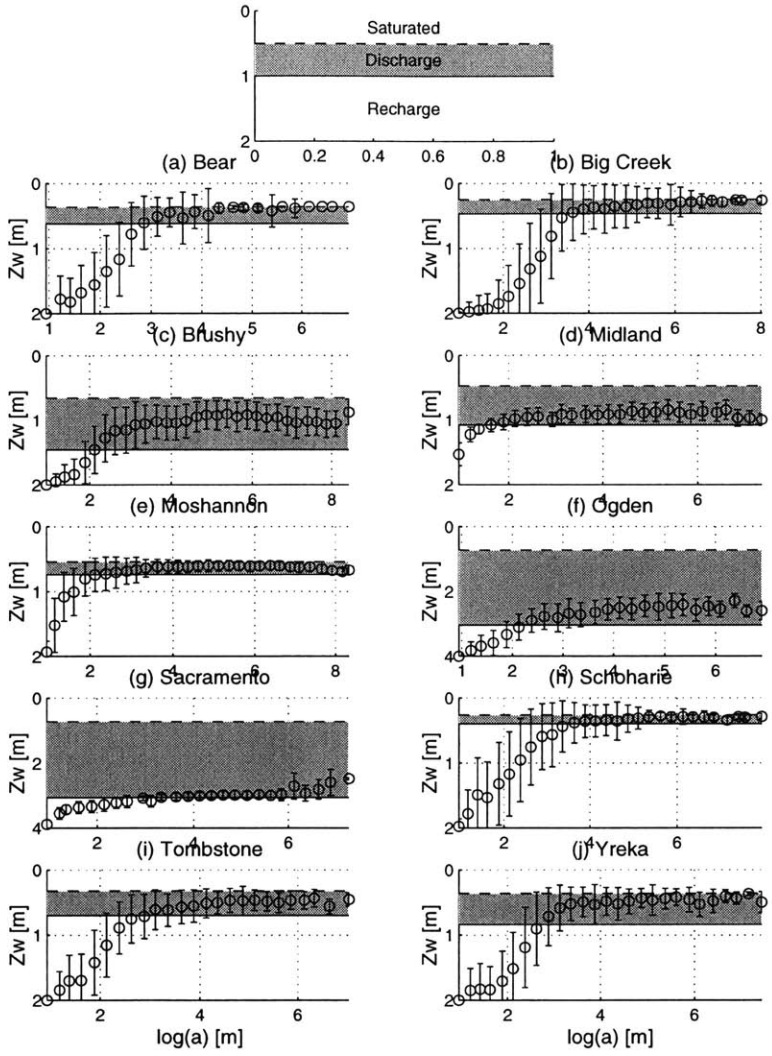

Figure 4-15: Mean water table depth as a function of contributing area per unit contour length, for all basins. Circles represent the mean water table depth within a half log-unit of contributing area. Vertical lines are plus/minus one standard deviation. The dashed horizontal line is Ψ_s; water table positions above this threshold indicate near-saturated conditions. The solid horizontal line is Z^*; water table positions near this value are indicative of midline regions. When the water table is below the Z^* line, net recharge is occurring.

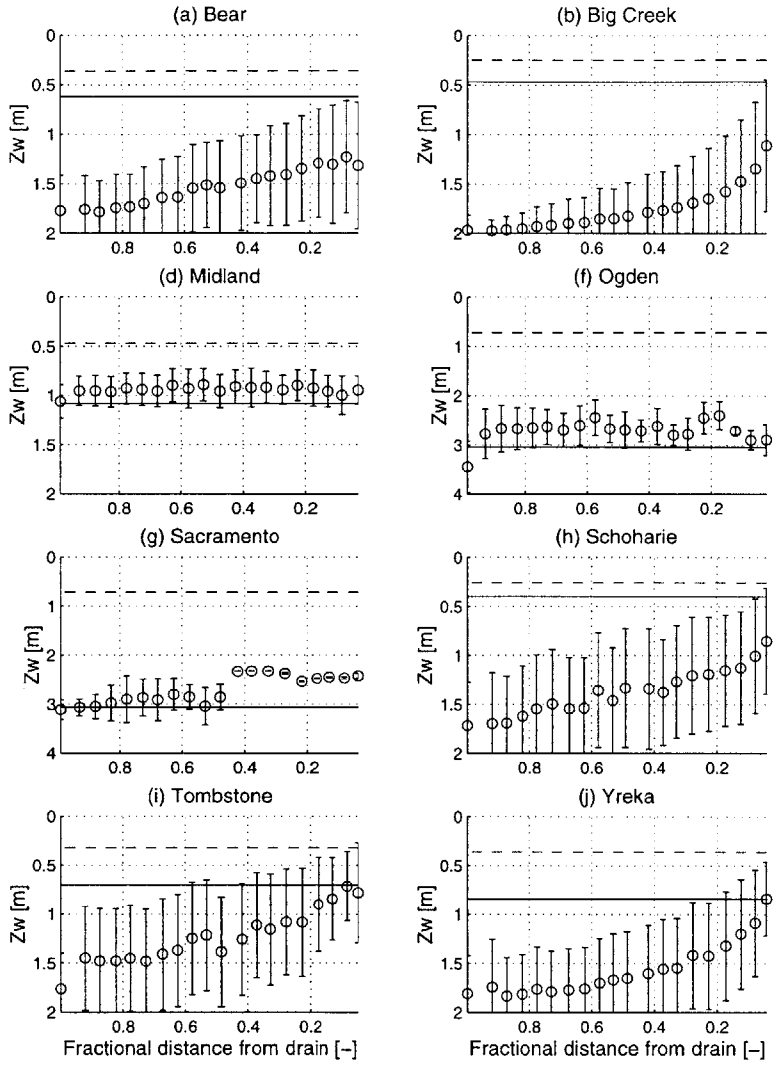

Figure 4-16: Mean water table depth as a function of fractional distance along a hillslope from the closest drain, for all basins. Circles represent the mean water table depth within a five-percent range of distances. Vertical lines are plus/minus one standard deviation. The dashed horizontal line is Ψ_s; water table positions above this threshold indicate near-saturated conditions. The solid horizontal line is Z^*; water table positions near this value are indicative of midline regions. When the water table is below the Z^* line, net recharge is occurring.

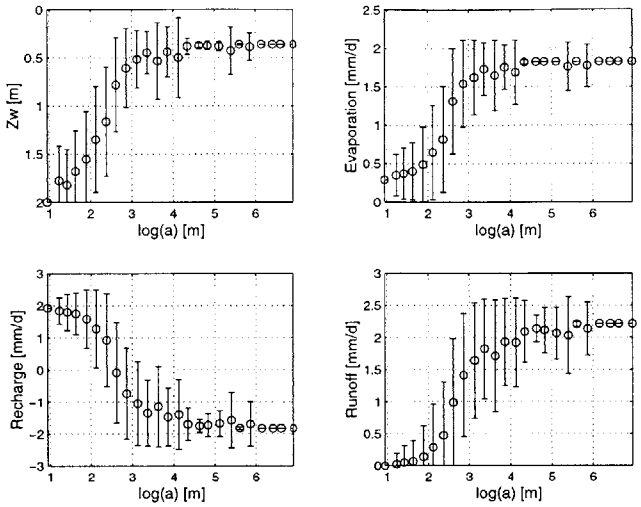

Figure 4-17: Equilibrium water table depth and fluxes as a function of a, Bear Valley, CA. Vertical lines represent one standard deviation around the average value in each bin.

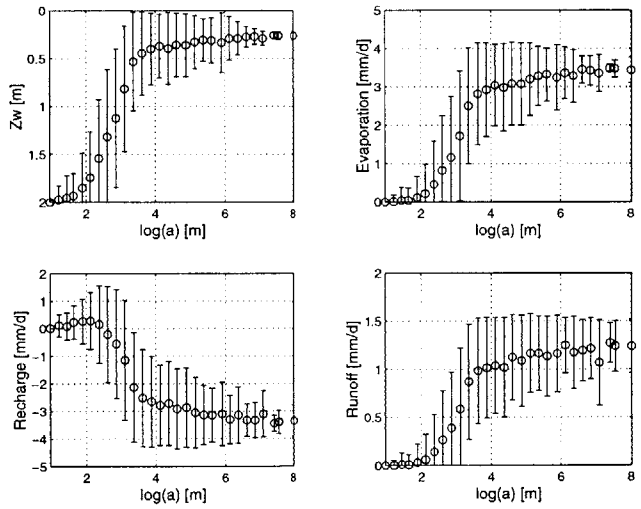

Figure 4-18: Equilibrium water table depth and fluxes as a function of a, Big Creek, ID. Vertical lines represent one standard deviation around the average value in each bin.

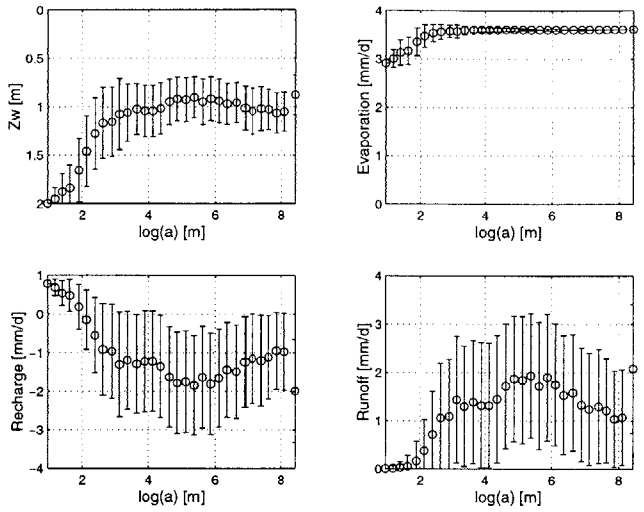

Figure 4-19: Equilibrium water table depth and fluxes as a function of a, Brushy, AL. Vertical lines represent one standard deviation around the average value in each bin.

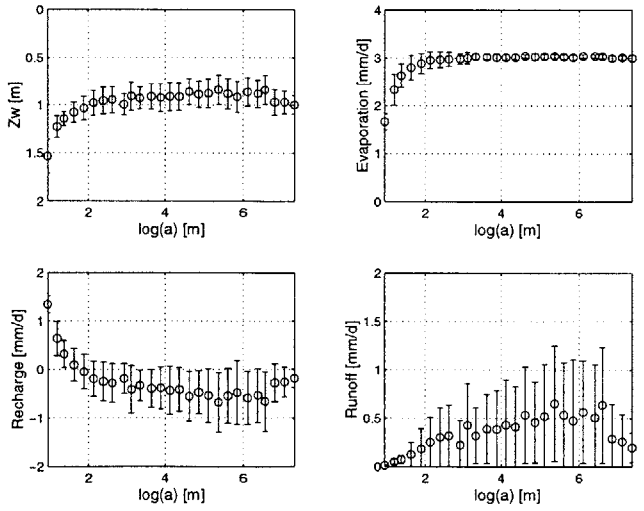

Figure 4-20: Equilibrium water table depth and fluxes as a function of a, Midland, VA. Vertical lines represent one standard deviation around the average value in each bin.

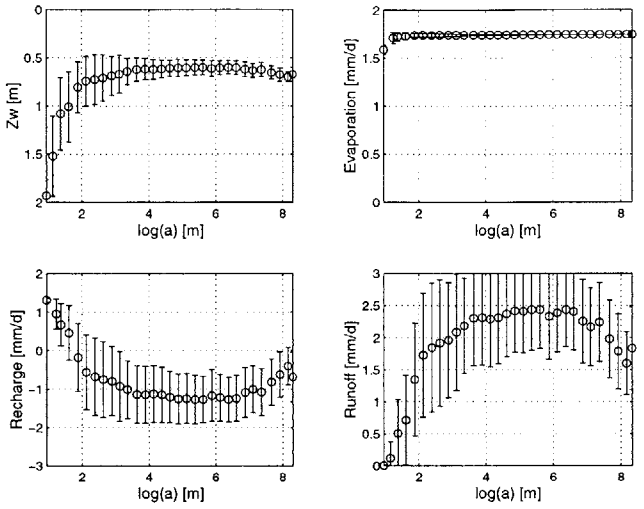

Figure 4-21: Equilibrium water table depth and fluxes as a function of a, Moshannon, PA. Vertical lines represent one standard deviation around the average value in each bin.

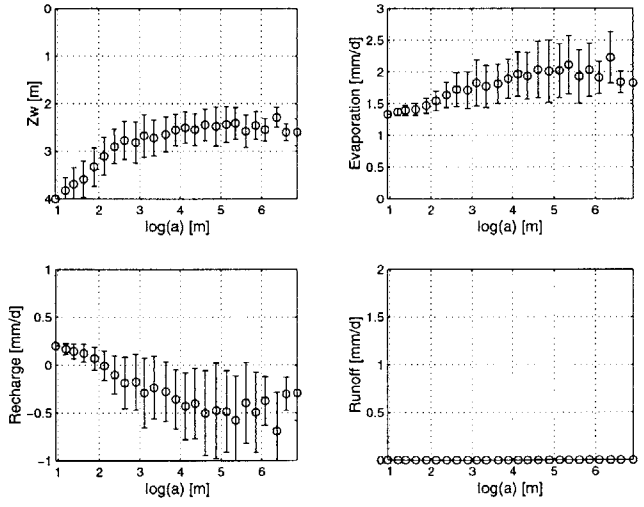

Figure 4-22: Equilibrium water table depth and fluxes as a function of a, Ogden, KS. Vertical lines represent one standard deviation around the average value in each bin.

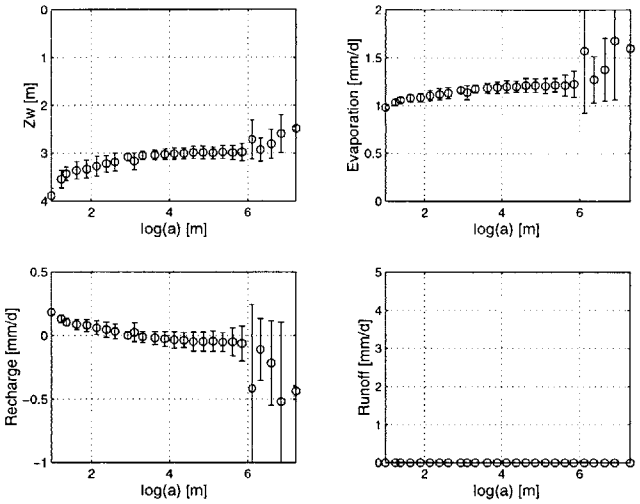

Figure 4-23: Equilibrium water table depth and fluxes as a function of a, Sacramento, CA. Vertical lines represent one standard deviation around the average value in each bin.

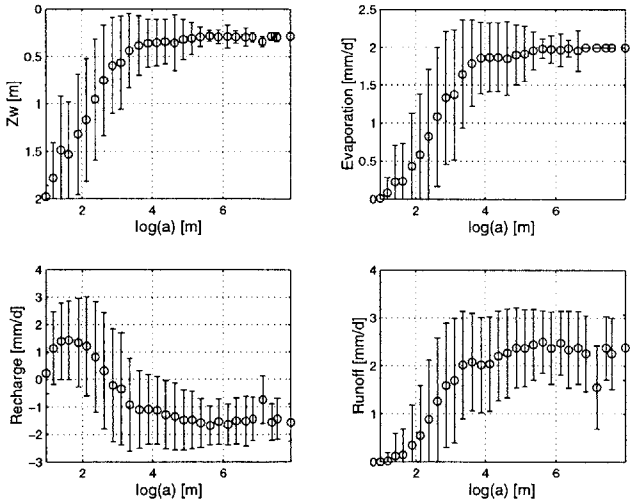

Figure 4-24: Equilibrium water table depth and fluxes as a function of a, Schoharie, NY. Vertical lines represent one standard deviation around the average value in each bin.

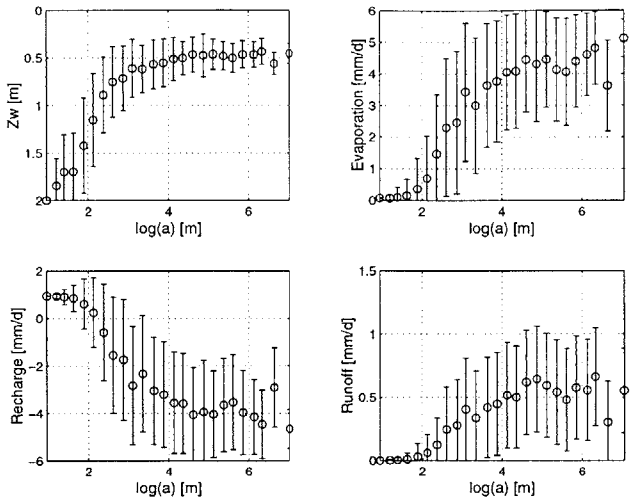

Figure 4-25: Equilibrium water table depth and fluxes as a function of a, Tombstone, AZ. Vertical lines represent one standard deviation around the average value in each bin.

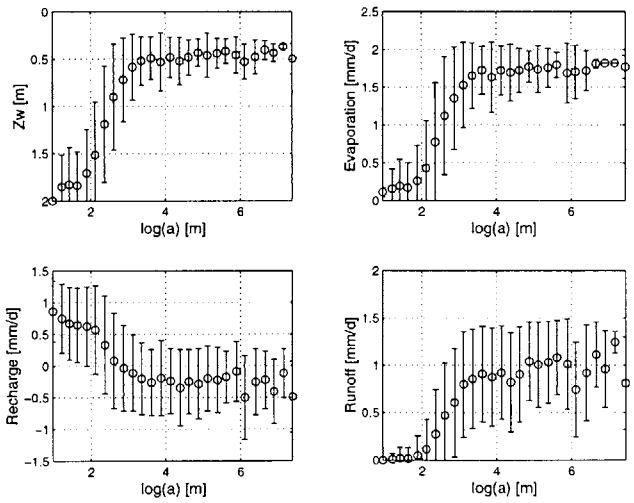

Figure 4-26: Equilibrium water table depth and surface fluxes as a function of a, Yreka, CA. Vertical lines represent one standard deviation around the average value in each bin.

depth and surface fluxes, recharge, runoff, and evaporation. As the water table lowers, evaporation decreases, runoff tends to zero, and recharge to the saturated zone increases. Correspondingly, a shallow water table is associated with high evaporation, measurable runoff, and net discharge from the saturated to the unsaturated zone. Below we examine how the nonlinear dependence of the hydrologic fluxes on water table position affects their spatial distribution within the basins.

Bear Valley is an example of a basin that exhibits a clear relationship between water table depth and surface fluxes. Evaporation and runoff increase with increasing a, in concert with the decreasing depth to saturation. In this basin, it would be possible to identify a scaling factor between each individual flux and water table location. This could be used either to estimate fluxes from soil moisture observations or to extract information on the water table position from measurements of runoff or evaporation. Tombstone and Yreka also show a strong positive relationship between the water table and surface fluxes; however, in riparian areas recharge and runoff vary significantly more than the water table, as seen from the plotted standard deviation. The difference in the degree of variability at a given location in the basin is due to the nonlinear sensitivity of the fluxes to the saturated depth shown in Figure 3-8.

Not all basins have surface fluxes closely following the pattern of water table depth. It is possible for some fluxes to mirror water table position while others do not. For example, the evaporation rates in Brushy and Moshannon are nearly uniform in space despite measurable variation in water table position. The uniformity in evaporation can be explained by consideration of Figure 3-8, which reveals a very low sensitivity of evaporation to water table depth. Table 3.3 also indicates that these two basins are among the most humid of the set. However, humid climate is not a sufficient explanation of this behavior. Schoharie basin is as humid ($P/E_p = 1.4$), but the soil texture is considerably more coarse (see Tables 3.4 and 3.5). The coarse soil texture leads to less capillary rise and more infiltration. In these basins, it would be impossible to measure either evaporation or water table position and make assumptions about the distribution of the other. The relationship between water table and the remaining two fluxes is also blurred. Because evaporation is nearly uniform in space, runoff and recharge contain all of the noise in the hydrologic response. These fluxes exhibit a larger variation around the mean than water table position, particularly in the riparian (high a) areas. Similarly, Ogden and Sacramento have uniform (zero) runoff everywhere in the basin even while the water table depth varies. Evaporation and recharge follow the pattern of water table depth, although the magnitude of the variability in space is small.

The plots in Figures 4-17 through 4-26 reveal that, while the surface fluxes generally follow the distribution of water table position, the sensitivity of the fluxes varies within and between basins. In some cases, one flux is insensitive to water table depth while other fluxes vary. In other environments, the deviation in some of the fluxes exceeds the variation in water table depth, highlighting an enhanced sensitivity of the surface fluxes. The nature of these relationships can be understood by looking at curves of the dependence of equilibrium fluxes on water table depth (Figure 3-8) and identifying the extreme values of the curve slopes. In cases where there is a strong linear relationship between water table and hydrologic flux, it may be possible to use knowledge of one variable to estimate values of the other, within a limited confidence range.

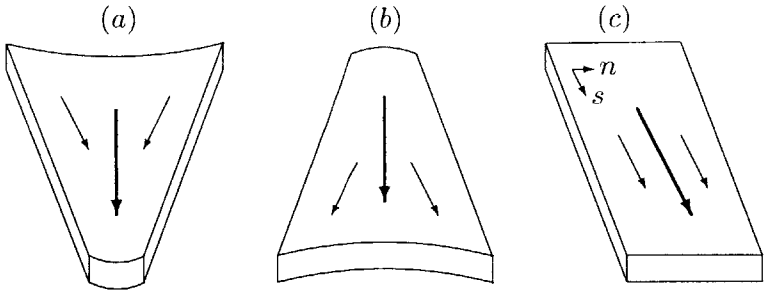

Figure 4-27: Schematic of hillslope shapes in the horizontal direction; (a) is convergent, (b) is divergent, (c) is rectilinear.

4.3.2 Hillslope curvature effects

In the previous section, we explored correlations between the water table depth and the position of a cell within the basin as quantified by the contributing area. The relationship indicates a deterministic spatial pattern seen to some degree in all of the basins despite marked interbasin differences in topography, climate, and soil. However, the mean water table data presented in Figure 4-15 are characterized by fairly large standard deviations. A range of hydrologic conditions is found in cells with the same positional index value. We hypothesize that this variability may be due at least in part to the hillslope curvature, a topographic feature that has been observed to influence hydrology (*e.g.*, Dunne and Black 1970a, 1970b; Anderson and Burt 1978) but is not fully taken into account in the either the a or the a/S index. In a natural landscape, complex terrain induces lateral moisture convergence or divergence that can introduce variability into the downslope moisture profile. In this section, we investigate whether the horizontal curvature of a hillslope explains any of the noise in the relationship between the positional indices and the equilibrium water table position.

We focus here on the effect of hillslope shape in the horizontal (planar) direction as illustrated in Figure 4-27. The hillslope type on which each pixel lies is determined from the second derivative of the surface elevation perpendicular to the direction of flow. We assume that flow occurs from a pixel to one of its eight nearest neighbors as determined by the direction of steepest descent (Tarboton *et al.* 1991). The shape of the hillslope is determined according to the following criterion:

$$\frac{d^2H}{dn^2} \begin{cases} > 0 & \text{concave} \\ < 0 & \text{convex} \\ = 0 & \text{rectilinear} \end{cases}$$

where H is the surface elevation and n is the horizontal distance in the direction perpendicular (normal) to flow. To avoid noise in the elevation data due to the relatively coarse resolution, the elevations used are the averages from the two adjacent pixels on either side of the pixel of interest. Table 4.1 summarizes the distribution of the basins into different hill curvatures; Figures 4-28 through 4-37 map the spatial distribution of the different hillslope types.

In most of the basins, the majority of pixels is either convergent or divergent, with a fairly even split between the two shapes. Generally speaking, hillslopes are divergent and

Basin	Convergent [% area]	Rectilinear [% area]	Divergent [% area]
Bear	38	8	54
Big Creek	48	5	47
Brushy	44	16	40
Midland	30	34	36
Moshannon	48	10	42
Ogden	39	19	42
Sacramento	10	74	16
Schoharie	46	10	44
Tombstone	41	16	43
Yreka	43	10	47

Table 4.1: Percent of basin area of each hill form type.

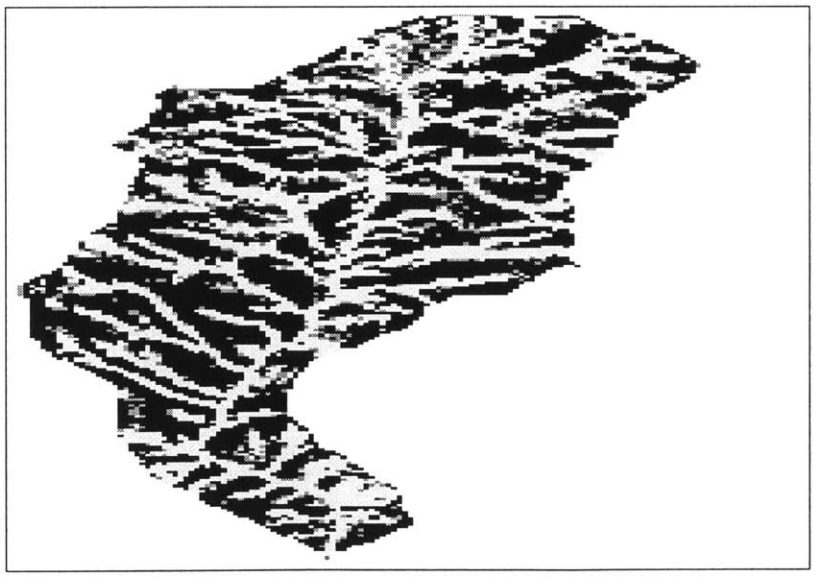

Figure 4-28: Map of hillslope shapes, Bear Valley, CA. Black is convergent, medium grey is rectilinear, and light grey is divergent. See Figure 3-11 for horizontal scale.

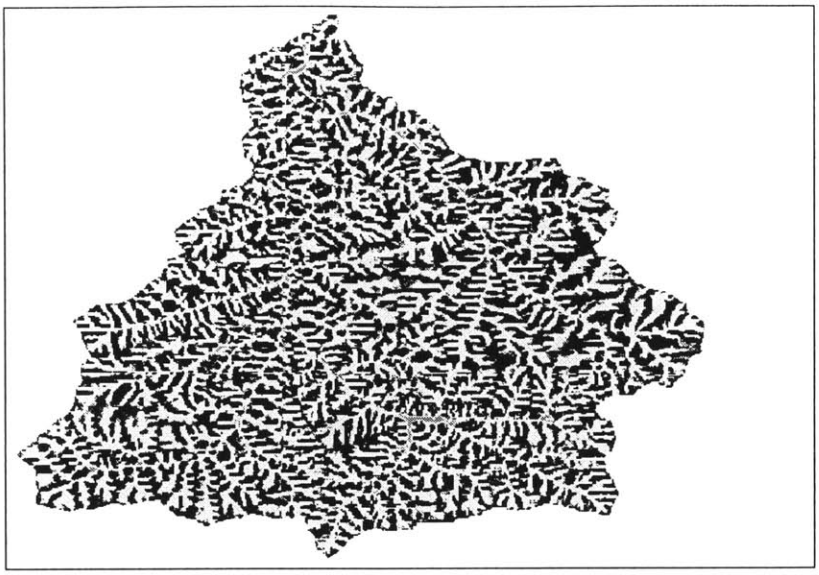

Figure 4-29: Map of hillslope shapes, Big Creek, ID. Black is convergent, medium grey is rectilinear, and light grey is divergent. See Figure 3-12 for horizontal scale.

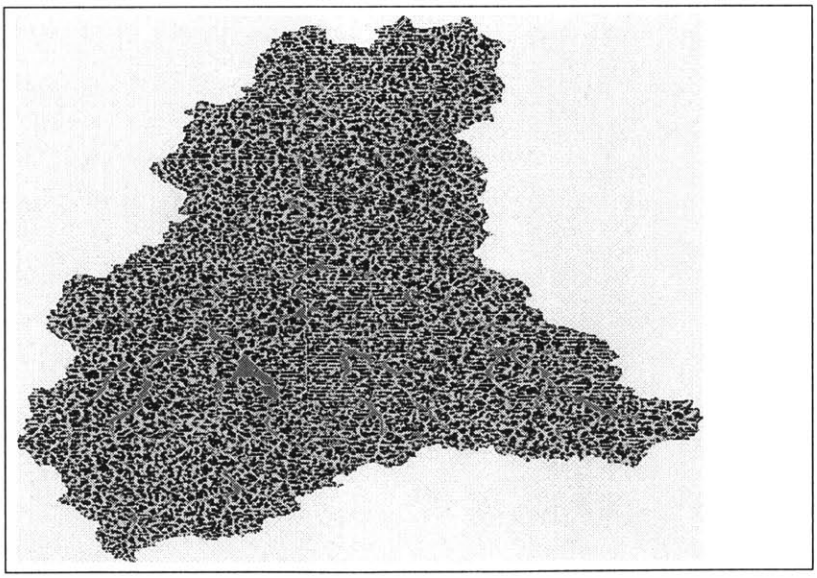

Figure 4-30: Map of hillslope shapes, Brushy Creek, AL. Black is convergent, medium grey is rectilinear, and light grey is divergent. See Figure 3-13 for horizontal scale.

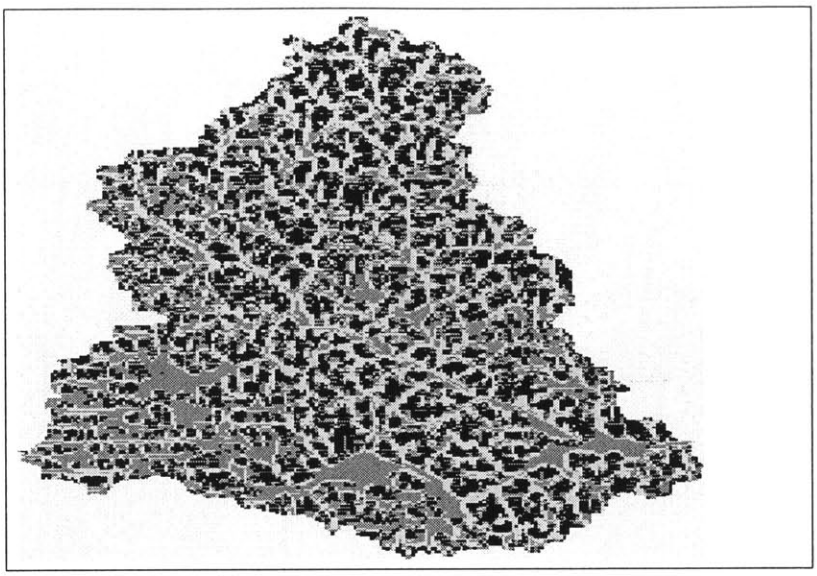

Figure 4-31: Map of hillslope shapes, Midland, VA. Black is convergent, medium grey is rectilinear, and light grey is divergent. See Figure 3-14 for horizontal scale.

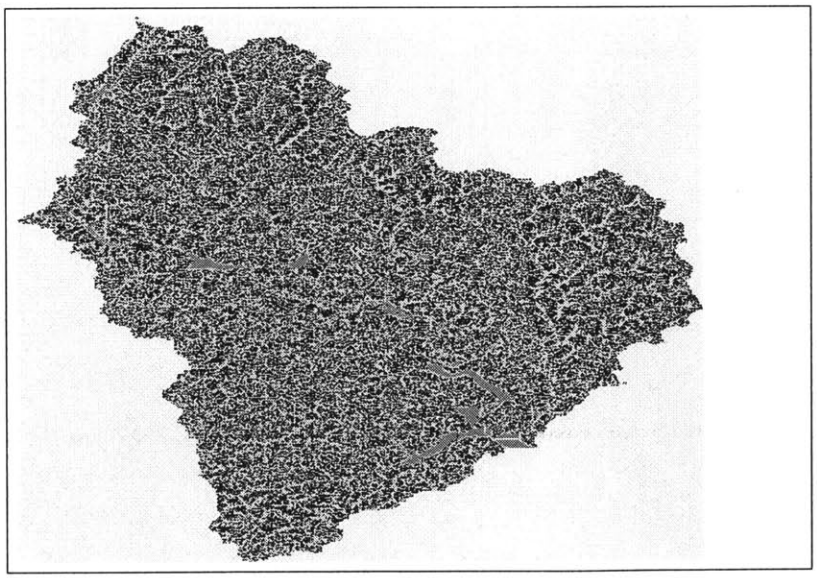

Figure 4-32: Map of hillslope shapes, Moshannon, PA. Black is convergent, medium grey is rectilinear, and light grey is divergent. See Figure 3-15 for horizontal scale.

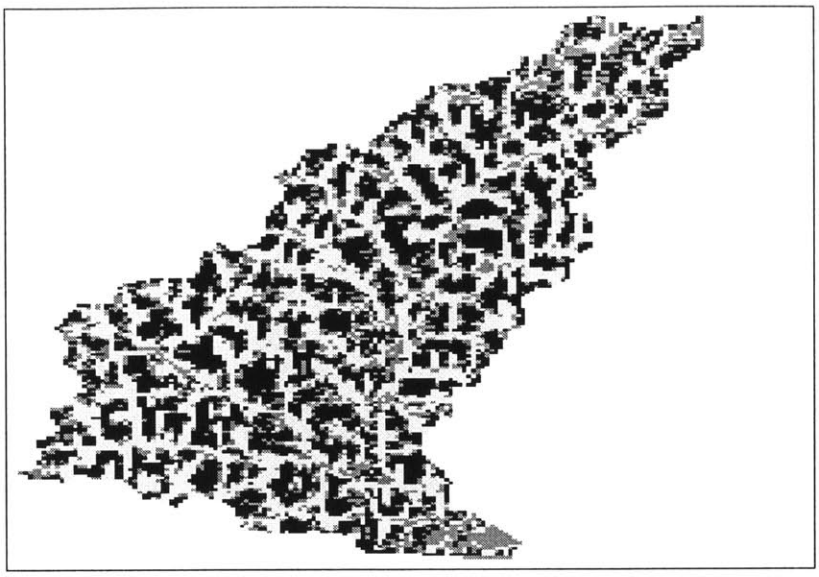

Figure 4-33: Map of hillslope shapes, Ogden, KS. Black is convergent, medium grey is rectilinear, and light grey is divergent. See Figure 3-16 for horizontal scale.

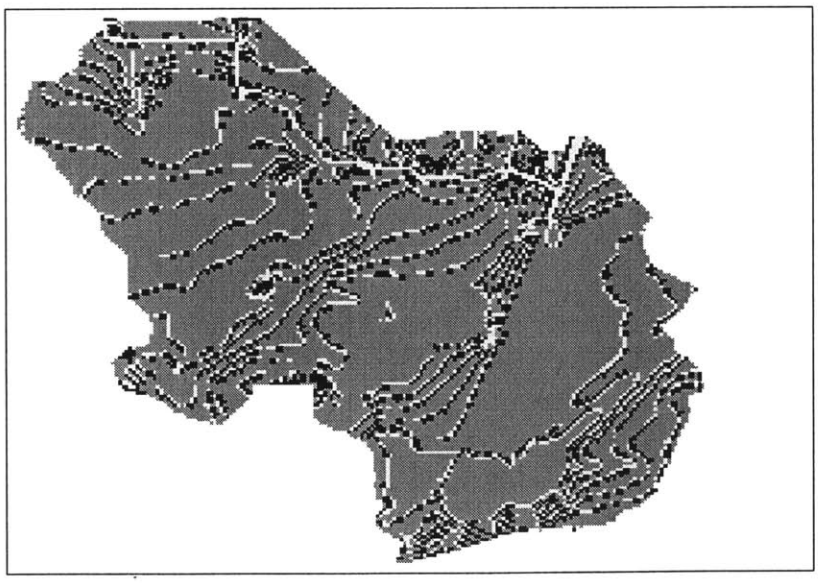

Figure 4-34: Map of hillslope shapes, Sacramento, CA. Black is convergent, medium grey is rectilinear, and light grey is divergent. See Figure 3-17 for horizontal scale.

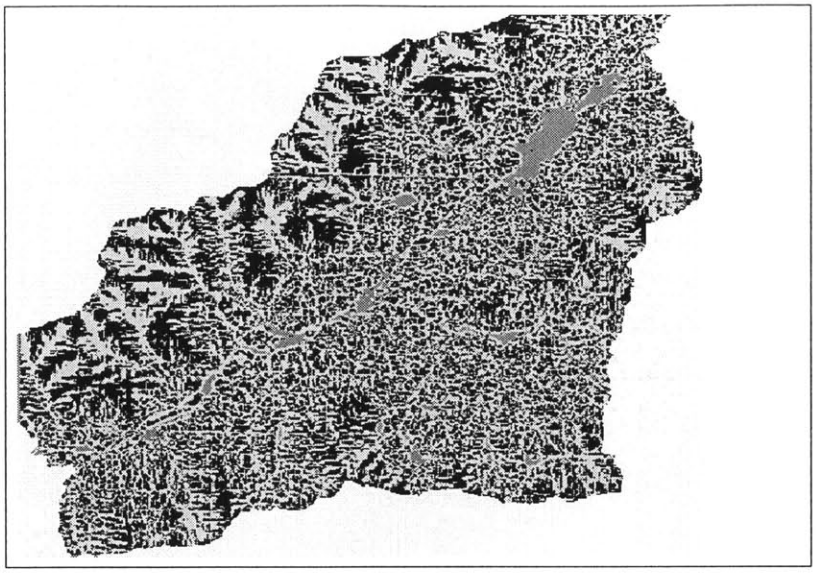

Figure 4-35: Map of hillslope shapes, Schoharie, NY. Black is convergent, medium grey is rectilinear, and light grey is divergent. See Figure 3-18 for horizontal scale.

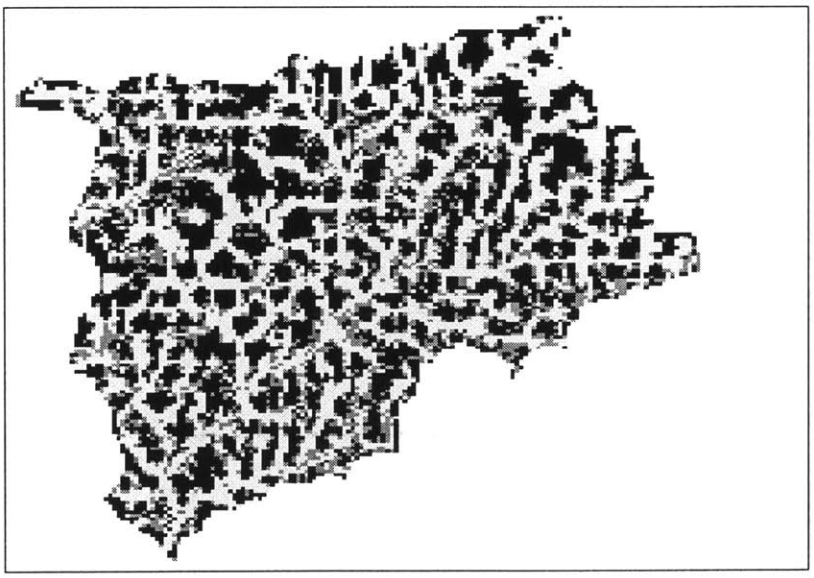

Figure 4-36: Map of hillslope shapes, Tombstone, AZ. Black is convergent, medium grey is rectilinear, and light grey is divergent. See Figure 3-19 for horizontal scale.

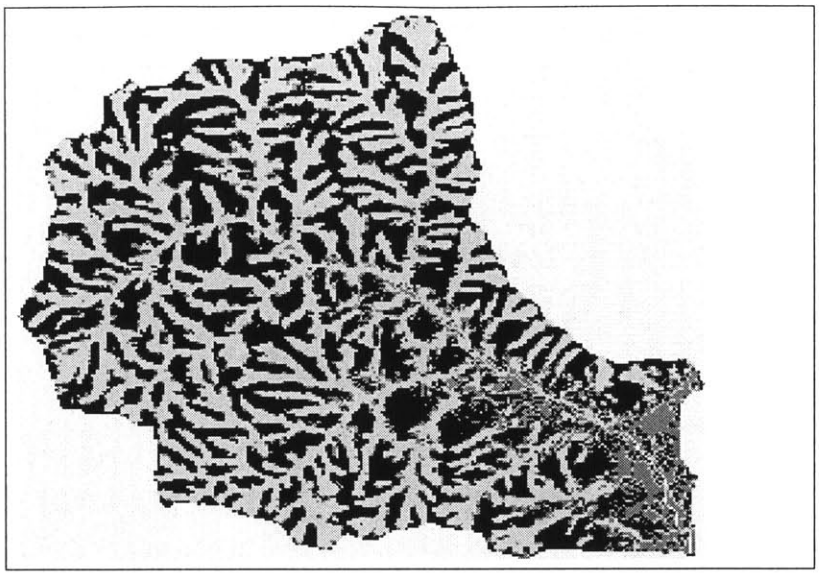

Figure 4-37: Map of hillslope shapes, Yreka, CA. Black is convergent, medium grey is rectilinear, and light grey is divergent. See Figure 3-20 for horizontal scale.

channels are convergent. Rectilinear pixels are scattered throughout the basins, often at the boundary between convergent and divergent slopes; however, they are found in some substantially sized clusters in Midland and Schoharie. This may be the result of the pit-filling algorithm, which raises pits up to the elevation of the neighboring cells. Locations where a number of adjacent pits have been raised to the same elevation will be classified as rectilinear. The one extreme exception to the general pattern of convergent and divergent pixels in valley and hillslopes, respectively, is Sacramento. In this basin, nearly three out of four pixels are rectilinear. The high proportion of rectilinear pixels is due to the basin's low relief; flat areas are rectilinear by definition. Convergent and divergent pixels are clustered along apparent contour gradients, corresponding to the discrete steps in DEM surface elevation.

We examine the influence of hill form on hydrology by creating plots of water table depth versus a and a/S with pixels separated by curvature type. These plots are shown in Figures 4-38 and 4-39. The symbols are filled if the mean depth on a convergent slope is significantly different at the 95 percent level from the divergent value for a given topographic index. The apparently counterintuitive unfilled symbols in locations where the mean values diverge noticeably is due to lower statistics from small samples sizes in that bin.

The hillslope shape in the horizontal direction has a significant influence on water table depth across most of the dynamic range: the water table is nearer the surface on convergent slopes than on divergent slopes. More moisture accumulates in convergent areas, bringing the water table closer to the surface. This intuitive finding, long observed in the field, is important because it highlights the inability of simple topography-based indices to fully capture the topographic forcing of soil moisture. The division of contributing area by the contour length was intended to incorporate some information about the horizontal curvature. The use of slope provides additional information about the shape of the topography in the downslope direction. Yet despite the consideration of two topographic variables—contour length and slope–to supplement the location index, the influence of topography on

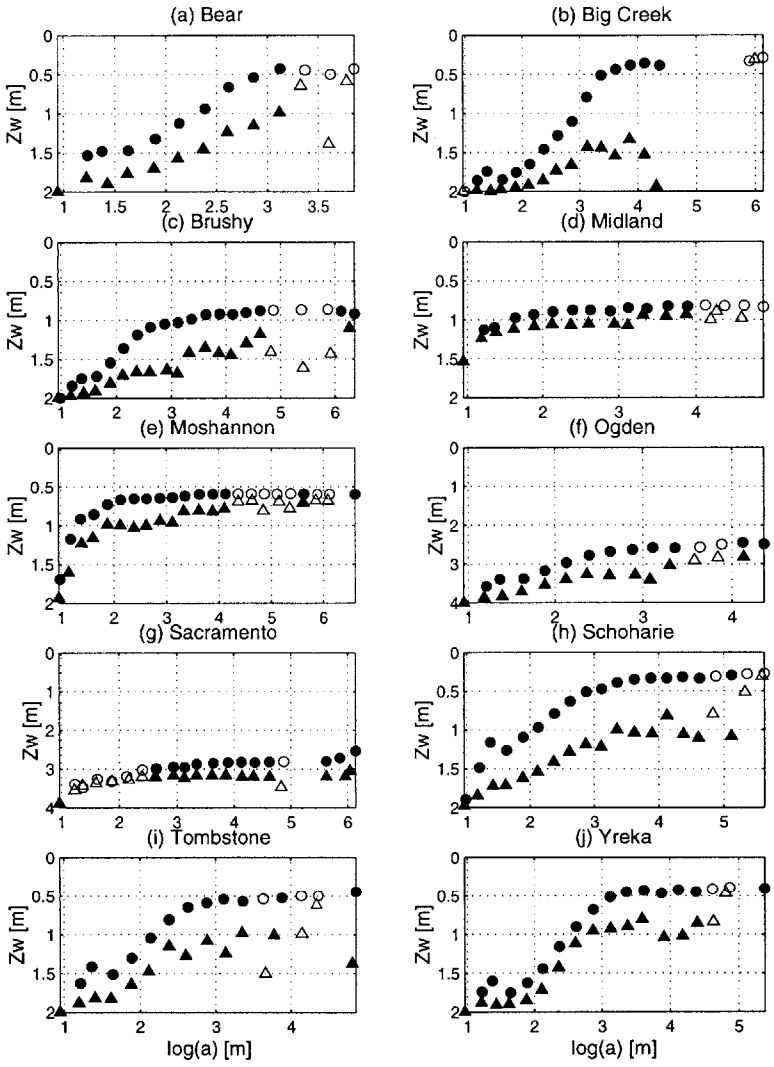

Figure 4-38: Mean water table elevation as a function of contributing area, separated by hillslope shape, for all basins. Symbols represent the mean water table elevation for all convergent (circle) or divergent (triangle) pixels for a given class of contributing area. When the symbols are filled, the convergent and divergent pixels are different in magnitude with 95% statistical confidence. Pixels where only one hillslope shape occurs at a location are omitted.

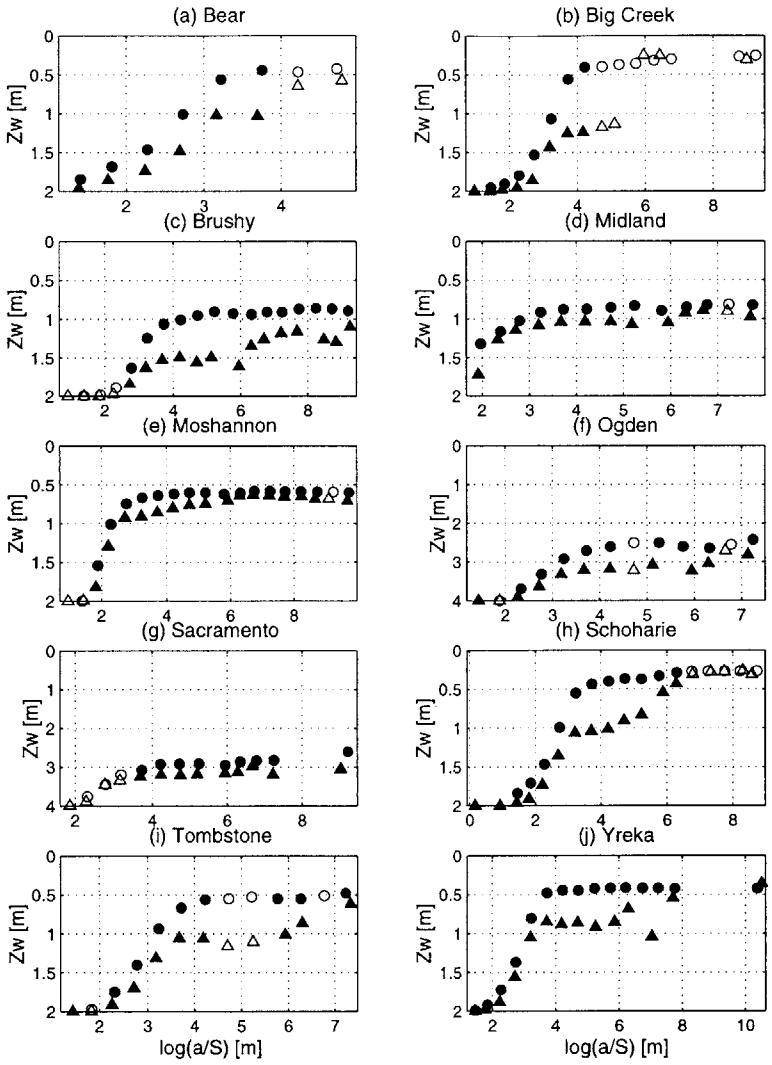

Figure 4-39: Mean water table elevation as a function of contributing area/slope, separated by hillslope shape, for all basins. Symbols represent the mean water table elevation for all convergent (circle) or divergent (triangle) pixels for a given class of contributing area. When the symbols are filled, the convergent and divergent pixels are different in magnitude with 95% statistical confidence. Pixels where only one hillslope shape occurs at a location are omitted.

water table position has not been sufficiently represented; the separation of pixels according to the horizontal hillslope shape provides even more significant information.

Figures 4-38 and 4-39 show that the effect of curvature on water table depth is larger than that incorporated in the area per unit contour length index. The failure of the contour length to capture the hillslope curvature is linked to the horizontal resolution of the elevation data. If the resolution of the surface topography were infinitely fine, the contour length would fully represent the curvature of the hillslope. On a divergent landscape, for example, the countour length could be as small as the width of a single flow line. In contrast, as a valley were incised and the curvature increased, the contour length would grow even as the contributing area remained constant. When the elevation is only available on a rectangular grid, however, the calculation of the contour length is by necessity approximate. A 30-m pixel is either fully included or excluded in the calculation of the contour length contributing to a given pixel; there is no partial contribution from a neighboring cell. As a result, a planar hillslope and a divergent hillslope would have equivalent contour lengths (equal to the width of one pixel). This is the case even if the upslope pixel were transporting moisture in the direction of multiple cells and thus the actual contour length were less than a pixel wide.

In an environment in which the surface elevation were known at an infinitely fine resolution, therefore, we expect that the area per unit contour length would fully capture the effect of curvature on the local hydrology. One analytical approach to incorporating curvature effects was introduced by Fan and Bras (1998), who collapsed a hillslope into a two-dimensional cross-section for modeling of downslope flows. The available moisture storage was integrated across the hillslope, explicitly capturing the curvature-related contour length at any distance downslope. However, most distributed models rely on gridded elevation data to represent the relevant topographic features. In environments where the grid resolution is fine, the effect of curvature is expected to decrease. In landscapes which have elevation data at a 30-m or coarser resolution, the use of the contour length in the location parameter appears insufficient. This indicates that reliance on topographic indices such as a/S, which depend on coarse determination of the contour length, may have limitations in accurately representing the hydrologic response on hillslopes with different curvatures.

4.3.3 Extent of midline region

The plots sorting water table depth on the basis of location in the basin can be divided into three sections: upslope areas, where the water table is deep; downslope areas, where the water table is at or near the surface; and an intermediate or midline zone. In an early application of the coupled model, Salvucci (1994) observed the corresponding partitioning of a planar hillslope into upslope recharge, midline, and downslope discharge zones as illustrated in Figure 4-12. The midline zone plays an important role in the translation of moisture from the recharge areas to the discharge and seepage face areas. In the midline zone, the water table is approximately parallel to the ground surface at a depth equal to Z^*, the depth at which the net flux between the unsaturated and saturated zones is zero. This region experiences no change in the saturated storage with distance downslope; on average, the moisture entering the soil column during storms is evaporated away during interstorm periods. The hydrologic conditions in the midline zone match those of models that use the surface slope as a proxy for the energy gradient driving lateral flow; the spatial extent of the midline region provides an index for the extent to which such an assumption is valid.

Salvucci and Entekhabi (1995) found that the midline extends across the majority of the total hillslope length under normal conditions (silt soil, semi-humid climate, ten-percent

surface gradient). We hypothesize that the large extent of the midline zone observed on a planar hillslope will not be seen in more complex topography. The presence of convergent and divergent slopes in both the downslope and normal directions may introduce lateral flow patterns and soil moisture variations that prevent the establishment of an extensive midline. The hypothesis is investigated by calculating the spatial extent of the midline zone in each of the study basins and seeking to identify a physical basis for differences between basins.

We differentiate the midline from the recharge and discharge zones based on the value of the equilibrium recharge flux. By definition, the midline is found where net recharge is zero; realistically, however, it is necessary to consider a range around $Q_e = 0$ to represent the midline. To establish a criterion, we consider the extreme values of Q_e and select a specific fraction of the possible dynamic range. The maximum and minimum average recharge fluxes can be derived from the steady-state water balance for the unsaturated zone, $Q_e = P - (E + R)$, for extreme conditions of a fully saturated and a fully unsaturated soil column. When the soil is saturated, all precipitation is converted to runoff and evaporation occurs at its atmospheric potential rate. To satisfy the water balance, the limiting recharge rate is $-E_p$, *i.e.*, the entire moisture supply for evaporation is met by water transported upward from the saturated zone. In the other extreme, for a very dry soil, both runoff and evaporation tend to zero. This gives a limiting maximum recharge rate equal to P, the incident precipitation at the surface. The midline zone can then be identified according to the criterion $-fE_p < Q_e < fP$, where f is some fraction of the dynamic range, selected here as 0.1. Figure 4-40 highlights the portion of the soil column associated with the midline region, identified by the position of the water table. The span around the zero net recharge depth varies depending on the values of P and E_p. It is asymmetric around Z^* and in some basins the height of the midline zone is negligible relative to the total soil depth. The midline zones are overlain on the equilibrium flux curves in Figure 4-41; these curves highlight the variability in the surface fluxes within the region considered to be the midline.

Figure 4-42 presents the fraction of each basin characterized as recharge midline, or discharge. The extent of midline ranges from 2 and 3 percent of basin area in Tombstone and Bear, respectively, to over 95 percent in Sacramento. The discharge zone covers less area than the recharge zone in all of the basins. Figures 4-43 through 4-52 contain maps of the spatial occurrence of recharge, midline, and discharge areas. Some of the basins have an extensive midline region; others are dominated by net recharge and discharge zones with very little midline. The noise in the maps is caused by the noise in the distribution of water table depth seen previously in this chapter. The factors which influence the formation of the midline are discussed below.

Salvucci (1994) found that the extent of the midline increased under a number of physical perturbations: a decrease in soil depth, an increase in hillslope length, a decrease in hillslope angle, and a decrease in hydraulic conductivity. Additionally, changing the climate impacted the shape of the water table profile, although there was no clear effect on the extent of the midline region. We attempt to combine the different variables seen to influence the midline through consideration of the physical processes driving the development and maintenance of a midline region.

The midline is influenced by processes in both the unsaturated and saturated zones. In the saturated zone, the extent of midline is inversely related to the ability of the soil to laterally transmit infiltrating moisture away from the recharge zone. When the soil is able to efficiently move moisture downslope, either due to a strong hydraulic gradient or high flow conductivity, the area of recharge needed to meet the lateral flow demand is high.

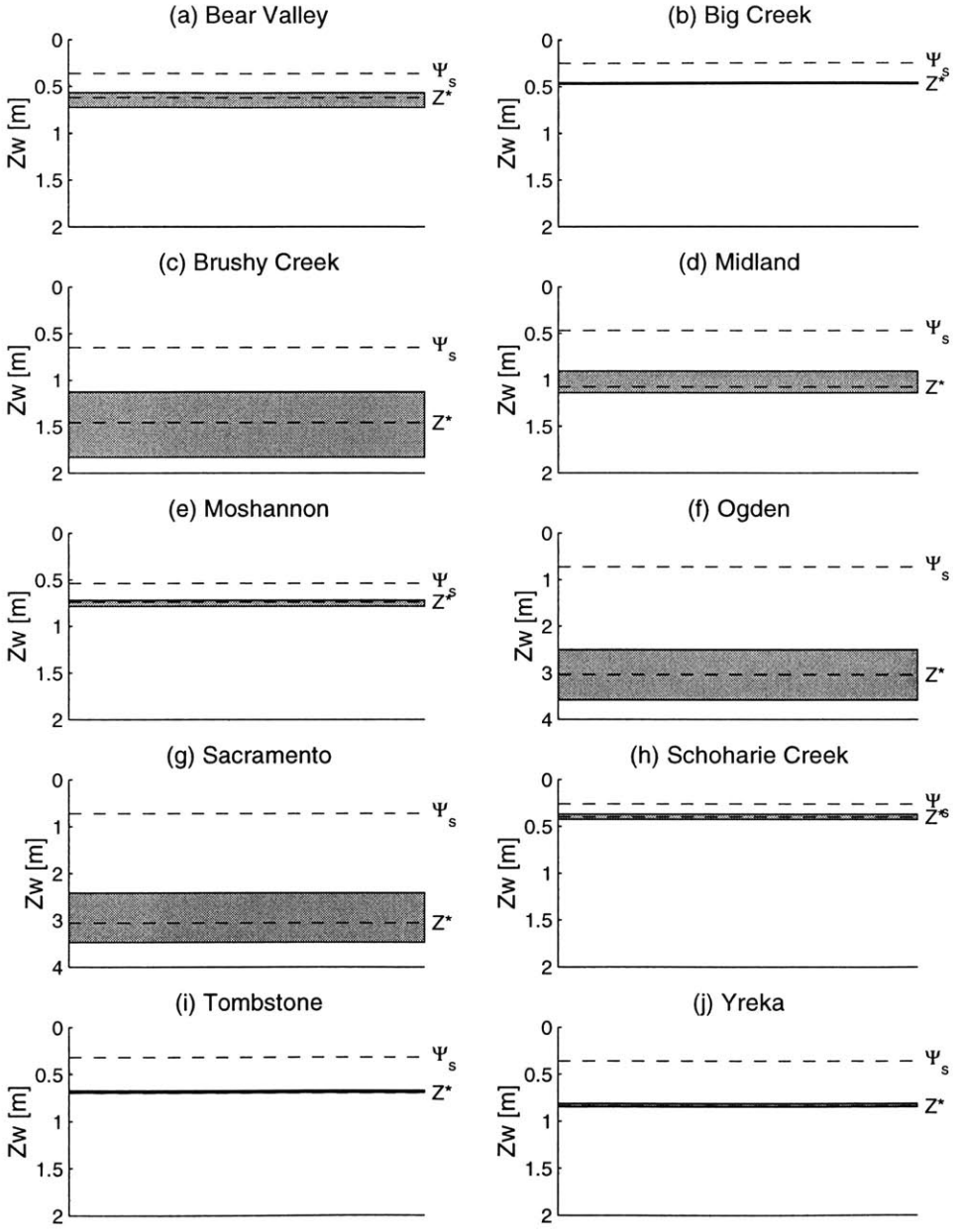

Figure 4-40: Delineation of the midline region derived from recharge criterion.

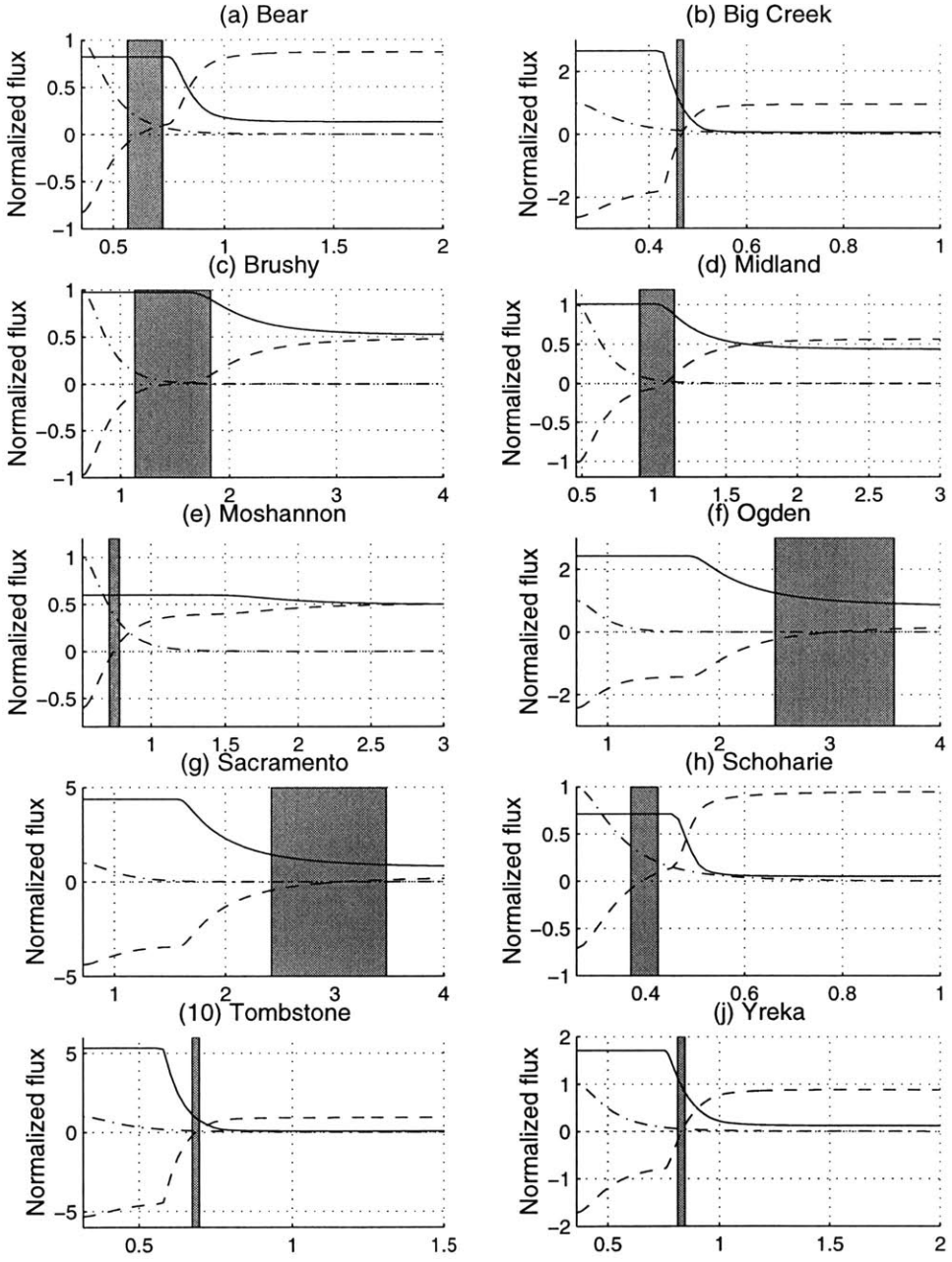

Figure 4-41: Delineation of the midline region derived from recharge criterion, overlain on equilibrium flux curves.

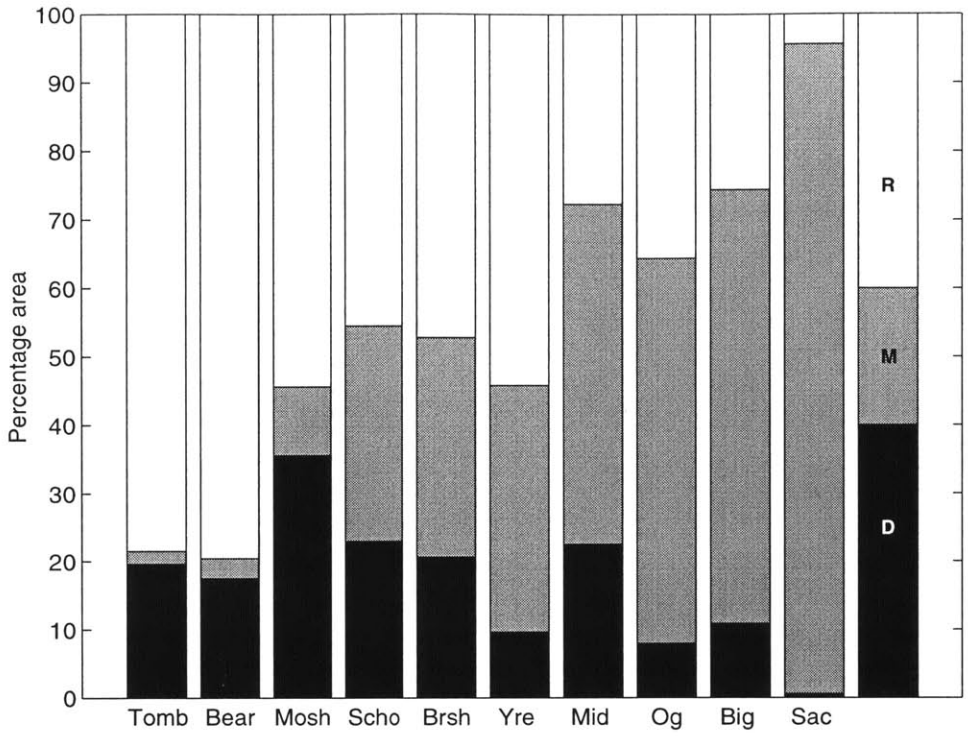

Figure 4-42: Percentage of basin area considered recharge (R), discharge (D), and midline (M) regions, as distinguished by recharge flux, sorted by increasing midline area.

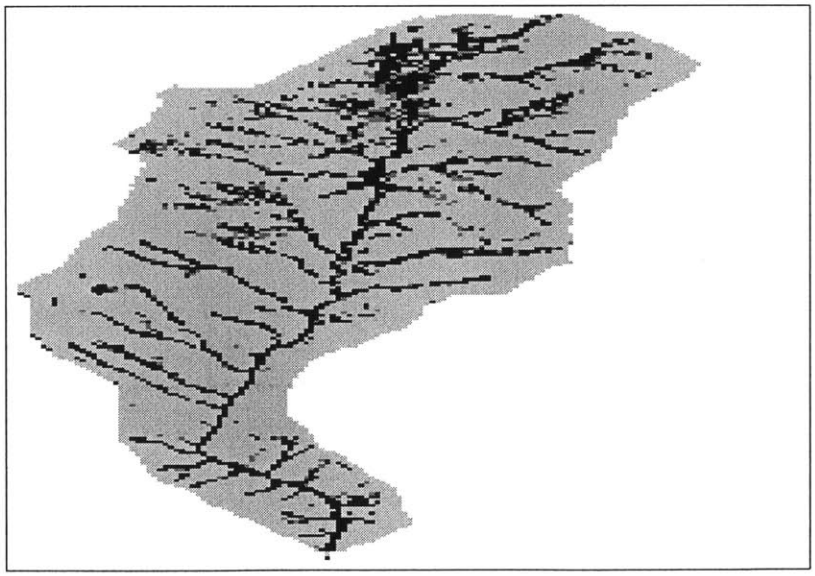

Figure 4-43: Map of recharge, midline, and discharge zones, Bear Valley, CA. Light grey is recharge, grey is midline, and black is discharge. See Figure 3-11 for horizontal scale.

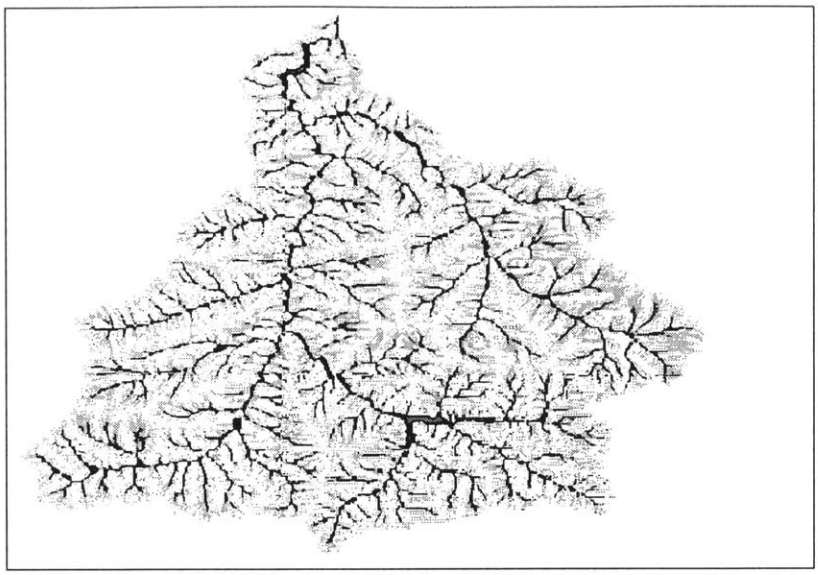

Figure 4-44: Map of recharge, midline, and discharge zones, Big Creek, ID. White is recharge, grey is midline, and black is discharge. See Figure 3-12 for horizontal scale.

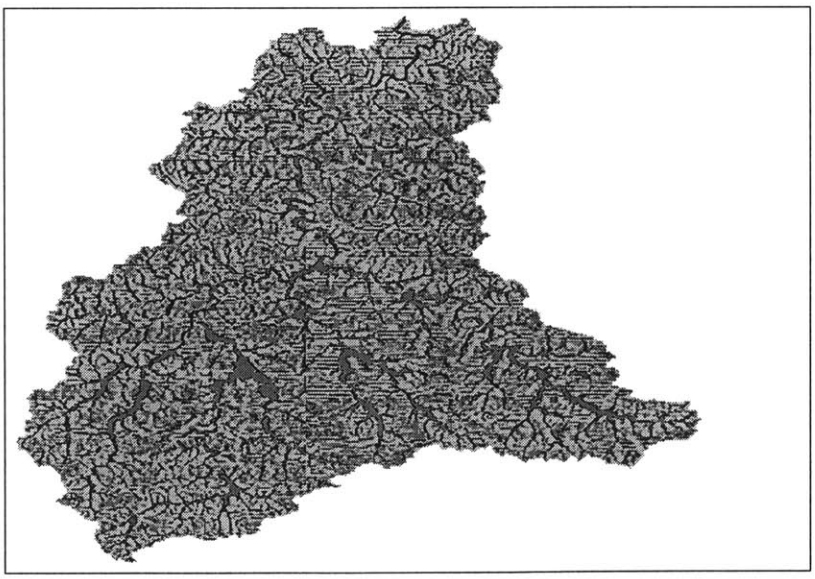

Figure 4-45: Map of recharge, midline, and discharge zones, Brushy Creek, AL. Light grey is recharge, grey is midline, and black is discharge. See Figure 3-13 for horizontal scale.

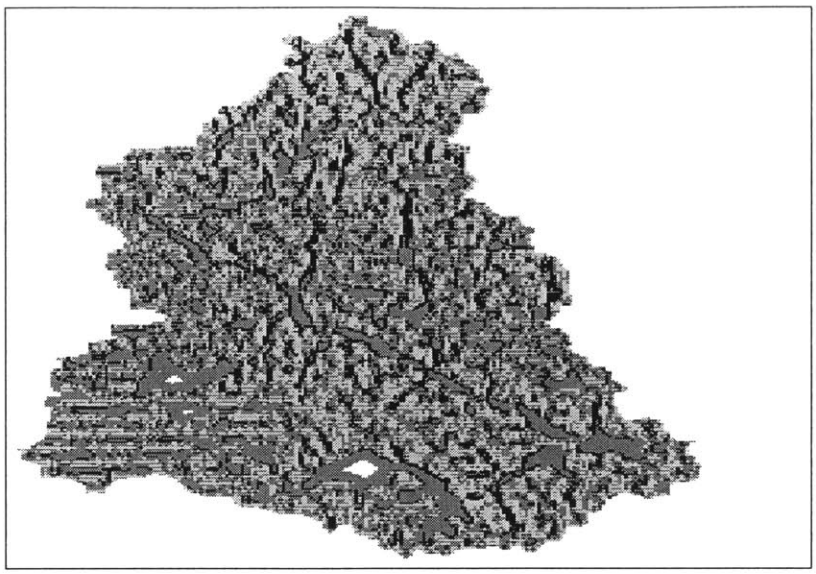

Figure 4-46: Map of recharge, midline, and discharge zones, Midland, VA. Light grey is recharge, grey is midline, and black is discharge. See Figure 3-14 for horizontal scale.

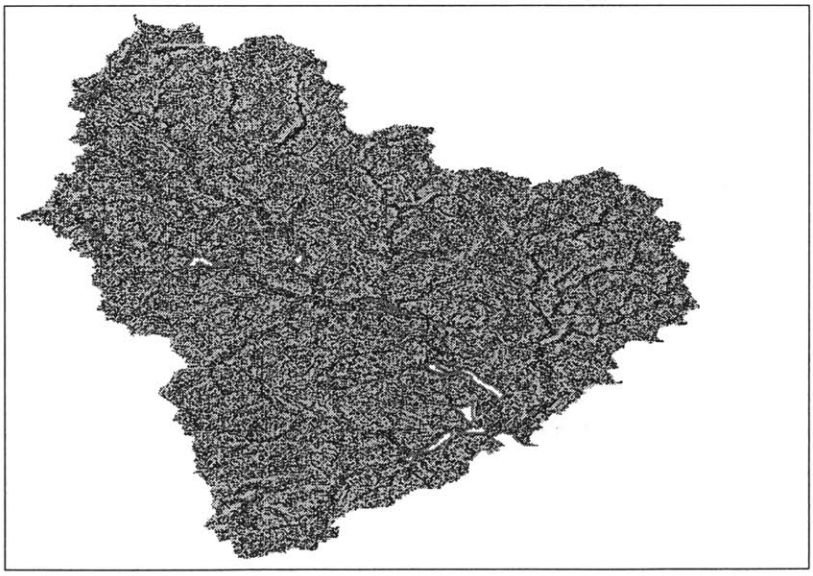

Figure 4-47: Map of recharge, midline, and discharge zones, Moshannon, PA. Light grey is recharge, grey is midline, and black is discharge. See Figure 3-15 for horizontal scale.

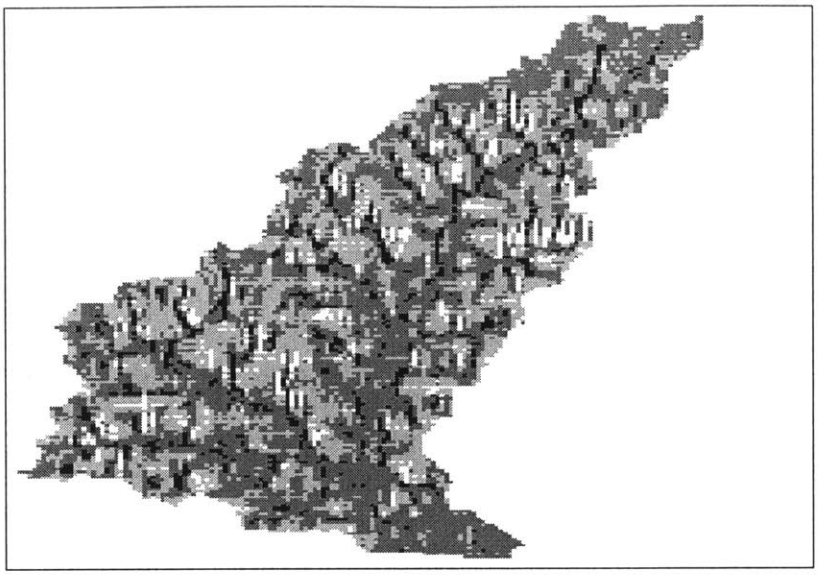

Figure 4-48: Map of recharge, midline, and discharge zones, Ogden, KS. Light grey is recharge, grey is midline, and black is discharge. See Figure 3-16 for horizontal scale.

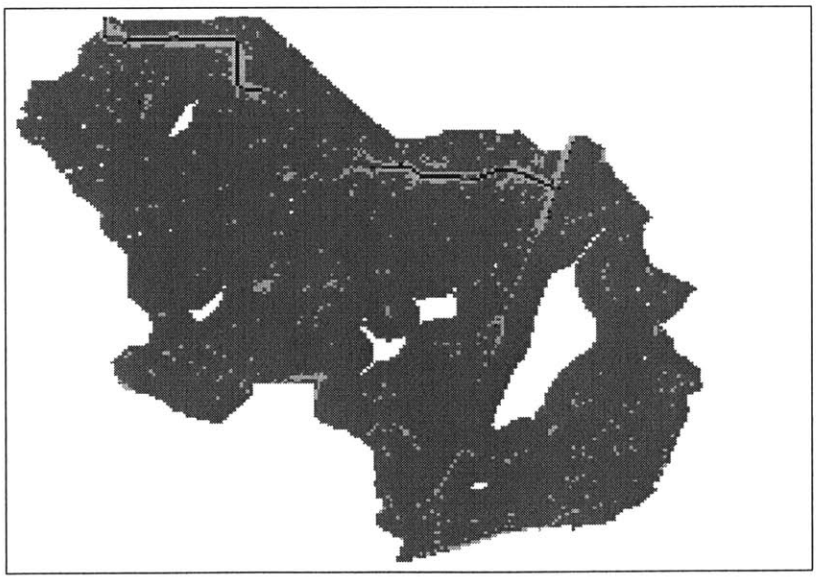

Figure 4-49: Map of recharge, midline, and discharge zones, Sacramento, CA. Light grey is recharge, grey is midline, and black is discharge. See Figure 3-17 for horizontal scale.

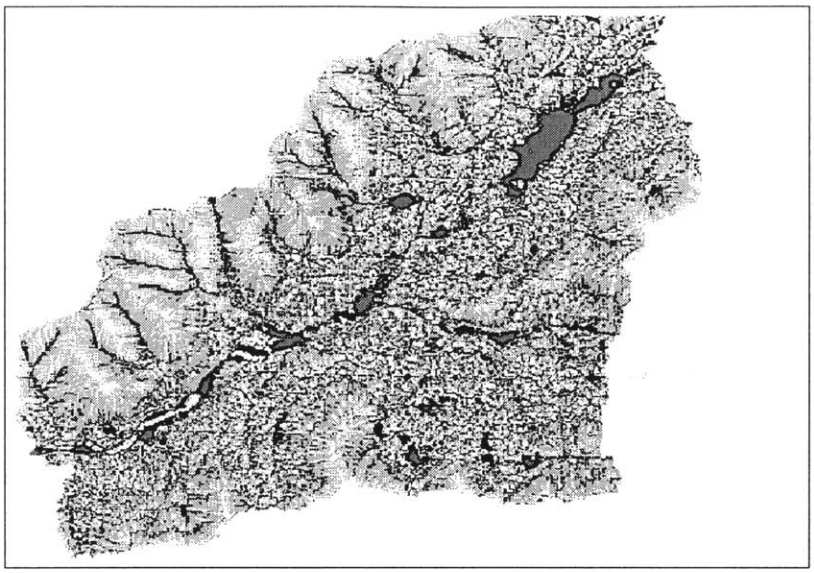

Figure 4-50: Map of recharge, midline, and discharge zones, Schoharie, NY. Light grey is recharge, grey is midline, and black is discharge. See Figure 3-18 for horizontal scale.

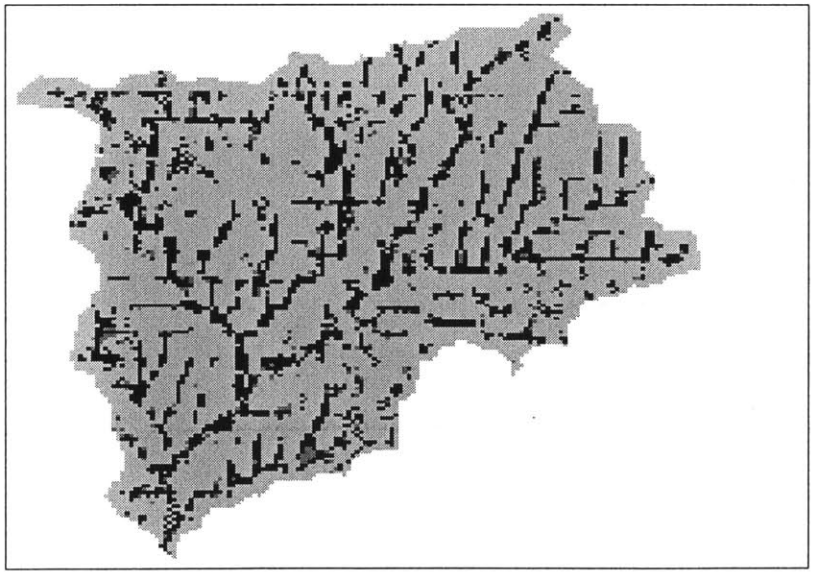

Figure 4-51: Map of recharge, midline, and discharge zones, Tombstone, AZ. Light grey is recharge, grey is midline, and black is discharge. See Figure 3-19 for horizontal scale.

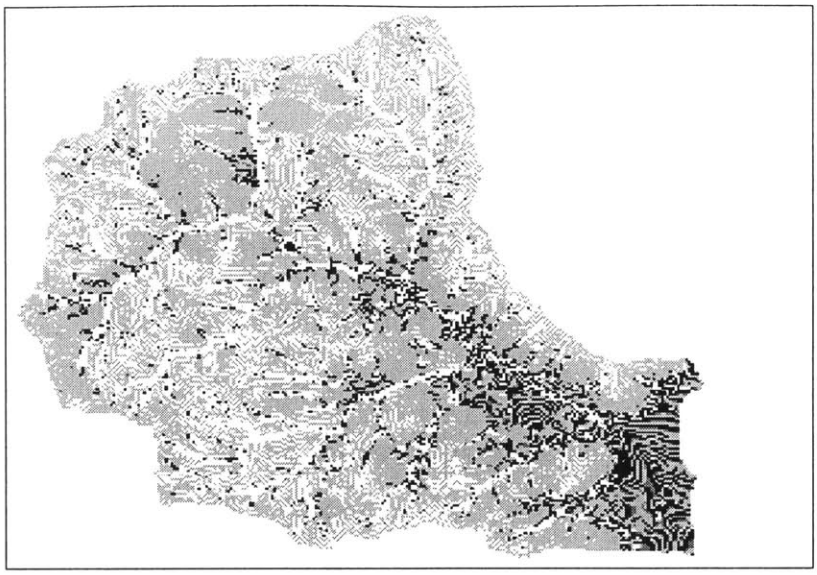

Figure 4-52: Map of recharge, midline, and discharge zones, Yreka, CA. Light grey is recharge, grey is midline, and black is discharge. See Figure 3-20 for horizontal scale.

Correspondingly, with a high lateral flux rate through the saturated layer, a large volume of moisture is available to discharge into the unsaturated zone. The result is extensive recharge and discharge regions and a small midline region. This is why Salvucci observed an increase in the midline when switching from a silt to a clay soil and to a lower hillslope angle; both factors reduced the lateral redistribution of moisture by gravity-driven Darcy flow. Salvucci and Entekhabi (1995) present an index of climatic and geologic control representing the maximum possible lateral flow at the midline, Q_{max}:

$$Q_{max} = K_s \left(Z_T - Z^*\right) \theta \tag{4.2}$$

where K_s is saturated hydraulic conductivity, $(Z_T - Z^*)$ is the depth of the saturated layer in the midline region, and θ is the hillslope angle relative to horizontal. We modify this index to provide a dimensionless representation of the maximum possible flow rate relative to incident rainfall. Because there is no single slope angle for a complex landscape, θ is replaced with the relief ratio H/L_b relating basin relief to basin length. This gives the following dimensionless index to represent the saturated zone's capacity for lateral moisture redistribution:

$$\alpha_s = \frac{K_s \left(Z_T - Z^*\right) H/L_b}{P\sqrt{A_\Omega}} \tag{4.3}$$

where P is the annual precipitation depth and A_Ω is the basin area (Ω is the order of the outlet stream). The numerator estimates the Darcy flux over the average basin relief $(\frac{H}{L_b})$ with $K_s \left(Z_T - Z^*\right)$ equal to the transmissivity of the midline saturated layer. The precipitation term in the denominator represents the maximum possible infiltration rate that could be recharging the saturated zone. For a simple hillslope with a single midline zone bounded at either end by long-term recharge and discharge zones, the denominator should technically only incorporate that precipitation which falls in the recharge zone above the

Basin	α_s	α_{us}
Bear	5.1e-2	1.2
Big Creek	2.0e-2	0.3
Brushy	2.5e-5	1.1
Midland	1.3e-4	1.0
Moshannon	8.7e-5	1.8
Ogden	4.1e-4	0.4
Sacramento	9.4e-5	0.2
Schoharie	8.4e-3	1.4
Tombstone	3.3e-2	0.2
Yreka	2.1e-2	0.6

Table 4.2: Values of the dimensionless saturated and unsaturated zone parameters, for all basins.

midline. Any precipitation falling in the discharge zone, for example, will not be transmitted through the midline. However, the fraction of the basin above the midline is unknown. We use the precipitation for the entire basin scale as a reasonable approximation of the incident moisture. For low values of α_s, the soil approaches a one-dimensional system; it is essentially unable to laterally transport moisture inputs. The index should therefore be inversely related to the extent of the midline.

The formation of the midline is also influenced by unsaturated zone processes. The spatial extent will be high when there is little flux into the saturated zone from the overlying unsaturated zone. This occurs when the evaporative demand is so high that all moisture reaching the surface as storm event precipitation evaporates during interstorm periods. One way of quantifying the ratio of moisture input to evaporative demand is by the ratio

$$\alpha_{us} = \frac{i_r t_r}{e_p t_b} \tag{4.4}$$

where i_r and t_r are storm intensity and duration, respectively, e_p is the potential evaporation rate, and t_b is the interstorm duration. The numerator, $i_r tr$, represents the mean storm depth; the denominator characterizes the mean interstorm evaporative flux when soil moisture is nonlimiting. A low value of α_{us} indicates that little or no moisture reaches the saturated zone from the average storm. When the evaporative load is high relative to the available incident moisture, the unsaturated zone is essentially one-dimensional, with flow occurring only in the vertical direction. We therefore expect this index to also be inversely associated with a high percentage midline. The calculated values of α_s and α_{us} are given in Table 4.2.

Figure 4-53 plots the areal extent of the midline region versus the two dimensionless indices, α_s and α_{us}. The figure reveals that the extent of midline is indeed related to the combined influence of saturated and unsaturated zone processes. The basins with the largest midline area—Sacramento, Calder, and Ogden—are found at low values of both α_s and α_{us}. At the other extreme, Tombstone, Bear, and Moshannon have negligible midline areas and are characterized by high values of one or both of the indices. Although the mean annual precipitation is present in both of the indices, its presence in the numerator of α_{us} and in the denominator of α_s refutes any argument that the relationship seen between the two dimensionless indices and the extent of midline is unduly influenced by the common

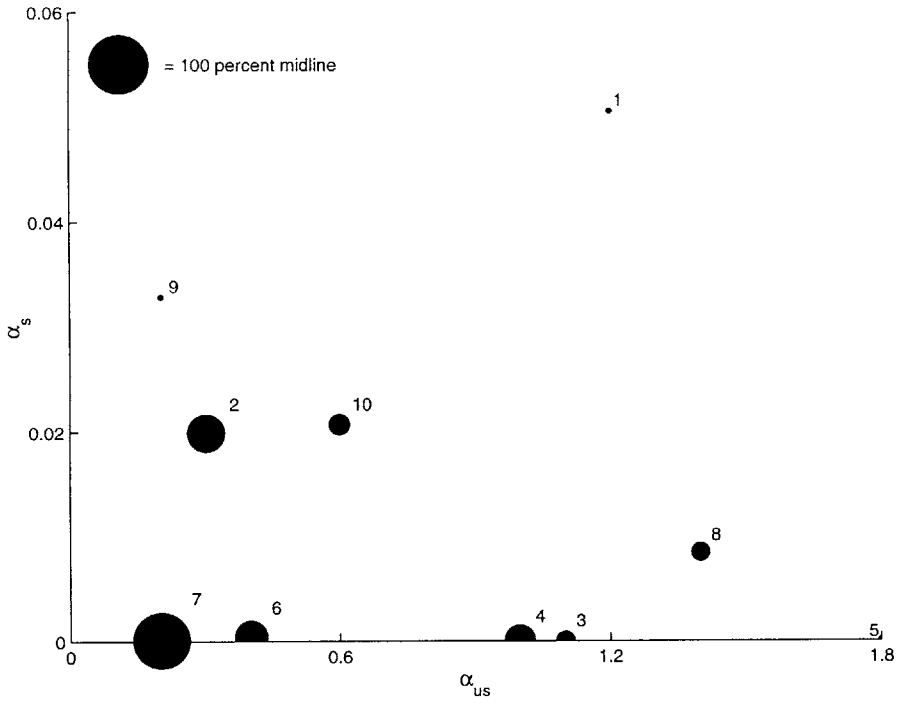

Figure 4-53: Areal extent of midline as a function of the saturated (α_s) and unsaturated (α_{us}) indices. The circle diameter represents the percentage midline; values less than 10 percent have been set to 10 percent to be visible. Numbered circles represent (1) Bear, (2) Big Creek, (3) Brushy, (4) Midland, (5) Moshannon, (6) Ogden, (7) Sacramento, (8) Schoharie, (9) Tombstone, and (10) Yreka.

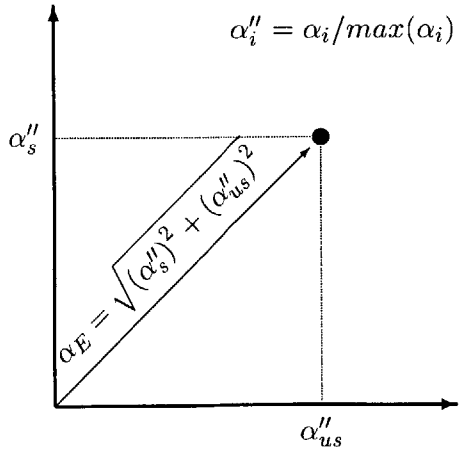

Figure 4-54: Schematic for calculating distance to the origin in Figure 4-53.

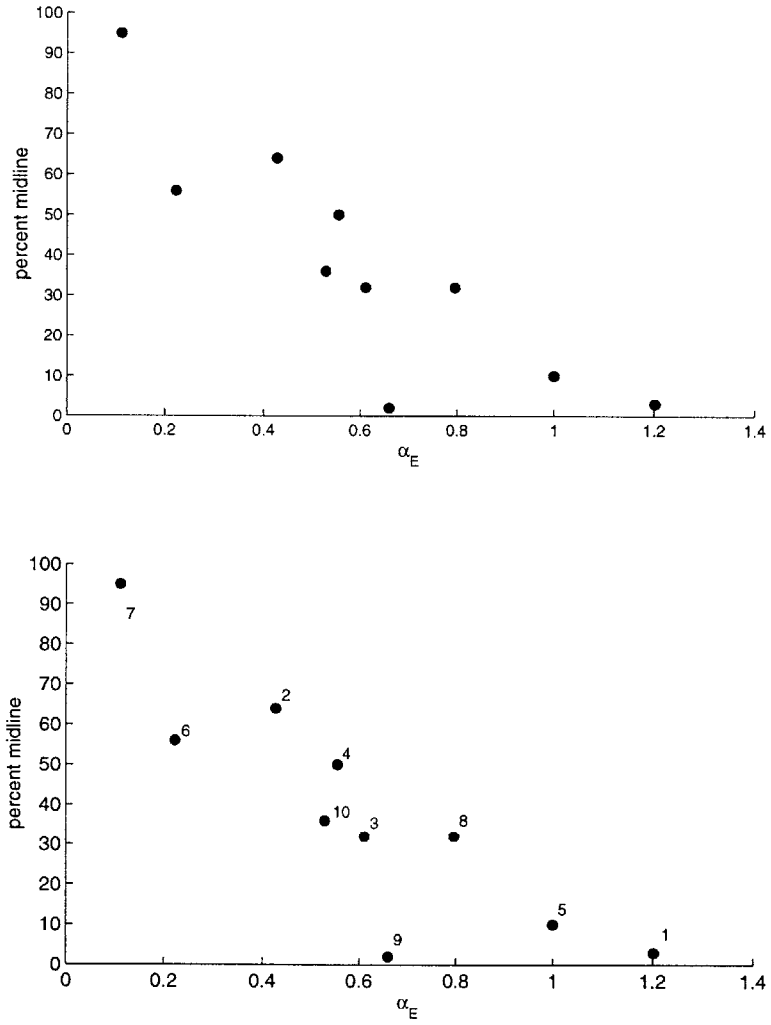

Figure 4-55: Areal extent of midline as a function of the combined efficiency parameter α_E. The indices are divided by their maximum values to provide the same dynamic range. The lower plot is provided for basin identification. Numbered points represent (1) Bear, (2) Big Creek, (3) Brushy, (4) Midland, (5) Moshannon, (6) Ogden, (7) Sacramento, (8) Schoharie, (9) Tombstone, and (10) Yreka.

precipitation parameter.

The pattern observed in Figure 4-53 is quantified by calculating a combined efficiency index α_E defined as the distance to the origin in Figure 4-54. Each index has been normalized by its maximum value so the two variables span the same dynamic range. The distance is then calculated as the square root of the sum of squares of the normalized indices. The results are plotted in Figure 4-55. There is a strong inverse relationship between the combined index and percentage midline. The highest percent midline is found for a low value of α_E; the low index value represents inefficient moisture transfer in both the saturated and unsaturated zones. The percentage midline decreases linearly with increasing values of α_E. The biggest outlier is Tombstone, with a combined index value of less than 0.7 and just 2 percent midline area. The small midline area in Tombstone may be caused by the subbasin heterogeneity in surface slope which is not reflected in the use of a single relief ratio to capture gravity-driven flow in α_s. Overall, however, the relationship seen in Figures 4-53 and 4-55 shows that the extent of midline is related to both the α_s and α_{us} indices. This supports the idea that the formation of the midline region is inversely determined by the efficiency of moisture transmission or degree of one-dimensionality in the saturated and unsaturated zones.

The combined index is dimensionless and serves as an indicator of the importance of distributed versus lumped approaches to estimating the hydrologic response of a basin. When α_E is small, the extent of recharge and discharge zones are small. Most of the basin is character by $Z_w \approx Z^*$ and a lumped hydrologic model will capture most of the hydrologic processes. But when α_E is high, due either to climate or topography, the extent of recharge and discharge zones is significant and the interaction of the surface water and groundwater systems may cause significant spatial variability.

4.4 Summary

The studies in this chapter, examining the spatial distribution of water table depth, the effect of hillslope curvature on water table position, and the physical influences on the extent of the midline region, have identified some general trends found in all ten of the study basins. The depth of the water table exhibits a spatial organization that reflects the surface topography. The long-term water table is shallow in and near the channel network (riparian zone) and deep in upslope areas. A fraction of the basin exhibits a linear relationship between hydrology and location, as quantified by contributing area per unit contour length, but the relationship does not hold in extreme upslope and downslope regions. The relationship is partially influenced by the hillslope shape; convergent and divergent pixels behave significantly differently across most of the range of locations. The intermediate midline area, where the net recharge is zero, is delineated using the distribution of equilibrium recharge rates. The formation of the midline region is shown to depend on the characteristics of the saturated and unsaturated zones.

The above studies assumed subbasin homogeneity of several important physical characteristics, including vegetation cover (assumed uniformly nonexistent), soil depth, and soil type. In nature, however, these properties often vary in space. In the next chapter we consider the change in hydrologic response when the assumed physical characteristics are perturbed.

Chapter 5

Sensitivity to other sources of spatial variability

The above discussion has focused on spatial patterns in hydrologic processes that arise from uniform atmospheric forcing of a field with mostly uniform characteristics. Homogeneity of soil and ground cover was assumed in order to focus on the topographic forcing of surface water–groundwater interaction and the resulting organization of water table position and related fluxes. In nature, both the climatic forcing and the physical characteristics influencing hydrology vary in space. Heterogeneities arise at a range of scales, from microscopic irregularities in the soil matrix to gopher holes and drainage ditches to large-scale variability in land use, precipitation, or soil type. In this chapter we examine the sensitivity of the equilibrium hydrologic conditions to perturbations in watershed characteristics. Three characteristics are investigated: vegetation, soil texture, and soil depth. In cases where there are few field studies identifying a relationship between the characteristic and basin topography (*i.e.*, soil texture and vegetation), we discuss possible physical processes which may influence the spatial heterogeneity of the characteristic. The scarcity of observations of the heterogeneity of some physical characteristics influencing the hydrologic cycle highlights an important area of future research. The results are presented for four of the study basins.

5.1 Effect of regional circulation on hydrologic sensitivity

The occurrence or absence of regional circulation of groundwater may have implications for the sensitivity of the hydrologic balance to perturbations in the soil or climate. The GSEM results presented here model the groundwater domain as a single layer. The use of a one-layer subsurface represents adherence to the Dupuit-Forchheimer assumptions about unconfined groundwater flow. The assumptions state that gravity flow toward a shallow sink has two important properties: all flow is horizontal (*i.e.*, all flow lines are horizontal), and the velocity is proportional to slope and independent of depth (*i.e.*, the hydraulic gradient equals the water table slope throughout the depth of flow). A sample cross-section under a regime of Dupuit flow is illustrated in Figure 5-1. The Dupuit assumptions are a reasonable approximation of actual conditions when the slope of the water table is small and the thickness of the saturated layer is shallow (Freeze and Cherry 1979).

The Dupuit-Forchheimer assumptions represent a simplification of the groundwater flow field. Since flow is assumed to be horizontal only, discharge only occurs by capillary rise. In fact, the pathways of groundwater movement have both horizontal and vertical components,

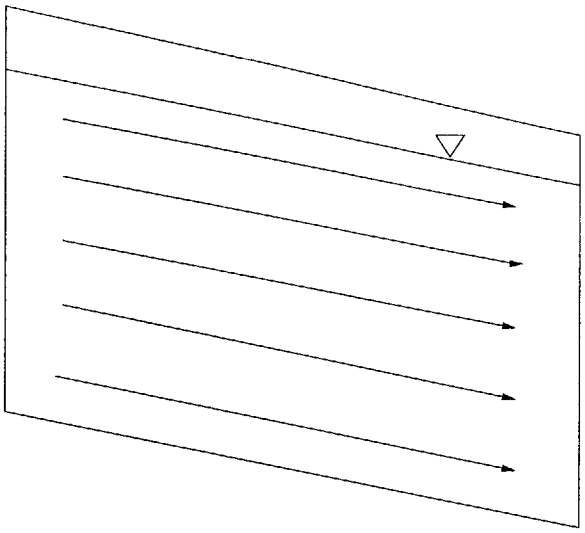

Figure 5-1: Schematic of groundwater flowlines in Dupuit-flow system.

as illustrated in Figure 5-2. Discharge occurs due to both capillary rise and the regional groundwater flow which brings moisture to the surface in downslope regions.

This difference in the patterns of groundwater flow affects the system's sensitivity to changes in the physical environment. In a non-Dupuit environment, the circulation patterns can adjust to minimize the effect of physical perturbations on the hydrology. Levine and Salvucci (1999a) found relatively low hydrologic sensitivity to perturbations in soil type and bedrock conductivity in a study of coupled surface water–groundwater flow in a Canadian prairie. They concluded that local and regional circulation of subsurface moisture is responsible for the relative insensitivity in the areally averaged water balance. As illustrated in Figure 5-2, moisture entering the subsurface in upslope regions flows downward into the soil, reemerging some distance downslope where there is a topographic low or local convergence. When recharge occurs at a higher rate in upslope areas, the downslope discharge area tends to increase because of the extra moisture entering the subsurface from the large-scale circulation. Consequently, lowered upslope evaporation is at least partially offset by higher downslope evaporation.

Under assumptions of Dupuit flow, however, the distribution of recharge and discharge zones is expected to be more sensitive to physical characteristics. Since flow is restricted to the horizontal direction, perturbations in the soil or moisture distribution cannot be accomodated through changes in regional groundwater circulation. Any increase in local discharge, for example, must be met through a rise in the water table position to increase the capillary rise, whereas an environment in which the Dupuit assumptions are not applied can meet the increase in discharge through a combination of capillary rise and regional groundwater flow. The relative inflexibility in the Dupuit groundwater system means that changes in the soil are translated more directly into changes in the water table distribution and on to the local recharge and discharge patterns.

Similarly, for a single soil column, changes in the physical or climatic parameters translate to a change in the relative distribution of precipitation into evaporation, runoff, and recharge. In a two-dimensional environment with non-Dupuit flow, regional circulation patterns may compensate between changes in different locations within the basin. This effect

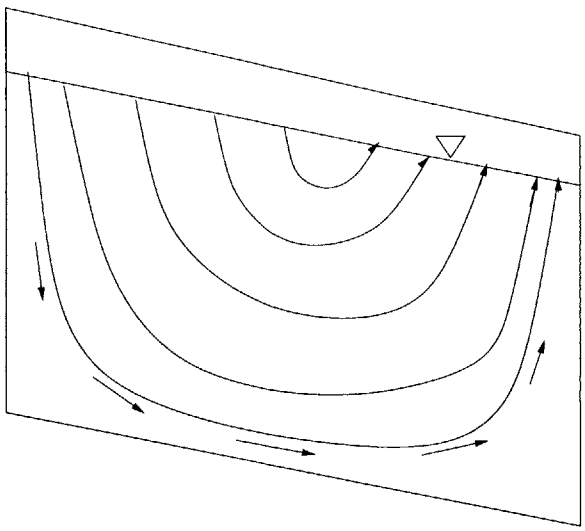

Figure 5-2: Schematic of groundwater flowlines in non-Dupuit system.

reduces the sensitivity of the hydrologic cycle to basin parameters, resulting in the low sensitivity of basin-scale fluxes observed by Levine and Salvucci (1999a). With Dupuit flow, however, moisture convergence and divergence are controlled by the water table position. If perturbations in the watershed characteristics significantly change the distribution of the water table, the overall water balance will be altered accordingly.

In order to test the sensitivity of equilibrium hydrology to watershed parameters in a two-dimensional system with Dupuit flow, the results in this chapter are presented for two cases: the model is applied to four study basins and to four soil columns with a semi-infinite water table and corresponding climate characteristics. A water table depth of 5 m is assumed to represent a semi-infinite boundary, following Salvucci and Entekhabi (1994a). A crucial difference between the perturbation of physical characteristics in the two cases is the fixed level of the water table in the soil column analysis. For the one-dimensional case, the water table is set at a fixed depth beneath the surface, chosen to represent semi-infinite conditions. The flux values calculated for this case are for this invariant water table depth only. In the two-dimensional case, however, GSEM iterates for the water table depth until equilibrium conditions are reached. This allows for feedbacks to arise between changes in the hydrologic fluxes and the water table position. Some of the circulation-induced dampening of the sensitivity seen in Levine and Salvucci's (1999a) work may arise even under the Dupuit-Forchheimer assumptions.

5.2 Vegetation

The model application in the preceding chapter assumed bare soil in the calculation of evaporation rates. However, most undisturbed areas in the continental United States have at least partial vegetation cover. To investigate the impact of our bare soil assumption, we model the hydrology for the extreme conditions of bare soil and full vegetation cover. The effect of different vegetation characteristics on equilibrium evaporation and water table position is considered. We then discuss possible exceptions to a fully vegetated watershed and the implications for the spatial structure of hydrologic conditions.

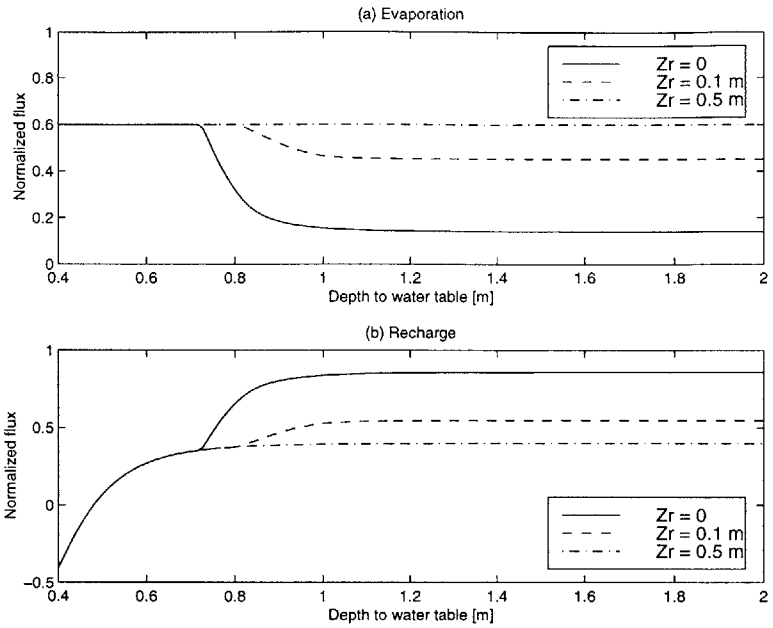

Figure 5-3: Effect of rooting depth on equilibrium evaporation and recharge across a range of water table depths in a loam soil column.

As described in Chapter 2, the primary effect of vegetation is to increase evaporation rates by using roots to access water stored deep in the soil column. Vegetation may further influence evaporation if the leaf area index (LAI) is greater than one (*i.e.*, the effective transpiring surface area exceeds the ground area, as is the case when there are multiple transpiring canopy layers); we neglect this effect in the following study. The land surface is assumed to be fully covered by a single layer of uniform vegetation. It is also assumed that interception of moisture by the plant canopy is negligible for the long-term water balance.

5.2.1 Results

Sensitivity of a one-dimensional system

We begin by examining the effect of vegetation on the equilibrium hydrology in a one-dimensional case. Figure 5-3 illustrates the effect of rooting depth on the long-term evaporation and recharge rates for a range of water table depths in a single soil column with a loam soil. The presence of vegetation, indicated by a nonzero rooting depth, increases the evaporation rate at all depths below Ψ_s, the maximum capillary rise. With an LAI of one, the rooting depth makes no difference on the fluxes at very shallow water tables because evaporation occurs at the atmospheric potential rate from a saturated soil regardless of whether or not there is vegetation. Saturation-excess runoff is insensitive to rooting depth because the roots are assumed to have zero volume; the same amount of moisture will therefore cause saturation in both the bare-soil and vegetated scenarios. Net recharge varies with rooting depth in response to the changes in evaporation because recharge is calculated as the residual of the surface water balance.

Table 5.1 contains the results for an application of the model to four soil columns

Basin	Hydrologic variable	Vegetation rooting depth $Z_r = 0$	$Z_r = 10$cm	Units
BEAR VALLEY	E_{vs}	0.29	1.83	mm/d
	Q_e	1.93	0.39	mm/d
MIDLAND	E_{vs}	0.94	3.02	mm/d
	Q_e	2.08	0.00	mm/d
TOMBSTONE	E_{vs}	0.13	1.02	mm/d
	Q_e	0.89	0.00	mm/d
YREKA	E_{vs}	0.15	1.28	mm/d
	Q_e	1.13	0.00	mm/d

Table 5.1: Sensitivity of equilibrium hydrology to vegetation in a semi-infinite soil column for four climates. E_{vs} is evaporation from a vegetated surface; Q_e is net recharge from the unsaturated to saturated zone. Infiltration-excess and saturation-excess runoff are negligible for all cases.

with a semi-infinite unsaturated zone (Z_w=5 m). For each column, the climate and soil characteristics of the corresponding basin are used. The direct impact of vegetation is a marked increase in evaporation. In order to meet the high evaporative demand, recharge declines significantly. In three of the four basins, the entire precipitation flux is evaporated from the soil. In these basins, evaporation is still below the potential rate; increases in precipitation would increase the evaporation rate rather than recharging the saturated zone. The extent of vegetation's impact depends on the combination of atmospheric forcing and soil characteristics. This is the case when the mean annual potential evaporation exceeds the mean annual precipitation. Bear Valley, in contrast, has less of a difference between evaporative demand and moisture supply; the introduction of vegetation has a smaller impact on its water balance.

Sensitivity of basin-average hydrology

We next introduce different rooting depths into an application of GSEM to the four selected basins. Table 5.2 summarizes the basin-average equilibrium fluxes, water table depth, and extent of midline. As we saw in the tests on the semi-infinite soil columns, the dominant effect of vegetation on the basin-average hydrologic fluxes is the increase in evaporation with increasing rooting depth. The increase in evaporation between a bare soil and a vegetated soil with $Z_r = 25$ cm ranges from just 6% in Midland, where evaporation was already occurring near its potential in the bare-soil case, to over 100% in Bear Valley. The increased evaporation draws down the water table, resulting in slightly lower saturation-excess runoff. The increased evaporation is primarily offset by decreases in the net recharge flux. Figure 5-4 illustrates the strong influence of rooting depth on evaporation.

Sensitivity of distributed hydrology

Figures 5-5 and 5-6 illustrate how the differences in hydrology are distributed in space. Figure 5-5 maps the spatial distribution of the sensitivity of evaporation to rooting depth

Basin	Hydrologic variable	Vegetation rooting depth $Z_r = 0$	$Z_r = 10$ cm	$Z_r = 25$ cm	Units
BEAR VALLEY	E_{vs}	0.66 ± 0.63	1.16 ± 0.32	1.52 ± 0.16	mm/d
	R_{se}	0.37 ± 0.78	0.30 ± 0.72	0.26 ± 0.69	mm/d
	Q_e	1.19 ± 1.36	0.75 ± 1.00	0.43 ± 0.81	mm/d
	Z_w	1.41 ± 0.61	1.55 ± 0.59	1.62 ± 0.57	m
	%M	3	2	2	
MIDLAND	E_{vs}	2.80 ± 0.34	2.87 ± 0.19	2.97 ± 0.08	mm/d
	R_{se}	0.22 ± 0.31	0.14 ± 0.25	0.06 ± 0.15	mm/d
	Q_e	0.00 ± 0.55	0.00 ± 0.38	0.00 ± 0.20	mm/d
	Z_w	1.04 ± 0.17	1.23 ± 0.29	1.54 ± 0.37	m
	%M	50	64	94	
TOMBSTONE	E_{vs}	0.92 ± 1.75	1.02 ± 1.52	1.21 ± 1.64	mm/d
	R_{se}	0.10 ± 0.25	0.07 ± 0.22	0.05 ± 0.21	mm/d
	Q_e	0.00 ± 1.97	0.00 ± 1.77	0.00 ± 1.55	mm/d
	Z_w	1.39 ± 0.60	1.49 ± 0.57	1.60 ± 0.51	m
	%M	2	4	5	
YREKA	E_{vs}	0.49 ± 0.69	0.78 ± 0.48	1.04 ± 0.35	mm/d
	R_{se}	0.18 ± 0.41	0.14 ± 0.37	0.12 ± 0.34	mm/d
	Q_e	0.50 ± 0.69	0.33 ± 0.82	0.10 ± 0.65	mm/d
	Z_w	1.52 ± 0.62	1.59 ± 0.59	1.66 ± 0.55	m
	%M	36	3	4	

Table 5.2: Mean and standard deviation of modeled hydrologic variables for different vegetation rooting depths, for four basins. E_{vs} is evaporation from a vegetated surface; R_{se} is saturation-excess runoff; Q_e is net recharge from the unsaturated to the saturated zone; Z_w is the depth of the water table beneath the surface; and %M is the areal percentage of the basin classified as midline. Infiltration-excess runoff is negligible for all cases.

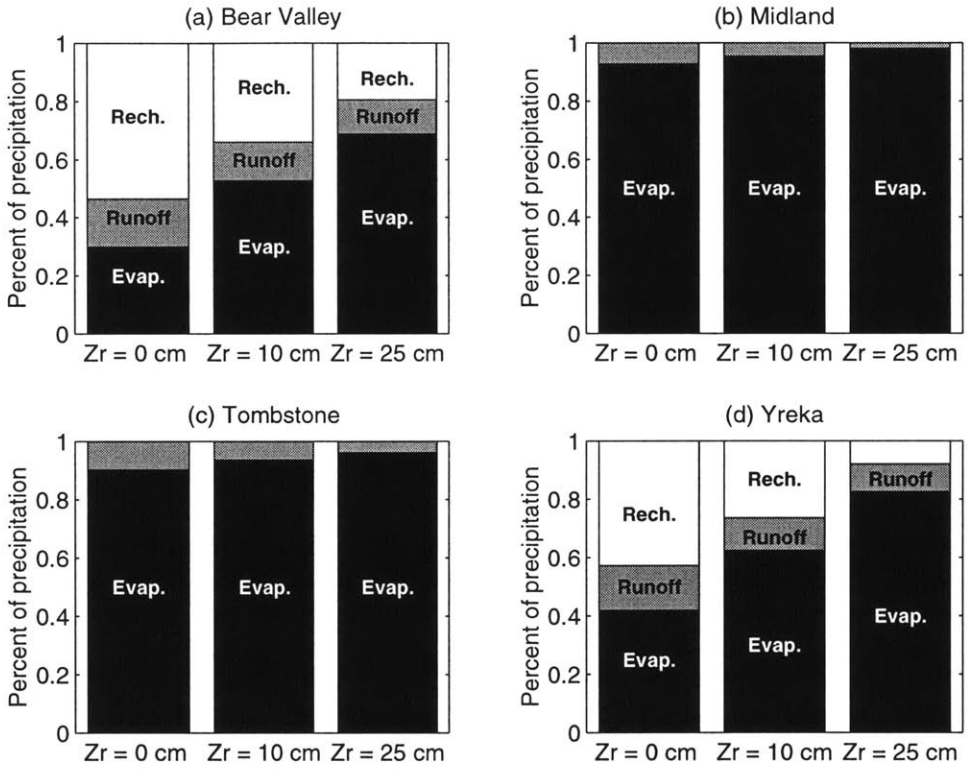

Figure 5-4: Modeled partitioning of precipitation into surface fluxes as a function of rooting depth, for four basins.

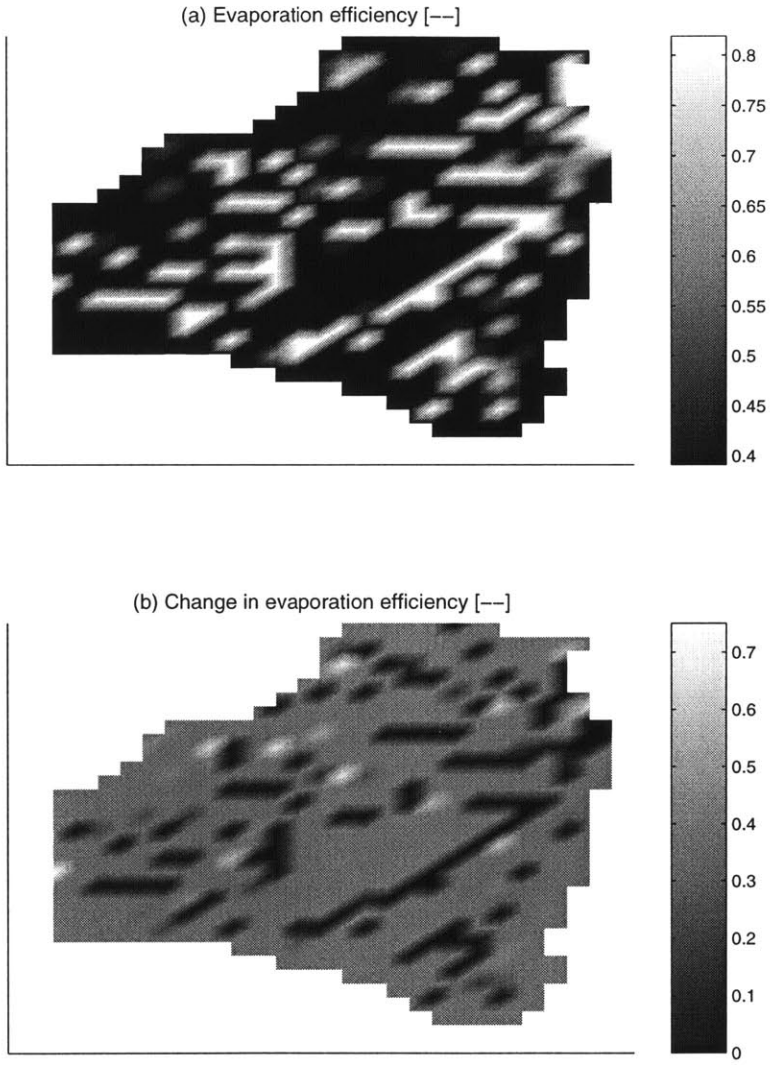

Figure 5-5: Effect of vegetation on the spatial distribution of equilibrium evaporation efficiency, Yreka, CA. (a) Evaporation efficiency (E/E_p) for vegetation with 25-cm rooting depth. (b) Difference between bare-soil and vegetated evaporation efficiency.

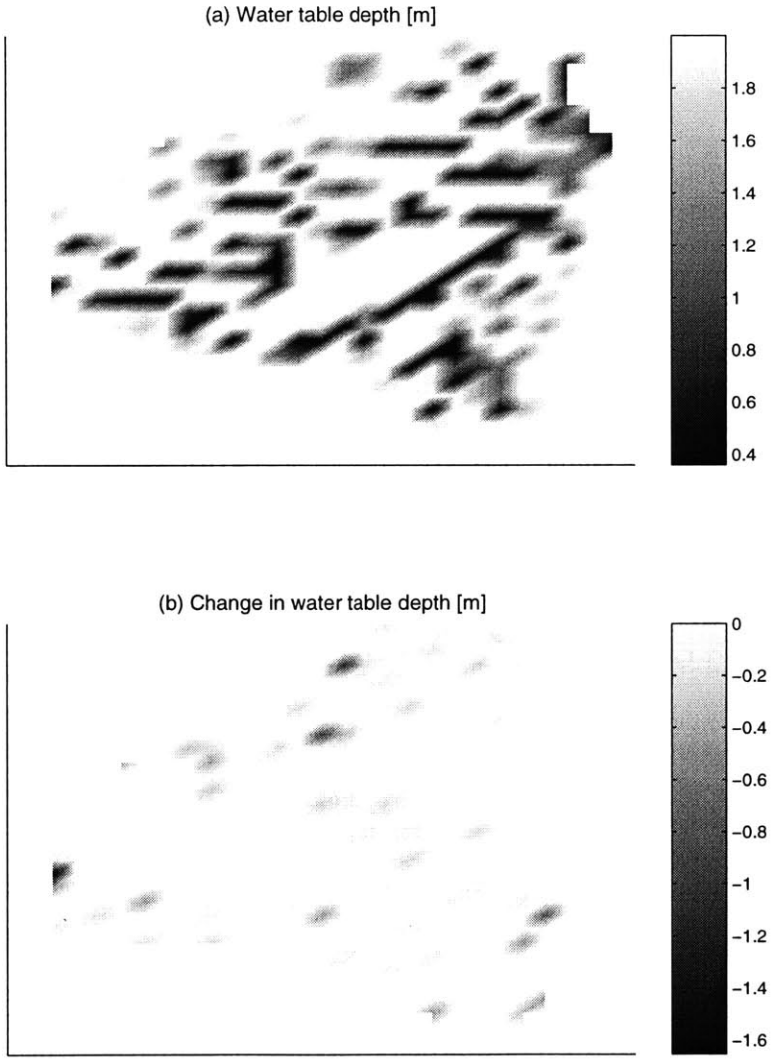

Figure 5-6: Effect of vegetation on the spatial distribution of water table depths, Yreka, CA. (a) Water table depth given vegetation with 25-cm rooting depth. (b) Difference between bare-soil and vegetated water table depths.

in a subbasin of the Yreka basin. The evaporation rate in the channel network is unaffected by vegetation, since evaporation from saturated soil occurs at the atmospheric potential rate regardless of the surface cover (given the assumptions of no interception and a single canopy layer). Vegetation increases the evaporation rate in upslope areas where the water table is relatively deep; these are the conditions in which the roots reach otherwise inaccessible soil moisture.

Unlike the effect on evaporation, the sensitivity of the water table position to vegetation does not show a strong spatial structure. Figure 5-6 presents a slight deepening but generally uniform change in the water table depth. The sensitivity of the water table position is weak because it is a secondary effect that is dampened by lateral moisture redistribution. The direct effect of vegetation is to increase the evaporation rate from the land surface. Increased evaporation reduces the amount of moisture entering the soil column, lowering the water table. Although the sensitivity of evaporation has a clear spatial pattern, its influence on the water table is weakened by reduced down-gradient flow. The sensitivity of these two hydrologic variables highlights how components of the hydrologic cycle may respond differently, both in magnitude and distribution, to a change in a uniform forcing. In summary, the presence of vegetation increases the evaporation rate and draws down the water table relative to a bare-soil scenario. The effect on evaporation shows a spatial organization that is related to the distribution of water table depths; the cumulative effect on the water table position has no clear spatial pattern.

5.2.2 Remaining issues

Introducing a uniform vegetation cover alters the distribution of the basin hydrology; variability in the vegetation itself could either enhance or reduce the spatial heterogeneity of hydrologic fluxes. Below we discuss two further potential sources of variability: partial vegetation cover and large-scale heterogeneity in vegetation characteristics.

Partial vegetation cover The ground surface is often covered by some combination of vegetation and bare soil. The juxtaposition of bare soil and vegetation may result in feedbacks, such as enhanced drying of bare areas if high transpiration rates induce a horizontal soil moisture flux to vegetated regions. Studies have looked at large-scale feedbacks of vegetation heterogeneities in climate models (*e.g.*, Klink and Wolmott 1994; Bonan 1996). It would also be useful to consider smaller-scale feedbacks and whether vegetation patterns hold any significant implications for the water balance within grid cells of catchment models. The proportions of vegetation and bare soil could also vary between cells. An alternative approach to calculating evaporation may be needed if subgrid variability in plant cover is substantial.

Large-scale spatial variability In addition to small-scale variability, the distribution of vegetation often has some larger-scale spatial structure that arises due to structured heterogeneity in lithology and moisture availability. In some environments, for example, vegetation is larger and denser in convergent valley bottoms. This may be caused by one or more of the following conditions: reduced exposure to wind and sun stress; moister soil due to lateral convergence of groundwater and runoff; or thicker and richer soil due to deposition of regolith eroded in upland source areas. An example of these effects is the clustering of trees along river channels in landscapes that are otherwise sparsely vegetated or dominated by grasses and shrubs.

Spatially organized vegetation could cause systematic error in our model through the assumption of homogeneous conditions (whether bare soil or full vegetation). In an environment where there is more vegetation in valleys, a homogeneous surface-cover model would tend to overpredict the extent of saturated areas and saturation-excess runoff. Convergent areas are still most likely to be saturated; however, if they have more vegetation, higher evaporation rates would reduce the likelihood of saturation. The overprediction could be enhanced by uphill flora, since the presence of upland vegetation would reduce the effective recharge, shrinking the moisture contributed through the groundwater system to low-lying or convergent areas.

In summary, vegetation acts to increase evaporation, reduce net recharge, and deepen the equilibrium water table. Its effect on saturation-excess runoff is negligible if root volume is assumed to be negligible; slight decreases are observed due to the secondary effect from a deeper water table. The sensitivity of evaporation has a strong spatial signal that is related to the local topography via the topography's influence on the water table position. The effect of vegetation on the water table distribution is dampened by the lateral redistribution of soil water. Systematic spatial variability in vegetation cover, either through a mix of vegetated and bare soil or differential vegetation types and/or density, may further influence the distribution of hydrologic fluxes. The magnitude and direction of the impact of land cover on model calculations depend on the pattern of soil moisture and vegetation heterogeneity.

5.3 Soil depth

The thickness of the soil layer often varies along a hillslope or channel valley. However, the extent and pattern of this variability is poorly known. Numerous processes affect soil production, transport, and resultant depth. These include (but are not limited to) creep, animal activity, freeze-thaw, wind transport, hydrologic weathering and erosion, and human intervention (Whipple, personal communication). Soil depth is hard to measure with low-technology field methods and may be difficult to scale up from point measurements to a spatial trend. The STATSGO database, the source of soil characteristics used in this study, often estimates the depth to bedrock as simply "greater than 60 inches," or deeper than the length of the rod used to identify the depth to refusal. Estimating distributed soil depth from theory is also problematic because there is no consensus on the parameterization of the many physical processes governing soil depth. A model put forth by Dietrich *et al.* (1995) solves a mass balance between soil production from underlying bedrock and diffusive soil transport. We apply this model to estimate the soil depth distribution in four basins and examine the effect of variable soil depth on the equilibrium hydrology.

5.3.1 Theory

The model is based on conservation of mass for soil thickness, Z_T, as expressed by the balance between the time rate of change in soil depth (first term), soil production from bedrock (second term), and downslope transport of sediment (third term):

$$\rho_s \frac{\partial Z_T}{\partial t} = -\rho_r \frac{\partial e}{\partial t} - \nabla \cdot \rho_s \tilde{q}_s \tag{5.1}$$

in which ρ_s and ρ_r are the bulk densities of soil and bedrock, respectively, e is the elevation of the soil-rock interface, and $\tilde{q}_s$ is the soil transport vector. Dietrich *et al.* (1995) assume

that slope-dependent diffusive transport adequately represents the assemblage of hillslope processes moving colluvium downhill:

$$\tilde{q}_s = -K\nabla H \tag{5.2}$$

where K is a homogeneous, isotropic diffusion coefficient and H is the elevation of the ground surface ($Z_T + e$). Diffusive soil transport has been employed in landscape evolution models and supported by field studies (see citations in Dietrich *et al.* 1995). It is considered the most appropriate transport representation in "unglaciated, hilly, mostly soil-mantled landscapes in humid to semi-arid climates where Horton overland flow is rare or absent and the underlying bedrock is mechanically strong" (Dietrich *et al.* 1995, p. 144). It represents dry, long-term hillslope processes; it does not characterize runoff-driven transport or landsliding.

Whereas there is fairly widespread acceptance of a diffusive soil-transport law, no field studies to date have definitively identified a soil-production law. The Dietrich *et al.* model assumes that soil production is highest when bedrock is exposed or is overlain by a thin colluvial layer, and production decreases to zero for deep colluvium. The model includes two general forms of a production law; we use the simple exponential decline:

$$-\frac{\partial e}{\partial t} = P_o e^{-\xi Z_T} \tag{5.3}$$

where P_o and ξ are empirical constants representing the maximum soil production rate and rate of decay with depth, respectively. Using Equations 5.2 and 5.3 for soil transport and production, the mass balance equation for soil depth becomes

$$K\nabla^2 H = \frac{\partial Z_T}{\partial t} - \frac{\rho_r}{\rho_s} P_o e^{-\xi Z_T} \tag{5.4}$$

We are interested in the steady-state soil depth distribution, where $\partial Z_T/\partial t = 0$. On divergent slopes ($\nabla^2 H < 0$), the equilibrium soil depth is determined by solving Equation 5.4 for Z_T:

$$Z_T = -\frac{1}{\xi}\left[\ln\left(\frac{K}{P_o}\cdot\frac{\rho_s}{\rho_r}\cdot(-\nabla^2 H)\right)\right] \qquad \text{for} \nabla^2 H < 0 \tag{5.5}$$

Mass wasting is neglected. As a result, our steady-state model is undefined for convergent slopes ($\nabla^2 H > 0$) where the removal of accumulated sediment by mass wasting is a significant part of the equilibrium system. In this sensitivity analysis, we are not interested in slope failure; we desire a reasonable profile of soil depths underlying a known surface topography at a single point in time. We therefore make the first-order assumption that all convergent pixels have a soil depth equal to the maximum soil depth found in divergent regions. The topography is then diffused in order to avoid abrupt jumps in the soil depth array and to achieve a specified average soil depth. The partial differential equation governing the smoothing of the soil thickness on convergent pixels is a balance of scour (first term) and diffusion (second term):

$$\frac{\partial Z_T}{\partial t} = -\alpha Z_T + K_T \nabla^2 Z_T \qquad \text{for} \nabla^2 H < 0 \tag{5.6}$$

where α is a decay parameter and K_T is the topography-based diffusivity. This equation allows the simultaneous smoothing of the soil-depth array and the achievement of a desired

	Value
ξ	0.035 cm^{-1}
K	12 cm^2/yr
P_o	0.030 cm/yr
ρ_r/ρ_s	2.0

Table 5.3: Parameter values used in Dietrich *et al.* (1995) soil production model. ξ is the depth-dependent decay rate of soil production; K is the soil diffusion coefficient; P_o is the maximum soil production rate, and ρ_r/ρ_s is the ratio of bedrock to soil densities.

average soil depth for compatibility with GSEM.

In addition to the model's inability to directly characterize the distribution of soil depths in convergent areas, the model is also limited by its assumption of a constant diffusivity in space. Diffusivity may vary with soil depth because of the dependence of many of the transport processes on the thickness of the colluvium. Despite these limitations, the model appears to be the best currently available, based as it is on a combination of physical processes and field observations and validation.

5.3.2 Results

Application of the model requires estimation of the diffusion parameter K, the ratio of soil to bedrock bulk density, and the empirical constants P_o and ξ. Dietrich *et al.* (1995) cite measured values of 49±37 cm^2/yr for the diffusion constant in two basins in the coastal mountains along the west coast of the United States. The ratio of bedrock to soil density is 1.7. An exponential function is fitted to measured soil conversion rates in the Tennessee Valley catchment, giving values of $P_o = 0.019$ cm/yr and $\xi = 0.05$. We calibrate the four model parameters by using values within the range from Tennessee Valley with the constraint that the mean soil depth approaches the uniform soil depth (2 m) previously assumed for the basins.

Using the range of model constants presented by Dietrich *et al.* (1995) and the assumption about soil depth in convergent regions, the mean soil depth in each basin is less than the uniform depth of 2 m. We select values within the range for the Tennessee Valley parameters while producing a soil depth as close to 2 m as possible; values are given in Table 5.3. The soil depth values on convergent slopes are then diffused until the average soil depth equals 2 m according to Equation 5.6. The topography-based diffusivity value needed to converge on the desired mean depth ranges from 0.001 in Bear Valley to 0.6 in Yreka. The spatial distributions of smoothed soil depths are shown in Figure 5-7 through 5-10; the surface topography was previously mapped in Figures 3-11, 3-14, 3-19, and 3-20. The extreme and median values of the soil depth distribution in each basin are summarized in Table 5.4.

Sensitivity of basin-average hydrology

We are interested in the effect of a heterogeneous soil depth distribution on the spatial pattern of water table depth and surface fluxes. GSEM is run on the four basins, assuming the surface topography is underlain by the soil depth distributions shown in Figures 5-7 through 5-10. Basin-average values for the surface fluxes are summarized in Table 5.5 and

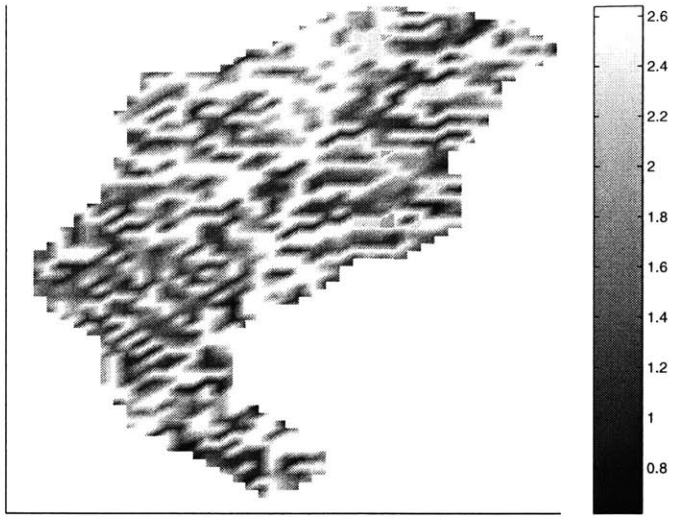

Figure 5-7: Diffused distribution of soil depths calculated from the Dietrich *et al.* model, Bear Valley, CA.

Figure 5-8: Diffused distribution of soil depths calculated from the Dietrich *et al.* model, Midland, VA.

Basin	Minimum Z_T [m]	Maximum Z_T [m]	Median Z_T [m]
Bear Valley	0.5	2.6	1.9
Midland	0.9	2.3	2.2
Tombstone	0.7	2.5	2.2
Yreka	0.6	3.6	1.9

Table 5.4: Minimum, maximum, and median values from modeled distribution of soil depth, for four basins.

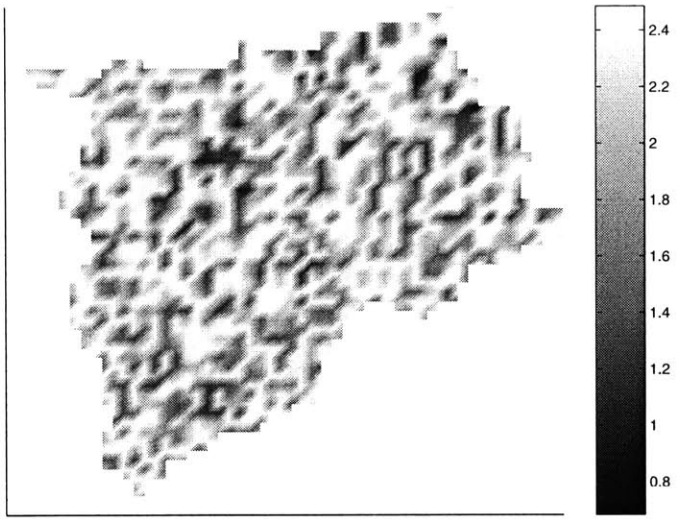

Figure 5-9: Diffused distribution of soil depths calculated from the Dietrich *et al.* model, Tombstone, AZ.

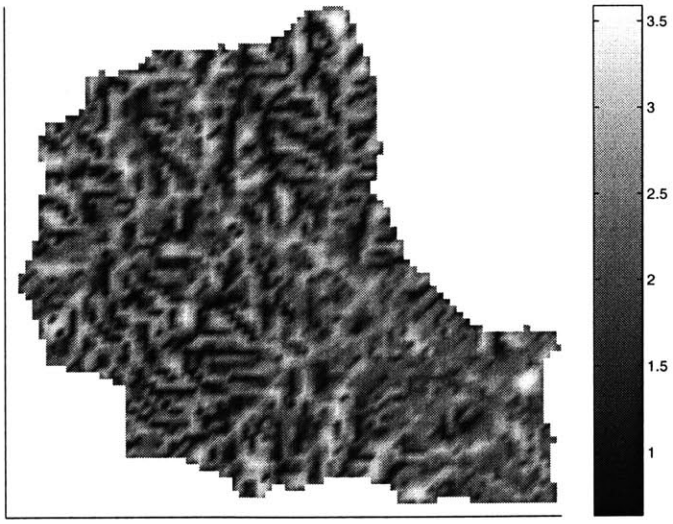

Figure 5-10: Diffused distribution of soil depths calculated from the Dietrich *et al.* model. Yreka, CA.

Basin	Hydrologic variable	Uniform soil depth	Variable soil depth	Units
BEAR VALLEY	E_{bs}	0.66 ± 0.63	0.65 ± 0.61	mm/d
	R_{se}	0.37 ± 0.78	0.37 ± 0.76	mm/d
	Q_e	1.19 ± 1.36	0.79 ± 1.33	mm/d
	Z_w	1.41 ± 0.61	1.26 ± 0.66	m
	%M	3	22	
MIDLAND	E_{bs}	2.80 ± 0.34	2.65 ± 0.30	mm/d
	R_{se}	0.22 ± 0.31	0.22 ± 0.32	mm/d
	Q_e	0.00 ± 0.55	0.00 ± 0.52	mm/d
	Z_w	1.04 ± 0.17	1.03 ± 0.16	m
	%M	50	48	
TOMBSTONE	E_{bs}	0.92 ± 1.75	0.86 ± 1.68	mm/d
	R_{se}	0.10 ± 0.25	0.12 ± 0.28	mm/d
	Q_e	0.00 ± 1.97	0.00 ± 2.04	mm/d
	Z_w	1.39 ± 0.60	1.22 ± 0.56	m
	%M	2	20	
YREKA	E_{bs}	0.46 ± 0.62	0.49 ± 0.59	mm/d
	R_{se}	0.20 ± 0.44	0.17 ± 0.39	mm/d
	Q_e	0.59 ± 1.07	0.57 ± 0.99	mm/d
	Z_w	1.59 ± 0.62	1.39 ± 0.68	m
	%M	36	2	

Table 5.5: Mean and standard deviation of modeled hydrologic variables for two soil depth scenarios. E_{bs} is bare-soil evaporation; R_{se} is saturation-excess runoff; Q_e is net recharge from the unsaturated to the saturated zone; Z_w is the depth of the water table beneath the surface; and %M is the areal percentage of the basin classified as midline. Infiltration-excess runoff is negligible for all cases.

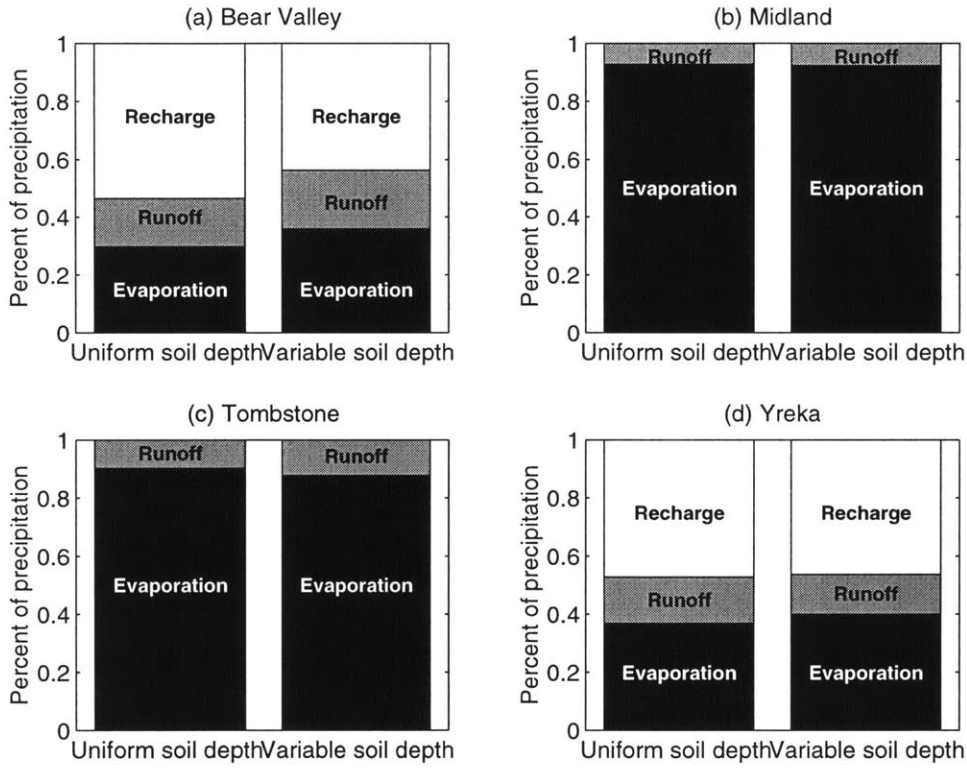

Figure 5-11: Modeled partitioning of precipitation into fluxes for uniform and variable soil depth, for four basins.

given in graphical form in Figure 5-11. The mean fluxes are relatively insensitive to the introduction of spatially varying soil depth. The calculation of the fluxes depends only on the water table depth and the overlying moisture profile in the unsaturated zone; the depth of saturated soil below the water table does not alter the surface fluxes. The mean water table is consistently slightly shallower in the variable-depth case due to the shallow soils in upslope regions. However, there the similarities between basins stop. Evaporation increases with the shallower water table in only one of the four basins (Yreka). The impact on saturation-excess runoff is negligible since the effect on the water table position is small.

The most striking effect of the heterogeneous soil depth is on the extent of midline, which responds differently in the different basins. Using the recharge-based criterion for midline described in Chapter 4, we observe a marked increase in the areal extent of midline in Bear Valley and Tombstone and a strong decrease in Yreka; the change in Midland is minimal. We expect that the midline extent should decrease in the basin where there is the greatest variability in soil depth. Greater divergence between the surface and bedrock slopes is expected to lead to greater variability in the water table slope. However, Bear and Yreka have highly similar distributions of soil depth ($\sigma(Z_T)$ of 0.650 and 0.654, respectively) while experiencing opposite behavior in midline extent. The other two basins, which have a less dramatic change in midline, have smaller values of $\sigma(Z_T)$. One possible explanation for the different behavior is the distribution of topographic features. Bear and Yreka have similar median slopes (34 and 32 percent, respectively), but Bear Valley has 145 m more total relief than Yreka in one-third the catchment area. Channels in Bear Valley are sharply incised, and the areal extent of divergent slopes is greater than in Yreka. However, the basin relief is not a clear indicator of the midline response to heterogeneous soil depth when one considers the behavior of Midland and Tombstone; those basins have significantly less relief yet their response is intermediate between Yreka and Bear Valley. Another possible explanation is the approximateness of the technique used for differentiating the midline region from recharge and discharge areas. With only four basins, it is difficult to discern any clear pattern between physical or climatic characteristics and the sensitivity of the midline region. Future application of the soil-depth model to additional basins may provide greater insight to the differing hydrologic response.

Sensitivity of distributed hydrology

The previous section found a relatively small change in basin-average fluxes when a distribution of soil depths was introduced beneath the known surface topography. However, the use of basin averages could mask greater sensitivity in the equilibrium hydrology at different locations within the basin. In this section we examine the spatial pattern of hydrologic sensitivity for one of the basins. Figure 5-12 shows the equilibrium water table depths for the variable soil scenario in Yreka; Figure 5-13 illustrates the difference in water table depth between the variable and uniform scenarios. The introduction of a variable soil thickness does not affect the general pattern of a near-surface water table in the riparian zone and deep water tables on ridges and hillcrests. The difference in water table depth in the channels is negligible since the soil is saturated (Z_w at or near zero) in both scenarios. The only consistent effect of the variable soil depth is that the water table is shallower on ridges and hill tops. This is due to the model formulation, which sets the water table at the bedrock interface in dry cells in order to maintain atmospheric moisture inputs from those areas. When the soil layer is relatively thin, as it is in upslope areas, the water table appears to be closer to the surface.

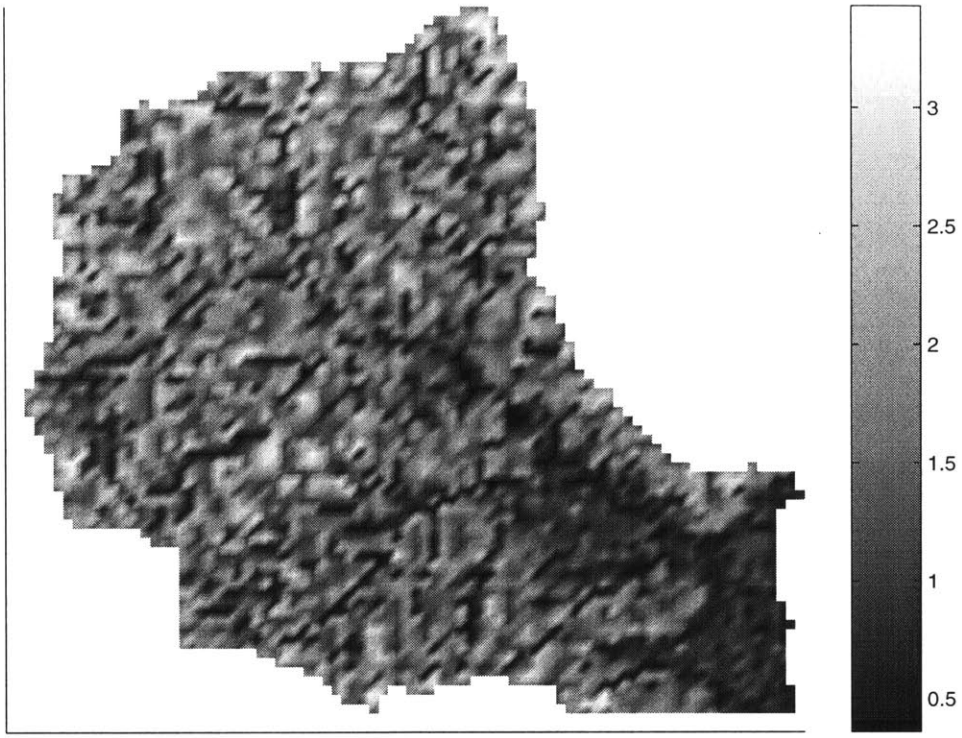

Figure 5-12: Map of equilibrium water table position for variable-depth soil, Yreka, CA.

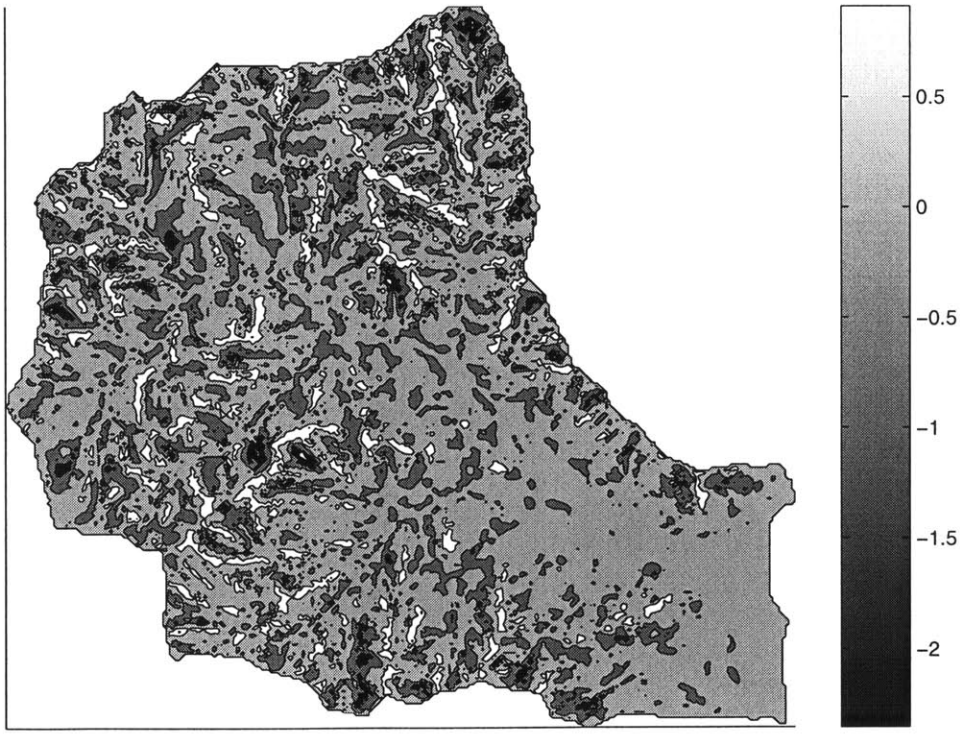

Figure 5-13: Map of the difference between modeled water table depth for the uniform-depth and variable-depth soil scenarios, Yreka, CA.

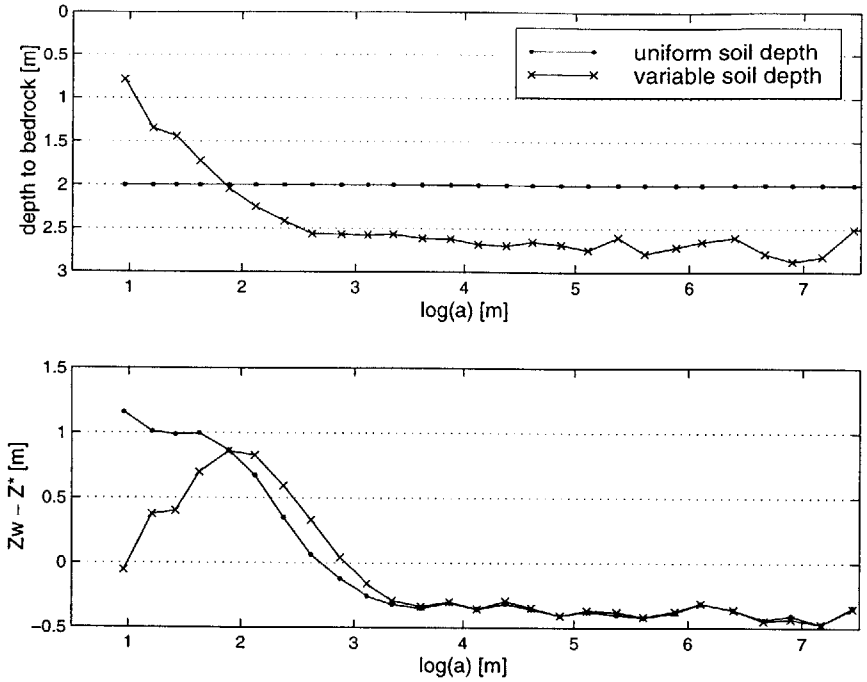

Figure 5-14: Water table depth and depth to bedrock for two soil-depth scenarios, sorted by contributing area, Yreka, CA.

Figure 5-14 plots the water table depth for the two soil scenarios as a function of contributing area. This figure accentuates the locations where the water table depth is and is not dependent on soil depth. For downslope pixels (large a), the water table depth is independent of the local soil thickness. In the upslope pixels, however, the water table depth sharply diverges. The average variable-soil water table depth is much shallower at small contributing areas. The lower subplot illustrates that, at these locations, the water table depth is constrained by the soil thickness in those locations. The model limits the water table depth to lie within the soil layer; when the soil is desaturated, the upper limit is set by the depth to bedrock. In the variable-soil case, the soil depth is reduced in upslope divergent areas, resulting in shallower water table depths. The effect on the overall water balance is relatively mild, since the dry upslope areas tend to have low evaporation and runoff rates in either scenario.

In summary, we find a shallower water table in regions where the soil thickness is reduced, and a thicker saturated layer in riparian areas that have a thick colluvium. The average effect on the surface fluxes is relatively small, however, as summarized in Table 5.5. The sensitivity study is only as good as the model used to generate the spatially varying soil depth. The results may be impacted by limitations of the Dietrich *et al.* model, such as the spatially uniform diffusivity, the lack of a physically-meaningful steady-state algorithm for soil depth in convergent regions, and the use of calibration parameters that are not readily available. Despite these concerns, it is observed that the equilibrium hydrology, both mean and spatial distribution, is relatively insensitive to the Dietrich *et al.* (1995) model of spatially variable soil depths applied to four watersheds.

5.4 Soil texture

In addition to the assumptions about the distribution of soil depths, two further challenges arise in using soil survey data in our hydrologic model: (1) the STATSGO data are distributed, so many soil textures may exist within a basin (and many are marked as "unknown"); and (2) we rely on pedotransfer functions to convert the soil classifications into hydraulic characteristics. We have assumed uniform soil texture across each basin and employed a systematic transfer function for the conversion of the descriptive soil types into the required Brooks-Corey parameters. In this section we examine the implications of uncertainty in soil texture on the equilibrium hydrology. We first investigate the overall sensitivity of hydrology to soil texture in a one-dimensional soil column and in the complex terrain of four study basins. We then discuss the concept of the catena and how soil chemistry and texture vary throughout a basin.

5.4.1 Uniform soil texture

The hydraulic conductivity of a soil is critical in determining the rate of saturated flow, as governed by the Darcy equation, $q = K_s \cdot d\Phi/ds$, where q is the flow rate, K_s is hydraulic conductivity, Φ is hydraulic head, and s is distance in the direction of flow. For a given head gradient, more conductive (*i.e.*, coarser) soil supports a higher rate of groundwater flow. Salvucci (1994) investigated the sensitivity of equilibrium hydrologic fluxes along a planar hillslope to changes in soil texture. He found that increased conductivity resulted in decreased hillslope-averaged runoff, increased recharge, and decreased evaporation. In coarser soils, precipitation moves rapidly down through the vadose zone to the saturated zone, where it is retained in the soil because at deep locations it is not easily available for evaporation. Coarse soils also have little infiltration-excess runoff, because intensities must be extremely high to exceed the infiltration capacity of the soil.

Figures 6.5 and 6.13 in Salvucci (1994) presented the equilibrium fluxes along a silt and a clay hillslope. Several observations can be made about the clay hillslope which provide insight into the sensitivity of hydrologic response to soil texture:

- Infiltration-excess runoff occurs. The fine soil has a relatively low infiltration capacity; even moderate-intensity storms may cause infiltration-excess runoff.
- Evaporation is greater than on the silt hillslope. The vertical conductivity of the clay soil is relatively small (K_s is assumed to be isotropic). The downward percolation of moisture through the vadose zone proceeds slowly, resulting in more moisture in the upper part of the soil column from where it is easily evaporated.
- The midline region extends across most of the hillslope. Along this stretch, flow is predominantly parallel to the ground surface and net recharge approaches zero.
- The water table is deeper overall than in the silt case. This is because infiltration-excess runoff is more likely to occur and evaporation is greater in clay soils. The heightened fluxes out of the unsaturated zone result in a net reduction in moisture available to recharge the saturated zone.

To summarize, we expect to find less spatial heterogeneity, greater net flux of moisture from the soil to the atmosphere, and deeper water tables in a fine-grained soil relative to a coarse-grained soil.

	Coarse loam	Sandy loam	Silty loam	Units
K_s	2.0	1.5	0.29	m/d
Ψ_s	0.32	0.36	0.45	m
n_e	0.29	0.31	0.35	
m	2.6	2.1	1.2	

Table 5.6: Brooks-Corey soil properties for soil texture study in study basins. K_s is the saturated hydraulic conductivity; Ψ_s is the bubbling head; n_e is the porosity; and m is the pore size distribution index.

Basin	Hydrologic variable	Soil texture		Units
BEAR VALLEY		*Sandy loam*	*Silty loam*	
	E_{bs}	0.29	0.62	mm/d
	Q_e	1.93	1.59	mm/d
MIDLAND		*Sandy loam*	*Silty loam*	
	E_{bs}	0.43	0.94	mm/d
	Q_e	2.58	2.08	mm/d
TOMBSTONE		*Coarse loam*	*Sandy loam*	
	E_{bs}	0.086	0.13	mm/d
	Q_e	0.92	0.89	mm/d
YREKA		*Sandy loam*	*Silty loam*	
	E_{bs}	0.15	0.34	mm/d
	Q_e	1.13	0.93	mm/d

Table 5.7: Sensitivity of equilibrium hydrology to soil texture in a semi-infinite soil column for four climates. E_{bs} is bare-soil evaporation; Q_e is net recharge from the unsaturated to the saturated zone. Infiltration-excess and saturation-excess runoff are negliglible for all cases.

5.4.2 Results

Sensitivity of a one-dimensional system

Table 5.7 summarizes the unsaturated zone fluxes for two soil texture scenarios for each of four different basin climates. The finer soil supports a higher evaporation rate and correspondingly lower recharge. In each case, evaporation from the finer soil is approximately double what it is in the coarser soil scenario. Both saturation-excess and infiltration-excess runoff are negligible due to the large depth of the water table (5 m). These results are consistent with the findings of Salvucci (1994).

Sensitivity of basin-average hydrology

GSEM is run on the four basins to examine whether the differences observed in a one-dimensional and two-dimensional case are similarly found in complex terrain. The Brooks-

Basin	Hydrologic variable	Soil texture		Units
BEAR VALLEY		*Sandy loam*	*Silty loam*	
	E_{bs}	0.66 ± 0.63	1.47 ± 0.37	mm/d
	R_{se}	0.37 ± 0.78	0.43 ± 0.73	mm/d
	Q_e	1.19 ± 1.36	0.31 ± 0.98	mm/d
	Z_w	1.41 ± 0.61	1.18 ± 0.49	m
	%M	3	11	
MIDLAND		*Sandy loam*	*Silty loam*	
	E_{bs}	2.10 ± 1.10	2.80 ± 0.34	mm/d
	R_{se}	0.73 ± 1.00	0.22 ± 0.31	mm/d
	Q_e	0.19 ± 1.88	0.00 ± 0.55	mm/d
	Z_w	0.79 ± 0.36	1.04 ± 0.17	m
	%M	11	50	
TOMBSTONE		*Coarse loam*	*Sandy loam*	
	E_{bs}	0.92 ± 1.75	0.97 ± 1.64	mm/d
	R_{se}	0.10 ± 0.25	0.07 ± 0.21	mm/d
	Q_e	0.00 ± 1.97	0.00 ± 1.81	mm/d
	Z_w	1.39 ± 0.60	1.43 ± 0.55	m
	%M	2	3	
YREKA		*Sandy loam*	*Silty loam*	
	E_{bs}	0.49 ± 0.69	1.08 ± 0.60	mm/d
	R_{se}	0.18 ± 0.41	0.11 ± 0.31	mm/d
	Q_e	0.50 ± 0.69	0.08 ± 0.83	mm/d
	Z_w	1.52 ± 0.62	1.50 ± 0.47	m
	%M	36	10	

Table 5.8: Mean and standard deviation of modeled hydrologic variables for two uniform soil texture scenarios, for four basins. E_{bs} is bare-soil evaporation; R_{se} is saturation-excess runoff; Q_e is net recharge from the unsaturated to the saturated zone; Z_w is the depth of the water table beneath the surface; and %M is the areal percentage of the basin classified as midline. Infiltration-excess runoff is negligible for all cases.

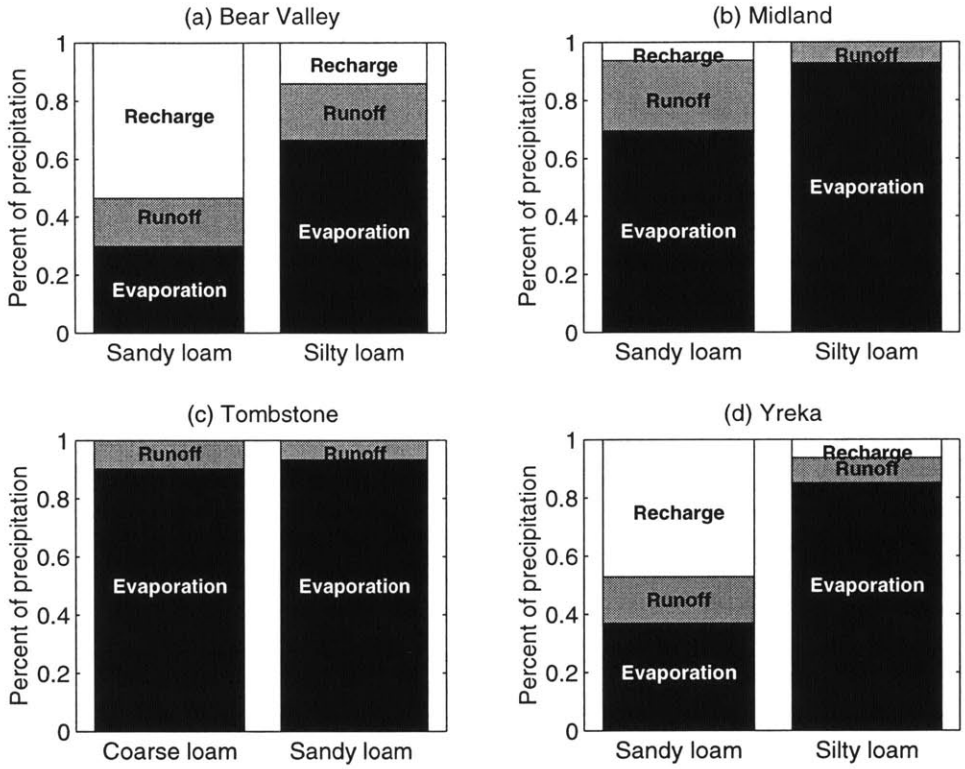

Figure 5-15: Modeled partitioning of precipitation into fluxes for two uniform soil texture scenarios, for four basins.

Corey parameters for the original and modified soil types are given in Table 5.6. The mean and standard deviations of the water table depth and hydrologic fluxes for the different soil textures are summarized in Table 5.8; a bar graph of the distribution of surface fluxes is given in Figure 5-15.

Again as expected, evaporation occurs at a higher rate from the finer soil in all four basins. The net recharge rate is also universally lower. The spatial heterogeneity within each basin, as represented by the standard deviation of Z_w, is consistently smaller in the finer soil, although the magnitude of the change is not significant. The extent of midline, which is related to the spread in water table position, is higher in the fine-soil case for three of the four basins. This supports the hypothesis stated in Section 4.3.3 that the extent of the midline is partially controlled by an inverse relationship to the coarseness of the soil.

The response of the remaining hydrologic characteristics to a perturbation in soil texture varies between basins. The equilibrium runoff increases in Bear Valley but decreases in the other three basins. Bear Valley is also the only catchment where the water table is significantly shallower in the fine-soil scenario. Yreka experiences a marginal decrease in Z_w with a reduction in soil conductivity. The inconsistent response in water table position is due to competing influences from the relationship of hydraulic conductivity to evaporation and recharge. A decrease in hydraulic conductivity deepens the water table via an increase in the evaporative flux of moisture out of the soil. However, an increase in evaporation results in a decrease in recharge; when recharge is substantially reduced, the water table does not to deepen so much to support the evaporation rate. The relative strength of these two effects varies between basins, resulting in their canceling each other out in some environments but not in others. Finer soil results in universally higher evaporation and universally lower recharge, but the unique set of topography and climate in each basin combines to induce variable effects on other basin-scale hydrologic processes.

5.4.3 Spatially variable soil texture

The above observations describe how hydrologic fluxes vary in response to a difference in uniform soil texture. This addresses the uncertainty in assigning soil parameters to a STATSGO soil classification. The second assumption we consider in this section is the sensitivity of the equilibrium hydrology to spatial variability in soil texture. We are concerned with variability that is organized, or large-scale, rather than stochastic.

The concept of the catena was introduced to characterize the broad relationship between soil and topography: it is defined as "a grouping of soils which while they fall wide apart in a natural system of classification on account of fundamental and morphological differences, are yet linked in their occurrence by conditions of topography and are repeated in the same relationships to each other wherever the same conditions are met with" (Milne 1935a, p. 197). The lateral variability in soil properties along a hillslope is governed by the particular combination of climatic, hydrologic, pedogenic, and geological surficial processes (Birkeland 1999). An extensive body of work has assembled identifying characteristics of catenas for different climates, ages, and surficial material. Widespread properties include an increase in clay content and acidity with distance downslope (Gerrard 1992). However, these properties are not universal; a decrease in clay content along the catena was found on tropical slopes in Natal and Malaysia where extensive surface wash and throughflow transported fine particles away from downslope areas (Ollier 1973).

Important catena features include those related to the soil chemistry (*e.g.*, amount of carbonates and other minerals, acidity, amount of organic matter) and soil texture (*e.g.*,

clay content and grain size). As an example of how the unique combination of pedogenesis, climate, hydrology, and geology in different environments influences catena characteristics, we present some of the processes that could contribute to differing patterns of grain size distribution along a hillslope. We use contributing area A_c as a proxy for distance downslope. Possible mechanisms include the following:

Mechanisms for decreasing grain size with increasing A_c

- Transport-limited water-based erosion may be better able to transport fine grains downslope. This is relevant when sheet wash or overland flow are dominant soil transport mechanisms.
- Grains may be physically weathered as they travel downhill.
- Grains may be chemically weathered over time (assuming that age of exposure increases downslope).

Mechanisms for increasing grain size with increasing A_c

- Fine grains deposited downslope in or near riparian zones may be selectively removed by floods or near-channel overland flow.
- Higher exposure of large grains may increase their likelihood of being transported downslope either by gravity or external perturbation.
- Hilltops may have greater exposure to physical and chemical weathering.

Mechanisms with an indeterminate effect on spatial patterns of grain size

- Spatial variability in the underlying bedrock or soil-production process could cause heterogeneity in the colluvium.
- Wind patterns may result in deposition of fine soil in valleys or on hilltops.
- Animals that dig in the soil and expose it for transport may selectively inhabit certain regions of a basin, for reasons such as availability of vegetation or water, physical protection from the elements, or competition with other animals.
- Differential land use (*e.g.*, selective cultivation of, or development on, non-clay soils) could alter the distribution of grain sizes.

5.5 Summary

The physical characteristics influencing the hydrologic cycle vary over a range of spatial scales. This chapter investigated the sensitivity of GSEM output to changes in the physical forcings not considered in the original formulation. The presence of vegetation increases the local evaporation rate for any soils not fully saturated. A homogeneous vegetation cover has a relatively minor impact on the spatial water table distribution because the enhanced flux from the soil is mitigated by reduced lateral groundwater flow. The effect of heterogeneity in the plant cover depends on the pattern or randomness of the vegetation and its characteristics (*i.e.*, rooting depth, LAI). Whereas vegetation alters the vertical flux

from the soil, the soil texture and thickness primarily influence the spatial water balance through differential lateral transmissivity. The introduction of topography-dependent soil thickness has little effect on the basin-averaged fluxes. Modification of the uniform soil texture illustrates that finer soils tend toward higher evaporation and lower recharge fluxes. However, the remaining hydrologic processes and states considered do not exhibit the same response to a decrease in soil conductivity. The variable response highlights the need to understand the unique combination of topography, climate, and soil properties occurring in individual basins. Furthermore, the exact influence of heterogeneous physical characteristics such as vegetation and soil thickness on the distribution and mean water balance depends on the specific pattern and extent of variability in any individual basin.

This chapter has examined the effect of heterogeneous, non-topographic factors on distributed hydrology. The patterns previously found in Chapter 4 are not significantly affected in the studies presented here. More significant are the differences found between basins, even while the deterministic patterns are qualitatively similar. The basins differ in their relationship of water table depth and fluxes to topographic index, both in the magnitude of variability and in the deviation around the mean in a single set of locations. The extent of dry and saturated regions also varies among the basins. The dominance of the midline region varies, reflecting interbasin differences in the balance of unsaturated and saturated zone processes. In the next chapter, statistical methods are used to search for physical explanations of the observed interbasin variability.

Chapter 6

Interbasin variability in hydrologic response

In the previous chapters, we identified patterns of hydrologic variability within individual basins. In this chapter, we investigate variability between basins with an examination of the relationships between various physical characteristics and the hydrologic properties of basins. Neither climate nor physiography can alone explain observed interbasin variability. Numerous climatic, geomorphologic, and lithologic variables that are commonly used to characterize watersheds are considered. Of these, nine variables are selected, each of which has a conceptual relationship to basin-scale equilibrium hydrology. These variables are used in a principal component analysis (PCA), a statistical technique which reduces a large dataset to a smaller number of linearly independent parameter groups. From the original nine variables, we derive four principal components which together explain 80 percent of the variance in the original data. The components represent groundwater efficiency, basin climatic wetness, surface-subsurface coupling, and an index of basin dissectedness. We then perform a stepwise regression to identify which combinations of variables are valuable in predicting the basin-average hydrologic fluxes. A combination of two variables estimate the runoff ratio with an R^2 of 0.76; use of all six variables increases the prediction to an R^2 of 0.90. The stepwise regression technique fails to achieve a statistically significant model for evaporation efficiency, but a regression model using all six variables nonetheless achieves an R^2 of 0.79.

6.1 Basin descriptors

A major challenge in quantitative geomorphology is the development of indices to characterize physically important characteristics of a natural landscape. Table 6.1 introduces a collection of basin and network parameters found in the literature from which a small number of parameters will be selected. The indices can be grouped into several categories, including those which capture information about basin relief (*e.g.*, median slope and the two relief ratios), basin shape (*e.g.*, basin shape, circularity, and elongation ratios), and network dissectedness (*e.g.*, drainage density and relative channel density). Additional indices include combinations of basin characteristics, such as the ruggedness ratio, which combines relief and network dissectedness.

A number of criteria are employed in the selection of morphologic variables for the interbasin analysis: a known or theorized physical relationship to distributed equilibrium

Parameter	Definition	Formula	Units	Reference
A, A_Ω	basin area		[L^2]	
a	area/unit contour length		[L]	
L_b	basin length		[L]	
P	basin perimeter		[L]	
H	basin relief		[L]	
S_{50}	median surface slope		[%]	
$\bar{S}$	mean surface slope		[%]	
L_T	total channel length		[L]	
N_T	number of channels		[–]	
L_{max}	longest-channel length		[L]	
$\bar{S}_{Lmax}$	mean slope of L_{max}		[%]	
$\bar{C}$	mean surface curvature		[–]	
D_d	drainage density	L_T/A	[L^{-1}]	Horton (1945)
R_r	relief ratio	H/L_b	[–]	Doornkamp and King (1971)
R_h	another relief ratio	H/P	[–]	Schumm (1956)
W	basin width	A/L_b	[L]	Zecharias and Brutsaert (1988)
F_s/D_d^2	relative channel density	$N_T A/L_T^2$	[–]	Zecharias and Brutsaert (1988)
R_f	basin shape	A/L_b^2	[–]	Strahler (1968)
R_e	elongation ratio	D_A/L_b	[–]	Strahler (1968)
HD_d	ruggedness ratio	HL_T/A	[–]	Strahler (1968)
T_T	texture ratio	N_T/P	[L^{-1}]	Doornkamp and King (1971)
R_c	circularity	A/A_P	[–]	Strahler (1968)

Table 6.1: Definition of geomorphologic indices from the literature. D_A refers to the diameter of a circle with area A; A_P represents the area of a circle with perimeter P.

Basin	S_{50} [-]	R_r [-]	D_d [km^{-1}]	α_{us} [-]	i_r/K_s [-]	α_s [-]	$\frac{(Z_w - Z^*)}{Z_T}$ [-]	E/E_p [-]	R/P [-]
Bear	3.3e-1	1.7e-1	1.8	1.2	1.3e-2	5.1e-2	0.47	0.36	0.21
Big Creek	4.3e-1	6.4e-2	1.2	0.3	4.5e-3	2.0e-2	0.66	0.11	0.72
Brushy	1.0e-1	5.8e-3	2.3	1.1	8.9e-2	2.5e-5	0.14	0.91	0.11
Midland	3.3e-2	9.0e-3	2.0	1.0	1.5e-1	1.4e-4	0.01	0.90	0.07
Moshannon	1.2e-1	1.6e-2	1.0	1.7	1.5e-1	8.7e-5	0.26	0.98	0.36
Ogden	7.1e-2	1.5e-2	1.6	0.4	2.4e-1	4.1e-4	0.12	0.41	0.00
Sacramento	1.0e-2	3.7e-3	3.4	0.2	1.4e-1	9.4e-5	0.02	0.23	0.00
Schoharie	1.9e-1	5.7e-2	1.7	1.4	1.1e-2	8.4e-3	0.54	0.30	0.53
Tombstone	7.0e-2	3.6e-2	2.4	0.2	1.3e-2	3.3e-2	0.44	0.25	0.14
Yreka	3.1e-1	8.6e-2	1.0	0.6	9.3e-3	2.1e-2	0.40	0.22	0.26

Table 6.2: Values of variables used in principal component analysis.

hydrology, a focus on equilibrium hydrology rather than on dynamic routing effects, nondimensionality (where possible), and independence from each other. Three indices are selected from Table 6.1: median slope, relief ratio, and drainage density. These three physiographic descriptors are added to variables which describe the climate, soil, and hydrologic responses of the basins. Below we describe the relevance of each of the nine parameters and its expected role. Table 6.2 contains the values of each parameter for all basins.

Median surface slope (S_{50}): The median surface slope contains limited information on the distribution of slopes within a basin. We consider the median as opposed to the mean slope to avoid bias from a few very steep or shallow areas. Since GSEM assumes that bedrock is parallel to the ground surface, the surface slope represents the gradient driving lateral Darcy flow when the saturated depth is constant. In basins with a high slope, lateral flow may transport moisture out of a cell faster than it is replenished by recharge or incoming groundwater, causing the cell to dry out.

The slope at each pixel is taken as the slope to the lowest neighboring cell, or the direction of steepest descent. This approach implicitly assumes that flow occurs in only one of eight directions, each separated by 45°. Some amount of error is introduced through this assumption, since in reality flow may occur at an angle other than one of the eight grid-dependent directions or in the direction of some combination of two or more downslope cells.

Relief ratio (R_r): The relief ratio is a measure of basinwide average slope. As opposed to the median surface slope, which is determined from the steepest slope at every pixel, R_r is the ratio of the total basin relief (the elevation difference between the highest and lowest points) and a representative basin length. The basin length is defined as the straight distance between the outlet and the farthest point in the basin from the outlet. This index provides an approximate estimate of the topographic gradient affecting lateral groundwater movement on the scale of the entire basin. High values of R_r should be correlated with efficient lateral redistribution of moisture.

Drainage density (D_d): Drainage density is defined as the ratio of total stream length to basin area. It is an approximate measure of the inverse mean horizontal hillslope

Basin	Threshold area [km^2]
Bear	0.13
Big Creek	0.27
Brushy	0.09
Midland	0.14
Moshannon	0.63
Ogden	0.19
Sacramento	0.06
Schoharie	0.18
Tombstone	0.10
Yreka	0.32

Table 6.3: Threshold areas for channel network delineation. Values for Big Creek, Brushy, Moshannon and Schoharie were taken from Tarboton *et al.* (1991).

length. It is often seen as a key indicator of the hydrologic response of a landscape, given the difference in velocity and residence time of water between the hillslope and stream channel. The drainage density also has implications for the extent of saturated areas and runoff generation. The soil is more likely to be saturated within the channel network than on the upper reaches of a hillslope; there is therefore a positive relationship between drainage density and the spatial extent of the riparian zone. A low value of D_d corresponds to a landscape with long hillslopes; a high D_d indicates a dissected landscape.

The estimation of a basin's drainage density requires delineation of the channel network. The identification of where a channel begins is an area of ongoing research. Channel heads may be estimated by field observation, visual estimation from topographic blue lines or aerial photographs, or from digital elevation models using automated techniques. We use the constant-drop approach described by Tarboton *et al.* (1991) for automated estimation of a channel network from a DEM. The approach holds that the elevation drop in each stream link should be independent of the Strahler order of that link. The minimum threshold contributing area is selected such that the resulting network has constant stream drops for different order links at the 95 percent significance level. The threshold areas generated for the study basins are summarized in Table 6.3.

Wetness ratio (α_{us} or P/E_p): The ratio of storm depth to evaporative depth ($i_r t_r / e_p t_b$) has dual significance for hydrologic processes. A measure of the ratio of moisture input to output in the unsaturated zone, α_{us} was found in Chapter 4 to be inversely related to the extent of midline. The ratio may also be seen as the wetness index P/E_p, which is an indicator of the atmospheric supply and demand of moisture. Potential evaporation is used instead of actual evaporation because the index is designed to represent climatic forcing only; reduction in evaporation rates below their potential is caused by limited soil moisture or vegetation effects. High values signify a moist environment and a small midline area due to the abundance of available water in the unsaturated zone.

Relative infiltration capacity (i_r/K_s): The ratio of mean precipitation intensity to saturated hydraulic conductivity combines soil and climate characteristics to provide a rough indicator of the soil's ability to absorb the average rainfall. The hydraulic conductivity is the maximum rate at which water may be transmitted through the soil given a unit pressure gradient. If the precipitation intensity is much less than K_s, the soil can transport water through the soil column without ponding or surface runoff. Conversely, a relatively high ratio indicates a greater likelihood of infiltration-excess runoff.

Saturated zone efficiency (α_s): In Chapter 4, we introduced the variable α_s to capture the ability of the groundwater to laterally redistribute moisture. The variable is a nondimensional combination of saturated hydraulic conductivity, saturated depth, relief ratio, mean annual precipitation, and basin area:

$$\alpha_s \equiv \frac{K_s \left(Z_T - Z^*\right) R_r}{P\sqrt{A}}$$

As discussed in Chapter 4, the moisture input estimated in the denominator should technically be reduced by the fraction of contributing area above the midline. However, not only is the fraction unknown, it is also inherently related to other key variables such as hydrology and climate. We therefore use the square root of basin area as the representative length scale and neglect any adjustment for the extent of the recharge area.

It was found that α_s is at least partially responsible for an inverse correlation with the extent of midline. (The second important influence on the midline zone is α_{us}, a measure of the unsaturated zone tendency to provide recharge.) It is expected that α_s will play an important role in basin behavior beyond just the formation of the midline, since it combines many physical features in a single variable that represents the overall efficiency of the saturated zone.

Normalized mean water table depth ($(Z_w - Z^*)/Z_T$): the mean water table location is characterized by the average depth relative to the zero-recharge depth Z^* normalized by total soil depth. Large, positive values indicate that the spatially-averaged water table is deep. Dry basins generally have a deep water table, while humid basins with a plentiful moisture supply tend to have a thick saturated zone. Soil texture also influences the water table location, since the conductivity of the soil governs the rate at which moisture is transmitted downward through the unsaturated zone and then laterally through the saturated zone. Efficient downslope moisture transport may cause deep water tables since water is discharged from the soil as runoff in downslope areas.

Evaporation efficiency (E/E_p): Evaporation efficiency, the spatial mean of actual over potential evaporation, is an indicator of the overall moisture supply in the soil. Evaporation is directly, albeit nonlinearly, dependent on water table depth. When the water table is deep, the surface soil has little soil moisture; this moisture deficit limits the rate of evaporation from the soil. In saturated soils, with unlimited moisture, the evaporation efficiency is unity.

Basin	S_{50}	R_r	D_d	α_{us}	i_r/K_s	α_s	$\frac{(Z_w - Z^*)}{Z_T}$	E/E_p	R/P
S_{50}	1.00	—	—	—	—	—	—	—	—
R_r	**0.76**	1.00	—	—	—	—	—	—	—
D_d	-0.62	-0.33	1.00	—	—	—	—	—	—
α_{us}	0.07	0.17	-0.41	1.00	—	—	—	—	—
i_r/K_s	-0.68	-0.64	0.16	-0.01	1.00	—	—	—	—
α_s	0.60	**0.88**	-0.12	-0.11	-0.71	1.00	—	—	—
$(Z_w - Z^*)/Z_T$	**0.82**	0.65	-0.49	0.06	**-0.82**	0.66	1.00	—	—
E/E_p	-0.43	-0.42	-0.11	0.65	0.51	-0.52	-0.57	1.00	—
$\frac{R}{P}$	0.75	0.32	-0.59	0.26	-0.60	0.20	**0.83**	-0.26	1.00

Table 6.4: Correlation coefficients between variables used in principal component analysis, $N = 10$. Values significant at the 95 percent level are in boldface.

Runoff ratio (R/P): The runoff ratio represents the amount of incident rainfall that is removed from the system as overland or rapid-response flow before entering the soil column. This ratio is important in flood-frequency analysis, since overland flow is the main cause of high streamflow volumes during storms. The modeled runoff value used in this analysis is the total flow depth, *i.e.*, it includes baseflow.

6.1.1 Pairwise correlations

The first step in identifying patterns in interbasin behavior is to examine the correlations between pairs of variables. Table 6.4 contains the correlation coefficients for the ten–basin, nine–variable dataset. Five pairs of basins are significant at the 95 percent level (correlation coefficient greater than 0.75). No coefficients are significant at 99 percent confidence. It is desirable that most of the variables are poorly correlated with each other; numerous high pairwise correlations could unduly influence the results of the principal component analysis.

Calculation of the correlation matrix of a multivariate dataset provides information on the relationships between pairs of variables, but it cannot identify significant multi-dimensional relationships. To understand the simultaneous interactions between climate, physiography, and hydrology, it is necessary to identify significant relationships between more than two variables at a time. We are interested in combinations of descriptors that vary in unison and the roles of the different clusters in determining the behavior of the study basins. These multi-variable combinations are investigated through the use of principal component analysis and stepwise regression. Methods and results are presented below.

6.2 Principal component analysis

Principal component analysis (PCA) is a data reduction technique that reduces a large number of variables (which may contain some redundant information) to a smaller set of variables that represents most of the information in the original data. Any set of measured variables has a total variance, which is the aggregated variance of each individual variable. The total variance is unaffected by linear operations performed on the data. When principal component analysis is performed on a dataset, the total variance remains constant while the distribution of variance among the independent components (each of which is a

linear combination of the original variables) changes. The goal of PCA is to identify a few components which explain a more significant amount of the original variance than if the original variables were considered individually.

Given a matrix of N variables measured in M samples, the principal components are determined by calculating the variance-covariance matrix and diagonalizing it. The components are the eigenvectors of the variance-covariance matrix with the largest eigenvalues, *i.e.*, they explain the most variance. Each component is a linear combination of all of the original variables, with the relative contribution of the variables quantified in the associated loading vector (the coefficients of the eigenvector). It is also possible to calculate the score of each principal component (the eigenvalue for a given basin); the score represents the extent to which that component explains the basin's behavior. Analysis and comparison of the loading vectors and scores of the most significant principal components allows us to identify combinations of variables that behave in unison and to assess how the basins are described by different subsets of easily measured variables. In the following section we describe the mathematical basis of principal component analysis and review applications of the technique to geomorphologic and hydrologic problems.

6.2.1 Theory

An $M \times N$ matrix $\mathbf{X}$ can be expressed as the sum of r independent matrices,

$$\mathbf{X} = \mathbf{M_1} + \mathbf{M_2} + \mathbf{M_3} + ... + \mathbf{M_r} \tag{6.1}$$

where r is the number of independent parameters in $\mathbf{X}$. Each matrix $\mathbf{M_i}$ can be written as the product of the $M \times 1$ vector of eigenvalues f_i and the $1 \times N$ eigenvector a_i.

$$\mathbf{X} = f_1 a_1 + f_2 a_2 + f_3 a_3 + ... + f_r a_r \tag{6.2}$$

$$= \mathbf{FA} \tag{6.3}$$

The loading vector a_i indicates the relative contribution of each variable to the principal component. The score f_i tells how much of the total variability of a basin is accounted for by the associated principal component.

The loading vector is generated from singular value decomposition. The decomposition works on any matrix that is either singular or very close to singular (Press *et al.* 1996). The method is based on the following premise: any $M \times N$ matrix $\mathbf{X}$ can be written as the product of an $M \times N$ column-orthogonal matrix $\mathbf{U}$, an $N \times N$ diagonal matrix $\mathbf{S}$, and the transpose of an $N \times N$ matrix $\mathbf{A}$:

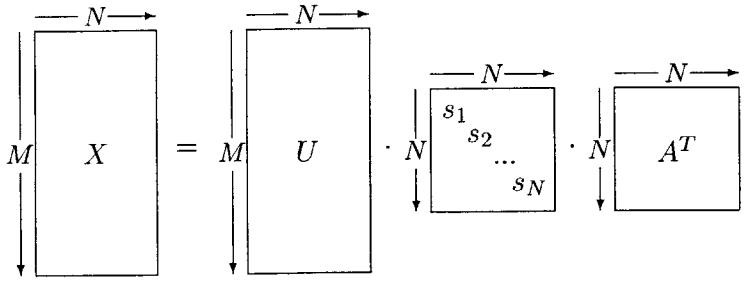

The singular values s_i in the diagonal matrix are nonnegative, decreasing elements that represent the variance explained by each component i. In the case where $M < N$, all values

s_j for $j = M+1, M+2, ..., N$ are equal to zero; the corresponding columns of $\mathbf{U}$ are also zero.

The matrix of component scores is determined from the original data and the loading matrix according to the equation

$$\mathbf{F} = \mathbf{ZA}\left(\mathbf{A}'\mathbf{A}\right) \tag{6.4}$$

where $\mathbf{Z}$ is the matrix $\mathbf{X}$ normalized for each variable (Reyment and Joreskog 1993).

6.2.2 Applications

PCA has been used for a range of applications. It is an efficient technique for identifying how parameters scale together and the dominant sources of variance in a complex system. In the earth sciences, several studies have used PCA to analyze geomorphologic information. Examples include Abrahams (1972), who compared the interdependence of geomorphology in five Australian basins; Onesti and Miller's (1973) examination of the downstream variability in hydromorphic parameters; and a study by Ebisemiju (1979) to identify "representative" basins within a large geographic region. These studies focused on morphologic parameters.

Two more recent studies have used PCA to identify relationships between geomorphology and hydrology. Zecharias and Brutsaert (1988) identified eight morphologic variables with a known or theorized effect on groundwater outflow. The parameters included purely geomorphologic descriptors, such as basin area and relief, and hydromorphic characteristics, such as the length of perennial streams. Principal components were determined from the parameter values for 19 basins along the Appalachian plateau. The first three components explained over 98 percent of the variance. Representing size, slope, and dissection, the three components were assumed to explain the observed interbasin variability in groundwater outflow. Sefton and Howarth (1998) used PCA to examine the relationships between modeled dynamic hydrologic response and physical basin descriptors. Hydrologic characteristics included loss and routing parameters; the physical descriptors included morphology, soil type, land cover, and climatic indices. Sefton and Howarth estimated the principal components from the physical descriptors and then regressed the most significant components against the hydrologic variables. The first four components explained 63 percent of the variance, but no significant relationships were established between the components and the six hydrologic variables.

Our application of PCA differs from the investigations cited above. Zecharias and Brutsaert (1988) only considered morphologic indices related to groundwater outflow and did not use any explicitly hydrologic variables in the analysis. Sefton and Howarth's (1998) hydrology included only dynamic hydrologic response characteristics. We look at long-term hydrologic variables that include both subsurface and surface processes.

6.2.3 Results

Before performing the principal component analysis on the data in Table 6.2, each variable is rescaled so that it is mean-centered and has a unit variance. This is done to remove spurious influences from differences in the dynamic ranges of the variables. By standardizing the range and mean of each variable, we can easily compare dimensional and dimensionless, bounded and unbounded variables in a single analysis.

The components generated by PCA are linear combinations of the original variables. A smaller set of variable combinations, or components, explains the variance found in the

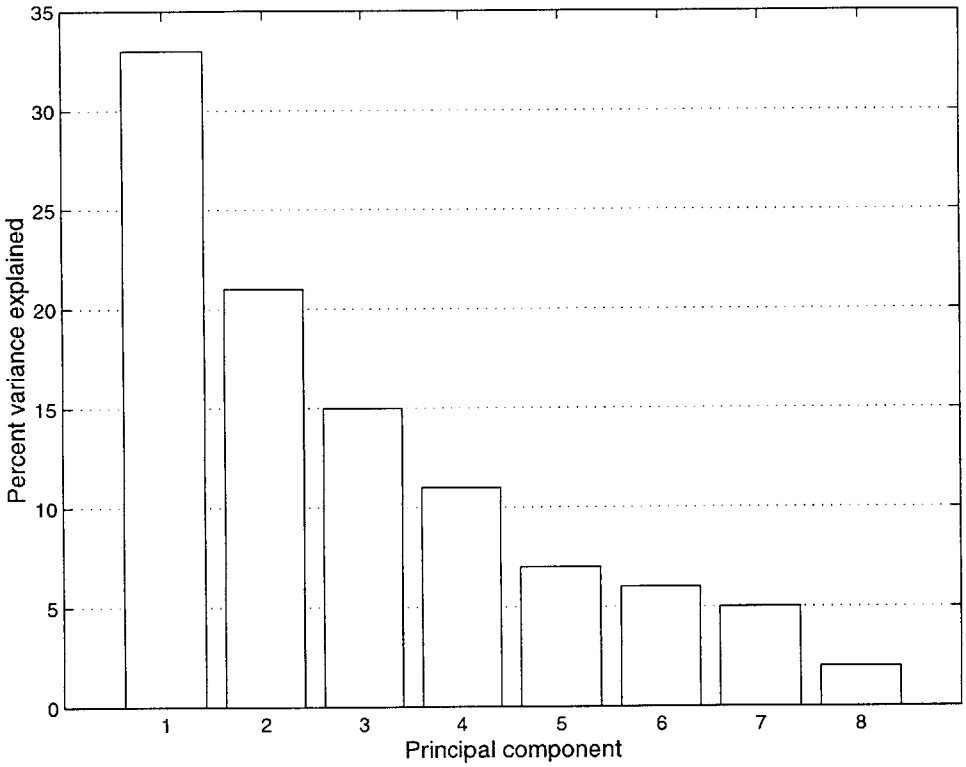

Figure 6-1: Percentage of variance explained by individual principal components.

Variable	PC 1	PC 2	PC 3	PC 4
S_{50}	0.42	-0.10	0.08	-0.25
R_r	0.37	0.04	-0.51	-0.22
D_d	-0.23	0.47	-0.18	0.60
α_{us}	0.02	-0.61	-0.38	0.34
i_r/K_s	-0.39	-0.11	0.06	-0.54
α_s	0.35	0.24	-0.47	-0.09
$(Z_w - Z^*)/Z_T$	0.43	-0.03	0.18	0.16
E/E_p	-0.26	-0.50	-0.28	0.10
R/P	0.33	0.28	0.47	0.29
Percent variance	33	21	15	11
Cumulative % variance	33	54	69	80

Table 6.5: Relative contribution of variables to principal components.

original data. Figure 6-1 shows the percentage of the total variance explained by the first eight principal components. The ability of PCA to efficiently explain variability can be illustrated by considering the first three components, which together explain almost 70 percent of the total variance in the data. Assuming the distribution of variance in the raw data to be equally distributed among the nine parameters, any three randomly selected variables from the original nine would explain only one-third of the basin behavior. We would need eight of the original nine parameters to explain the same amount of variance as the first three principal components. The creation of the new, composite variables allows us to analyze the causes of interbasin variability with fewer independent pieces of information.

The loading vector indicates the importance of a variable in a given component. Those variables with a high loading magnitude dominate the behavior of a component. The loading of each variable in the first four principal components (PCs) is presented in Table 6.5. Figure 6-2 presents the loading vectors with the variables sorted by the magnitude of their contribution. This allows visual identification of the most significant variables in each of the components. Below we discuss the overarching physical and climatic features affecting basin behavior as determined by which variables contibute significantly to each component.

PC 1: Groundwater efficiency The first component is dominated by the normalized water table depth, $(Z_w - Z^*)/Z_T$; two relief parameters, S_{50} and R_r; and the infiltration capacity, i_r/K_s. The component represents the efficiency with which steep slopes route moisture downslope. In fact, the next significant variable, with a loading of 0.35, is the saturated zone efficiency index α_s. Moisture is discharged to surface water and removed from the basin, resulting in an overall deepening of the water table. The negative loading on i_r/K_s is due to the enhancement of downslope transport by the hydraulic conductivity in the denominator of the variable. One-third of the interbasin variability is explained by PC 1, highlighting the importance of gravity-driven flow and downslope discharge in the overall basin behavior.

PC 2: Basin climatic wetness The main contributing parameters to this component are the wetness index α_{us} and the runoff ratio. Over 20 percent of the variance in the data is explained primarily by basin wetness. The wetness index and runoff ratio are strongly related to each other with a correlation coefficient of 0.65; for ten basins this

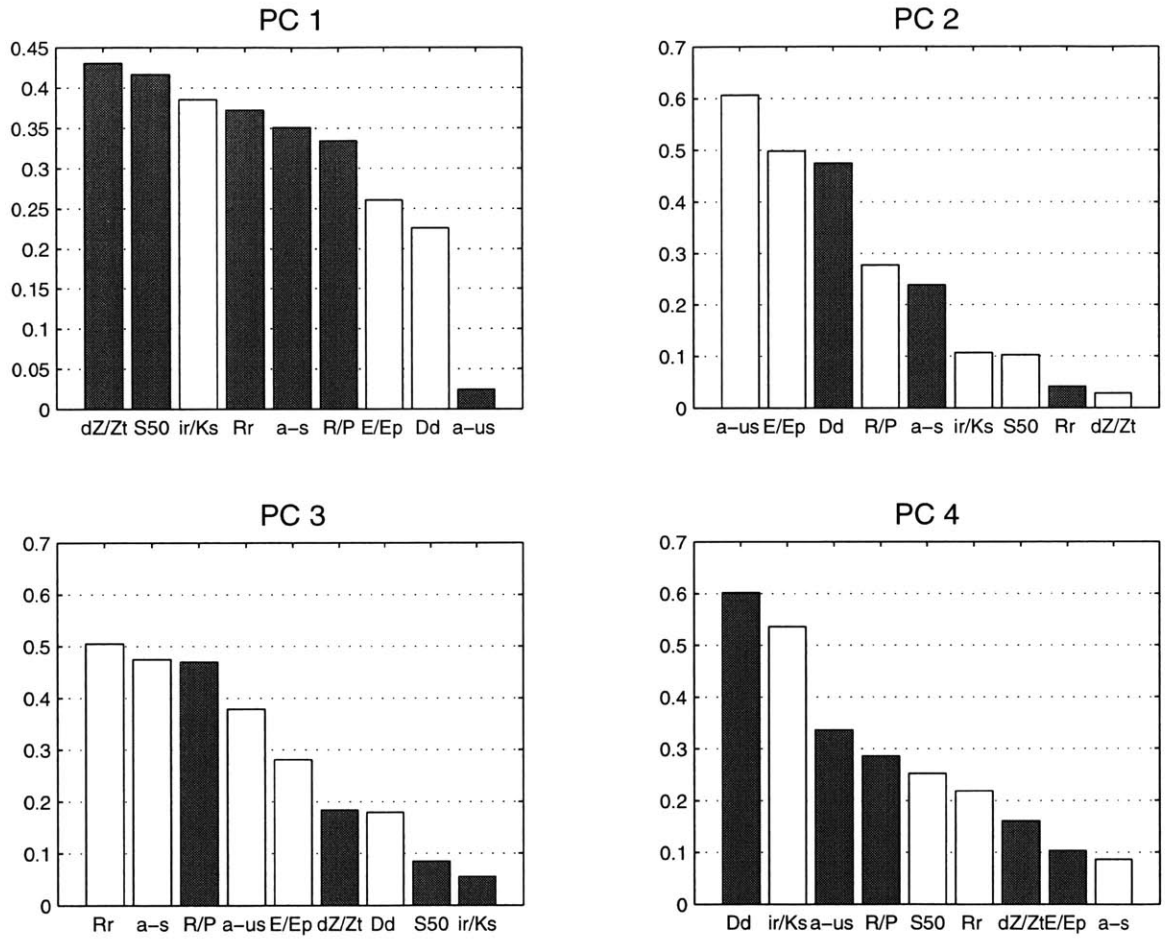

Figure 6-2: Loading vectors, sorted by absolute magnitude, for first four principal components. Positive loading factors are shaded, while negative values are left white.

is significant at the 90 percent level. The additional information reflected in PC 2 beyond the pairwise correlation between wetness and runoff is the secondary but still important role of drainage density. The network density plays a non-negligible role in the behavior of this component despite its small pairwise correlation to either α_{us} or R/P (0.16 and 0.21, respectively).

PC 3: Surface-subsurface coupling The third component, which explains 15 percent of the variance, is related to the extent of surface-subsurface coupling. The dominant variables are R_r, α_s, and R/P. The first two parameters represent the strength of gravity-driven lateral transport of moisture in the saturated zone. The runoff ratio, the third parameter in this component, is the surface indicator of subsurface moisture redistribution. The combination of variables highlighting subsurface transport and surface outflux may be characterized as an index of the degree of coupling between the two zones.

PC 4: Basin dissectedness The fourth component is dominated by the drainage density and infiltration capacity. These two parameters represent the input and output characteristics of long-term landscape evolution. The infiltration capacity i_r/K_s contains a precipitation term and a soil conductivity term. Both of these parameters are critical in the evolution of a landscape: rainfall drives the erosion of land surfaces, while soil conductivity is critical for regolith formation and mobility of surface sediments. The aggregate effect of long-term landscape evolution is seen in the drainage density of the network. The combination of drainage density, rainfall intensity, and soil conductivity in a single component relates to the long-term evolution of the landscape as evidenced by the current basin dissectedness.

The discussion of the loading vectors is centered on the relative contributions of parameters to each principal component. It is also informative to consider the loading of each component on an individual basin, or the component score. Figure 6-3 presents the scores for the first four components. Each basin is described by a linear combination of the four components; the strength of the contribution is the component score. Component scores can be evaluated by either looking for patterns of a given component between basins or of different components within a single basin.

Bear has a high score for PC 1, the moisture transport component. The relief component, PC 4, also exerts a strong influence on the behavior of Bear. (The loading of the relief terms in PC 3 is negative, resulting in the negative score for PC 3.) It is not surprising that this basin, which has a median slope of 34 percent, is best described by the two components that most reflect the role of relief. However, the influences of PC 1 and PC 3 are not tied to basin relief alone. If basin relief were the only significant influence in the two components, it would be expected that the pattern of scores would be consistent for all of the basins. This is not the case; half of the basins have scores with the same sign for the two PCs. This highlights the fact that PC 1 also reflects the water table position and infiltration capacity (climate-soil combination) and PC 3 includes the runoff ratio.

The values of the different component scores in a single basin provide information on the relative importance of different processes in a basin's behavior. Yreka, for example, is most strongly defined by the efficiency of downslope moisture transport. Drainage density also plays a significant role, as seem by the score on PC 4. Components 2 and 3 are of minor importance. The negligible score for PC 3, the relief-dominated component, indicates that steepness alone was not the reason for the high score on PC 1; it is the combination of

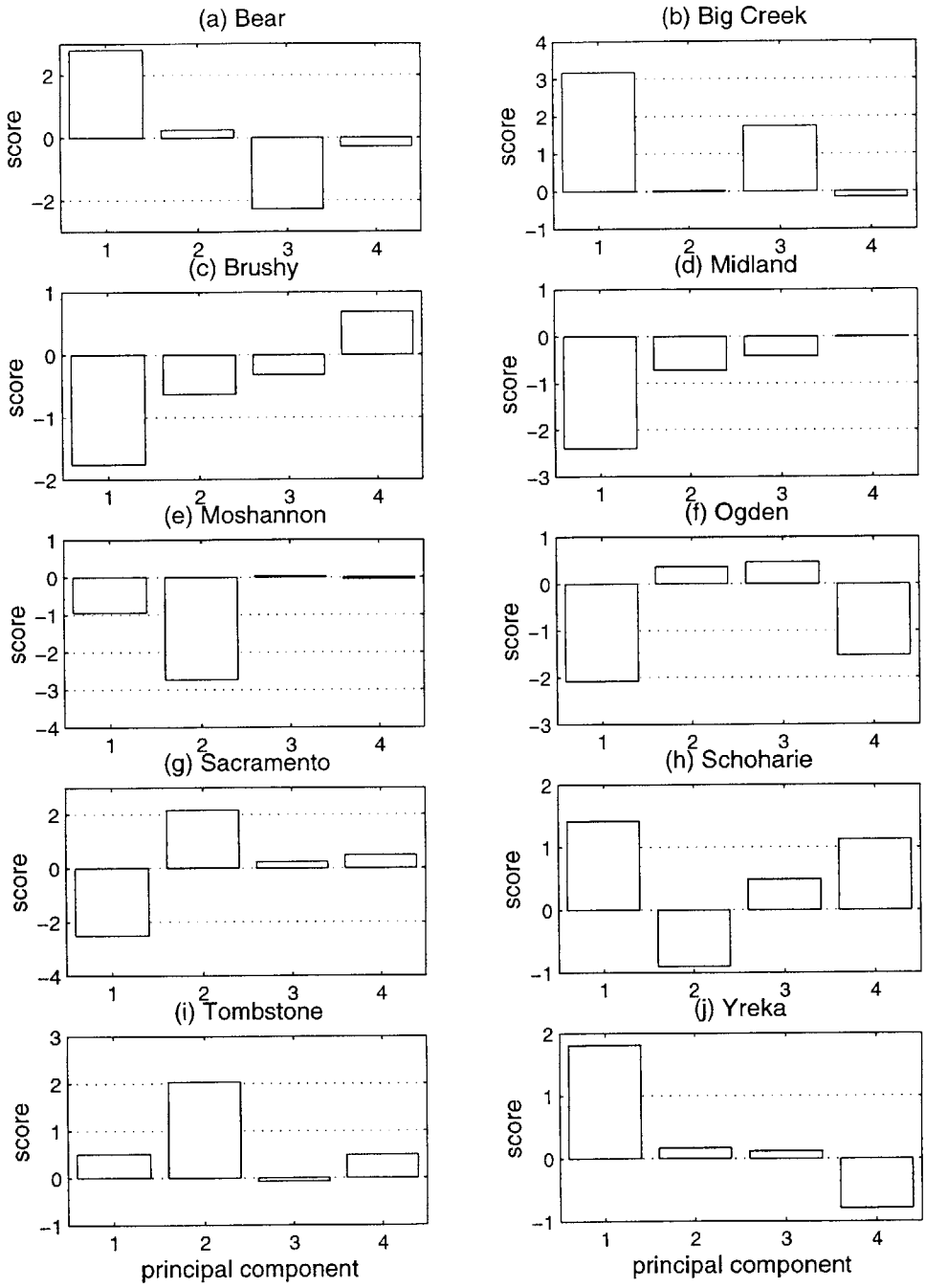

Figure 6-3: Scores of component contributions to basin behavior.

transmissivity, incident moisture, *and* relief that make PC 1 the most significant component in describing the behavior of Yreka.

In summary, PCA was performed on nine variables representing the morphology, climate, lithology, and hydrology of the ten basins. The analysis identified several components that help advance the understanding of interdependence among basin characteristics and behavior. The first four PCs explain 80 percent of the total variance in the data. They represent the efficiency of lateral moisture transport (33%), basin wetness (21%), surface-subsurface coupling (15%), and basin dissectedness (11%). The scores highlight the relative importance of the components in individual basins, providing an efficient way to determine which factors most influence basin behavior.

6.3 Stepwise regression

The above discussion has used the entire set of measured variables to identify which of many physical, climatic, and hydrologic characteristics tend to vary in unison. We are also interested in assessing whether combinations of topographic, soil, and climate variables can predict hydrologic response with reasonable accuracy. Stepwise regression is used to identify which variables contribute a significant amount toward the prediction of the runoff ratio and evaporation efficiency.

6.3.1 Methods

Stepwise regression is a selection procedure that involves testing of each individual variable to ensure its statistical significance in the regression model. The technique is described for predicting some variable Y given variables x_1, x_2, and x_3, after Walpole and Myers (1989).

1. Fit individual linear regression equations between Y and each of the x variables. Calculate the R^2 for each equation.

2. Select the variable with the highest R^2 (assume this is x_1 for illustration). Perform an F-test; if the model's f value is greater than that for the desired significance level, the variable is entered into the model.

3. Calculate linear regression equations between Y and pairs of x variables, where each pair includes x_1, the variable included in the previous step.

4. Again, select the variable with the highest R^2 (assume this is x_2). Two F-tests are performed: the first to test the significance of x_2 in the presence of x_1, the second to test the significance of x_1 in the presence of x_2. If both f values are significant, then x_2 is also included in the model.

5. Repeat the procedure until one of the variables fails the F-test or all of the variables have been included.

6.3.2 Results

The stepwise regression is performed for each of the hydrologic fluxes—evaporation efficiency and runoff ratio—and the six non-hydrologic variables: median slope, relief ratio, drainage density, basin wetness, infiltration capacity, and saturated efficiency index. The F-tests are performed for a significance level of 95 percent.

Variable	R^2
S_{50}	0.01
α_s	0.01
R_r	0.05
i_r/K_s	0.06
D_d	0.23
P/E_p	0.70

Table 6.6: R^2 values between runoff ratio and individual basin characteristics.

Variable(s)	R^2		Coefficients					Constant
P/E_p	**0.70**	0.16						0.05
P/E_p, i_r/K_s	**0.76**	0.16	-0.32					0.02
P/E_p, i_r/K_s, S_{50}	**0.77**	0.16	-0.46	-0.12				-0.02
P/E_p, i_r/K_s, S_{50}, D_d	**0.87**	0.13	-0.75	-0.46	-0.07			-0.27
P/E_p, i_r/K_s, S_{50}, D_d, α_s	**0.89**	0.13	-0.62	-0.52	-0.08	1.36		-0.26
P/E_p, i_r/K_s, S_{50}, D_d, α_s, R_r	**0.90**	0.15	-0.51	-0.39	-0.07	2.73	-0.59	-0.21

Table 6.7: R/P stepwise regression results for increasing numbers of model variables for runoff ratio prediction. Model coefficients are provided in the order listed in the first column. The regression model constant (y-intercept) is provided in the final column. The horizontal line represents the cut-off below which additional variables do not add statistically significant information to the model.

In order to determine the relevant variables in estimation of the runoff ratio, we begin by looking at the R^2 values for each individual variable. These values are provided in Table 6.6. The R^2 for models with increasing number of variables, together with the coefficients on each variable, are summarized in Table 6.7. Only the first two variables, P/E_p and i_r/K_s, pass the F-test as contributing a significant new amount of information to the regression model. However, inclusion of all of the variables improves the model prediction to explain 90 percent of the variance. The results for both the two-variable and six-variable models are presented in Figures 6-4 and 6-5. The model predictions are compared against the R/P values generated by GSEM.

The climatic wetness is the most significant variable; it represents the moisture available at the surface for runoff or evaporation. The infiltration capacity is related to runoff primarily because of the hydraulic conductivity in the denominator of the index: the soil conductivity governs the rate at which the saturated zone transmits moisture downslope to the saturated areas where it emerges as runoff. The remaining variables primarily capture physical features of the basin such as slope and channel density. The topographic characteristics improve the fit of the regression model, but remain of secondary importance relative to the large role of the climatic wetness.

A similar procedure is followed to determine the regression model for E/E_p. The R^2 values for single variables are summarized in Table 6.8. Of the individual variables, the basin wetness is again of greatest importance. P/E_p is correlated to E/E_p with an R^2 of 0.42. The f value for the significance test of the regression between E/E_p and P/E_p is 5.81, however, which is less than the 5.99 required for statistical significance. Using the variables

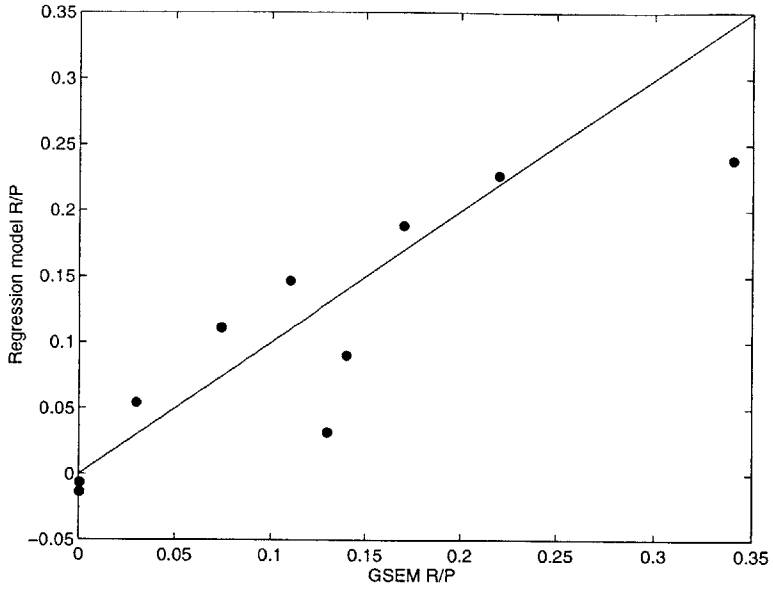

Figure 6-4: Performance of two-variable regression model in R/P prediction. The 1:1 line is plotted for reference.

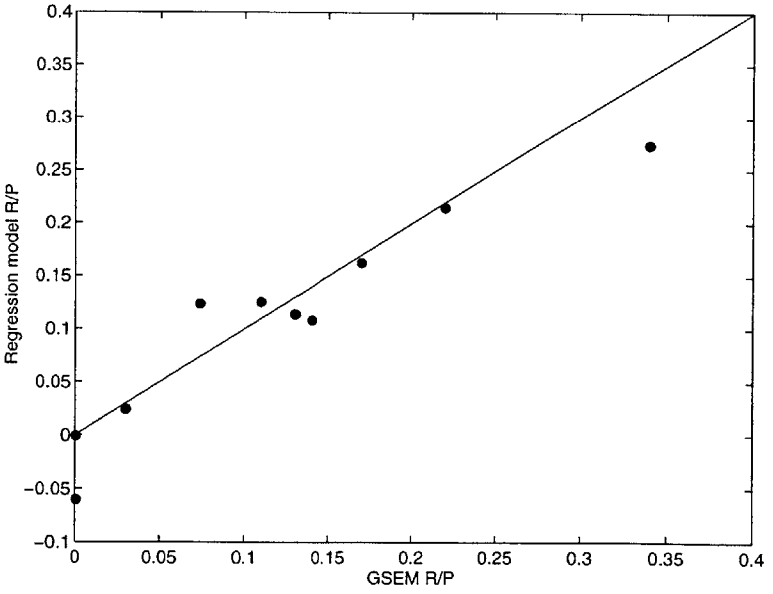

Figure 6-5: Performance of six-variable regression model in R/P prediction. The 1:1 line is plotted for reference.

Variable	R^2
D_d	0.01
R_r	0.19
S_{50}	0.21
α_s	0.25
i_r/K_s	0.25
P/E_p	0.42

Table 6.8: R^2 values between evaporation efficiency and individual basin characteristics.

Variable(s)	R^2		Coefficients					Constant
P/E_p	**0.42**	0.16						0.17
P/E_p, R_r	**0.70**	0.44	-3.37					-0.05
P/E_p, R_r, i_r/K_s	**0.74**	0.43	-2.25	1.06				0.06
P/E_p, R_r, i_r/K_s, α_s	**0.79**	0.50	-4.98	1.52	10.57			0.16
P/E_p, R_r, i_r/K_s, α_s, S_{50}	**0.79**	0.52	-5.95	1.78	12.57	0.30		0.21
P/E_p, R_r, i_r/K_s, α_s, S_{50}, D_d	**0.79**	0.53	-6.44	1.98	13.51	0.57	0.04	0.36

Table 6.9: R/P stepwise regression results for increasing numbers of model variables for evaporation efficiency prediction. Model coefficients are provided in the order listed in the first column. The regression model constant (y-intercept) is provided in the final column.

included in this study, there is no statistically significant regression model for predicting the evaporation efficiency at 95 percent significance.

If we relax the strict requirements for passing the F-test and examine the performance of the regression models for increasing numbers of variables, we find that linear combinations of the six variables can explain up to 79 percent of the variance in the evaporation ratio. The results for the one- to six-variable regression models for evaporation efficiency are summarized in Table 6.9. The one-variable and six-variable models are compared against the GSEM-generated fluxes in Figures 6-6 and 6-7. Although the evaporation efficiency cannot be predicted as reliably as the runoff ratio, the six-variable model brings the predicted values to within twenty percent of the GSEM values. This is a significant improvement over a single-variable model using the climatic wetness, which has errors on the scale of 50 percent.

The evaporation efficiency is more difficult to predict than the runoff ratio due to the pattern in which evaporation varies with water table position. The relationship between evaporation and Z_w is found in Figure 3-8. In the coarse-soiled basins (Bear, Big Creek, Schoharie, Tombstone, and Yreka), evaporation essentially behaves as a step function. When the water table is shallow, evaporation occurs at the climatically-determined potential rate. As the water table deepens, evaporation abruptly drops to a low value. As a result, for a smooth distribution of water table depths, the distribution of evaporative flux tends to be bimodal with very few intermediate values. This pattern makes it difficult to predict the basin-average evaporation rate used in calculating the evaporation efficiency. Despite these limitations, incorporation of multiple basin characteristics allows development of a predictive linear model which can explain nearly 80 percent of the variability in GSEM evaporation values.

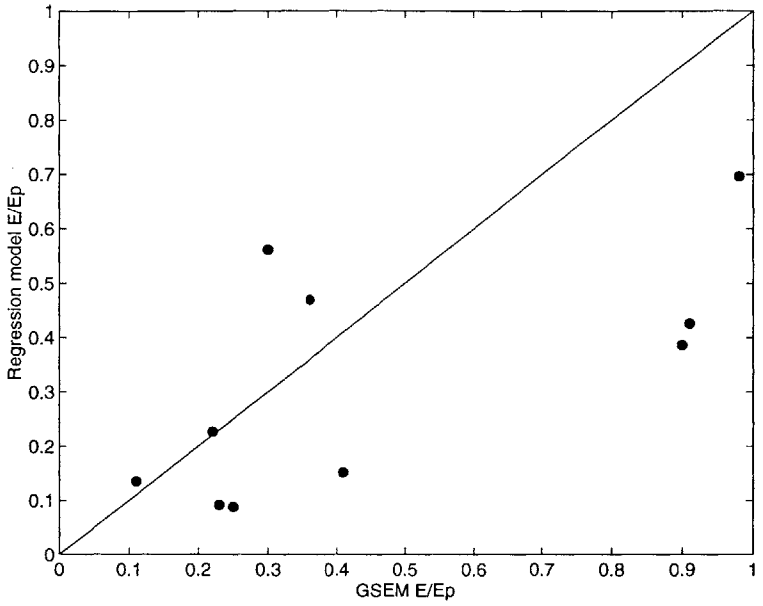

Figure 6-6: Performance of one-variable regression model in E/E_p prediction. The 1:1 line is plotted for reference.

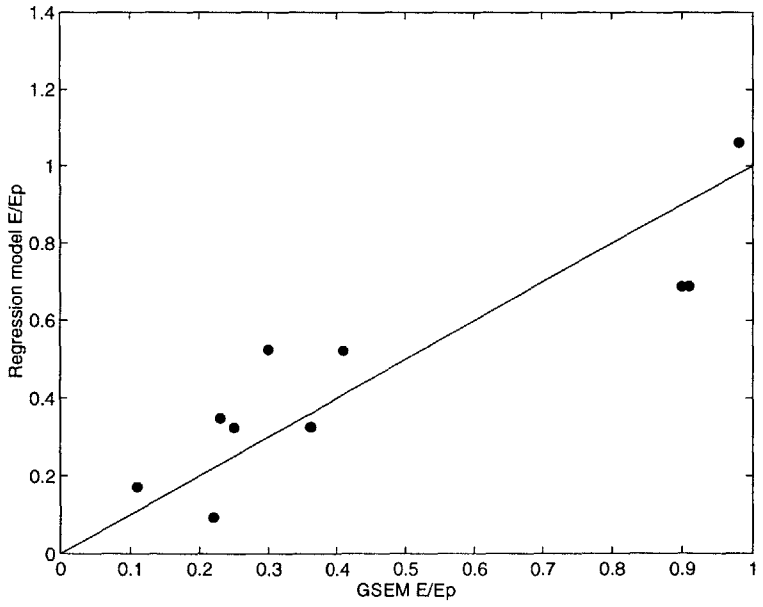

Figure 6-7: Performance of six-variable regression model in E/E_p prediction. The 1:1 line is plotted for reference.

6.4 Summary

In this chapter we have characterized the dominant modes of interbasin variability through principal component analysis. From nine parameters representing the main influences on catchment-scale hydrology, we identify subsets which vary in unison and explain significant amounts of the total variance in the original measured variables. Four components, representing the groundwater efficiency, basin climatic wetness, surface-subsurface coupling, and landscape evolution of ten basins, together explain 80 percent of the variance. Stepwise regression is then performed in an effort to predict the two flux parameters, R/P and E/E_p. The basin wetness and infiltration capacity together predict the runoff ratio with an R^2 of 0.76. A model that uses all six variables improves the fit to an R^2 of 0.90. The same technique fails to achieve a statistically significant model for evaporation efficiency, but a regression model using all six variables is able to achieve an R^2 of 0.79.

In the next chapter, the implications of spatially variable hydrology on the runoff response of basins to individual events are considered. The analysis has thus far focused on the variability in equilibrium hydrology. We now use the equilibrium conditions as the basis for a study of the dynamic response of basins to individual storms and the significance of distributed information in characterizing that response.

Chapter 7

Distributed hydrology and flood response

In the previous chapters, we sought to characterize the spatial variability of equilibrium hydrology both within and between basins. We found that basins in a range of physical environments exhibit similar patterns of subbasin variability. We now turn to the implications of that heterogeneity on floods. This chapter investigates the effect of spatially distributed soil moisture on the runoff response of a basin. We examine how a derived distribution of runoff, based on simple assumptions about storm characteristics and runoff generation, compares to the observed distribution of storm streamflow. From an assumption that saturation excess is the dominant runoff mechanism, cumulative distribution functions are derived for both constant and variable soil moisture. A comparison of the derived and observed probability distributions has several potential benefits, including the following:

- a good fit between observation and derivation could reduce the need for long time series of streamflow for calibration of current operational flood-frequency models, allowing instead the use of a short streamflow record and few climatic parameters to predict flood recurrence intervals; and
- the divergence between the uniform and heterogeneous soil moisture distributions may illuminate the value (or lack thereof) of distributed hydrologic properties for flood forecasting in different basins. This has implications for both modeling and data collection.

The variable-moisture derived distribution predicts runoff at lower probabilities than the uniform-moisture distribution. This is due to the formation of saturated areas in part of the basin; a uniform basin has no runoff until precipitation exceeds the mean available moisture storage capacity. In the comparison of observed and derived distributions, the observed data closely match the variable-moisture curve. This implies that distributed information may be valuable in modeling of runoff response to infrequent events.

7.1 Motivation

A basin's flood response may be characterized by its hydrograph, the response of the basin to a single event; or by the flood-frequency curve, which contains information on long-term recurrence patterns of runoff. The hydrograph provides data on the variation of streamflow

over time during and after a rainstorm. It is a single curve of runoff as a function of time that can be scaled for different depths and durations of precipitation. The hydrograph captures the physical characteristics of a basin that influence the routing of water through it; a dense channel network, for example, is efficient at transporting water from all locations in the basin to the outlet and has a more rapid hydrograph than a low-density basin. Operational hydrology depends on hydrographs for short-term reservoir management. Hydrographs may also be used for model calibration or estimation of base flow characteristics (*e.g.*, Beven and Kirkby 1979).

Whereas the hydrograph characterizes the response of a basin to an individual storm, the flood-frequency curve represents the likelihood of rare flows. Traditional flood-frequency curves are generated from a series of annual maximum flow rates. The flood data are fit to an assumed distribution which can be used to determine the flow rate associated with any recurrence interval of interest. Two commonly used distributions are the Gumbel and Log Pearson Type III; the latter became the standard for U.S. federal agencies in 1967 (Linsley *et al.* 1992). The fitted distributions are often used for flood management: estimation of a flood with a critical recurrence interval (*e.g.*, the 100-year flood) provides a basis for reservoir, drain, and levee design and delineation of flood-prone areas for protection or insurance purposes.

In the following analysis, we use cumulative probability distributions to generate distributions of exceedence probability rather than the standard flood-frequency distributions. We do not use the traditional fitted distributions for several reasons:

- Use of a fitted distribution introduces intrinsic assumptions about the frequency distribution of floods. By using instead the cumulative distribution determined directly from the observed values, we are not forcing a particular extreme value distribution on the basin response.

- We consider total runoff from a storm, not just peak flow rate. The peak flow rate depends both on precipitation and hydrograph shape. Integrating runoff from a single storm removes effects from interbasin differences in hydrograph shape. It also provides us with the potential to look at the runoff ratio (R/P) to assess the distribution of precipitation between runoff, recharge, and other moisture sinks.

- We consider the runoff response to all storms, not just the annual maximum. The distinction between variable- and uniform-moisture flood response arises across a range of storms. Consideration of annual maxima alone would limit our ability to capture the differences between the two antecedent moisture scenarios.

7.2 Relevant literature

Several studies have incorporated landscape characteristics into the derivation or generation of flood-frequency curves. Eagleson (1972) first derived a flood-frequency curve by combining a stochastic rainfall distribution with a constant runoff coefficient. Extensions of Eagleson's approach have focused on relaxing the constraint of a constant runoff coefficient (representing a constant contributing area for all storms) through incorporation of the role of geomorphology in controlling the runoff-contributing area. Approaches have included derivations based on the geomorphologic unit hydrograph (GUH) (Rodríguez-Iturbe and Valdes 1979) and kinematic wave routing. Hebson and Wood (1982) and Diaz-Granados

et al. (1984) derived flood-frequency curves using the GUH approach to route infiltration-excess runoff generated from a stochastic distribution of storms; the difference between the two derivations is the infiltration-excess formulation. Wood and Hebson (1986) generalized the Hebson and Wood (1982) approach into a dimensionless, scale-independent flood-frequency curve. The resulting curves depend on storm characteristics, Strahler stream indices, and soil infiltration capacity alone, allowing their use on ungaged basins. However, the models were shown to be sensitive to the calibrated infiltration parameters and the type of rainfall distribution (Moughamian *et al.* 1987; Raines and Valdes 1994). Moughamian *et al.* (1987) found that both the Hebson and Wood (1982) and Diaz-Granados *et al.* (1984) distributions performed poorly in comparison with flood records from three basins.

Kinematic wave routing is an alternative scheme that does not incorporate characteristics of the stream network. The routing is determined by a parameter representing the celerity of the wave. The kinematic wave approach works best in steep rivers where the ground surface slope and friction are the dominant terms affecting the rate of overland flow (Bras 1990). Studies that have generated flood-frequency distributions using this routing technique include Eagleson (1972), Shen *et al.* (1990), and Cadavid *et al.* (1991). Both the derivations using the GUII and kinematic waves have been characterized by a focus on infiltration-excess as the main runoff mechanism and homogeneous rainfall and antecedent moisture.

Recent efforts have focused on incorporating more complex models of effective rainfall and runoff generation. Sivapalan *et al.* (1990) expanded on the GUH-based dimensionless flood-frequency derived distribution of Wood and Hebson (1986) by coupling it to a runoff generation model described by Sivapalan *et al.* (1987). The runoff model assumes saturation-excess runoff occurs over some variable contributing area determined by the value of a topographic-soil index (a variant on the original TOPMODEL index). The sensitivity of the flood-frequency response to the model's dimensionless similarity parameters was examined, but no comparison to empirical measurements was provided.

An alternative approach to generating a runoff response curve was presented by Beven (1987). Similarly to Sivapalan *et al.* (1987), a topographic index is used to predict saturation-excess runoff. Instead of using the GUH, however, Beven assumed a stochastic distribution of rainfall and initial conditions similar to those in Eagleson (1972). The distribution of storms with a maximum flow rate above some threshold is generated via a Monte Carlo simulation. The approach adequately reproduced a flood-frequency curve for the Wye catchment in Wales. Blazkova and Beven (1997) modified the stochastic rainfall distribution to incorporate the high intensity events found at their study sites in the mountains of the Czech Republic. They created separate probability distributions for low- and high-intensity events which are interspersed according to the relative distribution of interstorm periods. The resulting rainfall distribution was used in a continuous TOPMODEL run to generate flood-frequency curves for three basins. The simulated curves matched the limited flood-frequency data available for the catchments reasonably well.

Lamb (1999) similarly used a continuous model run to generate a probability distribution of runoff. He employed a conceptual rainfall-runoff model with an assumed distribution of antecedent soil moisture. The peaks-over-threshold technique was used to fit flood-frequency distributions to the observed and simulated time series of runoff. Application to 40 catchments in Great Britain revealed that the simulation of peak flows is more important in flood-frequency analysis than matching either lower-magnitude flows or hydrograph shape.

7.3 Estimation of runoff distributions

In this section we use the assumed exponential distributions of storm intensity and duration to derive the cumulative probability distributions for runoff depth, given infiltration-excess and saturation-excess as the generation mechanisms. The derivation is based on that of Eagleson (1978e) with modifications for a finite soil column described by Salvucci (1994).

The depth of rainfall that falls during a single storm is the product of precipitation intensity i_r and storm duration t_r. A soil column saturates when the amount of rainfall equals the antecedent soil moisture deficit in the soil, $\forall_e$; any precipitation that occurs after the soil has saturated is routed overland as saturation-excess runoff. Infiltration-excess runoff occurs before the soil saturates when the rainfall intensity exceeds the infiltration capacity of the soil. The lateral redistribution of moisture between soil columns is assumed to be negligible over the time scale of a single storm.

Our goal is to obtain the probability that a given runoff depth is exceeded. In order to get the exceedence probability, we calculate the cumulative distribution function (CDF) of runoff; the exceedence probability is equal to one minus the CDF. This gives the probability that runoff exceeds a specified value in any individual storm. The distribution of runoff can be derived by integrating the joint probability density function of storm intensity and duration. The general form, which may be used for either infiltration-excess or saturation-excess runoff, is given as:

$$F_R(r) = \int\int f(i_r, t_r) di_r dt_r \tag{7.1}$$

The distributions of i_r and t_r are assumed to be independent and exponential (Eagleson 1978a). This gives the following expression for the cumulative distribution function of runoff,

$$F_R(r) = \int\int \alpha\delta e^{-\alpha i_r - \delta t_r} di_r dt_r \tag{7.2}$$

in which α is the inverse mean of storm intensity and δ is the inverse mean of storm duration. Equation 7.2 can be used to derive the distribution of either infiltration-excess or saturation-excess runoff; the difference between the two runoff mechanisms is in the limits of integration.

7.3.1 Derived distribution of infiltration-excess runoff

Under most conditions, the soil is able to absorb the precipitation at its input rate at the beginning of a storm. Eventually, as the soil moisture increases, the infiltration capacity is reduced so that it is less than the precipitation intensity and water begins to collect at the surface. This time is referred to as the time to ponding, t_p, and corresponds to the onset of infiltration-excess runoff. Runoff continues until either the storm ends or the soil saturates at time t_s. Once the soil has saturated, saturation-excess becomes the dominant mechanism for runoff generation for the duration of the storm. The use of t_s as the upper limit for the storm duration marks the difference between this and the Eagleson derivation, which assumed an infinite soil column and therefore never saturated.

Infiltration-excess runoff is the surplus of intensity over the soil-determined infiltration capacity. Using the Philip equation for infiltration, runoff is expressed as

$$R_{ie} = \int_{t_o}^{t_r} (i_r - f_i^*)dt = (i - A_o)t_r - S_i \left(\frac{t_r}{2}\right)^{\frac{1}{2}} \tag{7.3}$$

where f_i^* is the infiltration capacity, A_o is a gravitational constant from the Philips equation, and S_i is the infiltration sorptivity. When calculating the cumulative probability that $R \leq r$, the upper limit of intensity is defined by the maximum infiltration rate where $R = r$. The probability can be determined by rewriting Equation 7.3 in terms of i_{rmax},

$$i_{rmax} = \frac{r}{t_r} + \frac{S_i}{\sqrt{2t_r}} + A_o \tag{7.4}$$

This results in the following equation for the cumulative probability distribution of infiltration-excess runoff:

$$F_R(r) = \int_{t_p}^{t_s} \delta e^{-\delta t_r} \left[\int_0^{r/t_r + S_i/\sqrt{2t_r} + A_o} \alpha e^{-\alpha i_r} di_r \right] dt_r \tag{7.5}$$

We integrate over the range of intensities and write the time integral in terms of $\tau = t - t_p$; this reduces the equation to

$$\mathbf{P}[R_{ie} \geq r] = 1 - F_R(r) = \delta e^{-\alpha A_o} \int_0^{\tau_s} e^{-(\delta\tau + \alpha r/\tau + \alpha S_i/\sqrt{2\tau})} d\tau \tag{7.6}$$

No exact solution exists for an integral of the form

$$I^* = \int_0^C e^{-(a/x + bx + c/\sqrt{x})} dx \tag{7.7}$$

so the integral in Equation 7.6 must be integrated numerically. Storms that result in infiltration-excess runoff are characterized by high rainfall intensities, since runoff is only generated when intensity exceeds the soil infiltration capacity. We assume that the actual infiltration rate will be mostly soil-controlled because of the high rainfall intensity. Ponding time will therefore be small, and the limiting time to saturation can be estimated as the length of time necessary for infiltration infiltration at capacity to fill up the available storage (Salvucci 1994):

$$\forall_e = \int_0^{t_s^*} f_i^*(t)dt \tag{7.8}$$

Solving and inverting the integral, we get a limiting time to saturation of

$$t_s^* = \begin{cases} \left(\sqrt{\frac{S_i^2}{4A_o^2} + \frac{\forall_e}{A_o}} - \frac{S_i}{2A_o} \right)^2 & A_o > 0 \\ \left(\frac{\forall_e}{S_i} \right)^2 & A_o = 0 \end{cases} \tag{7.9}$$

It is now possible to numerically integrate Equation 7.7 up to its upper limit t_s^*. The integrated value can be substituted into Equation 7.6 to calculate the cumulative probability that infiltration-excess runoff is greater than or equal to a specified depth r.

7.3.2 Derived distribution of saturation-excess runoff

Uniform antecedent soil moisture

For calculation of saturation-excess runoff, the relevant time over which to integrate is from time to saturation t_s until the end of the storm t_r. For a storm with a given depth of rainfall, intensity and duration are interdependent. The constraints on the time window of integration may therefore be expressed as limits on the rainfall intensity. The Poisson model of independent storm events assumes a constant rainfall rate over the duration of a storm (Eagleson 1978a). This gives a storm intensity equal to rainfall depth divided by storm duration. In order to obtain the upper boundary of integration for i_r, we consider the rainfall intensity which corresponds to a runoff depth of r. This maximum intensity occurs when the total rainfall fills the soil column (a depth of $\forall_e$) and has a depth of r remaining as saturation excess; it can be expressed as

$$i_{rmax} = \frac{r + \forall_e}{t_r} \tag{7.10}$$

Once the storm intensity has been bounded for the desired runoff, there is no limit on storm duration. Equation 7.2 can thus be expressed with limits as

$$F_R(r) = \alpha\delta \int_0^{\infty} \int_0^{\frac{r+\forall_e}{t_r}} e^{-\alpha i_r - \delta t_r} \, di_r dt_r \tag{7.11}$$

We first integrate with respect to i_r to get

$$F_R(r) = -\delta \int_0^{\infty} e^{-\left(\delta t_r + \alpha\left(\frac{r+\forall_e}{t_r}\right)\right)} dt_r \tag{7.12}$$

The integral of the form

$$I^* = \int_0^{\infty} e^{-|ax + b/x|} dx \tag{7.13}$$

has an exact solution, given by Gradshteyn and Ryzhik (1965) as

$$I^* = 2\sqrt{b/a} \cdot \mathrm{K}_1\left[2\sqrt{ab}\right] \tag{7.14}$$

where $\mathrm{K}_n[\cdot]$ is the modified Bessel function of order n. The final solution for the cumulative distribution of saturation-excess runoff can then be expressed as

$$F_R(r) = -2\sqrt{\alpha\delta\,(r + \forall_e)} \cdot \mathrm{K}_1\left[2\sqrt{\alpha\delta\,(r + \forall_e)}\right] \tag{7.15}$$

Variable antecedent soil moisture

Equation 7.15 is applicable for a single value of antecedent soil moisture. To generate basin-scale runoff, each location in the basin is treated as an equal-sized bucket. Runoff either occurs nowhere or universally throughout the basin. Observations have shown, however, that runoff is often generated over only a fraction of the basin area (*e.g.*, Dunne and Black 1970a, 1970b). It is possible to derive a related distribution for runoff over a variable-moisture field by considering the marginal distribution of runoff dependent on soil moisture in conjunction with a soil moisture distribution:

$$f_R(r) = \int_0^{\max(\forall_e)} f_R(r|\forall_e) \cdot f_{\forall e}(\forall_e) \cdot d\forall_e \tag{7.16}$$

By definition, the marginal distribution can be used only with the probability density function (PDF), not the cumulative distribution. We derive the PDF of runoff by differentiating Equation 7.15 with respect to runoff:

$$\begin{aligned} f_R(r|\forall_e) &= \frac{d}{dr} F_R(r) && (7.17)\\ &= \frac{d}{dr}\left(-\gamma \cdot \mathrm{K}_1[\gamma]\right) && (7.18)\\ &= -\alpha\delta\left(\mathrm{K}_1[\gamma] - 2\mathrm{K}_0[\gamma] - \frac{2}{\gamma}\mathrm{K}_1[\gamma]\right) && (7.19) \end{aligned}$$

where

$$\gamma = 2\sqrt{\alpha\delta\,(r + \forall_e)} \tag{7.20}$$

The probability distribution of available soil moisture storage, $f_{\forall e}(\forall_e)$, is determined from the spatial distribution of equilibrium values generated by the model. Equation 7.16 is integrated numerically over the range of possible available soil moisture storage for each value of runoff. The maximum storage capacity is the total available pore space in the entire soil column, which is equal to the product of porosity and soil column depth. To derive the CDF, the PDF is integrated for all runoff values less than or equal to a maximum value r:

$$F_R(r) = -\alpha\delta \int_0^r \int_0^{\max(\forall_e)} \left(\mathrm{K}_1[\gamma] - 2\mathrm{K}_0[\gamma] - \frac{2}{\gamma}\mathrm{K}_1[\gamma]\right) f_{\forall e}(\forall_e) d\forall_e dr \tag{7.21}$$

The exceedence probability is then calculated as one minus the cumulative probability $F_R(r)$.

7.3.3 Distribution of observed storm runoff

Exceedence probability distributions can also be obtained from continuous observed records of precipitation and streamflow. The process of transforming a continuous time series into a set of independent events involves two main steps: isolation of independent rainstorms and determination of the streamflow associated with each storm. Figures 7-1 and 7-2 contain sample time series of precipitation and streamflow for the Brushy and Schoharie basins. Streamflow is continuous, and there is evidence of a time delay between the end of rainfall and the return of the streamflow to its pre-storm volume. Once the storms have been isolated, we differentiate between the streamflow caused by the storm and the background flow which is independent of precipitation (base flow); this is necessary because the derived distributions of runoff do not incorporate base flow. Below we describe the process of isolating independent events and separating base flow from storm runoff.

Isolation of independent precipitation events

A major challenge in separating storms is deciding whether breaks in precipitation signify the end of a storm or simply a pause in a single event. We isolate independent storms

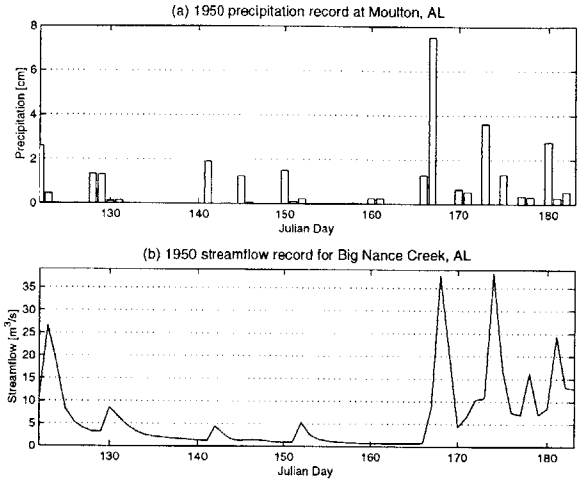

Figure 7-1: Time series of precipitation and streamflow, Brushy, AL.

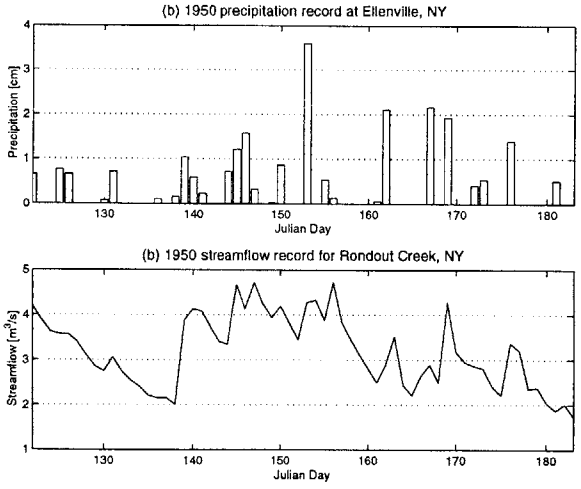

Figure 7-2: Time series of precipitation and streamflow, Schoharie, NY.

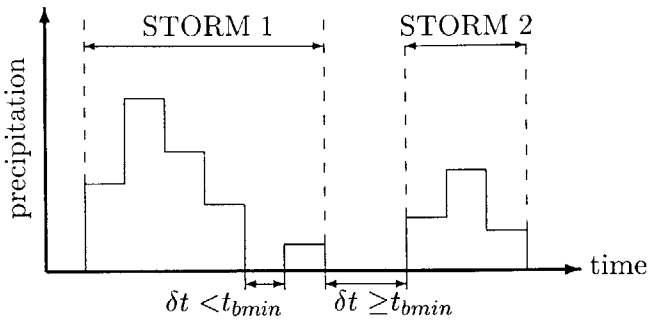

Figure 7-3: Schematic of technique using t_{bmin} to isolate independent storms from precipitation record.

based upon a minimum interstorm time, t_{bmin}. Periods of rain separated by dry periods of length less than t_{bmin} are considered part of the same storm; rain occurring after any interval longer than t_{bmin} represents a new storm. Figure 7-3 shows how t_{bmin} is used to separate the precipitation time series into discrete events.

The Poisson model used to parameterize precipitation assumes that both the interstorm duration t_b and the storm duration t_r are exponentially distributed. We select t_{bmin} such that the distributions of storm and interstorm durations are close to exponential (Restrepo-Posada and Eagleson 1982). This is done by dividing a precipitation time series into a set of storms using a range of values for t_{bmin}. We calculate the probability distributions of both t_b and t_r and look for similarity to an exponential distribution. While many storms occur on time scales of hours rather than days, we are limited in this study to daily values; there arises, therefore, the potential for some error in the distinction of individual storms. A more rigorous technique of estimating t_{bmin}, used to validate our values, is described below.

Wynn (1994) compared two methods of estimating t_{bmin} from hourly precipitation data. The first method is based on the assumption that the interstorm duration is exponentially distributed. The value of t_{bmin} which corresponds to the assumed distribution will be that for which the coefficient of variation of all interstorm durations greater than t_{bmin} is equal to one. An alternative approach identifies t_{bmin} from the graphical breakpoint in the cumulative probability distribution. This technique is based on the hypothesis that interstorm durations are described by two distinct patterns: durations greater than t_{bmin} are exponentially distributed, while shorter durations (corresponding to arbitrary dry periods during a storm) are characterized by some other, unknown distribution. Both approaches have some limitations. The coefficient of variation method assumes instantaneous, non-overlapping storm events and a small ratio between the average storm and interstorm durations. Error in the breakpoint method arises from the presence of extreme values which may skew the regression analysis used in determining the breakpoint between the distributions. For our purposes, however, the techniques are sufficient to use as a check that our selected value of t_{bmin} is no smaller than the range of values estimated at the location of interest. It is acceptable to have a value of t_{bmin} that is larger than the actual value; however, if our t_{bmin} were too small and we were separating single events into multiple, independent storms, significant errors could arise in the analysis. In neither method does Wynn (1994) find t_{bmin} in Alabama or New York to be greater than 24 hours; we conclude that any value of t_{bmin} one day or longer is acceptable for this analysis.

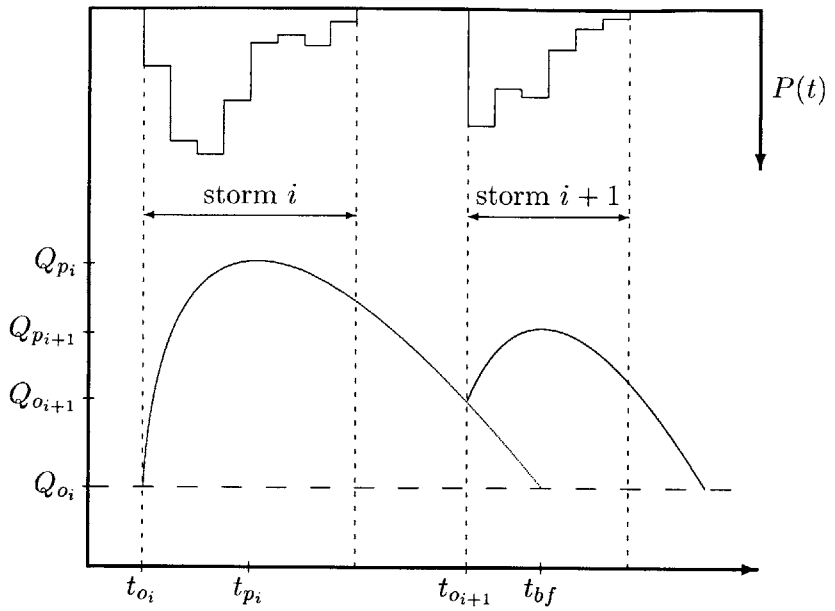

Figure 7-4: Schematic of technique to isolate runoff associated with independent rainstorms.

Isolation of related independent streamflow events

The identification of the streamflow response associated with a given storm is more complicated than the isolation of precipitation events because of the delayed nature of rainfall-runoff response. There is a time lag between the time when precipitation falls on a basin and when it reaches the outlet through the channel network. Runoff may be caused by a storm even after rain has stopped. The streamflow recession curve is often assumed to decay exponentially with time, according to the equation

$$Q_i(t) = Q_{p_i} d^{-\mu t} \tag{7.22}$$

where $Q_i(t)$ is the streamflow of storm i at time t, μ is an empirical decay parameter, and Q_{p_i} is the peak flow at the beginning of the recession curve (Nathan and McMahon 1990; Tallaksen 1995). We cannot assume that the entire river flow associated with a given storm has passed through the outlet by the end of the storm and subsequent interstorm period. Some storms may influence streamflow volumes for many days after the next storm has begun. We use the known form of the recession curve to attribute delayed flow to its causal storm.

A schematic of a segment from a streamflow record is presented in Figure 7-4. The calculation of the total runoff associated with storm i illustrates how the recession curve form is used. First, the observed streamflow values during the storm and subsequent interstorm period are numerically integrated (*i.e.*, from t_{o_i} to $t_{o_{i+1}}$). During this time, we assume that precipitation from storm i is the only source of storm runoff. After the onset of storm $i+1$, streamflow may be caused by either the new or the previous storm or storms. The temporal extent of the recession curve is governed by the time it takes for water to be routed from the most upstream pixel to the basin outlet. To account for this persistence of storm-related streamflow beyond the bounds of an individual storm, we use Equation 7.22 to analytically integrate the extra flow contribution after the onset of the subsequent storm.

We assume that the exponential decline of the recession curve begins at the peak streamflow Q_{p_i} during the storm or subsequent interstorm period. If the storm is very short, its peak flow may occur after rainfall has stopped. We calculate the exponential decay parameter μ between the peak flow and the flow at the onset of the next event, $Q_{o_{i+1}}$:

$$\mu = \frac{\ln\left(Q_{o_{i+1}}/Q_{p_i}\right)}{t_{o_{i+1}} - t_{p_i}} \tag{7.23}$$

The recession curve associated with storm i is assumed to decay at the calculated rate until t_{bf}, the time when the flow either reaches the minimum observed base flow or zero (if temporally variable base flow has already been removed), or a maximum of 20 days. The total streamflow is found by integrating Equation 7.22 from the onset of storm $i+1$ to t_{bf}:

$$Q_{E_i} = \frac{Q_{o_{i+1}}}{\mu}\left(\exp\left[\mu(t_{bf} - t_{o_{i+1}})\right] - 1\right) \tag{7.24}$$

The excess streamflow Q_{E_i} is then added to the integrated depth for storm i and subtracted from storm $i+1$. One potential source of error is that μ is calculated using observed flow values that are not adjusted for lagged flow contributed from prior storms. However, as the time from the storm increases, the change in flow with time will decrease and the effect on the decay parameter should be negligible. Another potential source of uncertainty is introduced in the separation of streamflow into storm-related runoff and base flow. Several techniques which may be used to segregate observed streamflow records are described in Appendix E; the implications for runoff are discussed in the following section.

7.4 Base flow separation

Appendix E discusses different techniques for separating slow-response base flow from rapid-response storm runoff. These include a constant base flow, moving minima, smoothed minima, and digital filter. As seen in Table E.1, base flow may be a significant fraction of the total streamflow; its separation is therefore crucial in hydrologic analysis of flood characteristics. Below we present two simple tests of the sensitivity of runoff and runoff elasticity to the technique of base flow separation.

Figure 7-5 examines the effect of the base flow separation technique on the runoff response of individual storms. We select the smoothed minima method as our reference point because it is least sensitive to parameter calibration. The smoothed minima approach is compared with the moving minima technique with two window widths (10 and 30 days) and the digital filter technique. The curves represent the average runoff generated by rainstorms with a precipitation depth within a few-centimeter range. The vertical lines represent one standard deviation above and below the average runoff in each bin from the smoothed minima technique. While there exists some systematic difference between the different methods for separating base flow from storm runoff, the pattern of runoff versus precipitation is the same, and the rejected techniques all fall within the variability of storm response over the time series calculated by the selected method.

An alternative technique for assessing the model sensitivity to the method of base flow separation is to consider the elasticity of runoff response. Risbey and Entekhabi (1996) observed that the Sacramento River basin in California exhibited a nonlinear streamflow response to precipitation. In wet years, streamflow increased nonlinearly with increasing precipitation. Correspondingly, there was a weakly nonlinear response when several dry

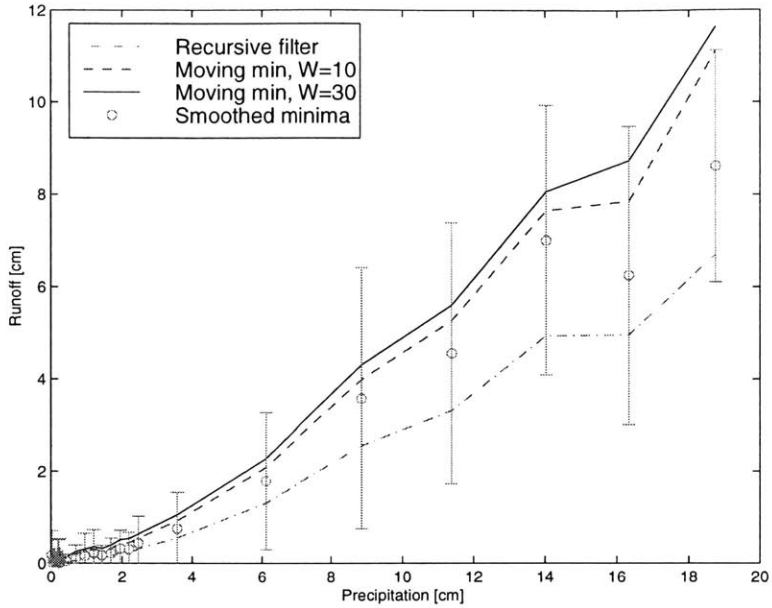

Figure 7-5: Sensitivity of storm runoff response to base flow separation technique for Brushy streamflow record.

years occurred in succession. The behavior was quantified by considering the elasticity of runoff above unity as a function of precipitation. The elasticity of runoff is equal to

$$\text{elasticity} = e = \frac{P}{R} \cdot \frac{dR}{dP} \tag{7.25}$$

For any storm, runoff R is equal to some fraction r of precipitation P. If the runoff fraction is constant ($r = \bar{r}$), the elasticity equals unity. The calculation of elasticity above unity ($e - 1$) therefore gives the departure of runoff from the mean runoff fraction $\bar{r}$.

We calculate the elasticity of runoff for different base flow techniques to see whether the runoff ratio exhibits similar behavior independent of base flow separation technique. Figures 7-6 through 7-9 show the elasticity above unity plotted against normalized storm precipitation depth for the four techniques.

The value $e - 1$ may also be interpreted as the percentage change in runoff minus the percentage change in precipitation. The line where this value equals zero shown in Figures 7-6 through 7-9 represents a linear relationship between precipitation and runoff. Negative values indicate a weak nonlinear relationship: changes in precipitation are not fully reflected in runoff depths. Positive values of $e - 1$ indicate a strong response whereby changes in runoff exceed changes in precipitation. This corresponds to a range of storms in which the saturated area is growing rapidly. The elasticity asymptotes to zero for the largest storms. Since base flow has been removed from these runoff series, only rapid-response fluxes (infiltration-excess and saturation-excess runoff) are included. Once the soil is saturated or has a reached a level where an increase in the saturated area is topographically unlikely, the runoff volume is constrained to equal the incident precipitation.

The streamflow elasticity behaves similarly for each of the four techniques. This provides further evidence that the selection of the smoothed minima technique over other possible approaches does not significantly bias the character of observed runoff response.

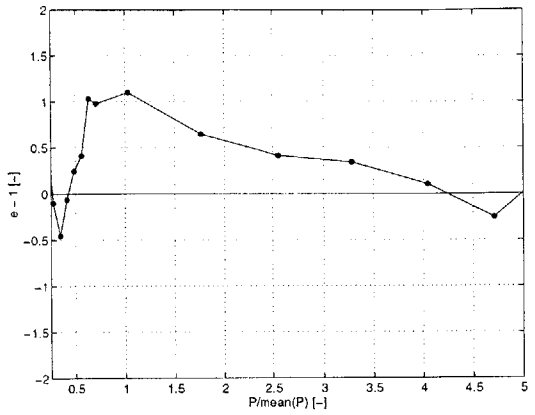

Figure 7-6: Elasticity of runoff above unity for filtered base flow separation, Brushy, AL.

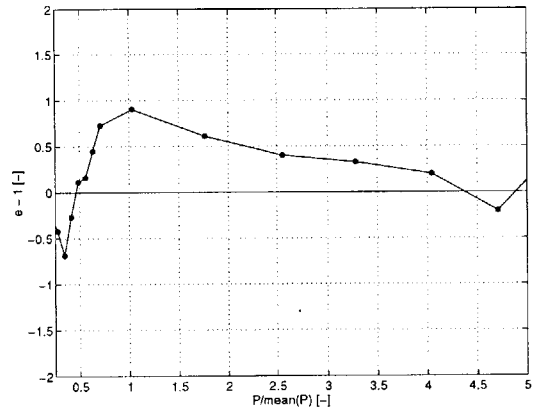

Figure 7-7: Elasticity of runoff above unity for moving minima (W=10) base flow separation, Brushy, AL.

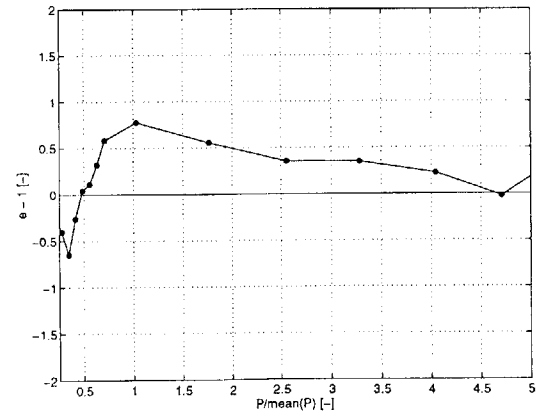

Figure 7-8: Elasticity of runoff above unity for moving minima (W=30) base flow separation, Brushy, AL.

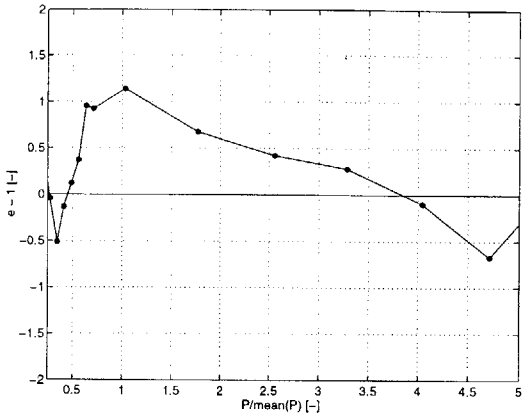

Figure 7-9: Elasticity of runoff above unity for smoothed minima base flow separation, Brushy, AL.

7.5 Results

7.5.1 Comparison of derived distributions

The derived distribution of infiltration-excess runoff predicts a negligible likelihood of any measurable runoff ($\leq$ 1 mm) for all of the study basins. This is probably due to the assumption that rainfall is distributed uniformly throughout a storm. Infiltration-excess runoff occurs only when the rainfall occurs at a higher intensity than the soil infiltration capacity. However, by distributing incident precipitation over the entire storm duration, the intensity is relatively low even during larger storms. Consequently, the probability of even 1 mm of infiltration-excess runoff does not exceed 10^{-10} in any basin. In the remainder of this chapter, any discussion of derived or modeled runoff refers to saturation-excess runoff only.

Equation 7.15 relates the probability of runoff to three basin-specific variables: available storage ($\forall_e$) and the product of the inverse mean precipitation intensity (α) and duration (δ). The available storage contains information about both soil and climate, so it is not redundant with the storm parameters. We look first at the cumulative distribution curves for saturation-excess runoff assuming uniform soil moisture, shown in Figure 7-10. Six basins are selected from the initial set of ten because they fully illustrate the role of distributed soil moisture on runoff response within a reasonable range of probabilities. The two relevant attributes of the curves in Figure 7-10 are the slope and the exceedence probability at which runoff first occurs. The onset of runoff is a function of both climate and soil, as represented by the antecedent available storage. Brushy has relatively little available storage; storms with a probability near 0.001 are likely to generate runoff. Big Creek has over 30 cm available storage, resulting in low levels of runoff in only the most extreme storms. The runoff generated in relatively frequent storms depends primarily on the climate and soil characteristics that together determine the equilibrium moisture deficit in the soil column.

Once runoff has been initiated, the major influence on the slope of the runoff probability curve transitions from the antecedent soil-climate combination to storm characteristics alone. The transition can be identified by comparing the responses of different basins.

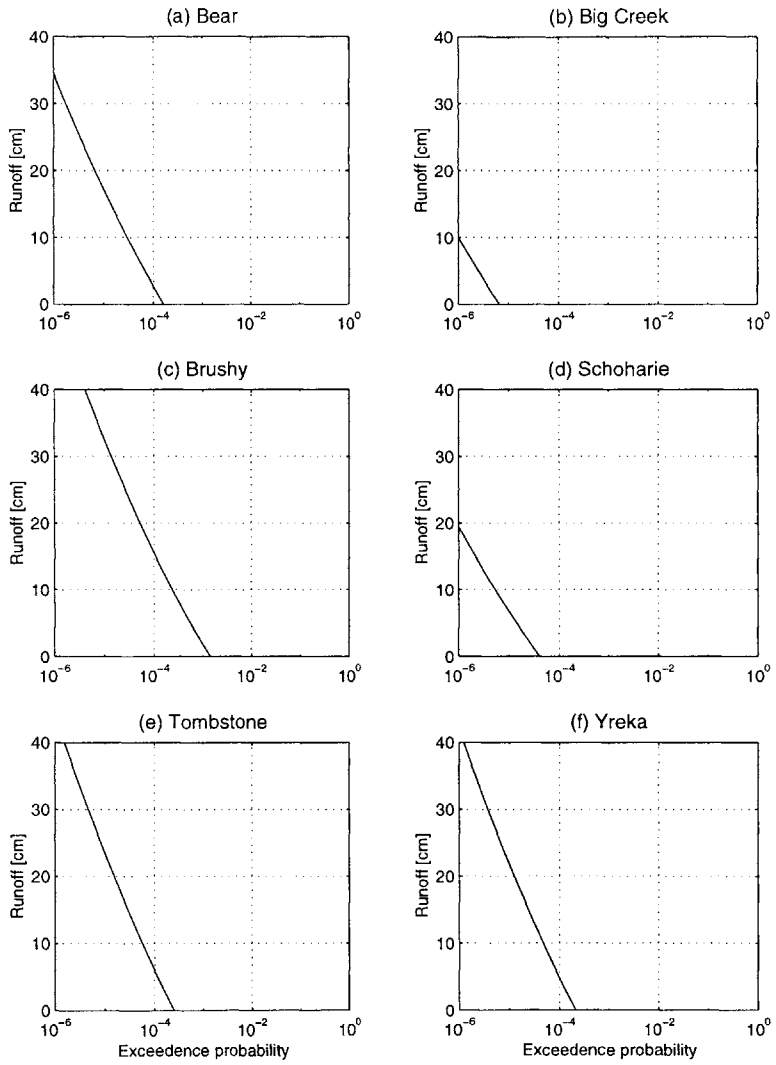

Figure 7-10: Derived exceedence probability distribution of saturation-excess runoff for six study basins, assuming uniform soil moisture equal to the basin average. Exceedence probability is on a per-storm basis.

Schoharie and Yreka represent two basins with similar x-intercepts and different slopes. In both basins, runoff begins in storms with a probability around 10^{-4}. In Schoharie, the runoff depth increases to approximately 20 cm over the plotted probability range. Runoff in Yreka increases to greater than 40 cm over the same range. The storm characteristics are the main reason for the discrepancy: the product of α and δ in Schoharie is over 50 percent larger than in Yreka. A climate with larger average storms (a low value of $\alpha\delta$) results in a greater slope in the cumulative distribution of runoff.

Uniform versus variable soil moisture

The preceding chapters of this thesis have identified patterns in the spatial variability of equilibrium soil moisture. We are interested here in the influence of that spatial structure of surface soil moisture on the runoff response, *i.e.*, the signature of distributed hydrologic properties in basin-aggregated streamflow. A basin is treated as an assemblage of adjacent buckets. Since lateral subsurface flow is assumed to be insignificant on the time scale of a single storm, the buckets are independent; moisture enters and exits each bucket only at the soil surface. Each bucket has a given depth, with the depth representing the available soil moisture storage prior to a storm.

In the uniform moisture scenario, each bucket has the same depth. If the depth of precipitation that occurs during the storm is less than the buckets' storage capacity, the input moisture enters storage and no runoff occurs. If precipitation exceeds the buckets' capacity, the excess precipitation becomes runoff. The transition between storage and runoff occurs simultaneously throughout the basin, since the buckets all have identical capacity.

In distributed systems, the buckets have different capacities. In areas where the water table is near the surface, the depth of available storage is small, whereas areas with a deep water table have a much larger potential to store new moisture. In this distributed system, the abrupt onset of basin-wide runoff, seen in the uniform moisture system when precipitation equals the storage capacity, will not occur. Instead, runoff will be initiated at an increasing number of buckets as precipitation increases. For low precipitation depths, then, variable-moisture runoff exceeds uniform-moisture runoff. Correspondingly, when rainfall is heavy, the entire basin in the uniform-moisture scenario will be contributing overland flow, while the driest areas of the variable-moisture basin may not yet be saturated. Only for the most extreme storms is the effect of the antecedent moisture conditions completely erased and the two curves converge.

The difference in the available moisture storage between the uniform and variable scenarios is illustrated in Figure 7-11. The figure shows the cumulative distribution functions for available storage for the two soil moisture cases. Saturation-excess runoff occurs when precipitation exceeds the available storage. When the rainfall depth is less than the mean available storage, the saturated area is greater in the variable-moisture scenario than in the uniform-moisture scenario. For rainfall amounts greater than the mean available storage, the uniform-moisture scenario has a higher percentage of saturated area (100%) than the variable-moisture scenario until both basins are fully saturated. Thus, we expect that the runoff from a heterogeneous soil moisture field will be larger than the uniform-moisture case for small rainfall events and smaller than the uniform-moisture case when the storm depth is large.

Figure 7-12 presents the cumulative distribution functions of saturation-excess runoff for the cases of uniform and spatially variable soil moisture. In three of the six basins, the uniform and variable curves intersect, as would be expected from the above explanation.

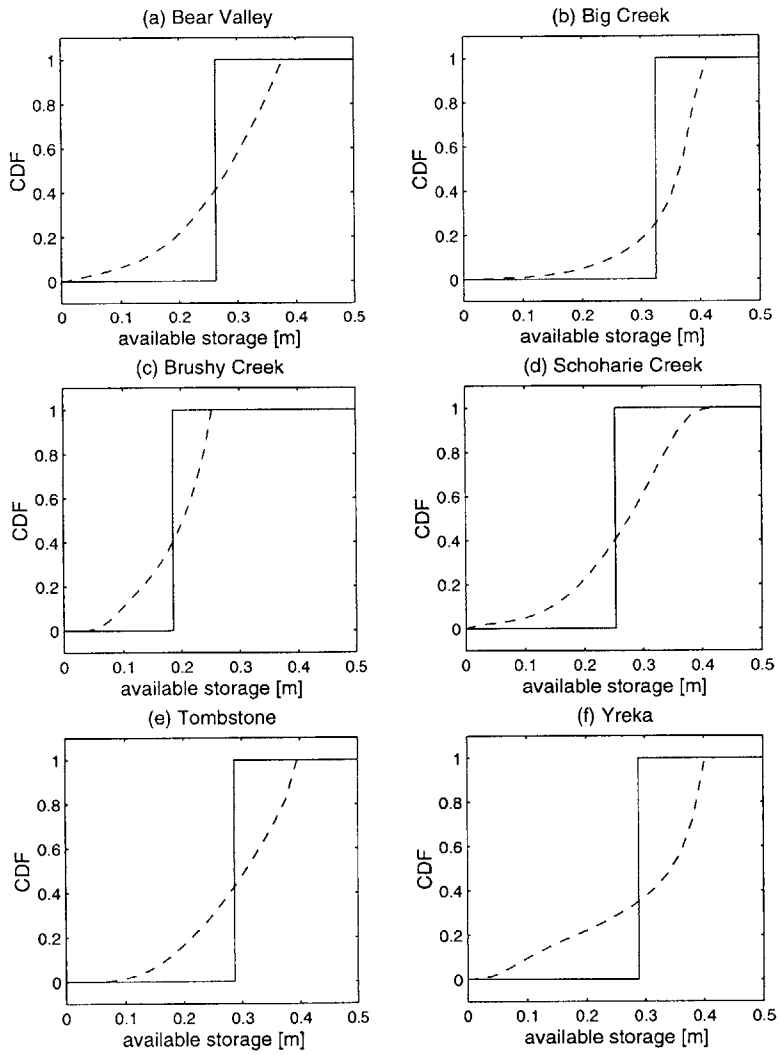

Figure 7-11: Cumulative distribution functions of antecedent soil moisture, uniform (solid line) and variable (dashed line) moisture scenarios.

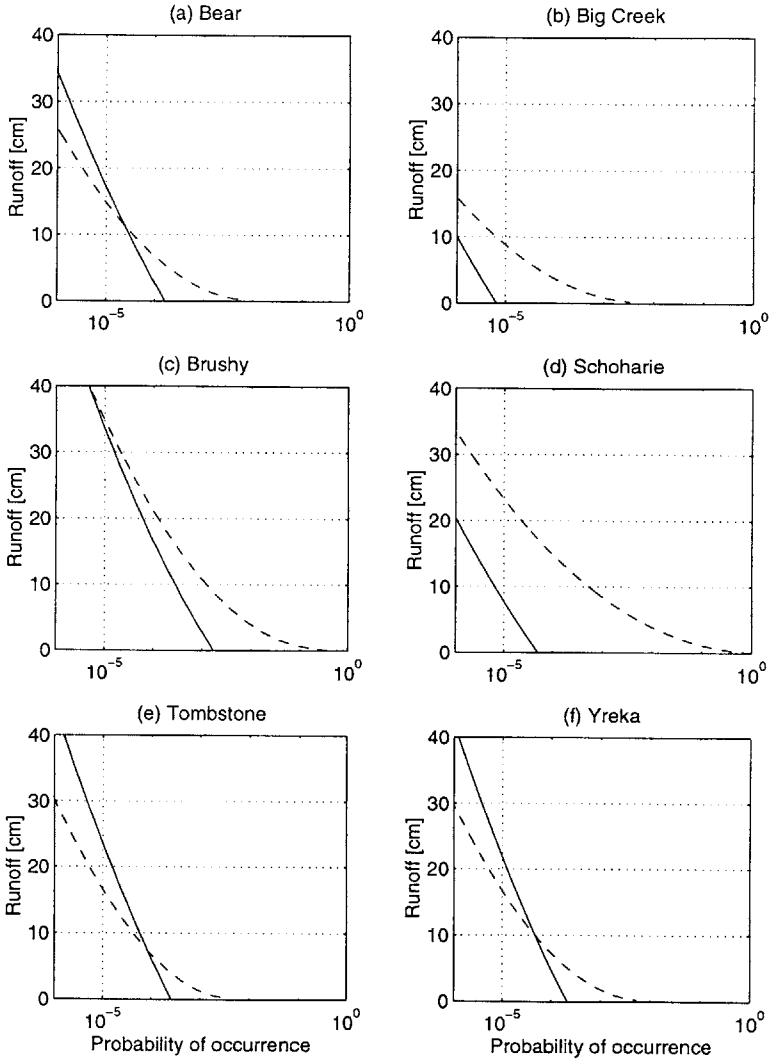

Figure 7-12: Comparison of variable (dashed line) and uniform (solid line) soil moisture in the derived distribution of saturation-excess runoff, for six basins. Exceedence probability is on a per-storm basis.

In the other basins, however, the intersection point is outside the plotted domain. In Big Creek, this is due to a large range in antecedent soil moisture caused by the steep landscape coupled to a fairly dry climate. There is a much greater likelihood of runoff occurring in some of the moister pixels in the distributed system than in the homogeneous environment. The curves intersect at an extremely low exceedence probability. In Brushy and Schoharie, the pattern is more influenced by the moist climate and relatively low change in precipitation with probability.

The significance of distributed soil moisture on the runoff response depends on the use of the information. For river management on small time scales, such as consideration of low flows for ecological health and fish survival, the response of basins to relatively small events is important. Estimates based on uniform moisture would underestimate the runoff resulting from the most common storms. If, however, the hydrologic information is needed for prevention of damage from extreme flood events, the response at low exceedence probabilities is of greater concern. The uniform-moisture case tends to overpredict runoff in the most extreme events (precipitation greater than the mean available storage). The effect of any difference between uniform and distributed moisture assumptions in runoff estimation depends on what recurrence interval of storms is of greatest concern.

Variable contributing area

The effect of distributed antecedent soil moisture on runoff may also be seen by considering the variable contributing area for different magnitude storms. The area of the basin which saturates during a given storm is the main source of rapid-response runoff through saturation-excess overland flow.

We investigate the expansion of saturated areas with storm magnitude by considering rainfall depths with differing probabilities of occurrence. After Eagleson (1978b), storm depth is assumed to follow a gamma distribution,

$$f_H(h) = \frac{\lambda(\lambda h)^{\kappa-1}\exp(-\lambda h)}{\Gamma[k]} \tag{7.26}$$

with storm depth h, shape parameter λ, and scale parameter κ. We can determine the values of the two parameters from the observation-based Poisson parameters using the exact solution of the storm depth distribution. The exact solution for the Poisson cumulative distribution function was given in Equation 7.15; replacing $r + \forall_e$ with h gives the following expression in terms of storm depth:

$$F_H(h) = -2\sqrt{\alpha\delta h}\cdot \mathrm{K}_1[2\sqrt{\alpha\delta h}] \tag{7.27}$$

The variables α and δ are the inverse storm intensity and duration, respectively. $\mathrm{K}_1[\cdot]$ is the modified Bessel function of first order. We calculate the partial derivatives of the exact cumulative distribution function,

$$\frac{\delta F}{\delta z} = 2\sqrt{\alpha\delta h}\cdot \mathrm{K}_0[2\sqrt{\alpha\delta h}] \tag{7.28}$$

$$\frac{\delta z}{\delta h} = \frac{2\alpha\delta}{z} \tag{7.29}$$

and then combine them using the chain rule to get an alternative expression for the proba-

Probability of occurrence	Storm depth [cm]	Number of saturated cells [-]	Percent area [%]
1e-1	2.9	258	0.7
1e-2	8.2	2460	6.7
1e-3	14.2	5562	15
1e-4	20.4	8210	23
1e-5	26.7	11414	31
1e-6	33.5	16982	47

Table 7.1: Extent of saturation for different probability storms, Yreka, CA.

bility density function of storm depth,

$$f_H(h) = \frac{\delta F}{\delta z} \cdot \frac{\delta z}{\delta h} = 2\alpha\delta \cdot \mathrm{K}_0[2\sqrt{\alpha\delta h}] \tag{7.30}$$

K_0 is the zeroth-order modified Bessel function. The values of λ and κ are determined by equating the moments of the gamma distribution and the distribution in Equation 7.30. The mean storm depth derived from the exact solution (Equation 7.30) is

$$m_1 = \int_0^\infty h f_H(h) dh = \frac{1}{\alpha\delta} \tag{7.31}$$

The variance of h is given by the expression

$$\sigma_h^2 = \int_0^\infty (h - m_1)^2 f_H(h) dh = \frac{3}{(\alpha\delta)^2} \tag{7.32}$$

The gamma distribution is characterized by the scale parameter κ and shape parameter λ. By definition, the mean and variance are combinations of the two parameters:

$$m_h = \frac{\kappa}{\lambda} \tag{7.33}$$

$$\sigma_h^2 = \frac{\kappa}{\lambda^2} \tag{7.34}$$

Combining these definitions with the mean and variance from the exact distribution, we can calculate the gamma parameters from the mean and variance of an observed dataset according to the following relationships:

$$\kappa = \frac{1}{3} \tag{7.35}$$

$$\lambda = \frac{\alpha\delta}{3} = \frac{1}{3m_h} \tag{7.36}$$

Given the calibrated values for κ and λ, we can calculate the probability of any storm depth. Any pixels which have an available storage $\forall_e$ less than the storm depth will saturate in the storm of that likelihood. This was done on the Yreka basin for illustration of the variability of saturated areas. Table 7.1 summarizes the storm depths and associated saturated area for a range of storms. As the likelihood of a rainfall depth decreases, more rainfall

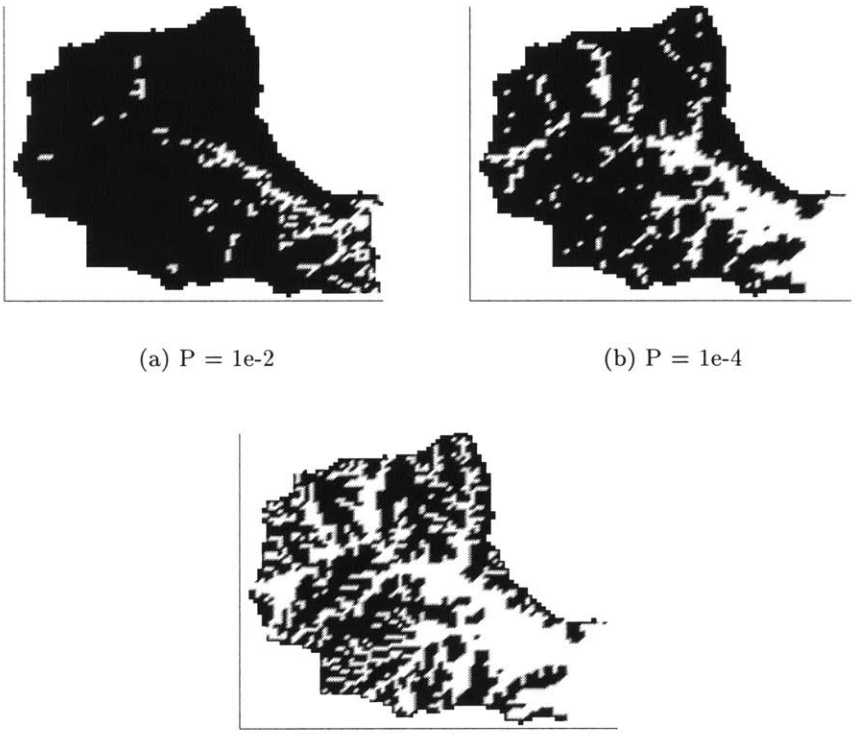

(a) P = 1e-2

(b) P = 1e-4

(c) P = 1e-6

Figure 7-13: Saturated area (white shading) as a function of storm probability for Yreka, CA, based on the modeled equilibrium soil moisture.

Basin	Season	i_r [mm/d]	t_r [d]	t_b [d]	e_p [mm/d]	P/E_p [–]
Brushy	annual	50	0.24	3.0	3.9	1.0
	summer	58	0.23	4.8	3.4	0.8
Schoharie	annual	30	0.25	2.4	2.2	1.4
	summer	43	0.23	6.8	2.9	0.5

Table 7.2: Comparison of annual and summer (May - October) climate characteristics.

occurs and the saturated area expands. Figure 7-13 provides maps of the saturated area for three of the storm scenarios. The maps show the expansion of saturated areas up the channel network with increasingly large (rare) storms. The spatial pattern of saturated areas further supports the importance of considering spatially distributed soil moisture when predicting runoff response.

7.5.2 Comparison of derived and observed distributions

In this section, we compare the exceedence probability distributions for derived and observed runoff. Results are presented for both lumped and distributed soil moisture. This again highlights the effect of spatially variable soil moisture on runoff response. Close agreement between the model and observations may be seen as validation of the model and an indication of the value of distributed information in characterizing basin response.

The derived distributions are based on the annual equilibrium climate characteristics, whereas the observed storm series are taken from the six summer months only. The differences between the annual and summer climates are summarized in Table 7.2. Summer storms are more intense than winter storms, but the increased rainfall is more than offset by the high summertime evaporation. As a result, the summer wetness index is substantially lower for both basins relative to the annual index.

Use of the drier summer climate as the antecedent storm conditions reduces the runoff predicted from the derived distributions. This weakens the agreement between the derived and observed distributions, particularly in Schoharie Creek where the wetness index is 65 percent lower in the summer. However, the available soil moisture used in the derived runoff distribution represents both the influences of atmospheric forcing and lateral flow in the saturated zone. The response of groundwater to changes in the surface hydrologic fluxes is greatly dampened in time. The groundwater levels found at the beginning of the summer persist at least partway through the season. Use of summer atmospheric forcing parameters neglects the long time scale of groundwater response and overestimates the influence of evaporative forcing on the water table position. The GSEM results are therefore presented for the annual equilibrium climate.

Figures 7-14 and 7-15 present comparisons of the observed and derived exceedence probability distributions of saturation-excess runoff for the Brushy and Schoharie basins. The distributions for observed runoff are taken from the gaged sites described in Chapter 3 assuming a Weibull distribution of storms (*e.g.*, Linsley *et al.* 1992). Storms with a net rainfall of less than 1 mm are neglected. The derived distribution is correspondingly adjusted by changing the lower integration limit of Equation 7.12 from an intensity of zero to an intensity equal to 1 mm divided by t_r. In the resulting distributions for uniform

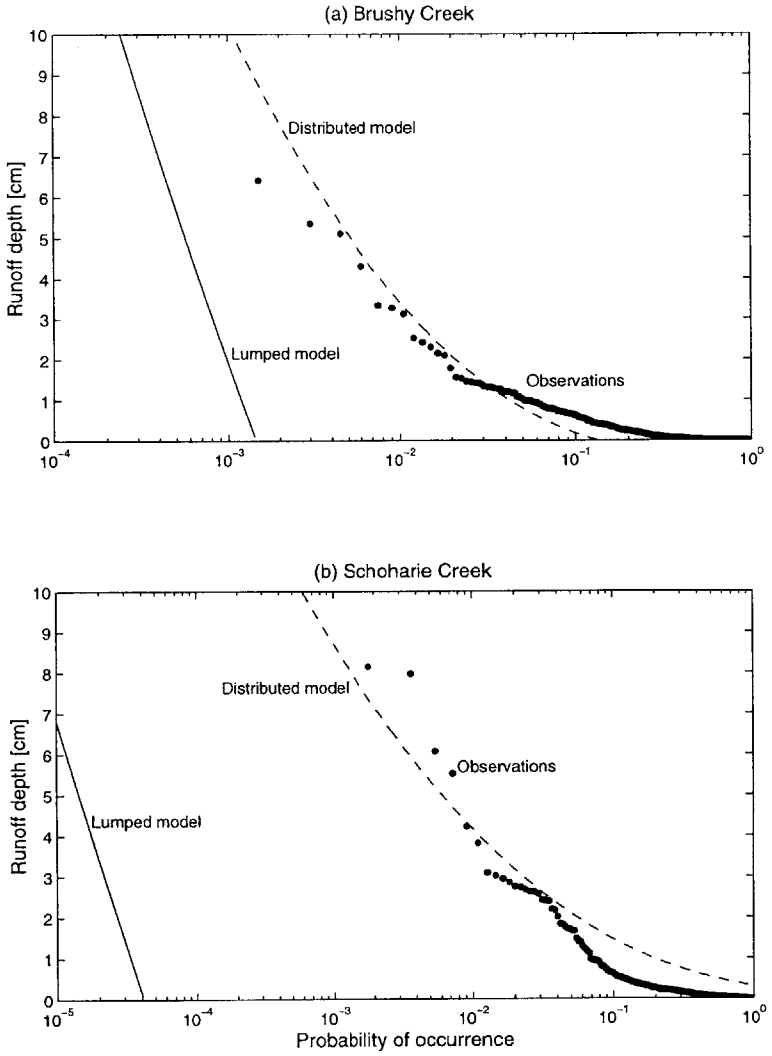

Figure 7-14: Semilog comparison of observed and derived runoff response curves, Brushy and Schoharie basins.

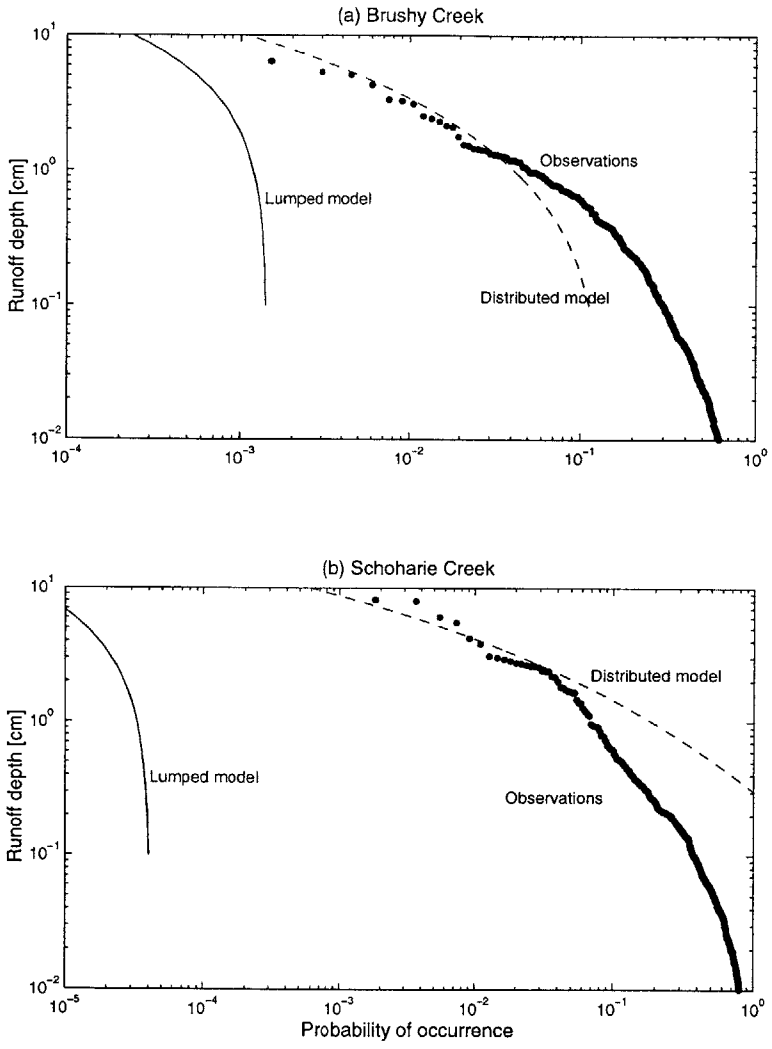

Figure 7-15: Log-log comparison of observed and derived runoff response curves, Brushy and Schoharie basins.

and variable soil moisture, the term $(r + \forall_e)$ is replaced by $(r + \forall_e - 0.001)$. The derived distribution is also adjusted so that the runoff found in the most likely storm is equal to zero; this is done to correspond with the base flow assumptions of the observed time series. In both cases the removed base flow is on the scale of 1 mm.

The resulting curves show fairly good agreement between observations and the derived distribution based upon variable soil moisture. Figure 7-15 highlights the difference between model and observations for small, high probability storms. The discrepancy is likely due to the difference between the gaged and modeled catchment areas. The ratio of modeled to gaged basin area for Brushy Creek is 0.75; for Schoharie Creek the ratio is 1.25. In humid environments, the runoff ratio increases with an increase in basin size (*e.g.*, Moore and Morgan 1969). In both basins, the larger catchment experiences higher runoff in small storms. The effect disappears as the probability decreases and storm size increases. For cases where the runoff from small storms is of greatest interest, it is important that the modeled catchment area match that of the gaged basin. If larger storms are of higher concern, however, some difference in basin area may be allowable without sacrificing the accuracy of the model prediction.

The good agreement between the observed distribution and the heterogeneous-moisture distribution highlights how characterization of the antecedent distribution of soil moisture is vital for estimating runoff response. Exceedence probability distributions may provide an alternative technique for validation and/or calibration of hydrologic models. The advantage of using probability distributions instead of streamflow time series is that they efficiently incorporate a greater range of storm magnitudes.

7.6 Summary

In this chapter we have investigated the role of distributed hydrologic information in the runoff response of a basin. The first step was to derive a probability distribution for runoff that could be used with either uniform or variable soil moisture. This was done by integrating over a stochastic distribution of rainstorms and interstorm periods. The observed time series of precipitation and streamflow were divided into discrete events which were then aggregated into an exceedence probability distribution. A comparison of the uniform- and variable-moisture derived distributions reveals higher runoff from the variable-moisture case for relatively frequent storms (precipitation less than mean available storage) and lower runoff from extreme events. The behavior reflects the cumulative distribution of antecedent available storage, which is a gradual function for variable-moisture conditions and a step function under uniform moisture conditions. The observed distribution is in good agreement with the variable-moisture derived distribution. This implies that knowledge of the distributed nature of pre-storm moisture is important for characterizing the runoff response of a basin. The close agreement also signals that exceedence probability distributions may be used as an alternative to continuous streamflow records for validation of distributed hydrologic models.

Chapter 8

Key findings and future work

8.1 Key findings

We have presented the results of a coupled hydrologic equilibrium model applied to ten basins across the United States. The results are used to investigate spatial variability in equilibrium conditions and the influence of that variability on the dynamic runoff response. The work is designed to identify links between geomorphologic characteristics and hydrologic conditions by using a coupled analytical-numerical model to search for relatively simple relationships between wet and dry characteristics. The key findings include the following:

- The spatial organization of soil moisture and related surface fluxes (runoff, evaporation, and recharge) is related to the combined effects of local surface topography and climate. The shape of the hillslope in the horizontal direction adds to the information in traditional topographic indices based on contributing area per unit contour length and surface slope.

- The extent of the midline area, in which the water table is parallel to the ground surface and the time-averaged vertical flux between the saturated and unsaturated zones is negligible, is related to the combined effects of climate and transmission efficiency of the two zones.

- The variability between basins is explained to a large degree by the efficiency of flow in the saturated zone, climatic wetness, surface-subsurface coupling, and basin dissectedness. The runoff ratio is best predicted by the basin climatic wetness and infiltration capacity; the evaporation efficiency has too much noise to be significantly predicted by a regression model.

- The probability distribution of observed runoff response matches the distribution of runoff derived from Poisson storm statistics, using the equilibrium soil moisture distribution as the antecedent conditions. Probability distributions may be used as a means of validating the long-term output of distributed models.

8.2 Future work

Several areas for further investigation and expansion of this work have been identified. The assumptions about spatial and temporal uniformity of physical and climatic characteristics

made in the course of the research may be relaxed; this will highlight the environments in which the current assumptions are valid and the extent to which the model input or output must be adjusted in other conditions. Outstanding questions that have emerged include the following:

Is the effect of non-topographic effects on spatially variable hydrology of the same magnitude as topographic effects?

The sensitivity studies performed with respect to vegetation and soil texture assumed uniformity of conditions. Both of these properties are known to vary in space. Future studies should consider the effects on hydrologic properties of partial vegetation cover within individual pixels and of varying evaporative properties of plants across a basin. Variability in soil texture could be incorporated through dividing the soil column into multiple layers and assigning different hydraulic properties to individual pixels and layers.

How do seasonality in the climate and subsurface moisture storage influence distributed hyrologic processes?

The results presented here correspond to the long-term equilibrium conditions and are based on annual average climate characteristics. Transient simulations of the model may capture aspects of the seasonal variations in saturated–unsaturated zone coupling that are not evident when the model is run to equilibrium. Seasonal effects include both variable precipitation and evaporation and delayed variability in groundwater storage. Snow cover and the freezing of soil water have not been included in this analysis; their influence may be of particular importance on the timing of runoff from basins where snow and ice occur.

How do interannual changes in groundwater storage affect the distribution of soil moisture?

Multi-year phenomena such as persistent droughts or floods cause variability in the groundwater store over longer time scales than the seasonal cycle. A transient run of the model using a low-frequency, non-stationary climate would provide insight into the delayed response of groundwater to climatic variability, and whether the storage response influences the distribution of hydrologic processes at any point in time and in the long-term average.

How do groundwater circulation and bedrock fractures influence the spatial distribution of equilibrium hydrology?

This research assumed that the soil column is underlain by impervious bedrock. However, deeper soil and rock layers often allow some moisture flow at a reduced conductivity. Deep groundwater circulation through lower-permeability soil layers may result in a different pattern of distributed hydrology from that based upon impervious bedrock. Additionally, fractures in the bedrock are highly transmissive conduits which may also significantly alter subsurface flow patterns and the resulting spatial distribution of soil moisture.

How can additional field data enhance hydrologic modeling efforts?

There are few publicly-available, detailed datasets which characterize the spatial variability of soil depth and its relation to the overlying topography. The model used

here to characterize this important physical parameter was developed from measurements in a single basin; it may not be appropriate in other environments. It would be beneficial to perform spatially intensive studies of other catchments in an effort to improve the confidence in the soil-depth model.

Additionally, the inclusion of field data could strengthen the findings of interbasin variability found in Chapter 6. Principal component analysis holds the potential for advancing understanding of the physical and climatic factors which are most related to the differential hydrologic response between basins. The results could be strengthened by increasing the number of study basins and supplementing the set of variables with field-measured parameters. One example of a comprehensive dataset is presented by Western *et al.* (1999) for the small Tarrawarra catchment in New Zealand. The addition of geomorphologic and hydrologic datasets to the public collection will enhance the community's ability to analyze modes of variability between basins in different climates and landscapes.

Appendix A

Definition of variables

A	contributing area $[L^2]$
a	contributing area per unit contour length $[L]$
A_0	second term of Philip-type infiltration equation $[LT^{-1}]$
A_Ω	total basin area $[L^2]$
c	Brooks-Corey pore disconnectedness index [–]
D_i	moisture deficit at pixel i $[L]$
D_d	drainage density $[L^{-1}]$
E	parameter group in bare-soil evaporation equation [–]
E_{bs}	annual (or seasonal) bare soil evaporation $[L]$
E_p	annual (or seasonal) potential evaporation $[L]$
E_{vs}	annual (or seasonal) vegetated-soil evaporation $[L]$
e	elevation of soil-bedrock interface $[L]$
e_p	annual average bare-soil potential evaporation rate $[LT^{-1}]$
f	TOPMODEL decay parameter of conductivity with water table depth $[L]$
f_i^*	infiltration capacity $[LT^{-1}]$
f_e^*	exfiltration capacity $[LT^{-1}]$
f_k	filtered streamflow response for base flow filtering algorithm $[LT^{-1}]$
H	surface elevation $[L]$
h	storm depth $[L]$
i_r	rainfall intensity $[LT^{-1}]$
K	sediment-transport diffusion constant $[L^2T^{-1}]$
K_s	saturated hydraulic conductivity $[LT^{-1}]$
K_o	surface hydraulic conductivity $[LT^{-1}]$
K_{s_*}	unsaturated hydraulic conductivity at soil saturation $[LT^{-1}]$
L_Ω	average length of streams of basin order Ω $[L]$
m	Brooks-Corey pore size distribution index [–]
m_h	mean storm depth $[L]$
m_s	mean number of storms per season [–]
m_v	mean number of storms per year [–]
n_e	effective porosity [–]
N_ω	number of streams of order ω [–]
P	annual (or seasonal) precipitation $[L]$
P_o	limiting soil production rate $[LT^{-1}]$

Q_{p_i} peak flow during a storm $[LT^{-1}]$
Q_{E_i} storm flow occurring after onset of the subsequent storm
Q_{b_i} base flow $[LT^{-1}]$
Q_{o_i} limiting base flow $[LT^{-1}]$
$\tilde{q}_s$ sediment transport vector $[LT^{-1}]$
$\langle q \rangle$ temporal mean unsaturated zone moisture flux in the vertical direction $[LT^{-1}]$
R annual runoff depth $[L]$
R_{ie} annual (or seasonal) infiltration-excess surface runoff $[L]$
R_{se} annual (or seasonal) saturation-excess surface runoff $[L]$
r runoff depth $[L]$
S_{50} median surface slope [–]
S_e exfiltration desportivity $[LT^{\frac{1}{2}}]$
S_i infiltration sorptivity $[LT^{\frac{1}{2}}]$
s soil saturation [–]
s_* surface soil moisture [–]
T transmissivity $[L^2T^{-1}]$
T_{D_i} transmissivity at moisture deficit D_i $[L^2T^{-1}]$
T_o surface transmissivity $[L^2T^{-1}]$
t_b interstorm duration $[T]$
t_{bmin} minimum time between independent storms $[T]$
t_r storm duration $[T]$
t_s time to saturation $[T]$
t_s^* limiting time to saturation assuming soil-controlled infiltration $[T]$
w maximum potential capillary rise $[L]$
Z^* zero-recharge water table depth $[L]$
Z_r rooting depth $[L]$
Z_T total depth of soil column $[L]$
Z_w vertical Cartesian location of the water table relative to the ground surface $[L]$
α inverse of mean precipitation intensity $[TL^{-1}]$
β angle of ground surface relative to the horizontal [°]
Γ dimensionless parameter group in derivation of infiltration capacity [–]
ΔH maximum elevation difference in a basin $[L]$
$\Delta\theta$ effective water content change [–]
δ inverse of mean storm duration $[T^{-1}]$
ϵ digital filter parameter [–]
η inverse of mean interstorm duration $[T^{-1}]$
Λ parameter group in evaporation equation [–]
λ mean TOPMODEL index $[L^{-1}]$
μ parameter group in infiltration-excess runoff equation [–]
ξ rate of soil production decay with soil depth $[L^{-1}]$
ρ_r bulk bedrock density $[ML^{-3}]$
ρ_s bulk soil density $[ML^{-3}]$
ϕ_e dimensionless desorption diffusivity [–]
ϕ_i dimensionless sorption diffusivity [–]
χ time constant in infiltration capacity expression $[T]$
Ψ_s Brooks-Corey bubbling head $[L]$
Ω parameter group in evaporation equation [–]

$\forall_e$	unsaturated storage capacity under steady state equilibrium with a water table $[L]$
$\langle\cdot\rangle$	temporal mean value operator
$\Gamma(\cdot)$	gamma function
$\gamma(\cdot,\cdot)$	incomplete gamma function
$K_2(\cdot)$	Bessel function of second type

Appendix B

Supplementary model equations

B.1 Equations used in calculation of infiltration-excess runoff

Philip's (1957) solution for infiltration into a semi-infinite, uniform soil moisture profile gives an infiltration capacity defined as

$$f_i^* = \frac{1}{2} S_i t^{-\frac{1}{2}} + A_o \tag{B.1}$$

where S_i is the sorptivity and A_o is dominated by gravitational effects. Salvucci (1994) modifies the variables for a finite water table depth, giving

$$A_o = \begin{cases} \left(\frac{2+\Gamma}{3}\right) K_s & \Gamma \geq -2 \\ 0 & \Gamma < -2 \end{cases} \tag{B.2}$$

and

$$S_i = (2\chi)^{1/2} K_s \tag{B.3}$$

The variable combinations used in these equations are defined as

$$\Gamma \equiv \frac{-\phi \Psi_s (1 - s_*)}{1 + \frac{1}{2}(c-3)(1-s_*)\hat{s}^{\frac{c+1}{2}}} \tag{B.4}$$

$$\phi \equiv \frac{m\left[1 + \frac{-\langle q \rangle}{K_s}\right](s_*^{1-c})}{\Psi_s} \left(\frac{Z_w}{\Psi_s}\right)^{-mc-1} \tag{B.5}$$

$$\chi \equiv \frac{-n_e(1-s_*)\Psi_s}{K_s}\left[1 + \frac{1}{2}(c-3)(1-s_*)\hat{s}^{(c+1)/2}\right] \tag{B.6}$$

The surface soil moisture, s_*, depends on the recharge rate and water table depth, along with the soil characteristics:

$$s_* \equiv \left(\frac{-\langle q \rangle}{K_s} + \left(1 + \frac{-\langle q \rangle}{K_s}\right)\left(\frac{Z_w}{\Psi_s}\right)^{-mc}\right)^{1/c} \tag{B.7}$$

Other variables abbreviations include the following:

$$\hat{s} = \frac{1}{2}(1 + s_*) \tag{B.8}$$

$$c = (2 + 3m)/m \tag{B.9}$$

The limiting time to saturation, t_s^*, is defined as:

$$t_s^* = \begin{cases} \left(\sqrt{\frac{S_i^2}{4A_o^2} + \frac{\forall_e}{A_o}} - \frac{S_i}{2A_o}\right)^2 & A_o > 0 \\ \left(\frac{\forall_e}{S_i}\right)^2 & A_o = 0 \end{cases} \tag{B.10}$$

while the available storage in the unsaturated zone can be expressed as

$$\forall_e = n_e(1 - s_*)Z' + \frac{1}{2}n_e\phi Z'^2 - \frac{1}{2}n_e\lambda(Z_w + Z' - \Psi_s)^2 \tag{B.11}$$

with intermediate variables

$$\lambda \equiv m\left[1 + \frac{-\langle q \rangle}{K_s}\right]/\Psi_s \tag{B.12}$$

$$Z' \equiv \frac{(1 - s_*) - \lambda(Z_w - \Psi_s)}{\lambda - \phi} \tag{B.13}$$

B.2 Equations used in calculation of evaporation

The exfiltration capacity, f_e^*, has the same form as the Philip's solution for infiltration capacity, although the second term does not appear in the equation,

$$f_e^* = \frac{1}{2}S_e t^{-\frac{1}{2}} \tag{B.14}$$

The exfiltration desorptivity is expressed as

$$S_e = 2s_*^{1+(c+1)/4}[n_e K_s|\Psi_s|\phi_e/(m\pi)]^{1/2} \tag{B.15}$$

with desorption diffusivity ϕ_e defined as

$$\phi_e = \frac{2m^2\pi}{3(1 + 3m)(1 + 4m)} \tag{B.16}$$

For bare soil, the dimensionless parameter groups Λ and Ω are defined as:

$$\Lambda = \frac{\left(1 + \frac{\kappa}{2e_p} - \frac{w}{2e_p}\right)}{\left(1 + \frac{\kappa}{e_p} - \frac{w}{e_p}\right)^2} \tag{B.17}$$

$$= \frac{e_p\,(2e_p + \kappa - w)}{2(e_p + \kappa - w)^2} \tag{B.18}$$

$$\Omega = 2\left(\frac{K_s s_*^c}{e_p - \frac{2w}{e_p}}\right)^2 \tag{B.19}$$

with maximum capillary rise

$$w = \frac{K_s(Z_w/\Psi_s)^{-mc}}{1 - (Z_w/\Psi_s)^{-mc}} \tag{B.20}$$

The final term appearing in the solution for bare-soil evaporation is E; this is defined as

$$E = \eta S_e^2/(2e_p^2) \tag{B.21}$$

Evaporation from a vegetated surface follows the Richards-Cowan model (Levine and Salvucci 1999b). The expression for Λ is determined by divided the time to stress by Et_b to get:

$$\Lambda = \frac{\frac{\pi^2}{16}S_e^2 + \eta B + \sqrt{-4e_p\eta^2 C + \left[\frac{\pi^2}{16}S_e^2 + \eta B\right]^2}}{Et_b 2e_p C} \tag{B.22}$$

where B and C are defined as

$$B = 2e_p + K_s s_*^c - w \tag{B.23}$$

$$C = e_p + K_s s_*^c - w \tag{B.24}$$

Appendix C

Location of observations

Basin	Latitude [deg:min N]	Longitude [deg:min W]
Big Creek	47:38	117:32
Brushy Creek	37:39	86:46
Midland	37:30	77:20
Ogden	39:34	97:40
Tombstone	32:01	110:57

Table C.1: Location of precipitation stations for model input. Values for Bear, Moshannon, Sacramento, Schoharie, and Yreka were taken from contour maps.

Basin	Latitude [deg:min N]	Longitude [deg:min W]
Bear Valley	39:10	120:08
Big Creek	47:38	117:32
Brushy Creek	32:40	85:55
Midland	36:41	76:47
Moshannon	41:30	80:28
Ogden	37:40	97:18
Sacramento	38:32	121:46
Schoharie	41:06	72:22
Tombstone	32:14	110:57
Yreka	40:36	124:17

Table C.2: Location of pan evaporation measurements for model input.

Appendix D

Supplementary maps of water table position

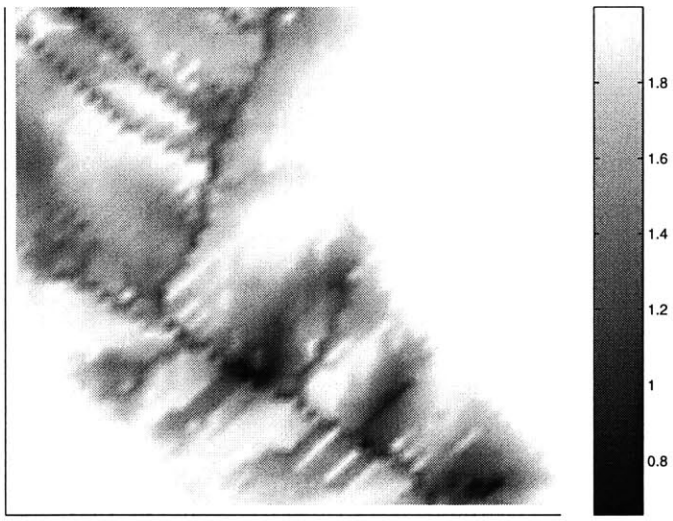

Figure D-1: Map of water table depth for 2-km^2 square subsection of Bear, CA.

Figure D-2: Map of water table depth for 2-km^2 square subsection of Brushy, AL.

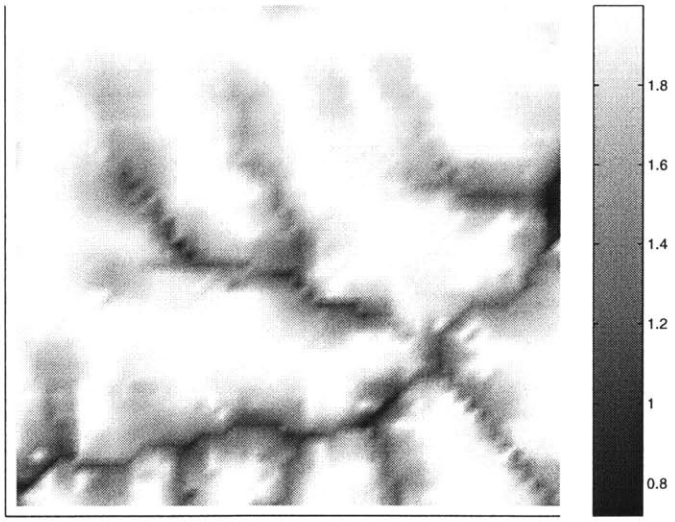

Figure D-3: Map of water table depth for 2-km^2 square subsection of Big Creek, ID.

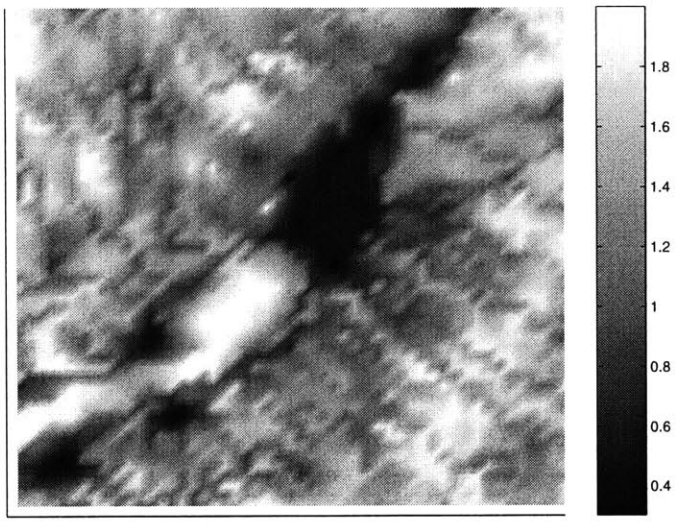

Figure D-4: Map of water table depth for 2-km^2 square subsection of Schoharie, NY

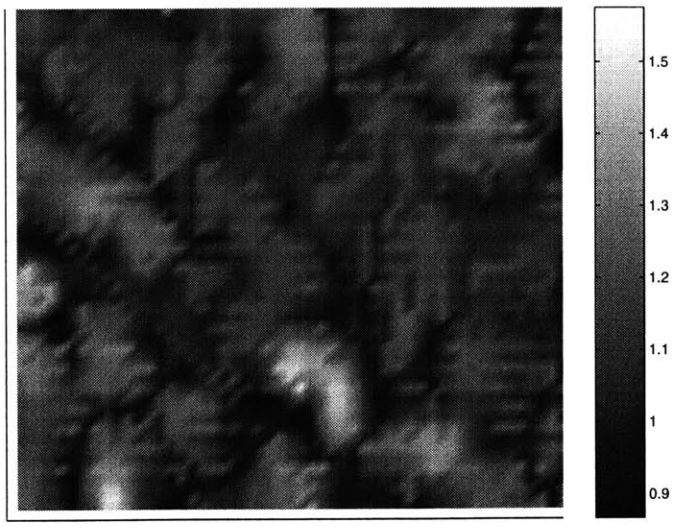

Figure D-5: Map of water table depth for 2-km^2 square subsection of Midland, VA.

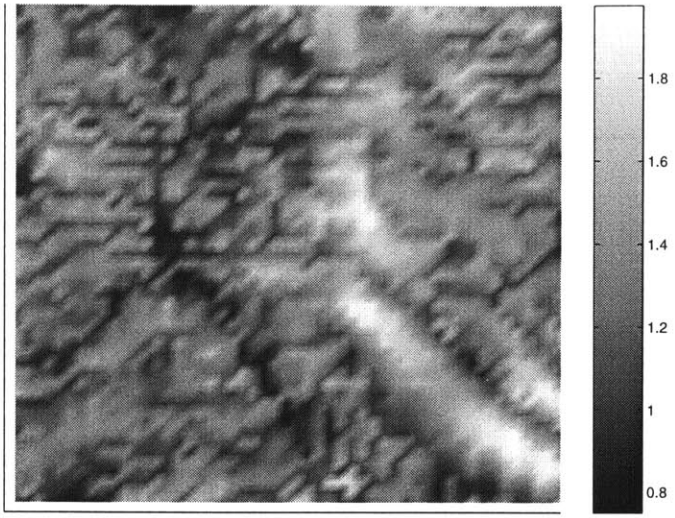

Figure D-6: Map of water table depth for 2-km^2 square subsection of Moshannon, PA.

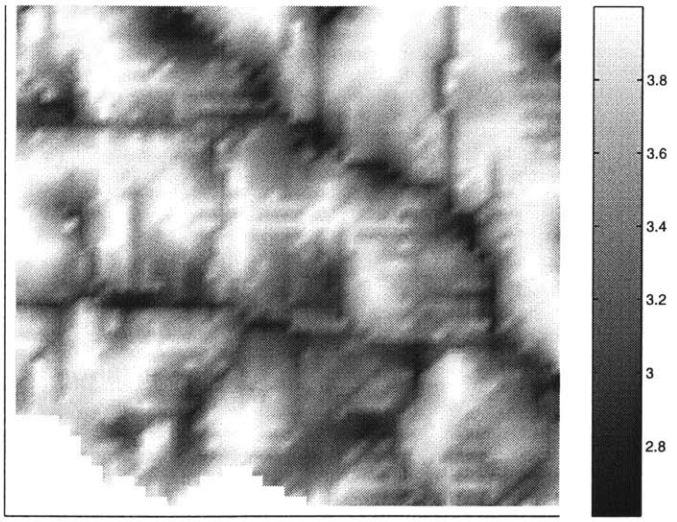

Figure D-7: Map of water table depth for 2-km^2 square subsection of Ogden, KS.

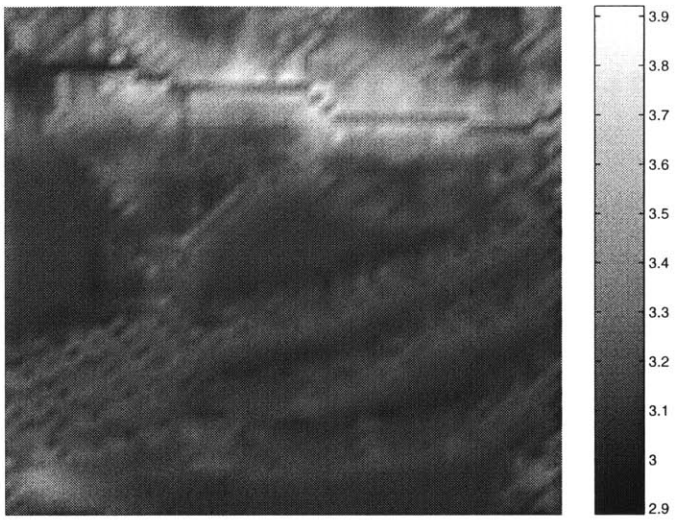

Figure D-8: Map of water table depth for 2-km^2 square subsection of Sacramento, CA.

Figure D-9: Map of water table depth for 2-km^2 square subsection of Tombstone, AZ.

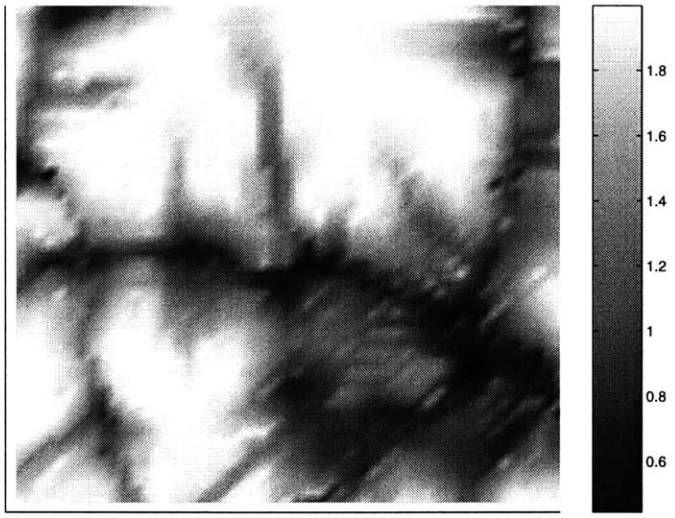

Figure D-10: Map of water table depth for 2-km^2 square subsection of Yreka, CA.

Appendix E

Base flow separation

Channel flow comes from both overland and subsurface sources. Saturation-excess and infiltration-excess runoff provide quick pulses of water to a channel with a relatively short time lag from the onset of precipitation. Groundwater flow, in contrast, travels at a much slower rate than overland flow and is thus delayed in time. Base flow is considered the portion of streamflow coming from groundwater or other delayed sources (Tallaksen 1995). It depends on surface inputs of precipitation but varies over longer time scales than surface runoff.

In GSEM, the equilibrium base flow is calculated as the amount of drainage, or the flow coming from perenially saturated regions. The modeled base flow values as a fraction of precipitation and total runoff are summarized in Table E.1. Ogden and Sacramento are omitted from the table because they experience no runoff. In Big Creek, Schoharie, and Yreka, base flow comprises a significant fraction of the total runoff depth. It is therefore vital that observed streamflow have base flow removed when compared against modeled saturation-excess runoff.

A variety of techniques exists for isolating base flow from time series of total streamflow. Simple graphical approaches include the following:

- drawing a straight line between the points on the hydrograph corresponding to the onset of precipitation and the greatest curvature of the recession limb, and

Basin	P [m]	Q_b/P [–]	$Q_b/(Q_b + R_{se})$ [–]
Bear	0.81	0.04	0.19
Big Creek	0.48	0.69	0.96
Brushy	1.35	0.00	0.00
Midland	1.10	0.00	0.00
Moshannon	1.06	0.02	0.06
Schoharie	1.03	0.31	0.58
Tombstone	0.37	0.01	0.07
Yreka	0.47	0.12	0.46

Table E.1: Sample annual average base flow as a fraction of precipitation and total runoff estimated by the model, using the smoothed minima approach. Ogden and Sacramento have no measurable baseflow or surface runoff.

- following the pre-storm negative slope for some time lag t and then increasing base flow until it intersects the hydrograph at some time after storm cessation.

Dingman (1993) illustrates the application of these approaches on theoretical hydrographs. With the use of computers in hydrology, more complicated, automated techniques have recently been developed. Two techniques described by Nathan and McMahon (1990) involve a recursive digital filter and a smoothed minima approach. These methods are described below.

Recursive digital filter This separation technique employs a recursive digital filter to smooth the streamflow signal. Nathan and McMahon (1990) present a simple filter which was modified by Chapman (1991) to the form

$$f_k = \frac{3\epsilon - 1}{3 - \epsilon} f_{k-1} + \frac{2}{3 - \epsilon} (y_k - y_{k-1}) \tag{E.1}$$

where f_k is the filtered quick-response streamflow at time k, y_k is the original streamflow, and ϵ is the filter parameter, assigned a value between 0.90 and 0.95. Base flow is the total streamflow minus the quick-response flow. An example of base flow separation using the filter with $\epsilon = 0.925$ on a short time series of streamflow in Brushy Creek is presented in Figure E-1, subplot (a). Base flow follows the general pattern of total streamflow but is damped and slightly lagged in time. The digital filter technique is sensitive to the model parameter; higher values of ϵ will result in lower levels of base flow.

Smoothed minima An alternative approach described by Nathan and McMahon (1990) is the smoothed minima technique which linearly connects low-flow points. The method has three steps:

1. Calculate the minimum of each five-day nonoverlapping period;
2. Identify which of the minima correspond to turning points, defined as a value less than a constant (they use 1.11) times the two extreme values; and
3. Construct the base flow hydrograph by connecting all the turning points.

In a comparison of the smoothed minima technique with recursive digital filtering, Nathan and McMahon found the smoothed minima technique to be slightly inferior. The base flow partitioning using the smoothed minima technique on the Brushy Creek streamflow series is given in Figure E-1, subplot(b).

Moving minima The simplest technique for estimating base flow is to assume a constant value over time. Base flow levels are known to vary, however, over time scales ranging from within an individual storm to seasonally and interannually, as governed by larger scale climatic fluctuations. One way to incorporate some of the mid-scale variability is to estimate base flow as the moving minimum of flow in a specified window of time. The approach is simple and does not require parameter estimation like the previous two methods, yet it retains some temporal variability. This technique is illustrated in Figure E-1, subplot (c). The moving minima technique is quite sensitive to the width of the window over which the minimum is determined.

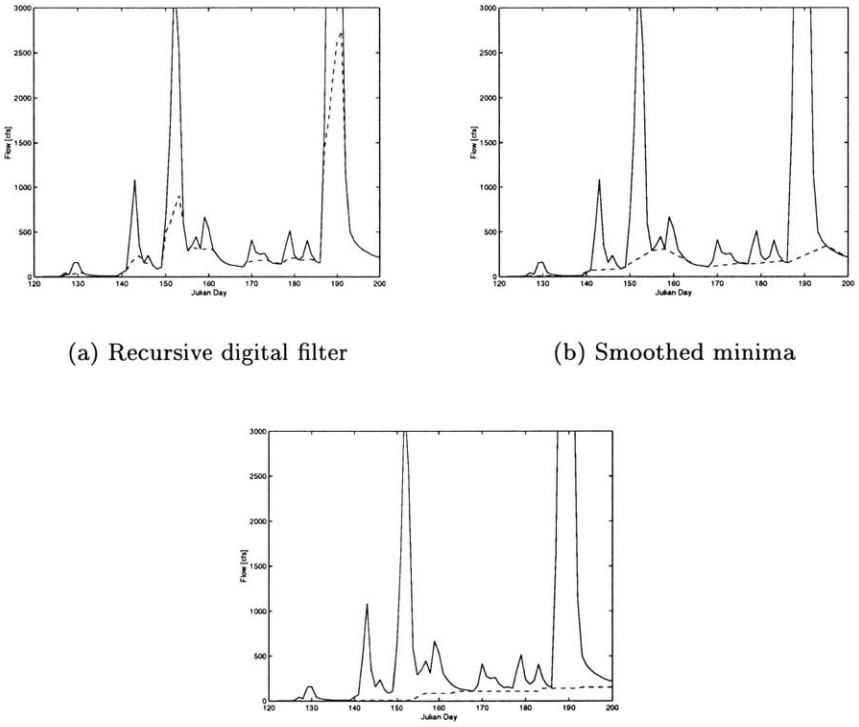

(a) Recursive digital filter

(b) Smoothed minima

(c) Moving minima

Figure E-1: Comparison of base flow separation techniques on a streamflow record from Brushy, AL.

Appendix F

Spatial variability in a quasi-distributed model

The desire to represent spatially variable hydrology resulting from topographic forcing in an efficient manner has led to the widespread use of quasi-distributed models. Such models use simplifying assumptions to collapse multiple hydrologic processes into a physically-based index that identifies hydrologically similar locations. The most widely used and adapted model framework is TOPMODEL (Beven and Kirkby 1979). TOPMODEL was designed to be physically based (the model parameters are estimated from measurable field properties), flexible (*e.g.*, it can be modified for different runoff generation mechanisms, evaporation routines, or soil characteristics), and computationally efficient (the full distribution of hydrology is determined from the distribution of the similarity index). These characteristics have made the model popular for hydrologic investigations for a variety of purposes in a range of environments.

Because the hydrology in TOPMODEL is generated from the distribution of a topographic index, the accuracy of the model predictions depends on the quality of the assumptions made in defining the index. In this appendix we investigate whether the TOPMODEL simplification is warranted and the effect of the assumptions on hydrologic response. The formulation of the distributed model GSEM does not depend on the same TOPMODEL assumptions; comparison of the two models indicates whether it is worthwhile to incur the computational expense of a distributed model, or whether the predicted spatial patterns are adequately captured by the more efficient quasi-distributed model. The goal is not to identify which model is "better", but rather whether any significant, consistent differences exist which could affect model use or interpretation.

F.1 Introduction to TOPMODEL

In this section we introduce the three fundamental assumptions of TOPMODEL and the original model framework built from those assumptions. The ongoing debates about the validity of the individual assumptions are discussed, followed by a literature review of some of the many applications of TOPMODEL to field studies that have been undertaken with varying success.

F.1.1 Theory

The essence of TOPMODEL is that locations in a basin with the same value of a topographic index are hydrologically similar. Once the range of index values is known, calculations can be made about the hydrologic response across the dynamic range. This knowledge is combined with the probability distribution of the index to generate the distribution of soil moisture and the basin-aggregated runoff response. The model is quasi-distributed because it combines an explicitly-generated distribution describing the basin topography with assumptions of hydrologic similarity in space and time.

The topographic index is derived using simplifying assumptions about surface and subsurface hydrologic processes. The underlying assumptions are the following:

1. Saturated zone dynamics can be represented as a series of successive steady states.
2. Effective rainfall (recharge) is spatially constant.
3. The effective hydraulic gradient is parallel to the ground surface at all points within the basin.
4. Hydraulic conductivity declines exponentially with depth in the soil column.

Since recharge is assumed to be spatially constant ($\bar{\imath}$), the flow at any one point is the integrated recharge over the upstream area (a) draining to that point. Assuming steady-state conditions, the moisture flux into a pixel from upstream must be equal to the topographically-driven flux out of the pixel:

$$q = \bar{\imath}a = T_o e^{-D_i/m} \tan\beta \tag{F.1}$$

where T_o is the transmissivity when the soil column is saturated, D_i is the local soil moisture deficit, m is the calibrated conductivity decay rate parameter, and $\tan\beta$ is the ground surface slope. Equation F.1 can be rewritten to calculate the saturated storage at location i:

$$D_i = -m \ln\left(\frac{\bar{\imath}a}{T_o \tan\beta}\right) \tag{F.2}$$

The spatially averaged moisture deficit is determined by integrating over the basin area to get

$$\bar{D} = m\lambda + D_i + m\ln(a/\tan\beta) \tag{F.3}$$

where λ is the spatial mean of the topographic index $\ln(a/\tan\beta)$. Knowledge of the mean moisture deficit allows identification of the areal extent of saturation ($D_i \leq 0$). The spatial distribution of saturated areas identifies riparian zones that expand and contract during and between storms.

F.1.2 TOPMODEL assumptions and debates

The essence of a quasi-distributed model is the use of a physically based index as an indicator of hydrologic similarity. There is no perfectly defined relationship between physiographic features and hydrologic response. Quasi-distributed models rely on assumptions about the driving processes to reduce similarity relationships into a quantifiable parameter. Some

of the limitations of the original model assumptions have been addressed in subsequent modifications of the original model (*e.g.*, the inclusion of transmissivity in the topographic index introduced by Beven 1986b), yet a number of questions regarding the validity of the basic assumptions and the best techniques for calculating model parameters remain unresolved.

- **Uniformity of recharge**

  Inherent in TOPMODEL's current approach is spatially and temporally invariant recharge (see Equation F.1). In natural systems, this rarely occurs. The equilibrium hydrology calculated by GSEM showed the division of basins into recharge, midline, and discharge zones. The distribution of recharge depended on the unique combination of climate, soil, and topography in each basin. Recharge may further vary in space due to other sources of spatial variability such as patchy rainfall, soil inhomogeneities, variable vegetation cover, and macroscopic or microscopic topography. The dependence of recharge on the soil moisture content is one of the key mechanisms behind the two-way (bidirectional) coupling of the unsaturated and saturated zones. TOPMODEL neglects the bidirectionality of this interaction.

- **Water table profile**

  TOPMODEL assumes that the hydraulic gradient governing flow in the saturated zone is equal to the slope of the overlying surface; the implicit assumption is that the water table is parallel to the ground surface. This assumption is the source of the surface slope in the denominator of the topographic index $\ln(a/\tan\beta)$. However, the water table does not always follow the overlying topography. Along a planar hillslope, for example, TOPMODEL predicts a depth to saturation that varies along the slope. The water table depth at location i can be determined from Equation F.1. The local transmissivity written in terms of moisture deficit ($T_i = T_o e^{-D_i/m}$) is replaced by the water table–dependent transmissivity ($T_i = K_o/f \cdot e^{-fZ_i}$). The equation may be written in terms of Z_w, giving

$$Z_w = -\frac{1}{f} \ln\left(\frac{f\bar{\imath}a}{K_o \tan\beta}\right) \tag{F.4}$$

  The variables f (decay rate of hydraulic conductivity with depth), $\bar{\imath}$ (spatially-constant recharge rate), and K_o (surface hydraulic conductivity) are all assumed to be constant in space. Along a planar hillslope, the surface slope $\tan\beta$ is constant and the contributing area a is a linear function of distance downslope. The water table depth therefore varies logarithmically with distance downslope. The developers of TOPMODEL were aware of the inconsistency between the water table distribution and the assumed saturated hydraulic gradient (Beven 1997). For shallow soils, the discrepancy is relatively insignificant. However, if the soil is thick or irregular, if there is marked spatial variability in the texture of the soil, or if the recharge rate varies in space or time, the assumption about the parallel profile of the water table could introduce error.

- **Soil conductivity profile**

  TOPMODEL assumes that the hydraulic conductivity of the soil decreases exponentially with depth. The relationship may be expressed either in terms of the soil

moisture deficit ($K_i = K_o e^{-D_i/m}$) or water table depth ($K_i = K_o e^{-fZ_i}$). The exponential behavior is considered to well represent conditions under which the soil column is underlain by an impervious zone (Beven and Kirkby 1979). However, one drawback with the exponential conductivity profile is that it leads to a hyperbolic baseflow recession curve, as opposed to the widely-observed exponential recession curve (*e.g.*, Nathan and McMahon 1990; Tallaksen 1995). Several recent studies have examined alternatives to the original soil conductivity profile. Ambroise *et al.* (1996) compared baseflow recession data for a small catchment with recession curves derived from exponential, parabolic, and linear conductivity profiles. The best match between model and observations was for a parabolic conductivity profile. A flexible formulation was proposed by Duan and Miller (1997). They introduced a parameter which allows the relationship between transmissivity and moisture deficit to range from linear to exponential, encompassing the formulations described by Ambroise *et al.* (1996). Lamb *et al.* (1997) proposed an empirical power-law relationship between discharge and relative storage that can be derived from recession curve analysis. The empirical relationship can be used to develop a modified topographic index for predicting where saturation will occur.

- **Sensitivity to DEM resolution**

  The resolution of the topographic grid is of critical importance because of TOPMODEL's dependence on a topographic-based index to describe the hydrologic behavior of a basin. DEM resolution affects both the mean and distribution of the $\ln(a/\tan\beta)$ index (*e.g.*, Chairat and Delleur 1993; Zhang and Montgomery 1994; Wolock and Price 1994; Bruneau *et al.* 1995). Coarser resolutions increase the mean value and reduce the dynamic range of the topographic index. The mean index, λ, affects the base flow rate, which influences the spatially averaged soil moisture during a simulation. The tail of the $\ln(a/\tan\beta)$ distribution governs the expansion and contraction of saturated areas that are crucial for estimating runoff generation.

  One way to account for coarsely resolved elevation data is through calibration of the TOPMODEL parameters. Several approaches have been introduced (*e.g.*, Bruneau *et al.* 1995; Quinn *et al.* 1995; Wolock and McCabe 1995; Saulnier *et al.* 1997). Calibration methods may allow TOPMODEL to be used with reasonable confidence even in the absence of fine-resolution DEMs. The resolution above which accurate estimation of the hydrologic processes requires parameter calibration varies between basins; it depends on the scale of the DEM relative to the scale of topographic variability in the landscape.

F.1.3 Comparison with field observations

TOPMODEL was not designed for every possible combination of climate and landscape. The original model assumes that infiltration is non-limiting (*i.e.*, saturation-excess is the only runoff generation mechanism) and that return flow is negligible. These assumptions may be inappropriate in arid climates where precipitation intensities can exceed infiltration capacities, resulting in Hortonian flow, and where parched soils may allow for downslope re-infiltration of surface runoff (return flow). The model is most appropriate for basins with a total area of less than 500 km^2 underlain by impermeable rock and existing in moderate to steep topography (Beven and Kirkby 1979; Quinn and Beven 1993).

Basin	$E[Q]$ [mm/d]	$\sigma(Q)$ [mm/d]	CV(Q) [–]
Bear Valley	1.19	1.36	1.1
Big Creek	0.76	1.42	1.9
Schoharie	1.51	1.89	1.3
Tombstone	-8.8e-3	1.97	-220
Yreka	0.89	0.62	0.7

Table F.1: Mean, standard deviation, and coefficient of variation of recharge in five basins.

Studies comparing the topographic index $\ln(a/\tan\beta)$ with the observed water table have had varying results. Burt and Butcher (1985) found that $\ln(a/\tan\beta)$ is poorly correlated with depth to saturation on a small hillslope in England, especially in drier conditions. Thompson and Moore (1996) found, however, that $\ln(a/\tan\beta)$ was a better predictor of water table depth than a, $\tan\beta$, or a surface curvature parameter. In a related study, Moore and Thompson (1996) developed a TOPMODEL-based linear function relating water table depths in time and space. Field observations from convergent areas provided a good fit to the model; this implies that the water table shifts up and down over time without a significant change in shape. Troch *et al.* (1993) similarly found that the TOPMODEL assumption about a linear water table matched with observed water table profiles over a 12-day period. In an application of a TOPMODEL-based model to seven catchments in Australia, Coles *et al.* (1997) found that runoff source areas were identified fairly accurately in catchments where Hortonian runoff was negligible.

These studies are only a few of many that have investigated the reliability of TOPMODEL in the field. A comprehensive list of additional sites where TOPMODEL has been applied is provided in Beven (1997).

F.2 Compatibility of TOPMODEL assumptions with GSEM

We investigate whether the equilibrium hydrology calculated by GSEM is consistent with the assumptions on which TOPMODEL is based. The investigation corresponds to the latter three TOPMODEL assumptions; we look at (1) the extent of spatially variable recharge, (2) the extent to which the modeled water table slope does or does not deviate from the ground surface slope, and (3) the effect of a deep soil column on the equilibrium water table profile.

F.2.1 Effective recharge

The TOPMODEL index assumes that effective recharge is spatially constant. The flow into any pixel is set equal to the recharge rate integrated over the contributing area of the pixel. Modeling and field studies contradict this assumption: basins contain areas of both recharge and discharge. TOPMODEL in its original formulation does not allow the negative (upward) recharge that occurs in riparian zones when the water table is at or near the surface and is discharging moisture. Is TOPMODEL able to adequately capture the saturated–unsaturated zone dynamics in the riparian zone, despite its assumption of uniform positive recharge throughout the basin?

Basin	Percent area with $Q > 0$	$E[Q]$ [mm/d]	$\sigma(Q)$ [mm/d]	CV(Q) [–]
Bear Valley	82	1.80	0.39	0.22
Big Creek	89	1.25	0.06	0.05
Schoharie	75	2.57	0.41	0.16
Tombstone	79	0.91	0.12	0.13
Yreka	89	1.09	0.16	0.15

Table F.2: Mean, standard deviation, and coefficient of variation of recharge in five basins, excluding areas where recharge is negative.

TOPMODEL is not designed to incorporate negative recharge, yet GSEM predicts discharge or zero flux in up to 25 percent of the basin area in the study basins. Tables F.1 and F.2 contain the statistics for all cells and for those cells in which recharge is positive, respectively, in five of the study basins. The standard deviations of recharge given in Table F.1 are large; in four of the five basins the coefficient of variation exceeds one. Although most of the pixels recharge at the maximum rate, a substantial area also recharges at the minimum rate. The large deviation is caused by the bimodal distribution in recharge rates. Consideration of only those pixels with positive recharge significantly decreases the coefficient of variation. By excluding the discharging cells, we have essentially converted the distribution into a unimodal form with the great majority of pixels recharging at the maximum rate.

The significance of the discrepancy between TOPMODEL's uniform recharge rate and the variable recharge predicted by GSEM depends on catchment characteristics and the hydrologic output of interest. TOPMODEL may be able to provide a reasonable estimate of the basin-average recharge rate, since most of the drainage area in all five basins is recharging the groundwater at a nearly constant rate. So long as discharge is allowed through base flow or other groundwater–surface water interaction in saturated areas, the assumption of spatially uniform recharge is reasonably compatible with the distributed GSEM output.

F.2.2 Water table slope

It is expected that along a hillslope cross-section, the deviation between the surface and water table slopes will follow a distinct pattern. At a ridge, if the soil column is dry, GSEM sets the water table at the bedrock interface; the deviation between the two slopes therefore will be zero. In the recharge zone, the GSEM water table flattens out, resulting in a slope that is less than the ground surface slope. The difference between the slopes should be large in the recharge zone. The deviation between slopes is small in the midline zone where the water table depth is relatively constant. In the discharge zone, the water table again flattens out relative to the overlying surface; however, the deviation should be less than in the recharge zone because the valleys contain less relief than the upslope area. At the bottom of the hillslope, where a seepage face develops, the water table is constrained to be at the surface and the deviation is zero. It is expected that those basins with a large percentage midline will have a better fit between the surface and water table slopes. It was found in Chapter 4 that the extent of the midline region ranges widely between basins, depending on the efficiency of the saturated and unsaturated zones.

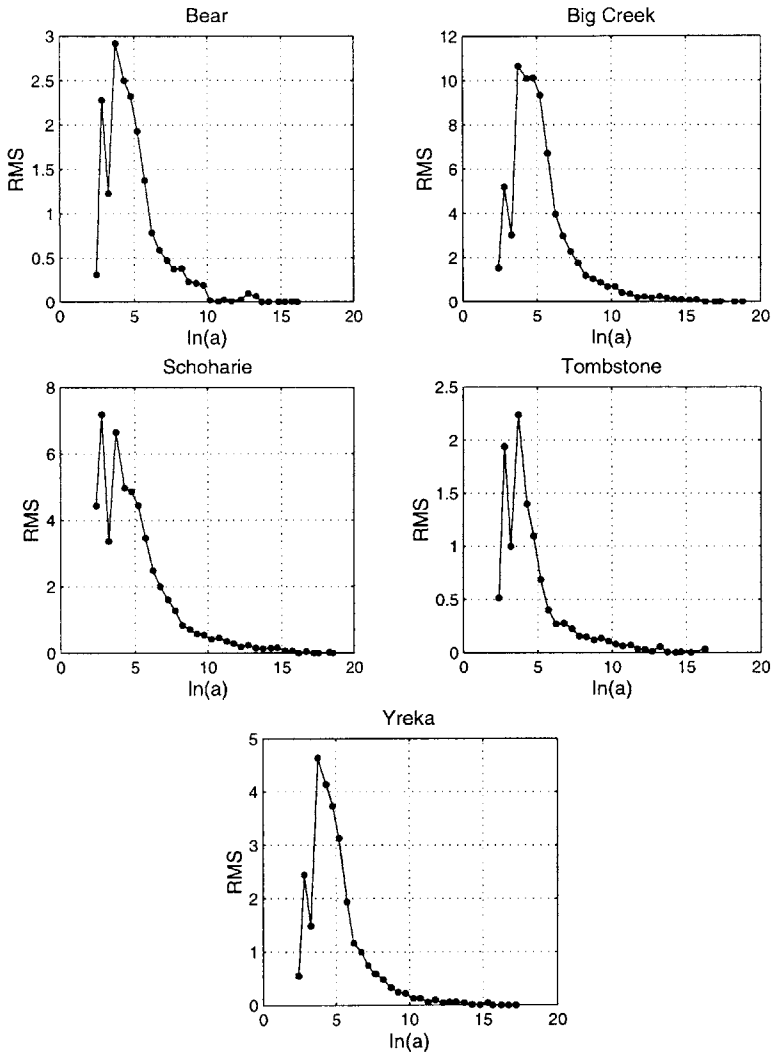

Figure F-1: RMS between water and ground surface slopes, sorted by Kirkby area.

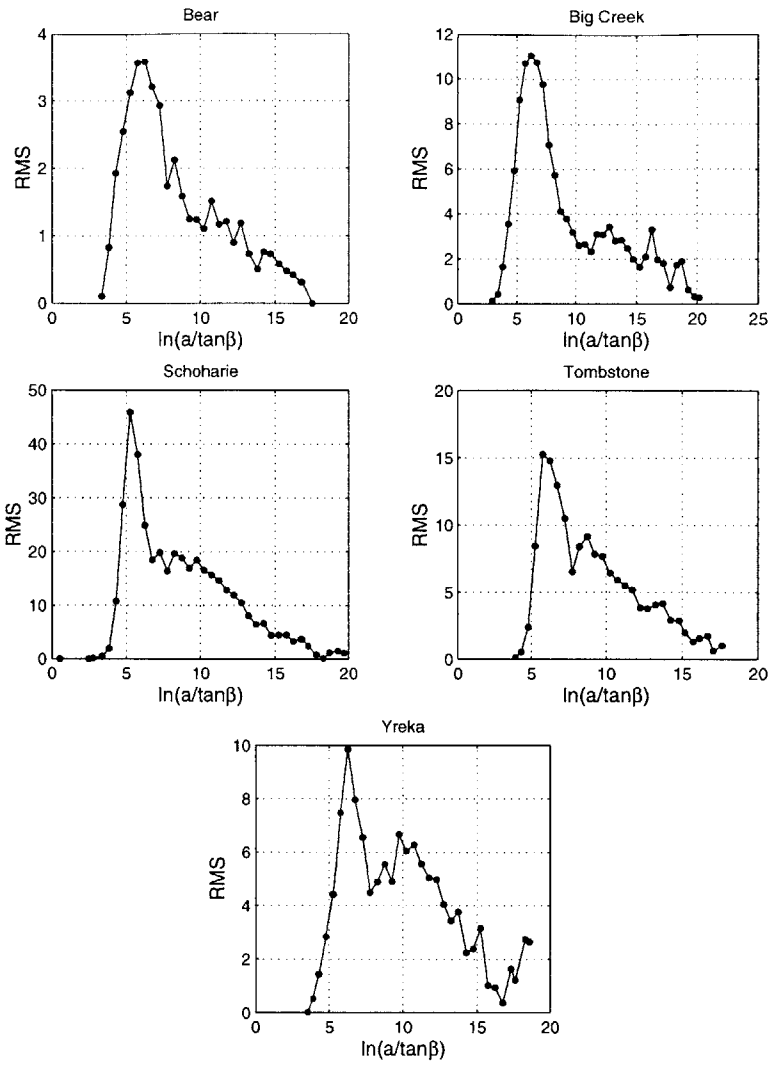

Figure F-2: RMS of the difference in the TOPMODEL index, sorted by the surface-based index. Pixels with a zero slope have been excluded to avoid numerical instability.

Figure F-1 presents the root mean sqare (RMS) between the water table and surface slopes sorted by the area per unit contour length (a). The five basins exhibit a similar pattern of behavior: the RMS begins at low values for small a, increases to a maximum below $\ln(a) = 5$, and then decreases fairly rapidly. The RMS is negligible across approximately half of the dynamic range. The behavior in upslope areas (low a) is as expected, if the plots are taken as an aggregate cross-section, where a represents distance downslope. The RMS is small for dry or nearly-dry areas, increases in the recharge zone, and then decreases in the midline zone. However, the figure does not contain an increase in RMS with further distance toward the outlet, as was expected in the discharge zone. This is likely due to the very low surface slopes in the riparian zone; even if two slopes differ by almost 100 percent, the associated RMS is small if the slopes themselves are small.

The actual indicator of hydrologic response is the TOPMODEL index, $\ln(a/\tan\beta)$; saturation—and therefore also runoff—occurs only when the index exceeds a value based on

the basin-averaged antecedent moisture deficit ($\bar{D}$) and TOPMODEL index (λ). Figure F-2 presents the RMS between the topographic index calculated with the surface and water table slopes. The data are plotted versus the surface-based index to highlight the sensitivity of the index at different ranges.

Figure F-2 excludes pixels with either a water table or surface slope of zero. This removes any effect of the arbitrary minumum slope that must be used to avoid numerical errors from dividing by zero. The surface-based TOPMODEL index deviates consistently from the GSEM-based water table index in upslope areas. A negative feedback arises, limiting the effect of the deviation on the basin-scale water balance: as the water table falls, the transmissivity declines, which reduces the subsurface flow rate. The opposite response will occur when the water table rises. Thus, upslope deviations in the slope-based index are expected to have little effect on the large-scale water balance, even for basins such as Schoharie with a high RMS in upslope areas.

The topographic index is also important for the prediction of saturated areas. Overland flow is primarily generated in the saturated areas that expand and contract under different moisture conditions. Evaporation is also highest in these wet soils. Discrepancies in the calculation of the fluxes in the riparian zone could have an impact on the water balance that is disproportionate to the area of the basin covered by the zone. The RMS values for downslope regions plotted in Figure F-2 indicate an acceptable level of agreement in the two models' prediction of the saturated area between the models.

One striking difference between Figure F-1 and Figure F-2 is that the RMS of slope approaches zero around the mid-range of contributing areas, while the RMS of the topographic index declines more slowly. There are two possible explanations for this. The first is the difference in the values against which the RMS is compared (a vs. $\ln(a/\tan\beta)$). The contributing area is an index of location in the basin only, while $\ln(a/\tan\beta)$ incorporates both location and local gradient. Thus, there is some bias introduced in the sorting of pixels by $\ln(a/\tan\beta)$ since the sorting is influenced by surface slope. The highest values of a correspond to pixels in convergent channels, close to the outlet. These areas generally have a permanent seepage face; the deviation between surface and water table slope is therefore zero. In contrast, a high $\ln(a/\tan\beta)$ may represent a pixel that is very near the outlet (large a) or one that is further from the outlet but has a very low slope (low $\tan\beta$). The sorting of pixels in Figure F-2 mixes these two types of pixels, resulting in a more gradual approach to a low RMS (due to the seepage face) than was seen in Figure F-1. The second potential influence is the exclusion of pixels with a surface or water table slope of zero in Figure F-2. The number of pixels excluded is small—only in Schoharie and Tombstone does it exceed a few percent—but the excluded pixels are by definition found at large values of $\ln(a/\tan\beta)$. However, inclusion of pixels when one of the two models predicts a zero or very small slope would *increase* the deviation, since the index is calculated with slope in the denominator. Therefore, the first reason cited above, the variable against which the RMS is sorted and calculated, is the likely cause of the difference in the behavior seen in Figures F-1 and F-2.

F.2.3 Soil column depth

The exponential decrease in hydraulic conductivity with depth underlies the form of the TOPMODEL index used to predict hydrologic response. The assumption of exponential decay dictates the shape of the baseflow recession curve and the active depth of the soil. Although a few studies have proposed altering the shape of the conductivity profile (*e.g.*,

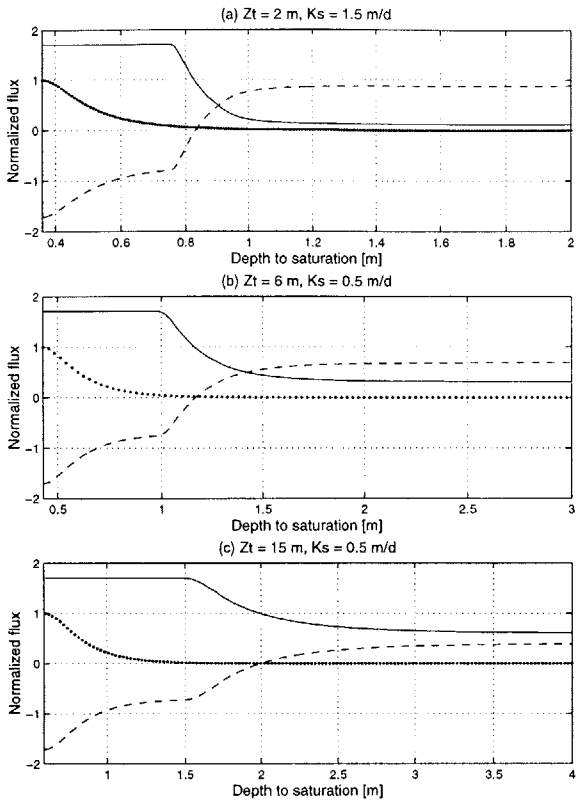

Figure F-3: Equilibrium surface fluxes as a function of water table depth for three soil depths with the same transmissivity. The solid line is evaporation; the dotted line is saturation-excess runoff; and the dashed line is recharge. Fluxes are normalized by mean annual precipitation.

Ambroise *et al.* 1996; Beven 1997; Duan and Miller 1997), the exponential form remains the most widely used.

The exponential profile is best suited for shallow soils. What happens to the equilibrium hydrology when the soil column deepens? We address this question by modeling the most likely water table distribution for a subbasin of Yreka with three different soil depths. The hydraulic conductivity is adjusted so that the transmissivity is the same in each case. This study is designed to highlight the range of water table positions which can result from the same effective parameters but for different soil depths.

Figure F-4 presents the cumulative distribution of water table depth of the three soil depth scenarios. The modeled spatial variation in water table depth increases with increasing soil depth. This result is consistent with the two-dimensional analysis performed by Salvucci (1994) on a planar hillslope. He found that as the soil deepens, the extent of the midline zone shrinks as the recharge and discharge zones expand. While the exponential decay parameter m can be adjusted to account for a deep soil column, it cannot adequately represent the properties of a deep, conductive soil column. The exponential shape dictates a rapid decrease in hydraulic conductivity with depth. In many environments, the hydraulic conductivity has been observed to decline rapidly with depth in the soil column (Beven 1984), as characterized in TOPMODEL. However, in locations with a deep soil

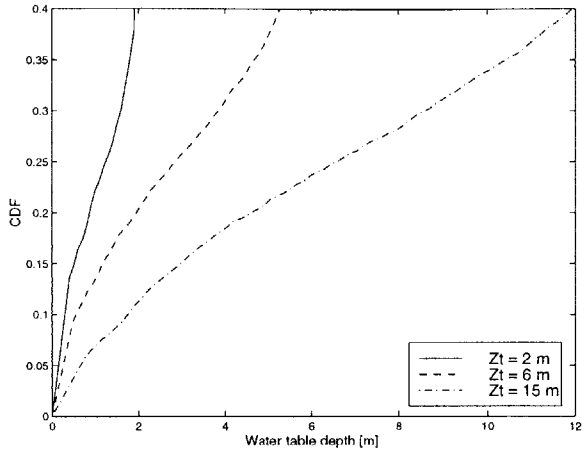

Figure F-4: Cumulative distributions of water table depth for three soil depth scenarios.

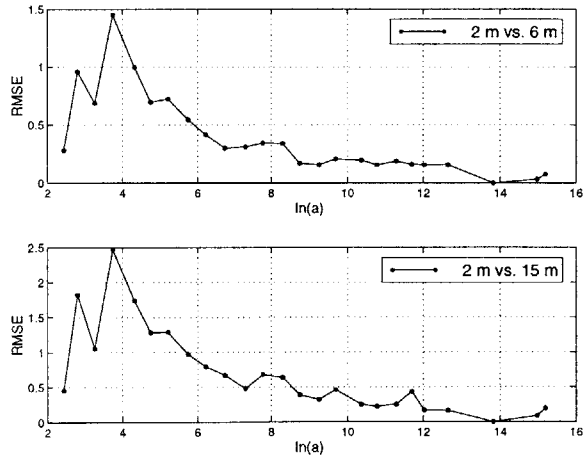

Figure F-5: RMS between water table slopes for different soil depths as a function of Kirkby contributing area.

profile, an exponential conductivity profile may limit the amount of distributed information incorporated in the hydrologic response. The reduction of the midline zone also holds implications for the adequacy of the previous two assumptions: the hydraulic gradient will deviate more from the surface slope in deep soils, and there will likely be greater spatial heterogeneity in saturated-zone recharge rates.

Figure F-5 shows the root mean sqare (RMS) of water table slope for the different soil-depth scenarios. Changes in water table slope affect the agreement between the surface-based topographic index and the actual hydraulic gradient. The effect of increased soil depth is less significant than the initial discrepancy between the water table and surface slopes seen in Figure F-1. While the exponential conductivity profile may break down in deep, conductive soils, its influence on the hydraulic gradient is relatively minor.

F.3 Comparison of model predictions

One way to summarize the discrepancies between the TOPMODEL assumptions and the GSEM hydrology is to compare the shape of the water table distribution across hillslope cross-sections. Juxtaposition of the water table profiles allows comparison of a suite of complex hydrologic processes as represented by a single variable. The water table position determines the hydrological response in both models. In GSEM, the unsaturated zone fluxes depend on the depth to saturation. In TOPMODEL, the water table depth is directly related to $\ln(a/\tan\beta)$, the index of hydrologic similarity.

The models must be calibrated to the same units before they can be compared directly. The parameters that require calibration are the storage decay term m (or its equivalent for water table depth, f) and the surface hydraulic conductivity K_o. We estimate both parameters using the basin-averaged GSEM hydrology. The resulting values can be used to generate the distribution of any other variable of interest. The decay parameter is calculated by calibration with the GSEM storage and recharge values; surface conductivity is determined by matching the model transmissivities. The calibration procedure is described below.

F.3.1 TOPMODEL calibration

The parameter m is the exponential decay rate of conductivity with available storage D_i, defined by the relationship $K_i = K_o e^{-D_i/m}$ where K_o is the hydraulic conductivity when the soil is saturated. Equation F.3 gave the expression for the basin-average moisture deficit:

$$\bar{D} = m \ln T_o - m \ln \bar{\imath} - m\lambda \tag{F.5}$$

which is written in terms of m to provide the calibration equation

$$m = \frac{\bar{D}}{\ln T_o - \ln \bar{\imath} - \lambda} \tag{F.6}$$

Of the four TOPMODEL parameters needed to estimate m in Equation F.6, three have direct complements in the GSEM formulation: surface transmissivity is the product of the saturated hydraulic conductivity K_s and the depth of the soil column Z_T; λ may be calculated directly from the DEM; and $\bar{D}$ is set equal to the basin-average equilibrium available moisture storage $\bar{\forall}_e$. However, there is no direct parallel between TOPMODEL's recharge,

Basin	$ln(\bar{\imath})$ [mm d^{-1}]	λ [m^{-1}]	$\forall_e$ [m]	m [m^{-1}]	f [m]	K_o [m d^{-1}]
Bear Valley	0.61	6.2	0.26	0.22	1.40	2.14
Big Creek	0.21	6.0	0.33	0.14	1.83	3.17
Schoharie Creek	0.91	7.1	0.25	0.44	0.59	9.50
Tombstone	-0.09	7.6	0.29	0.36	0.81	4.94
Yreka	0.008	6.5	0.29	0.19	1.59	1.88

Table F.3: Parameters used in calibration of TOPMODEL to equilibrium model mean hydrology. See text for details.

assumed spatially homogeneous and vertically downward, and the equilibrium recharge calculated by GSEM, which varies spatially and may occur in either vertical direction. An approximate estimate of $\bar{\imath}$ is made from the spatial average of all model cells where recharge is downward (positive). The value of m can then be determined from the estimates of the parameters in Equation F.6.

The second parameter which requires calibration is the surface conductivity K_o. It is determined by equating the GSEM transmissivity ($K_s Z_T$) to the TOPMODEL transmissivity T_o. The relationship between surface transmissivity and conductivity in TOPMODEL is determined by integrating the exponential relationship $K_i = K_o e^{-fZ_i}$ over the entire soil column and solving for K_o to give

$$K_o = \frac{T_o}{f} \tag{F.7}$$

The value of the surface conductivity depends on the depth-dependent decay parameter f rather than the previously determined moisture-equivalent m. The parameters are related by the soil characteristic $\Delta\theta$:

$$f = \frac{\Delta\theta}{m} \tag{F.8}$$

The parameter $\Delta\theta$ is defined as the "effective water content change per unit depth in the unsaturated zone due to rapid gravity drainage down to 'field capacity'" (Beven 1995). It is approximated by the effective porosity, n_e, which has been estimated from the Brooks-Corey hydraulic model. Given the soil descriptors of porosity, hydraulic conductivity, and depth to bedrock used in GSEM, TOPMODEL's K_o can be calculated for each basin.

The values of the calibration parameters and intermediate variables for five of the study basins are provided in Table F.3. In the other five basins, the calibration of m to the modeled equilibrium hydrology results in a negative value; m is only physically meaningful when positive. In low-relief basins, large values of λ (due to small slopes in the denominator) prohibit the calibration of TOPMODEL using the technique described here.

A complete list of parameter values used in different TOPMODEL applications can be found in Beven (1997). The values for m generated in the TOPMODEL studies are consistently one to two orders of magnitude smaller than the values calibrated to GSEM. The bias probably arises from the estimation of $\bar{\imath}$ and the differences in transmissivities between the models. As stated previously, there is a conceptual discrepancy between the recharge fluxes in the two models. The exclusion of all cells with negative recharge may overestimate the mean flux; this would exaggerate any positive bias in the m estimate.

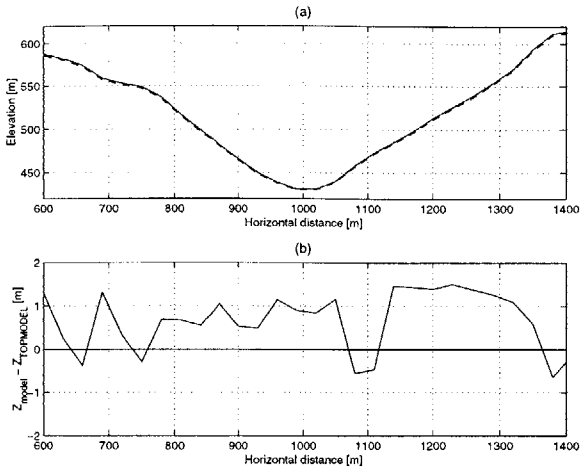

Figure F-6: Sample cross-section of surface elevation and GSEM and TOPMODEL water table, Bear Valley, CA. Subplot (a) presents the ground surface (solid line) and GSEM water table (dashed line). Subplot (b) presents the difference between GSEM and TOPMODEL water table depths along the cross-section.

The second probable source of bias is in the surface transmissivity T_o. GSEM has a high transmissivity because the saturated hydraulic conductivity is assumed to be constant across the entire soil column (2 m depth). This results in a higher transmissivity than is found in the TOPMODEL studies; the exponential transmissivity profile results in a lower value when integrated over the soil column. The bias in transmissivity also raises the estimate of m. In the subsequent comparison of the two models, the calibrated values shown in Table F.3 are used. The discussion includes the sensitivity of the results to the values of m (f) and K_o.

F.3.2 Comparison of water table profiles

We compare cross-sectional profiles of the water table to investigate the effect of the discrepancies between the TOPMODEL assumptions and GSEM output on water table depth. The location of the water table influences all components of the water balance, including the saturated flow rate, runoff, and evaporation. The previous section identified patterns of variation between conditions assumed by TOPMODEL (*i.e.*, that surface slope is a reasonable approximation of the hydraulic gradient) and the equilibrium hydrologic conditions generated by GSEM. However, there may be feedbacks in the models that reduce or enhance the significance of the basic discrepancies on the water table position. For example, a deviation in hydraulic gradient from the ground surface may alter flow rates such that the hydraulic gradient more closely matches the surface. A comparison of the water table profiles groups together the effects of the different assumptions into one spatially resolved characteristic that is easily calculated.

Figures F-6 through F-10 contain sample cross-sections of each of the five basins. Subfigures (a) present the surface topography and the smoothed GSEM water table profile. The water table is plotted to illustrate the magnitude of water table depth variation relative to the relief of the land surface. Subfigures (b) plot the difference between GSEM and TOPMODEL water table depths along the cross-section. We use the smoothed water table

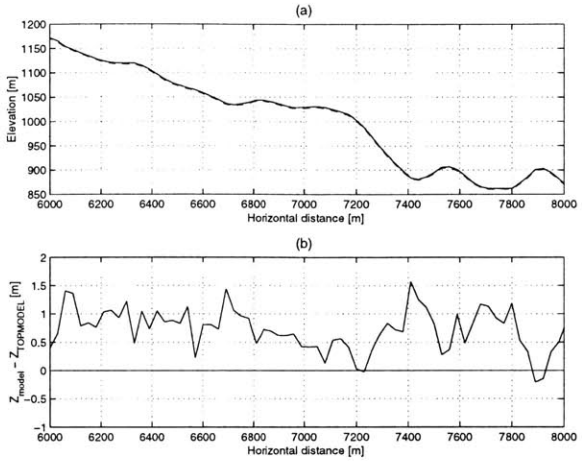

Figure F-7: Sample cross-section of surface elevation and GSEM and TOPMODEL water table, Big Creek, ID. Subplot (a) presents the ground surface (solid line) and GSEM water table (dashed line). Subplot (b) presents the difference between GSEM and TOPMODEL water table depths along the cross-section.

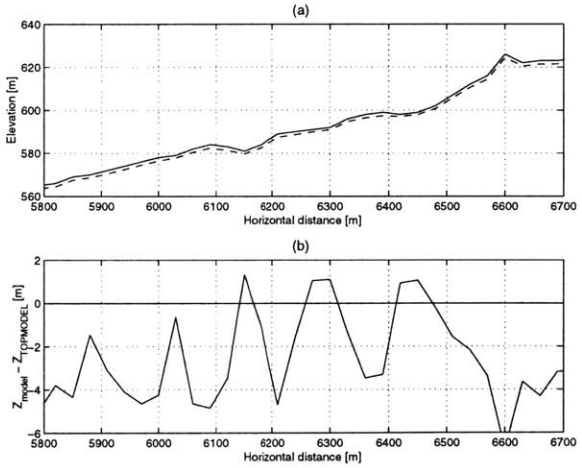

Figure F-8: Sample cross-section of surface elevation and GSEM and TOPMODEL water table, Schoharie, NY. Subplot (a) presents the ground surface (solid line) and GSEM water table (dashed line). Subplot (b) presents the difference between GSEM and TOPMODEL water table depths along the cross-section.

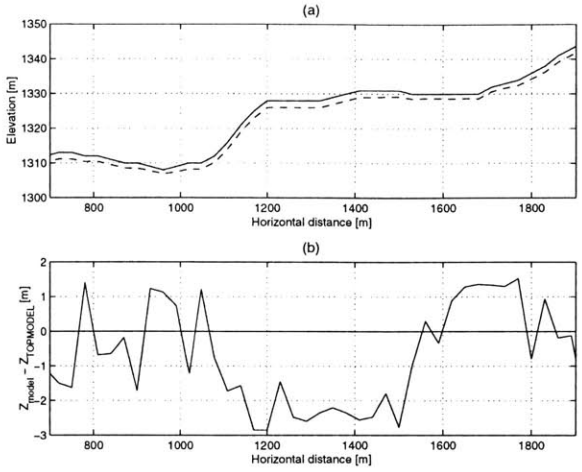

Figure F-9: Sample cross-section of surface elevation and GSEM and TOPMODEL water table, Tombstone, AZ. Subplot (a) presents the ground surface (solid line) and GSEM water table (dashed line). Subplot (b) presents the difference between GSEM and TOPMODEL water table depths along the cross-section.

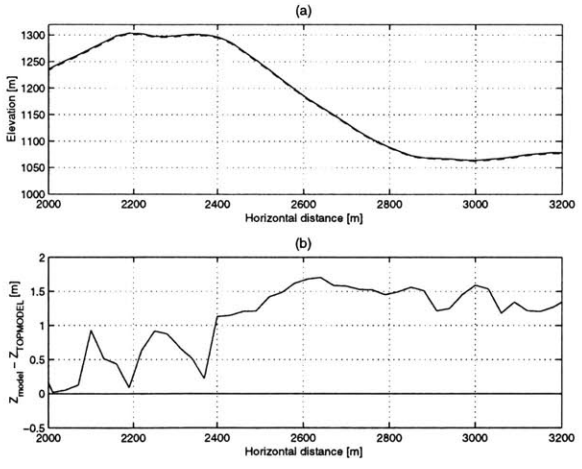

Figure F-10: Sample cross-section of surface elevation and GSEM and TOPMODEL water table, Yreka, CA. Subplot (a) presents the ground surface (solid line) and GSEM water table (dashed line). Subplot (b) presents the difference between GSEM and TOPMODEL water table depths along the cross-section.

depth from GSEM to minimize the effects of the relatively coarse vertical resolution of the DEM. The GSEM water table depth is bounded by the soil depth of two meters. There is no such limit on the water table depth in TOPMODEL; TOPMODEL assumes an infinite soil depth with declining conductivity.

The basin cross-sections provide two sets of information in a comparison of GSEM and TOPMODEL: (1) the magnitude of the difference between the water table depths predicted by the two models, and (2) the relationship of the difference to the overlying topography. We first consider the magnitude of the difference. In Bear Valley, Big Creek, and Yreka, the difference between the GSEM and TOPMODEL water table depths is positive for most of the pixels. In contrast, it is predominantly negative in Schoharie and Tombstone. The difference can be understood from the equation used to calculate water table depth in TOPMODEL:

$$Z_w = -\frac{1}{f}\left(\ln\frac{\bar{\imath}f}{K_o} + \ln\frac{a}{\tan\beta}\right) \tag{F.9}$$

The two basins in which TOPMODEL predicts deep water tables, Schoharie and Tombstone, are both characterized by low values of f and high values of K_o; this results in a large first term in Equation F.9 and a deep water table for most values of $\ln(a/\tan\beta)$.

Since surface conductivity K_o depends on f, an understanding of the physical determinants of f fully explains the behavior observed in Figures F-6 through F-10. The parameter f is inversely related to λ. On average, lower slopes require a greater depth of conductive soil to support the same amount of downslope moisture flux. This causes the inverse relationship between f and λ in the calibration process: a steep slope (large λ) causes a small f. At the scale of individual pixels, the value of f affects the local water table depth, as seen in Equation F.9. For almost all values of $\ln(a/\tan\beta)$, the water table depth is deeper in the relatively flat basins (Schoharie, Tombstone) than in the steeper basins (Bear Valley, Big Creek, Yreka).

The magnitude of the difference in water table depths may also be influenced by biases in the calibration procedure. The calibration resulted in high values of m relative to those in the literature and correspondingly low values of f. From Equation F.9, a low f would cause spuriously large water table depths. This could account for the large differences seen in the cross-sections. However, the bias in the calibrated TOPMODEL parameters should not influence the pattern of differences within each cross-section, since a single value of f is used for each basin. It is still possible to identify connections between surface features and deviations in the models' predictions of water table depth.

The second aspect of the cross-section figures is the relationship between the differences in water table depths and the overlying topography. The juxtaposed plots in Figures F-6 through F-10 indicate a relationship between the shape of the hillslope and the difference between the water table depths of the two models. Convex sections of the hillslope generally correspond to locations where the TOPMODEL water table depth is greater than or near the GSEM depth. Conversely, TOPMODEL predicts a shallower water table than GSEM on concave slopes. The presence of a relationship between hillslope shape and difference in water table depth is confirmed by Figure F-11, in which the mean-centered difference in water table depth is plotted versus the second derivative of the elevation along the cross-section. Although the plots are noisy, the slope of the best-fit line is negative for each basin at a 95 percent confidence level. It is expected that the line should go through the origin, since the difference between the models should be minimal when the slope is planar (zero curvature).

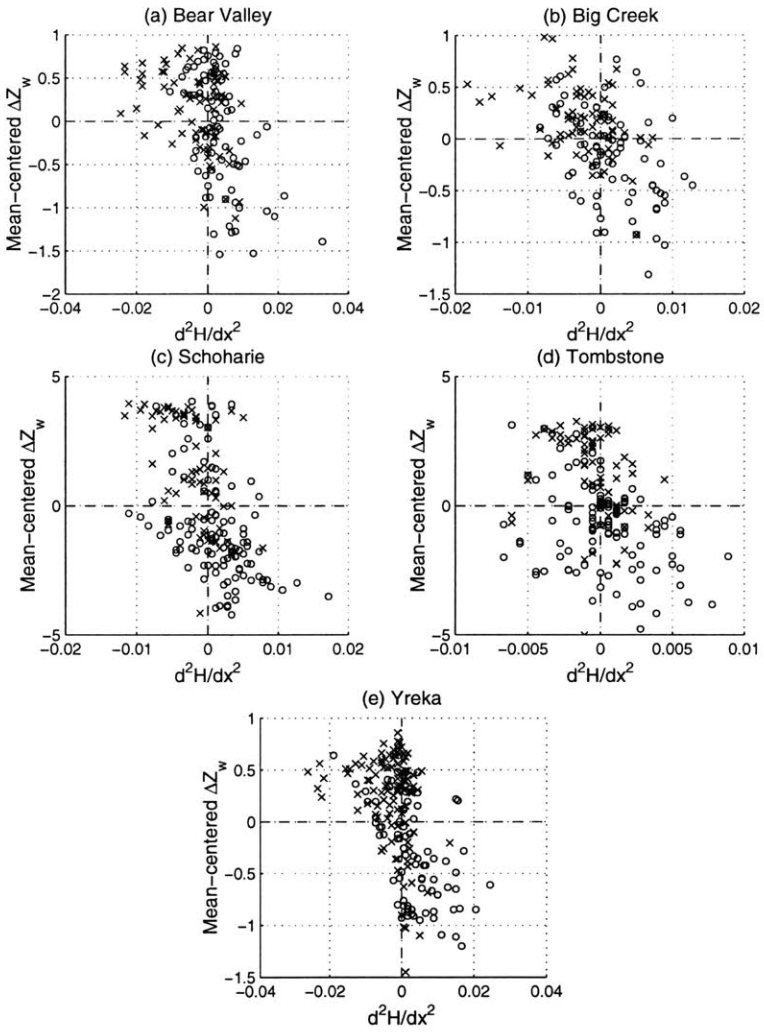

Figure F-11: Relationship of the hillslope curvature to the difference in modeled water table depth between GSEM and TOPMODEL. Depth differences have been mean-centered to remove calibration effects. Circles represent $d^2H/dy^2 < 0$; X's represent $d^2H/dy^2 > 0$.

We hypothesize that the relationship between curvature and differences in water table position stems from the fact that the TOPMODEL index, used to represent the influence of topography on hydrology, only considers the relief directly adjacent to the pixel of interest. The parameter $\ln(a/\tan\beta)$ does not incorporate any information beyond the slopes of the neighboring uphill pixels and the total contributing area feeding a pixel. This may be acceptable on simple terrain, where there is little spatial variation in slope. However, as the cross-sections of water table position illustrate, natural terrain contains both convex and concave slopes. When TOPMODEL finds itself in a concave slope, it calculates a shallow water table because the topographic index indicates a shallow water table in concave areas. The algorithm may err when a divergent slope lies directly upslope of the concave section. Similarly, TOPMODEL may exaggerate the water table depth on convex slopes since it cannot accommodate upslope convergence of moisture in concave stretches. Because GSEM is continuous across the basin (it does not limit its calculations to adjacent pixels), it is able to incorporate the effect of juxtaposed concave and convex slopes on the water table. On short hillslopes or in areas where there is little variability in slope, the difference will lose significance. However, in complex terrain, the difference between the two models is on the order of one meter, which could result in TOPMODEL's overprediction of saturation in convergent regions and underprediction of evaporation in upslope areas.

F.3.3 Comparison of flood response indicators

The previous sections have investigated the differences between GSEM and TOPMODEL in the spatial distribution of equilibrium hydrology. We now look at the possible implications for flood runoff predictions. This is done through a comparison of the models' distributions of pre-storm available soil moisture storage.

A series of papers have used TOPMODEL as a basis for the generation of flood-frequency characteristics (Wood and Hebson 1986; Beven 1987; Sivapalan *et al.* 1987; Sivapalan and Wood 1990). The distribution of the TOPMODEL $\ln(a/\tan\beta)$ index is assumed to predict saturation-excess runoff under a range of forcing conditions. Full application of the flood-frequency technique requires extensive calibration of both soil and hydrologic variables. Our goal in comparing TOPMODEL with GSEM predictions is to minimize the number of parameters to be estimated. We focus on the distribution of antecedent available storage as a proxy for basin response. In large storms, saturation-excess runoff is the dominant mechanism of streamflow generation; the available storage distribution is the best indicator of how the basin will respond to precipitation.

Figure F-12 shows the cumulative distribution functions of available storage from the two models. The most striking feature of the data shown in Figure F-12 is the consistent positive bias of available storage predicted by TOPMODEL. Even though m was calibrated for the mean GSEM available storage, the mean TOPMODEL storage deficit differs because of the different soil profile shapes of the two models. TOPMODEL has an infinite soil column with declining conductivity; the soil column in GSEM is a step function with an impermeable layer located 2 m below the surface. The surface transmissivity used in calibration has a very different implication for depth to saturation: for the same transmissivity, the water table must be much deeper in TOPMODEL than in GSEM. This results in the overestimation of m and the prediction of very deep water tables, as reflected in Figures F-6 through F-10. The bias in water table depths is transferred to a bias in available storage, since the moisture deficit is positively correlated with depth to saturation.

The relative shapes of the available storage curves are better seen by rescaling the

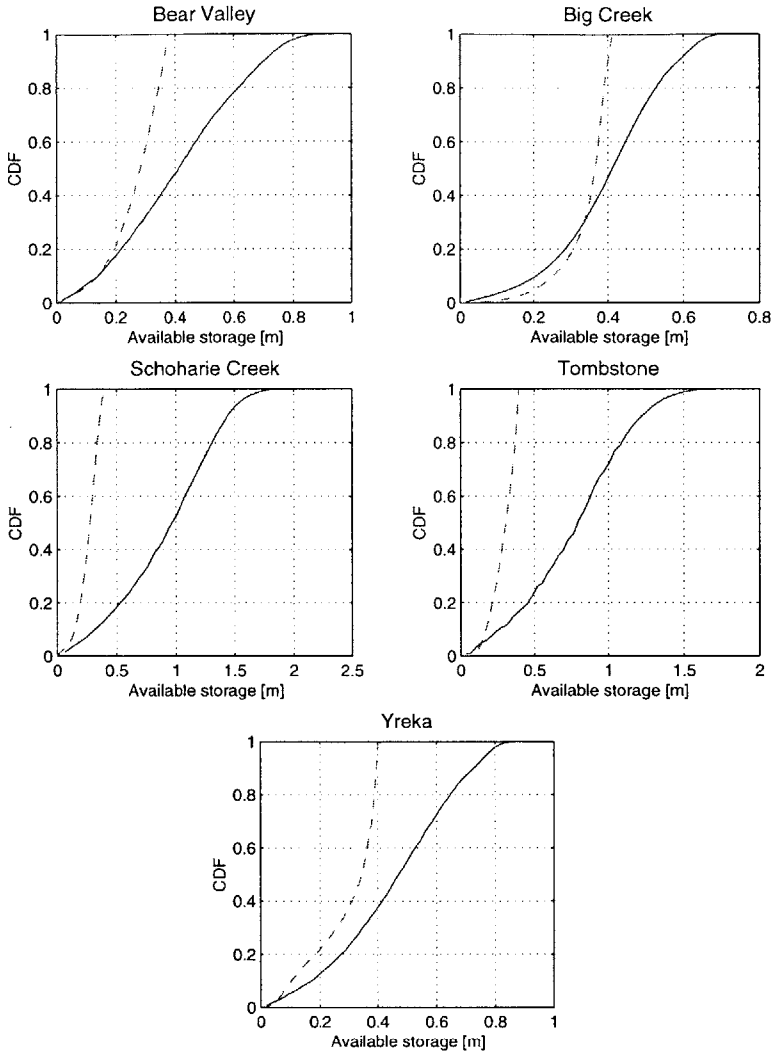

Figure F-12: Comparison of calibrated available storage distribution from TOPMODEL (solid line) and GSEM(dashed line).

Basin	Ratio of medians	Adjusted m
Bear Valley	0.70	0.15
Big Creek	0.87	0.12
Schoharie Creek	0.29	0.13
Tombstone	0.37	0.13
Yreka	0.72	0.14

Table F.4: Adjustment of parameter m for equal median available storage between GSEM and TOPMODEL.

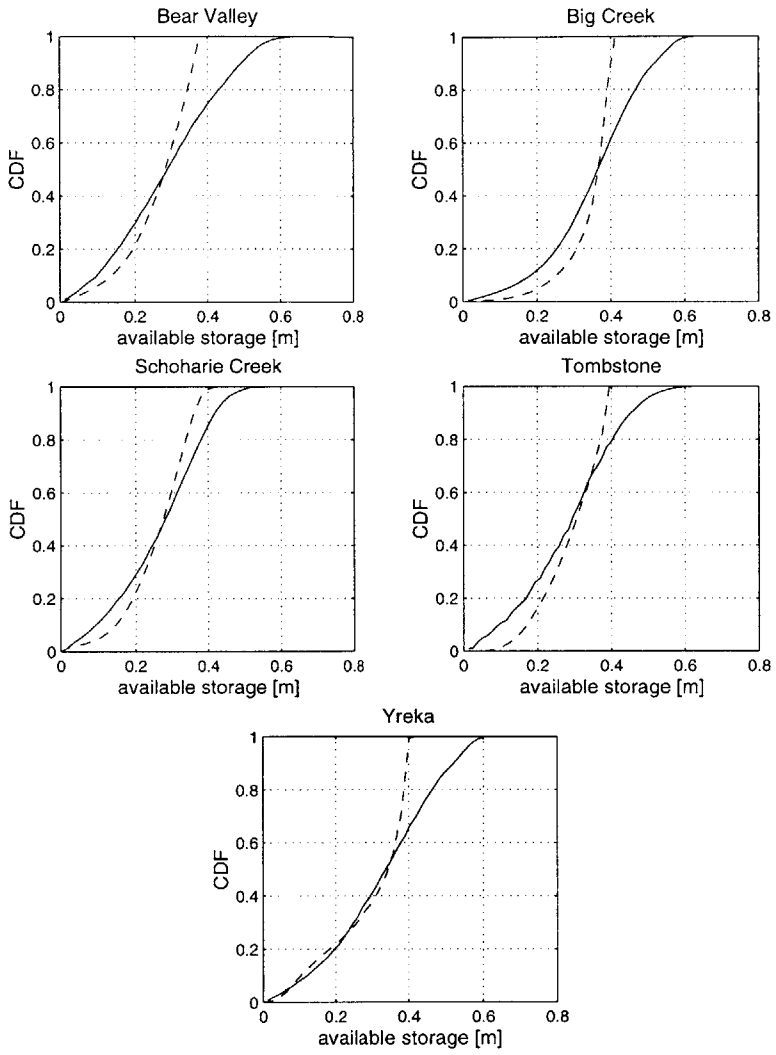

Figure F-13: Comparison of available storage distribution from TOPMODEL (solid line) and GSEM (dashed line). TOPMODEL curve is rescaled to have an equal median to the GSEM curve.

TOPMODEL values so that the median values of the two distributions are the same. The adjusted curves are shown in Figure F-13; the scaling factors and resulting m values are given in Table F.4. The adjusted values of m are still one to two orders of magnitude greater than the values from the literature. However, the adjusted curves shown in Figure F-13 provide the opportunity to compare the qualitative runoff response of the basins predicted by the two models.

The GSEM distributions end sharply at an available storage of between 25 and 50 cm. This is because the impermeable bedrock boundary creates an upper limit on the storage capacity of the soil. In contrast, the soil column in TOPMODEL has no such discrete limit; the exponential decline in conductivity with depth causes a gradually decreasing permeability. As a result, the TOPMODEL curves in Figure F-12 have a smoother distribution of available storage values. The response curves for saturation-excess runoff will reflect the differences in the antecedent distribution of available storage. TOPMODEL will generally predict runoff occurring over a larger percentage of the basin in low-rainfall storms, corresponding to the greater cumulative distribution at low storage values. In extreme storms, GSEM will predict complete saturation at precipitation depths up to 20 cm less than TOPMODEL. The one exception to this pattern is Yreka, in which the adjusted curves are nearly identical for approximately 60 percent of the basin.

Bibliography

[1] M. B. Abbott, J. C. Bathurst, J. A. Cunge, P. E. O'Connell, and J. Rasmussen. An introduction to the European Hydrological System – Systeme Hydrologique Europeen, 'SHE', 2: Structure of a physically-based, distributed modelling system. *Journal of Hydrology*, 87:61–77, 1986.

[2] A. D. Abrahams. Drainage densities and sediment yields in eastern Australia. *Australian Geographical Studies*, 20:161–188, 1972.

[3] Agricultural Research Service. ARS water database. http://hydrolab.arsusda.gov/wdc/az.htm, 1999.

[4] B. Ambroise, K. Beven, and J. Freer. Toward a generalization of TOPMODEL concepts: Topographic indices of hydrological similarity. *Water Resources Research*, 32(7):2135–2145, July 1996.

[5] M. G. Anderson and T. P. Burt. The role of topography in controlling throughflow generation. *Earth Surface Processes*, 3:331–334, 1978.

[6] E. S. Ateljevich. Seasonal variation and spatial organization of hydrologic fluxes over complex topography. Master's thesis, MIT, 1995.

[7] R. D. Barling, I. D. Moore, and R. B. Grayson. A quasi-dynamic wetness index for characterizing the spatial distribution of zones of surface saturation and soil water content. *Water Resources Research*, 30(4):1029–1044, 1994.

[8] R. P. Betson. What is watershed runoff? *Journal of Geophysical Research*, 69(8):1541–1552, 1964.

[9] K. Beven. Towards the use of catchment geomorphology in flood frequency predictions. *Earth Surface Proesses and Landforms*, 12:69–82, 1987.

[10] K. Beven. TOPMODEL: A critique. *Hydrological Processes*, 11:1069–1085, 1997.

[11] K. Beven, R. Lamb, P. Quinn, R. Romanowicz, and J. Freer. Topmodel. In V. P. Singh, editor, *Computer models of watershed hydrology*, pages 627–668. Water Resources Publications, Highlands Ranch, CO, 1995.

[12] K. J. Beven. Infiltration into a class of vertically non-uniform soils. *Hydrological Sciences Journal*, 29:425–434, 1984.

[13] K. J. Beven. Runoff production and flood frequency in catchments of order n: an alternative approach. In V. K. Gupta, I. Rodriguez-Iturbe, and E. F. Wood, editors, *Scale problems in hydrology*, pages 107–131. Reidel, Dordrecht, 1986b.

[14] K. J. Beven and M. J. Kirkby. A physically based, variable contributing area model of basin hydrology. *Hydrological Sciences Journal*, 24(1):43–69, 1979.

[15] C. R. Beverly, R. J. Nathan, K. W. J. Malafant, and D. P. Fordham. Development of a simplified unsaturated module for providing recharge estimates to saturated groundwater models. *Hydrological Processes*, 13(5):653–675, 1999.

[16] P. W. Birkeland. *Soils and Geomorphology.* Oxford University Press, New York, 3rd edition edition, 1999.

[17] S. Blazkova and K. Beven. Flood frequency prediction for data limited catchments in the Czech Republic using a stochastic rainfall model and TOPMODEL. *Journal of Hydrology*, 195:256–278, 1997.

[18] G. B. Bonan. Sensitivity of a GCM simulation to subgrid infiltration and surface runoff. *Climate Dynamics*, 12:279–285, 1996.

[19] R. L. Bras. *Hydrology: an introduction to hydrologic science.* Addison-Wesley, Reading, MA, 1990.

[20] P. Bruneau, C. Gascuel-Odoux, P. Robin, P. Merot, and K. Beven. Sensitivity to space and time resolution of a hydrological model using digital elevation data. *Hydrological Processes*, 9:69–81, 1995.

[21] R. J. C. Burnash, R. L. Ferral, and R. A. McGuire. A generalized streamflow simulation system — conceptual model for digital computers. Technical report, U.S. Department of Commerce National Weather Service and State of California Department of Water Resources, March 1973.

[22] T. P. Burt and D. P. Butcher. Topographic controls of soil moisture distributions. *Journal of Soil Science*, 36:469–486, 1985.

[23] L. Cadavid, J. T. B. Obeysekera, and H. W. Shen. Flood frequency derivation from kinematic wave. *Journal of Hydraulic Engineering ASCE*, 117:489–510, 1991.

[24] A. Calver and W. L. Wood. The Institute of Hydrology distributed model. In V. P. Singh, editor, *Computer models of watershed hydrology*, pages 595–626. Water Resources Publications, Highlands Ranch, CO, 1995.

[25] M. A. Carson and M. J. Kirkby. *Hillslope form and process.* Cambridge University Press, 1972.

[26] S. Chairat and J. W. Delleur. Effects of the topographic index distribution of predicted runoff using GRASS. *Water Resources Bulletin*, 29(6):1029–1034, 1993.

[27] T. G. Chapman. Comment on 'evaluation of automated techniques for base flow and recession analyses' by R. J. Nathan and T. A. McMahon. *Water Resources Research*, 27(7):1783–1784, 1991.

[28] N. A. Coles, M. Sivapalan, J. E. Larsen, P. E. Linnet, and C. K. Fahrner. Modelling runoff generation on small agricultural catchments: can real world runoff responses be captured? *Hydrological Processes*, 11:111–136, 1997.

[29] A. Crave and C. Gascuel-Odoux. The influence of topography on time and space distribution of soil surface water content. *Hydrological Processes*, 11:203–210, 1997.

[30] C. Daly, R. P. Neilson, and D. L. Phillips. A statistical-topographic model for mapping climatological precipitation over mountainous terrain. *Journal of Applied Meteorology*, 33:140–158, 1994.

[31] C. Daly, G. H. Taylor, and W. P. Gibson. The PRISM approach to mapping precipitation and temperature. In *10th Conf. on Applied Climatology*, pages 10–12, Reno, NV, 1997. American Meteorological Society.

[32] M. A. Diaz-Granados, J. B. Valdes, and R. L. Bras. A physically-based flood frequency distribution. *Water Resources Research*, 20(7):995–1002, 1984.

[33] W. E. Dietrich, R. Reiss, M.-L. Hsu, and D. R. Montgomery. A process-based model for colluvial soil depth and shallow landsliding using digital elevation data. *Hydrological Processes*, 9:383–400, 1997.

[34] S. L. Dingman, editor. *Physical hydrology.* Prentice Hall, 1993.

[35] P. A. Domenico and F. W. Schwartz. *Physical and chemical hydrogeology.* John Wiley and Sons, New York, 1990.

[36] J. C. Doornkamp and C. A. M. King. *Numerical analysis in geomorphology: an introduction.* St. Martin's Press, New York, 1971.

[37] J. Duan and N. N. Miller. A generalized power function for the subsurface transmissivity profile in TOPMODEL. *Water Resources Research*, 33(11):2559–2562, 1997.

[38] T. Dunne and R. D. Black. An experimental investigation of runoff production in permeable soils. *Water Resources Research*, 6(3):478–490, 1970a.

[39] T. Dunne and R. D. Black. Partial area contributions to storm runoff in a small New England watershed. *Water Resources Research*, 6(5):1296–1311, 1970b.

[40] T. Dunne, T. R. Moore, and C. H. Taylor. Recognition and prediction of runoff-producing zones in humid regions. *Hydrological Sciences Bulletin*, 20(3):305–327, 1975.

[41] P. S. Eagleson. Dynamics of flood frequency. *Water Resources Research*, 8(4):878–898, 1972.

[42] P. S. Eagleson. Climate, soil, and vegetation, 1–7. *Water Resources Research*, 14(5):705–776, 1978.

[43] P. S. Eagleson. Climate, soil, and vegetation, 1, Introduction to water balance dynamics. *Water Resources Research*, 14(5):705–712, 1978a.

[44] P. S. Eagleson. Climate, soil, and vegetation, 2, The distribution of annual precipitation derived from observed storm sequences. *Water Resources Research*, 14(5):713–721, 1978b.

[45] P. S. Eagleson. Climate, soil, and vegetation, 3, A simplified model of soil moisture movement in the liquid phase. *Water Resources Research*, 14(5):722–730, 1978c.

[46] P. S. Eagleson. Climate, soil, and vegetation, 4, The expected value of annual evapotranspiration. *Water Resources Research*, 14(5):731–739, 1978d.

[47] P. S. Eagleson. Climate, soil, and vegetation, 5, A derived distribution of storm surface runoff. *Water Resources Research*, 14(5):741–748, 1978e.

[48] P. S. Eagleson. Climate, soil, and vegetation, 6, Dynamics of the annual water balance. *Water Resources Research*, 14(5):749–764, 1978f.

[49] P. S. Eagleson. Climate, soil, and vegetation, 7, A derived distribution of annual water yield. *Water Resources Research*, 14(5):765–776, 1978g.

[50] F. Ebisemiju. An objective criterion for the selection of representative basins. *Water Resources Research*, 15:148–157, 1979.

[51] J. Famiglietti and E. F. Wood. Multiscale modeling of spatially variable water and energy balance processes. *Water Resources Research*, 30:3061–3078, 1994a.

[52] J. Famiglietti and E. F. Wood. Application of multiscale water and energy balance models on a tallgrass prairie. *Water Resources Research*, 30:3079–3093, 1994b.

[53] Y. Fan and R. L. Bras. Analytical solutions to hillslope subsurface storm flow and saturation overland flow. *Water Resources Research*, 34(4):921–927, 1998.

[54] R. K. Farnsworth and E. S. Thompson. Mean monthly, seasonal, and annual pan evaporation for the United States. NOAA Technical Report 34, National Weather Service, December 1982.

[55] J. Freer, J. McDonnell, K. Beven, D. Brammer, D. Bruns, R. Hooper, and C. Kendal. Topographic controls on subsurface storm flow at the hillslope scale for two hydrologically distinct small catchments. *Hydrological Processes*, 11:1347–1352, 1997.

[56] R. A. Freeze. Role of subsurface flow in generating surface runoff, 2, Upstream source areas. *Water Resources Research*, 8(5):1272–1283, 1972.

[57] R. A. Freeze and J. A. Cherry. *Groundwater.* Prentice-Hall, Inc., Englewood Cliffs, NJ, 1979.

[58] F. Gallart, J. Latron, P. Llorens, and D. Rabada. Hydrological functioning of Mediterranean mountain basins in Vallcebre, Catalonia: some challenges for hydrological modelling. In K. J. Beven, editor, *Distributed hydrological modelling: applications of the TOPMODEL concept*, Advances in hydrological processes, pages 181–190. John Wiley and Sons, New York, 1997.

[59] L. Garrote and R. Bras. A distributed model for real-time flood forecasting using digital elevation models. *Journal of Hydrology*, 167:279–306, 1995.

[60] J. Gerrard. *Soil geomorphology: An integration of pedology and geomorphology.* Chapman and Hall, London, 1992.

[61] I. Gradshteyn and I. Ryzhik. *Table of integrals, series and products.* Academic Press, New York, 1965.

[62] R. B. Grayson, G. Bloschl, and I. D. Moore. Distributed parameter hydrologic modelling using vector elevation data: THALES and TAPES-C. In V. P. Singh, editor, *Computer models of watershed hydrology*, pages 669–696. Water Resources Publications, Highlands Ranch, CO, 1995.

[63] R. B. Grayson, A. W. Western, and F. H. Chiew. Preferred states in spatial soil moisture patterns: local and nonlocal controls. *Water Resources Research*, 33(12):2897–2908, 1997.

[64] K. Hawk and P. S. Eagleson. Climatology of station storm rainfall in the continental United States: Parameters of the Barlett-Lewis and Poisson rectangular pulse models. Technical report, MIT, 1992.

[65] K. L. Hawk. Climatology of station storm rainfall in the continental United States: parameters of the Bartlett-Lewis and Poisson rectangular pulse models. Master's thesis, MIT, 1992.

[66] C. S. Hebson and E. F. Wood. A derived flood frequency distribution using Horton order ratios. *Water Resources Research*, 18(5):1509–1518, 1982.

[67] J. D. Hewlett. and A. R. Hibbert. Moisture and energy conditions within a sloping soil mass during drainage. *Journal of Geophysical Research*, 68(4):1081–1087, 1963.

[68] D. Hillel. *Environmental soil physics.* Academic Press, Boston, 1998.

[69] R. C. Johanson, J. C. Imhoff, and H. H. Davis. User's manual for the Hydrologic Simulation Program – Fortran (HSPF). Technical Report EPA-600/9-80-105, U.S. EPA Environmental Research Lab, Athens, GA, 1980.

[70] J. A. A. Jones. Some limitations to the a/s index for predicting basin-wide patterns of soil water drainage. *Zeitschrift fur Geomorphologie Neue Folge*, 60:7–20, 1986.

[71] P. Y. Julien and B. Saghafian. CASC2D user's manual. Technical report, Dept. of Civil Engineering, Colorado State University, Fort Collins, CO, 1991.

[72] C. P. Kim, G. D. Salvucci, and D. Entekhabi. Groundwater–surface water interaction over simple hillslopes. *In Progress*, 1997.

[73] M. J. Kirkby. Hydrograph modelling strategies. In R. F. Peel, M. D. Chisholm, and P. Haggett, editors, *Processes in physical and human geography*, pages 69–90. Heinemann Educational, London, 1975.

[74] M. J. Kirkby. Hillslope hydrology. In M. J. Kirkby, editor, *Implications for sediment transport*, pages 325–363. Wiley and Sons, 1978.

[75] M. J. Kirkby and R. J. Chorley. Throughflow, overland flow and erosion. *Bulletin of the International Association of Sciences Hydrology*, 12:5–21, 1967.

[76] G. W. Kite. Development of a hydrologic model for a Canadian watershed. *Canadian Journal of Civil Engineering*, 5(1):126–134, 1978.

[77] K. Klink and C. J. Willmott. Influence of soil moisture and surface roughness heterogeneity on modeled climate. *Climate Research*, 4:105–118, 1994.

[78] A. R. Ladson. Soil water predictions by microwave remote sensing and topographic attributes. Master's thesis, University of Minnesota, St. Paul, 1990.

[79] R. Lamb. Calibration of a conceptual rainfall-runoff model for flood frequency estimation by continuous simulation. *Water Resources Research*, 35(10):3103–3114, 1999.

[80] R. Lamb, K. Beven, and S. Myrabø. Discharge and water table predictions using a generalized TOPMODEL formulation. *Hydrological Processes*, 11:1145–1167, 1997.

[81] H. Lettau. Evapotranspiration climatonomy. Part I: A new approach to numerical prediction of monthly evapotranspiration, runoff, and soil moisture storage. *Monthly Weather Review*, 97(10):691–699, 1969.

[82] H. H. Lettau and M. W. Baradas. Evapotranspiration climatonomy. Part I: Refinement of parameterizations exemplified by application to the Mabacan River watershed. *Monthly Weather Review*, 101(8):636–649, 1973.

[83] J. B. Levine and G. D. Salvucci. Equilibrium analysis of groundwater–vadose zone interactions and the resulting spatial distribution of hydrologic fluxes across a Canadian prairie. *Water Resources Research*, 35(5):1369–1383, 1999a.

[84] J. B. Levine and G. D. Salvucci. Characteristic rate scale and timescale of supply-limited transpiration under a Richards-Cowan framework. *Water Resources Research*, 35(12):3947–3954, 1999b.

[85] G. Li, S. H. Luk, and Q. G. Cai. Topographic zonation of infiltration in the hilly loess region, North China. *Hydrological Processes*, 9:227–235, 1995.

[86] R. K. Linsley, J. B. Franzini, D. L. Freyberg, and G. Tchobanoglous. *Water-resources engineering*. McGraw-Hill, Inc., New York, fourth edition, 1992.

[87] G. Marie Saulnier, C. Obled, and K. Beven. Analytical compensation between DTM grid resolution and effective values of saturated hydraulic conductivity within the TOPMODEL framework. In K. J. Beven, editor, *Distributed hydrological modelling: applications of the TOPMODEL concept*, Advances in hydrological processes, pages 249–264. John Wiley and Sons, New York, 1997.

[88] M. McDonald and A. Harbaugh. A modular three-dimensional finite-difference ground-water flow model. Technical report, U.S. Geological Survey, 1988.

[89] P. C. D. Milly and P. S. Eagleson. Effects of spatial variability on annual average water balance. *Water Resources Research*, 23(11):2135–2143, 1987.

[90] G. Milne. Some suggested units of classification and mapping particularly for East African soils. *Soils Research*, 4(2):183–198, 1935.

[91] I. D. Moore, E. O'Loughlin, and G. Burch. A contour-based topographic model for hydrological and ecological applications. *Earth Surface Proesses and Landforms*, 13:305–320, 1988.

[92] R. D. Moore and J. C. Thompson. Are water table variations in a shallow forest soil consistent with the TOPMODEL concept? *Water Resources Research*, 32(3):663–669, 1996.

[93] W. Moore and C. Morgan, editors. *Effects of watershed changes on streamflow.* University of Texas Press, 1969.

[94] M. S. Moughamian, D. B. McLaughlin, and R. L. Bras. Estimation of flood frequency: an evaluation of two derived distribution procedures. *Water Resources Research*, 23(7):1309–1319, 1987.

[95] R. Nathan and T. A. McMahon. Evaluation of automated techniques for base flow and recession analyses. *Water Resources Research*, 26:1465–1473, 1990.

[96] National Soil Survey Center. State soil geographic (STATSGO) data base. Technical Report 1492, USDA Natural Resources Conservation Survey, 1991.

[97] Climatedata, NCDC hourly precipitation CDROM, 1997.

[98] S. E. Nicholson and A. R. Lare. A climatonomic description of the surface energy balance in the central Sahel, Part II: The evapoclimatonomy model. *Journal of Applied Meteorology*, 29:138–146, 1990.

[99] L. Nyberg. Spatial variability of soil water content in the covered catchment at Gaardsjon, Sweden. *Hydrological Processes*, 10(1):89–103, 1996.

[100] F. L. Ogden. CASC2D reference manual. Technical report, Dept. of Civil Engineering, Univ. of Connecticut, Storrs, CT 06369, 1997. 106 pp.

[101] C. D. Ollier. Catenas in different climates. In E. Derbyshire, editor, *Geomorphology and Climate*, pages 137–169. John Wiley and Sons, New York, 1973.

[102] E. M. O'Loughlin. Saturation regions in catchments and their relations to soil and topographic properties. *Journal of Hydrology*, 53:229–246, 1981.

[103] E. M. O'Loughlin. Prediction of surface saturation zones in natural catchments by topographic analysis. *Water Resources Research*, 22(5):794–804, 1986.

[104] L. J. Onesti and T. K. Miller. Patterns of variation in a fluvial system. *Water Resources Research*, 10(6):1178–1186, 1973.

[105] S. Orlandini, M. Mancini, C. Paniconi, and R. Rosso. Local contributions to infiltration excess runoff for a conceptual catchment scale model. *Water Resources Research*, 32(7):2003–2012, 1996.

[106] L. Pan, A. W. Warrick, and P. J. Wierenga. Downward water flow through sloping layers in the vadose zone: Time-dependence and effect of slope length. *Journal of Hydrology*, 199:36–52, 1997.

[107] H. L. Penman. Vegetation and hydrology. Technical communication, Commonwealth Bureau of Soils, Harpenden, England, 1951.

[108] C. D. Peters-Lidard, M. S. Zion, and E. F. Wood. A soil-vegetation-atmosphere transfer scheme for modeling — spatially variable water and energy balance processes. *Journal of Geophysical Research*, 102(D/4):4303–4324, 1997.

[109] J. Philip. Evaporation, moisture, and heat fields in the soil. *Journal of Meteorology*, 14(1):354–366, 1957.

[110] W. H. Press, S. A. Teukolsky, W. T. Vetterling, and B. P. Flannery. *Numerical recipes in C.* Cambridge University Press, New York, second edition edition, 1996.

[111] P. F. Quinn and K. J. Beven. Spatial and temporal predictions of soil moisture dynamics, runoff, variable source areas and evapotranspiration for Plynlimon, Mid-Wales. *Hydrological Processes*, 7:425–448, 1993.

[112] P. F. Quinn, K. J. Beven, and R. Lamb. The $\ln(a/\tan\beta)$ index: how to calculate it and how to use it within the TOPMODEL framework. *Hydrological Processes*, 9:161–182, 1995.

[113] T. H. Raines and J. B. Valdes. Estimation of flood frequencies for ungaged catchments. *Journal of Hydraulic Engineering ASCE*, 119:1138–1154, 1994.

[114] P. J. Restrepo-Posada and P. S. Eagleson. Identification of independent rainstorms. *Journal of Hydrology*, 55:303–319, 1982.

[115] R. A. Reyment and K. G. Joreskog. *Applied factor analysis in the natural sciences.* Cambridge University Press, New York, 1993.

[116] J. S. Risbey and D. Entekhabi. Observed Sacramento basin streamflow response to precipitation and temperature changes and its relevance to climate impact studies. *Journal of Hydrology*, 184:209–223, 1996.

[117] I. Rodríguez-Iturbe and J. B. Valdes. The geomorphologic structure of hydrologic response. *Water Resources Research*, 15(6):1409–1420, 1979.

[118] G. D. Salvucci. *Hillslope and climatic controls on hydrologic fluxes.* PhD thesis, MIT, 1994.

[119] G. D. Salvucci and D. Entekhabi. Comparison of the Eagleson statistical-dynamical water balance model with numerical simulations. *Water Resources Research*, 30(10):2751–2757, 1994a.

[120] G. D. Salvucci and D. Entekhabi. Equivalent steady soil moisture profile and the time compression approximation in water balance modeling. *Water Resources Research*, 30(10):2737–2749, 1994b.

[121] G. D. Salvucci and D. Entekhabi. Hillslope and climatic controls on hydrologic fluxes. *Water Resources Research*, 31(7):1725–1739, 1995.

[122] C. E. M. Sefton and S. M. Howarth. Relationships between dynamic response characteristics and physical descriptors of catchments in England and Wales. *Journal of Hydrology*, 211:1–16, 1998.

[123] H. W. Shen, G. J. Koch, and J. T. B. Obeysekera. Physically-based flood features and frequencies. *Journal of Hydraulic Engineering ASCE*, 116:494–514, 1990.

[124] V. P. Singh. Watershed modeling. In V. P. Singh, editor, *Computer models of watershed hydrology*, pages 1–22. Water Resources Publications, Highlands Ranch, CO, 1995.

[125] M. Sivapalan, K. Beven, and E. F. Wood. On hydrologic similarity, 2, A scaled model of storm runoff production. *Water Resources Research*, 23(12):2255–2278, 1987.

[126] M. Sivapalan, E. F. Wood, and K. J. Beven. On hydrologic similarity, 3, A dimensionless flood frequency model using a generalized geomorphologic unit hydrograph and partial area runoff generation. *Water Resources Research*, 26(1):43–58, 1990.

[127] M. Sivapalan, R. A. Woods, and J. D. Kalma. Variable bucket representation of TOPMODEL and investigation of the effects of rainfall heterogeneity. *Hydrological Processes*, 11(9):1307–1330, 1997.

[128] J. R. Slack and J. M. Landwehr. HCDN: A U.S. Geological Survey streamflow data set for the United States for the study of climate variations, 1874–1988. Technical Report 92–129, USGS, 1992.

[129] J. R. Slack, A. M. Lumb, and J. M. Landwehr. Hydro-Climatic Data Network (HCDN): Streamflow data set, 1874–1988. Technical Report 93–4076, USGS, 1993.

[130] M. A. Sophocleous, J. K. Koelliker, R. S. Govindaraju, and T. Birdie. Integrated numerical modeling for basin-wide water management: the case of the Rattlesnake Creek basin in south-central Kansas. *Journal of Hydrology*, 214:179–196, 1999.

[131] A. N. Strahler. Quantitative geomorphology. In R. W. Fairbridge, editor, *The Encyclopedia of Geomorphology*, pages 898–912. Reinhold Book Corporation, New York, 1968.

[132] L. M. Tallaksen. A review of baseflow recession analysis. *Journal of Hydrology*, 165:349–370, 1995.

[133] D. G. Tarboton, R. L. Bras, and I. Rodríguez-Iturbe. The analysis of river basins and channel networks using digital terrain data. Technical Report 326, Ralph M. Parsons Laboratory for Water Resources and Hydrodynamics, Department of Civil Engineering, MIT, September 1989.

[134] D. G. Tarboton, R. L. Bras, and I. Rodríguez-Iturbe. On the extraction of channel networks from digital elevation data. *Hydrological Processes*, 5:81–100, 1991.

[135] J. C. Thompson and R. D. Moore. Relations between topography and water table depth in a shallow forest soil. *Hydrological Processes*, 10:1513–1525, 1996.

[136] J. Toth. A theory of groundwater motion in small drainage basins in central Alberta. *Journal of Geophysical Research*, 67:4375–4387, 1962.

[137] J. Toth. Mapping and interpretation of field phenomena for groundwater reconnaissance in a prairie environment, Alberta, Canada. *International Association for Hydrological Science Bulletin*, 11(2):1–49, 1966.

[138] P. A. Troch, M. Mancini, C. Paniconi, and E. F. Wood. Evaluation of a distributed catchment scale water balance model. *Water Resources Research*, 29(6):1805–1817, 1993.

[139] U. S. Geological Survey. National water information system. http://waterdata.usgs.gov/nwis-w/US/, 1999.

[140] R. E. Walpole and R. H. Myers. *Probability and statistics for engineers and scientists.* Macmillan Publishing Company, New York, 1989.

[141] A. W. Western, G. Bloschl, and R. B. Grayson. Geostatistical characterisation of soil moisture patterns in the Tarrawarra catchment. *Journal of Hydrology*, 205:20–37, 1998a.

[142] A. W. Western, G. Bloschl, and R. B. Grayson. How well do indicator variograms capture the spatial connectivity of soil moisture? *Hydrological Processes*, 12:1851–1868, 1998b.

[143] A. W. Western, R. B. Grayson, and T. R. Green. The Tarrawarra project: high resolution spatial measurement, modelling and analysis of soil moisture and hydrological response. *Hydrological Processes*, 13:633–652, 1999.

[144] K. X. Whipple, 1998. Personal communication.

[145] D. M. Wolock and J. Gregory J. McCabe. Comparison of single and multiple flow direction algorithms for computing topographic parameters in TOPMODEL. *Water Resources Research*, 31(5):1315–1324, 1995.

[146] D. M. Wolock and C. V. Price. Effects of digital elevation model map scale and data resolution on a topography-based watershed model. *Water Resources Research*, 30(11):3041–3052, 1994.

[147] E. F. Wood and C. S. Hebson. On hydrologic similarity, 1, Derivation of the dimensionless flood frequency curve. *Water Resources Research*, 22(11):1549–1554, 1986.

[148] E. F. Wood, D. P. Lettenmaier, and V. G. Zartarian. A land-surface hydrologic parameterization with subgrid variability for general circulation models. *Journal of Geophysical Research*, 97(D3):2717–2728, 1992.

[149] R. A. Woods and L. K. Rowe. Consistent temporal changes in spatial variability of subsurface flow across a hillside. *Journal of Hydrology New Zealand*, 35(1):51–86, 1996.

[150] J. K. Wynn. Seasonal and geographic variability in rainstorm parameter distributions. Master's thesis, MIT, 1994.

[151] J. A. Yeakley, W. T. Swank, L. W. Swift, G. M. Hornberger, and H. H. Shugart. Soil moisture gradients and controls on a southern Appalachian hillslope from drought through recharge. *Hydrology and Earth System Sciences*, 21(1):41–49, 1998.

[152] Y. B. Zecharias and W. Brutsaert. The influence of basin morphology on groundwater outflow. *Water Resources Research*, 24(10):1645–1650, 1988.

[153] W. Zhang and D. R. Montgomery. Digital elevation model grid size, landscape representation, and hydrologic simulations. *Water Resources Research*, 30(4):1019–1028, 1994.